



HAL
open science

Controlled quantum dot array segmentation and complete two-electron spin state readout

Martin Nurizzo

► **To cite this version:**

Martin Nurizzo. Controlled quantum dot array segmentation and complete two-electron spin state readout. Physics [physics]. Université Grenoble Alpes [2020-..], 2023. English. NNT : 2023GRALY006 . tel-04122643

HAL Id: tel-04122643

<https://theses.hal.science/tel-04122643>

Submitted on 8 Jun 2023

HAL is a multi-disciplinary open access archive for the deposit and dissemination of scientific research documents, whether they are published or not. The documents may come from teaching and research institutions in France or abroad, or from public or private research centers.

L'archive ouverte pluridisciplinaire **HAL**, est destinée au dépôt et à la diffusion de documents scientifiques de niveau recherche, publiés ou non, émanant des établissements d'enseignement et de recherche français ou étrangers, des laboratoires publics ou privés.

THÈSE

Pour obtenir le grade de

DOCTEUR DE L'UNIVERSITÉ GRENOBLE ALPES

École doctorale : PHYS - Physique

Spécialité : Physique de la Matière Condensée et du Rayonnement

Unité de recherche : Institut Néel

Segmentation d'une chaîne de boîtes quantiques et lecture complète d'un état de spin à deux électrons

Controlled quantum dot array segmentation and complete two-electron spin state readout

Présentée par :

Martin NURIZZO

Direction de thèse :

Tristan MEUNIER

Directeur de recherche, CNRS Délégation Alpes

Directeur de thèse

Pierre-André Mortemousque

CEA

Co-encadrant de thèse

Rapporteurs :

ANDREA MORELLO

Professeur, University of New South Wales

ISABELLE ROBERT-PHILIP

Directeur de recherche, CNRS DELEGATION OCCITANIE EST

Thèse soutenue publiquement le **16 janvier 2023**, devant le jury composé de :

ANDREA MORELLO

Professeur, University of New South Wales

Rapporteur

ISABELLE ROBERT-PHILIP

Directeur de recherche, CNRS DELEGATION OCCITANIE EST

Rapporteuse

DAVID FERRAND

Professeur des Universités, UNIVERSITE GRENOBLE ALPES

Président

MATTHIEU DESJARDINS

Docteur en sciences, C12 QUANTUM ELECTRONICS

Examineur

Invités :

BAPTISTE JADOT

Docteur en sciences, CEA CENTRE DE GRENOBLE



A mes parents

Contents

Contents	iv
Introduction	1
1 Isolation and readout of electron spins	5
1.1 Isolating electrons in quantum dots	6
1.1.1 Fabrication of lateral quantum dots	6
1.1.2 Model of a quantum dot	8
1.1.3 Remote charge sensing	11
1.2 Electron spin states	14
1.2.1 Electron spin states in a single quantum dot	15
1.2.2 Two-electron spin states in a double quantum dot	17
1.3 Couplings to the environment	21
1.3.1 Bloch sphere, relaxation, and decoherence	21
1.3.2 Hyperfine interaction	23
1.4 Spin readout techniques	27
1.4.1 Single spin readout	28
1.4.2 Pauli spin blockade readout	29
1.5 Recent advancements for Pauli spin blockade readout	31
1.5.1 Latching mechanism	31
1.5.2 Cascade mechanism	32
1.6 Conclusion	34
2 Experimental setup and RF-reflectometry	36
2.1 Introduction	37
2.2 Device presentation	37
2.3 Sample fabrication	38
2.3.1 Process flow in the clean room	38
2.3.2 Electrostatic potential simulations	41
2.4 Cryogenics	42
2.5 Electronics	44
2.5.1 DC/AC signal generation and signal acquisition	44
2.5.2 Printed circuit board design	45
2.6 Software environment	46
2.6.1 Measurement software	46
2.6.2 Raw data analysis	49
2.7 High fidelity RF-SET based charge readout	50
2.7.1 Introduction	50
2.7.2 RF-SET working principle and theoretical design	51
2.7.3 Device and resonant circuit elements	53
2.7.4 Reflectometry setup	56
2.7.5 Single-shot readout and fidelity benchmark	59

2.7.6	Conclusion	62
3	Charge control in an isolated quantum dot array and on-demand segmentation	64
3.1	Introduction	65
3.1.1	Device presentation	65
3.1.2	Charge readout via DC current measurements	67
3.2	Operation of a QD array in the isolated regime	67
3.2.1	Stability diagrams in the open regime	67
3.2.2	Electron loading procedure	69
3.2.3	Probing the isolated regime boundaries	72
3.2.4	Detuning control of a double quantum dot in the isolated regime	73
3.3	Controlled quantum dot array segmentation via a highly tunable interdot tunnel coupling	74
3.3.1	Introduction	74
3.3.2	Metastable charge state lifetime	76
3.3.3	Demonstration of on-demand array segmentation	77
3.4	Conclusion	83
4	Complete two-electron spin state readout in a double quantum dot	85
4.1	Introduction	86
4.2	Pauli spin blockade in the fully isolated regime	86
4.2.1	Frozen Pauli spin blockade readout protocol	87
4.2.2	Spin initialization	92
4.2.3	Readout fidelity benchmark	96
4.2.4	Application: Exchange interaction characterization	99
4.2.5	Application: Exchange oscillations	101
4.3	Tools for complete spin state readout	106
4.3.1	S-T+ adiabatic transformation	106
4.3.2	Parity readout	109
4.4	Complete two-electron spin state readout protocol	113
4.4.1	Presentation of the protocol	113
4.4.2	Characterization on various initial spin states	115
4.4.3	Complete readout procedure for two-electron spin manipulations	117
4.5	Conclusion	119
	Conclusion and perspectives	122
	Bibliography	I
	Acknowledgements	XXI

Introduction

ALONG with general relativity, quantum electrodynamics is among the most tested theories in physics allowing for predictions in a myriad of physical systems with unprecedented precision [Peskin2018]. This framework allowed for so many major scientific and technical achievements during the last century that it would be elusive to make an exhaustive list, however, we can cite the ones that most impacted the different scientific domains to demonstrate how much quantum physics is important. In solid state physics the understanding of superconductivity, in particle physics the development of the standard model, the advent of quantum chemistry to understand the influence of the electronic structure on the properties of molecules and finally in medicine the possibility to perform magnetic resonance imaging to generate live images of the organs.

While being used by a large part of the scientific community quantum physics intricacies are difficult to grasp even for experts, indeed, the framework comes with intriguing principles that have no equivalent in classical physics. For instance, the Heisenberg principle states the existence of complementary variables such as speed and position that cannot be known with infinite precision [Kennard1927]. Even more specific to the quantum realm is the possibility to witness a quantum superposition of states where, until measurement, the system can be represented by a sum of distinct quantum states. On top of that quantum entanglement, arising when a particle cannot be described without considering the state of the others, produces correlations when measured that is not grasped by classical physics [Aspect1982].

Considering this ensemble of properties makes the simulation of quantum systems with more than 50 particles nearly impossible without dramatic approximations highly limiting the precision of the output [Georgescu2014]. Indeed, the number of parameters describing the quantum state composed of N particles is e^N , making it very demanding in terms of memory even for supercomputers. To tackle this issue Feynman proposed in 1981, during his famous talk "*Simulating physics with computers*", that the simulation of such a system could be efficiently tackled by a novel type of computer called quantum computer composed of elements already integrating the laws of quantum mechanics [Feynman1982]. A few years later, Deutsch formalizes such a computer by introducing its core element the quantum bit or qubit [Deutsch1985] and Lloyd proves almost a decade later that it can be used to create a universal quantum simulator [Lloyd1996]. The qubit is defined as a quantum mechanical two-level system usually noted $|0\rangle$ and $|1\rangle$ with the ability to be put in a superposition of state described as $a|0\rangle + b|1\rangle$ where $a, b \in \mathbb{C}$ and $|a|^2 + |b|^2 = 1$. The ability of such a computer to simulate large quantum systems could have important repercussions in pharmaceu-

tics for instance and is today a field of research on its own called quantum simulation. In parallel to quantum simulation, researchers started considering using a quantum computer to tackle more efficiently problems that are poorly treated by classical computers. In 1994, Shor demonstrated through an algorithm using the characteristics of the quantum computer, that it was possible to accelerate the factorization of large numbers in two prime numbers [Shor1994]. Through this work, the community realized the potential of quantum computing and the repercussions it could have on today's cryptography protocols for instance and it led the path to many more algorithms harnessing the quantum properties of qubits.

From there, strong objections were raised concerning the capability to experimentally build such a computer [Preskill2021]. The decoherence and the relaxation to which every qubit is subject could be limiting too much the fidelity of the operations needed to perform the theorized algorithms efficiently. Indeed, while every two-level quantum system can act as a qubit they are not all good candidates. Therefore Di Vincenzo proposed a set of five rules for the experimental implementation of a quantum computer [DiVincenzo2000]:

1. *A scalable physical system with well-characterized qubits.*
2. *The ability to initialize the state of the qubits.*
3. *Long coherence time compared to the operation time.*
4. *A universal set of quantum gates.*
5. *The capability to measure specific qubits.*

One of the first realizations of a qubit was performed using the outer electron of an ion trapped by electromagnetic waves. These qubits are today notoriously known to be weakly coupled to their environment and therefore to have a very long coherence time (3 s) [Cirac1995, Ladd2010]. Nowadays, many platforms are being developed with their pros and cons, and it will be irrelevant to make an exhaustive list in this thesis introduction. However, we can cite along trapped ions, qubits with long coherence times such as photons polarization [Crespi2011], Nitrogen Vacancy (NV) centers in diamond [Jelezko2004] and nuclear spins ensemble controlled by Nuclear Magnetic Resonance [Jones2011]. Solid state qubits such as superconducting circuits [Nakamura1999, Barends2014, Arute2019] or electrons stored in semiconducting quantum dots demonstrate smaller coherence times [Philips2022], but it is usually compensated by smaller gate operation times and in the end, achieve comparable operation fidelities.

Independently of the chosen platform to encode it, the qubit is prone to errors due to decoherence, relaxation, and dephasing and cannot be used directly as a computational qubit. The implementation of surface code, which consists in using several physical qubits to build a single errorless logical qubit could be a solution for practical quantum computing with imperfect qubits [Bravyi1998, Fowler2012]. The requirements to implement such code are an already high enough gate fidelity (> 99%) and connectivity between the qubits and their closest neighbors in a square lattice. The use of electron spins trapped in semiconductor quantum dots seems to

be a promising platform for such implementation and will be the focus of this thesis. Thanks to recent developments in material fabrication, spin initialization, control, and readout, 99% fidelity is now routinely achieved in different devices and host materials [Warren2022, Mądzik2022, Noiri2022, Xue2022]. On top of that, spin qubits have another advantage compared to other qubit platforms, their potential scalability for large-scale quantum computing. Indeed, the fabrication techniques used to create potential traps for the electrons are very similar to the ones used in the microelectronic industry, especially now with the recent demonstrations of qubits in silicon Metal-Oxide-Semiconductor (MOS) structures [Niegemann2022]. It should be in theory possible to leverage this industrial power to create large arrays of quantum dots in a reproducible manner and to integrate them with classic CMOS electronics for their control [Li2018, Veldhorst2017, Vinet2018, Vandersypen2017].

Given the current state of the art, large-scale spin-based quantum computing remains out of reach due to the variability between the quantum dot parameters and the hardware footprint needed. Among all the challenges to be tackled such as device fabrication, electronics, cryogenics, software development, and qubit control, in this thesis we decided to focus on the reduction of complexity and hardware overhead to operate and readout spin qubits. More precisely, we will perform charge control in a linear array of quantum dots and demonstrate array segmentation to reduce the number of available charge states by the system. Using this new capability, we will demonstrate a novel type of readout allowing the discrimination between the four two-electron spin states. This thesis is divided as follows. [chapter 1](#) is dedicated to the basic concepts used thorough the whole thesis, we start by discussing electron isolation and charge sensing before defining electron spins and how they couple to their environment. Finally, we focus on spin readout techniques and the recent developments for their integration on dense quantum dot arrays. In [chapter 2](#), we present the experimental setup used to perform the experiments of array segmentation and complete readout as well as the work made on RF-reflectometry for charge readout. In [chapter 3](#), we demonstrate in a triple quantum dot linear array the control of the interdot tunnel barrier at the nanosecond timescale from the GHz to sub-Hz regime. We use this development to isolate a subpart of the array in a metastable configuration while performing charge displacement and readout in the rest of the system. We show that partitioning of the system with the help of the inter-dot tunnel barriers can lead to a simplification for tuning and offers protection against unwanted charge displacement. Using this new capability we develop in [chapter 4](#) a protocol of readout allowing to discriminate the four two-electron spin states. The protocol is based on repetitive single shot measurements using Pauli spin blockade and our ability to tune on fast timescales the interdot tunnel coupling rate over more than ten orders of magnitude.

1

Isolation and readout of electron spins

Contents

1.1	Isolating electrons in quantum dots	6
1.1.1	Fabrication of lateral quantum dots	6
1.1.2	Model of a quantum dot	8
1.1.3	Remote charge sensing	11
1.2	Electron spin states	14
1.2.1	Electron spin states in a single quantum dot	15
1.2.2	Two-electron spin states in a double quantum dot	17
1.3	Couplings to the environment	21
1.3.1	Bloch sphere, relaxation, and decoherence	21
1.3.2	Hyperfine interaction	23
1.4	Spin readout techniques	27
1.4.1	Single spin readout	28
1.4.2	Pauli spin blockade readout	29
1.5	Recent advancements for Pauli spin blockade readout	31
1.5.1	Latching mechanism	31
1.5.2	Cascade mechanism	32
1.6	Conclusion	34

1.1 Isolating electrons in quantum dots

Quantum dots (QD) are artificial atoms used to trap, manipulate and probe a few electrons or holes. They recreate a local trapping potential analogous to the one generated by atoms, over lengths comparable to electrons/holes Fermi wavelength and therefore exhibit the wave-like behavior of the trapped particles. These trapped particles are the source of rich physics, certain aspects of which are grasped by classical electrostatic models. However, these systems also exhibit some purely quantum phenomena such as coherent superposition of states or entanglement that need to be treated with the appropriate quantum formalism. In the past years several realizations of such quantum dots have been realized using a myriad of different platforms and techniques, such as self-assembled quantum dots [Klein1996], ion-implanted donors [Pla2013], electrostatically trapped molecules [Urdampilleta2011], carbon nanotubes [Dekker1999] and finally semiconductor lateral [Kouwenhoven1997] or vertical dots [Kouwenhoven2001]. The work presented in this thesis has been performed using lateral quantum dots defined electrostatically in a GaAs/AlGaAs heterostructure platform.

1.1.1 Fabrication of lateral quantum dots

The GaAs/AlGaAs heterostructure

Thanks to the recent developments in semiconductor fabrication, it is possible today to deposit atomic layers of different semiconducting materials one after the other. This is achieved with a high level of control on the interface roughness and with a low density of unintentional impurities using a technique called molecular beam epitaxy. When two different materials are successively deposited, the result is called a heterostructure and it is central to the platform used to create quantum dots in this work. The GaAs/AlGaAs heterostructure involves two semiconductors of different band gaps, creating a sharp potential well at the interface 110 nm below the crystal (see Figure 1.1(a)). Thanks to the small lattice mismatch (7 %) between the two semiconductors the interface is almost defect-free, yielding a high mobility electron gas in this region of the heterostructure [Manfra2014]. The AlGaAs layer is doped with Si donors and separated from the potential well by a spacer formed by undoped AlGaAs, providing protection against electron scattering in the potential well. At cryogenic temperatures (100 mK), a fraction of the Si donors is ionized providing each one electron to the potential well. In this region, electrons accumulate in such a tightly confined region of space that quantization of the electron states is observed with a large energy splitting (typically 16 meV) [Nakata1994]. At 100 mK, the thermal energy ($\sim 8\mu\text{eV}$) is small compared to the energy level splitting, electrons are therefore only occupying the first level of the quantum well. In the end, the system is considered purely bi-dimensional and will be referred to as two-dimensional electron gas (2DEG). Such heterostructures are widely used to fabricate high electron mobility transistors (used in cryogenic amplifiers for instance [Weinreb2007]) and are used as a highly versatile test bed to study mesoscopic physics [Meirav1990, Park2002].

We used in this work a GaAs/Al_{0.33}Ga_{0.67}As heterostructure provided as part of a scientific

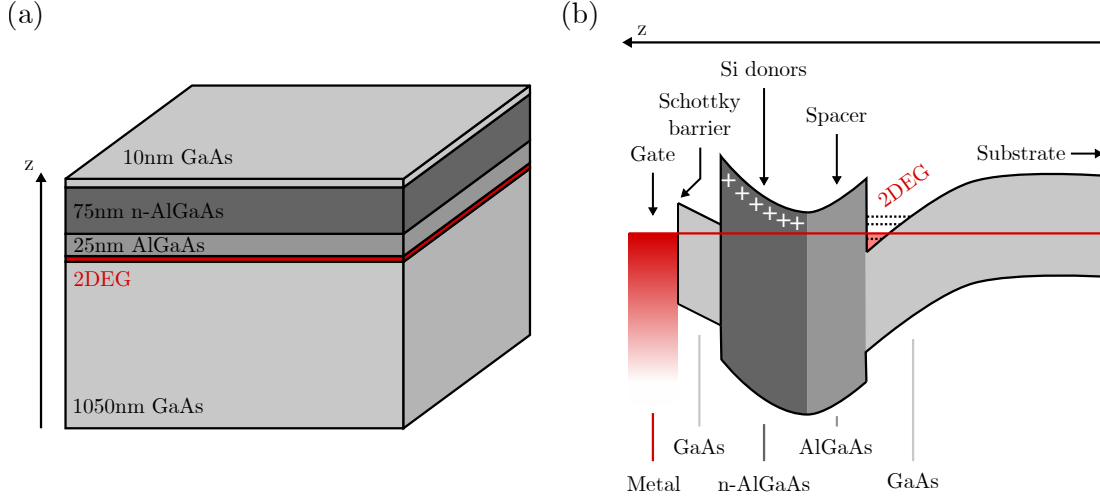


Figure 1.1: Schematic of the AlGaAs/GaAs heterostructure used. **a**, Schematic of the heterostructure used to fabricate the devices presented in this work. The 2DEG is located at the AlGaAs/GaAs interface 110 nm below the surface. **b**, Band structure along the growth axis. A triangular potential well is formed at the buried GaAs/AlGaAs interface below the Fermi level. The Si donors implemented in the AlGaAs allow to bend the bands and provide electrons to the 2DEG. The spacer is formed to separate spatially the ionized donors from the 2DEG.

collaboration by the group of Andreas D. Wieck from the Ruhr-University in Bochum, Germany. The heterostructure fabrication recipe and especially the doping location and concentration have been carefully engineered to provide a low density of scatterers in the 2DEG region. It is located 110 nm below the surface of the crystal and has an electron mobility μ_e and density n_e of:

$$\begin{aligned}\mu_e &= 9 \times 10^5 \text{ cm}^2 \text{ V}^{-1} \text{ s}^{-1} \\ n_e &= 2.79 \times 10^{11} \text{ cm}^{-2}.\end{aligned}\tag{1.1}$$

From this, we can infer the mean free path of the electrons in the 2DEG:

$$l_e = \sqrt{2\pi n_e} \frac{\hbar \mu_e}{e} = 8 \mu\text{m},\tag{1.2}$$

where e is the electron charge and \hbar the reduced Planck constant. Using this heterostructure it is therefore possible to define micrometer-length structures where the electron transport is fully ballistic.

Gate-defined structures

Now that we have seen how the heterostructure provides electron confinement along the z -axis, we focus on the completion of the potential well in order to create a quantum dot confining the electrons along the x and y -axis. A variety of methods exists to achieve this such as etching of the 2DEG [Kristensen2000], local oxidation [Fuhrer2001], or charging [Crook2003]. While these methods have shown great results, they lack the versatility and tunability of the electrostatic potential landscape needed to create large-scale quantum dot structures.

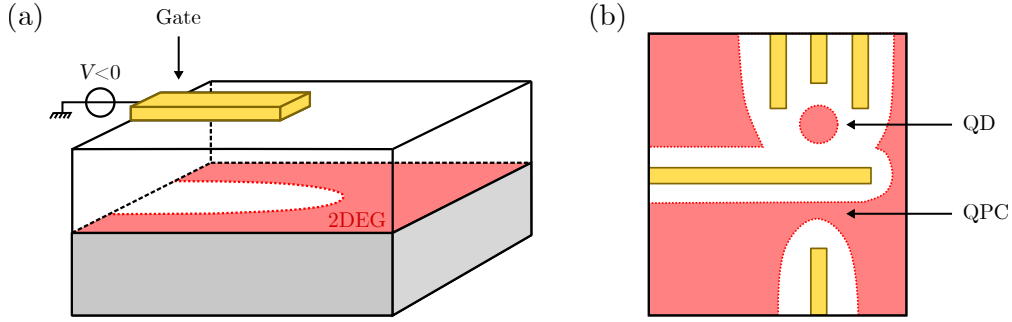


Figure 1.2: Depletion and shaping of the 2DEG gas by surface gates. **a**, Schematic illustrating the depletion of the 2DEG when a negative voltage is applied to a gate deposited on the surface of the crystal. **b**, By polarizing metallic gates it is possible to shape an arbitrary potential landscape at the 2DEG depth and therefore pattern it into various shapes. In this work, we will typically form quantum dots and quantum point contacts.

In this work, lateral confinement is obtained by depositing metallic gates on top of the heterostructure and polarizing them with negative voltages. As shown in Figure 1.1(b), the gate forms a Schottky barrier with the semiconductor allowing to apply negative voltages without current flowing from the gate to the 2DEG. This specificity allows the experimenter to create an arbitrary potential landscape at the 2DEG level and create nanostructures as depicted in Figure 1.2. Indeed, by applying negative voltages to the gates it is possible to modulate the electrons density and even completely deplete the 2DEG in specific regions of the device. By carefully layering multiple gates and applying the correct voltages of each gate it is even possible to form small fully isolated islands of electrons. In order to observe the wave-like behavior of the electrons, it is necessary to reduce the size of this island at the scale of the Fermi wavelength defined as follows:

$$\lambda_F = \sqrt{\frac{2\pi}{n_e}} \simeq 50 \text{ nm}. \quad (1.3)$$

As we will see in section 2.3, in a clean room it is possible to form arbitrarily shaped metallic gates using electron beam lithography and lift-off techniques with a resolution as low as 20 nm. We will therefore be able to create nanostructures with a typical size smaller than λ_F .

1.1.2 Model of a quantum dot

When considering the total energy of a quantum dot, two main effects must be taken into account. The quantization of the energy states within the quantum dot due to the tight confinement, and the electrostatic repulsion of the electrons stored.

Energy level quantization

Due to the small size of the quantum dot compared to the Fermi wavelength, the electrons are occupying quantized energy states. As we have seen previously, the electrons in the GaAs/AlGaAs heterostructure are considered with a two-dimensional motion. When confined electrostatically using metallic gates, the physical system is modeled by considering an electron with an effective

mass m^* trapped in a 2D harmonic potential [Kouwenhoven1997]. The result of this model is the apparition of quantized states, analogous to orbital states in atomic physics and with a typical energy spacing of:

$$\Delta E_{orb} \simeq \frac{\hbar^2 \pi^2}{m^* L^2} \simeq 0.5 \text{ meV}, \quad (1.4)$$

where $L \simeq 100 \text{ nm}$ is the characteristic size of the confinement potential and $m^* = 0.067 m_0$ is the effective mass of the electrons in GaAs. Thanks to the low effective electron mass in GaAs and the small size of the electrostatic confinement, we obtain a large energy separation of the orbital states equivalent to the thermal energy obtained at 6 K. Thus, we can resolve this orbital energy spacing using commercially available cryogenic equipments (10 mK to 4 K).

Constant interaction model

On top of these quantum phenomena, some classical energy scales must be defined. Since electrons in quantum dots are charged particles, in proximity they exhibit a strong Coulomb repulsion.

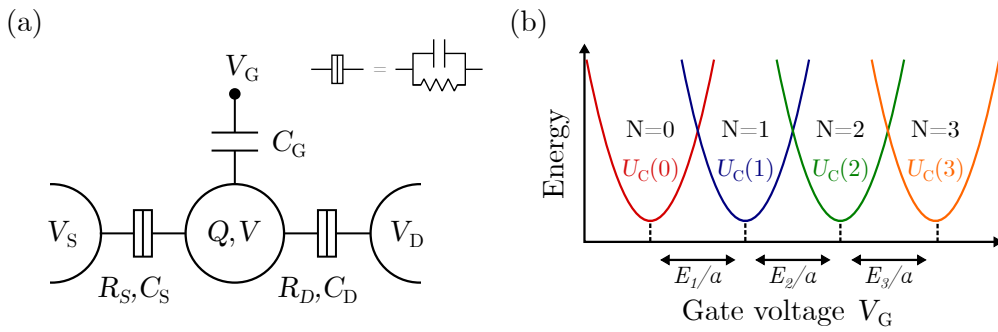


Figure 1.3: Quantum dot in the constant interaction model. a, Circuit equivalent of a quantum dot in the constant interaction model. The quantum dot (middle circle) contains Q electrons and has a potential V . It is capacitively coupled to a control gate V_G and can exchange electrons with the source and drain via tunneling resistances (resistance in parallel with a capacitor). **b**, Energy stored in the quantum dot has a function of the voltage V_G . The number of charges in the quantum dot ground state increases with the voltage V_G , the gate is an efficient way to electrically tune the occupation of the quantum dot.

To evaluate the energetic cost of adding one electron when N are already present (charging energy), we will develop a semi-classical approach, the constant interaction model [Kouwenhoven1997]. We consider a quantum dot with a source (S) and drain (D) from which electrons can be exchanged and a metallic gate (G) used to tune the chemical potential of the quantum dot. The quantum dot is modelled as a charged island tunnel-coupled to the source, drain, and capacitively coupled to the metallic gate. The tunnel barriers are electrically described as leaking capacitors (capacitance in parallel with a resistor) and the full electric circuit is depicted in Figure 1.3(a).

The electrostatic energy stored in the quantum dot U_{el} is defined as:

$$U_{el} = \frac{1}{2}(C_S + C_D + C_G)V^2, \quad (1.5)$$

where C_S , C_D , and C_G are the capacitances formed between the quantum dot and the source, drain, and gate respectively, and V is the potential of the quantum dot. We define $C = C_S + C_D + C_G$ as the total capacitance of the quantum dot. If we now consider the quantum dot having a total charge Q due to the N electrons, we have :

$$Q = -Ne = C_S(V - V_S) + C_D(V - V_D) + C_G(V - V_G), \quad (1.6)$$

where e is the absolute value of the electron charge and V_S , V_D , and V_G are the potentials applied to the source, drain, and gate respectively. To obtain the electrostatic energy U_{el} of the quantum dot as a function of the electrons stored in it, we combine [Equation 1.5](#) and [Equation 1.6](#) and obtain:

$$U_{el}(N) = \frac{1}{2C}(-eN + C_S V_S + C_D V_D + C_G V_G)^2. \quad (1.7)$$

We observe that the electrostatic energy of the quantum dot is modified through the different parameters of the system (V_S , V_D , and V_G). However, in this work, we will see that it is experimentally easier to control the number of charges N by tuning the voltage applied on G and setting the source and drain voltages to ground as depicted in [Figure 1.3\(b\)](#).

Now to obtain the total energy of the quantum dot, one must add the energy of the discrete levels the electrons are occupying in the quantum dot. This contribution is written as:

$$U(N) = U_{el}(N) + \sum_{i=1}^N E_i, \quad (1.8)$$

where E_i is the energy of the orbital containing electron i . Finally, the chemical potential is defined as the change of total energy between the states where the quantum dot contains N and $N - 1$ electrons, we consider here the simple case where the source and drain are grounded $V_S = V_D = 0$:

$$\mu(N) = U(N) - U(N - 1) = (N - \frac{1}{2})E_C + E_N + e\frac{C_G}{C}V_G, \quad (1.9)$$

with $E_C = \frac{e^2}{C}$ the charging energy defining the electrostatic energy cost to add an electron to the quantum dot. In this result, $e\frac{C_G}{C}$ defines the so-called gate lever arm or α -factor which gives the conversion from the voltage applied to the metallic gate to the chemical potential of the quantum dot. This α -factor is an important parameter to estimate and optimize while designing quantum dot structures since it defines the efficiency of a gate voltage to change the electron occupation of a given quantum dot. Experimentally it is defined by several factors such as the gate shape, the gate-dot distance, the nature of the dielectric separating the gate and the quantum dot, and the screening of neighbor gates [[Volk2019](#), [Chanrion2021](#)].

To evaluate the charging energy we approximate the quantum dot as a charged disk of diameter $L = 100$ nm. The capacitance of such a disk is defined as:

$$C_{self} = 4\epsilon_r\epsilon_0L = 46 \text{ aF}, \quad (1.10)$$

where ϵ_0 is the vacuum permittivity and ϵ_r the relative permittivity of GaAs. This gives a charging energy of around $E_C = 3.5$ meV, this value is an overestimation since we are not considering additional capacitances towards the 2DEG around the quantum dot, or the other gates of the device. But nevertheless, this is close to the experimentally obtained values in previous works [Baumgartner1997].

Concluding this evaluation of the energy scales, we observe that $E_C > E_{orb} > k_B T$, where k_B is the Boltzmann constant and $T \simeq 10$ mK is the base temperature of a dilution cryostat. The electron occupation of the quantum dot is therefore mostly defined by the Coulomb repulsion and each level of the quantum dot can be resolved thanks to the low temperature of the system.

1.1.3 Remote charge sensing

We have seen that the quantum dot chemical potential is varied in an experimentally controlled fashion via voltages applied to metallic gates. However, probing the charge dynamics of such systems requires the ability to detect single electron charges inside the nanostructure. To do so, we develop here a non-invasive method based on a single electron transistor (SET) acting as a local electrometer for the quantum dot.

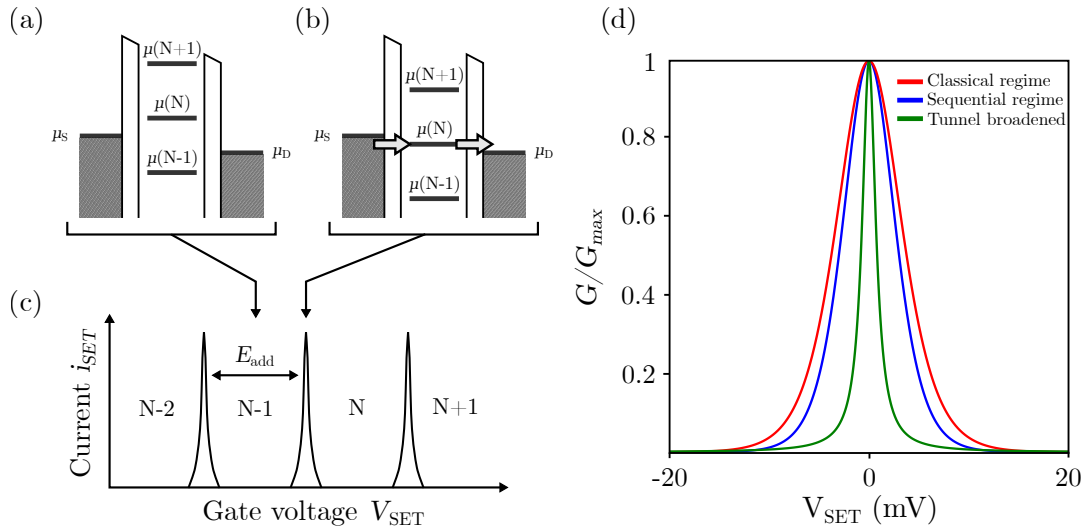


Figure 1.4: Single electron transistor. **a**, Chemical potential of the SET in the blocked configuration. The SET is biased using the source and drain located on each side of the SET. **b**, Chemical potential of the SET in the transmitting regime. When $\mu(N)$ is present in the bias window, current is measured through the SET. **c**, I - V_{SET} characteristic curve of the SET, adapted from [Hanson2007]. As mentioned previously the gate voltage V_{SET} is used to adjust the SET chemical potential and therefore its electron occupation. Peaks of current (Coulomb peaks) are observed for precise values of V_{SET} and correspond to the SET being in the configuration depicted in **b**. It is worth noting that on the side of Coulomb peaks i_{SET} is highly sensitive to V_{SET} . **d**, Coulomb peak shape as a function of the working regime considered. The parameters taken are $T = 100$ mK, $\alpha = 1/20$ and $\Gamma = 1$ MHz. The peaks are normalized by the maximum conductance G_{max} for clarity.

To understand this technique, we first need to detail the I-V response of a quantum dot connected to a source and drain. This particular configuration is often referred to as SET. A repre-

sensation of the energy diagram of the considered system is shown in [Figure 1.4\(a\)](#), with in the middle the quantum dot chemical potential and on each side the source and drain modeled as cold electron reservoirs following a Fermi distribution. We assume here that $\mu(N) \ll k_B T$ so that each level of the quantum dot is resolved and the Fermi distribution approximated as a step function. In the case of a small bias window, most of the configurations of the system will result in a blockade of the current flowing from the source to the drain. Indeed, as depicted in [Figure 1.4\(a\)](#) it is energetically favorable for the electrons to flow from the source to the drain, however, no energy levels are available in between the chemical potentials of the reservoirs. This situation is called Coulomb blockade and has been first observed in a SET in 1986 by D.V. Averin *et al.* [[Averin1986](#)]. The Coulomb blockade regime is lifted by adjusting the quantum dot chemical potential using the dedicated gate voltage V_{SET} . If the system is tuned so that the chemical potential of the system sits in the bias window ($\mu_S > \mu(N) > \mu_D$) electron tunneling through the quantum dot is observed. This situation, shown in [Figure 1.4\(b\)](#), induces a non-zero current i_{SET} through the structure. Thus, by sweeping the voltage applied to the gate controlling the chemical potential of the quantum dot we observe peaks of current alternating with Coulomb blockaded regions as shown in [Figure 1.4\(c\)](#). We notice here that on the side of a Coulomb peak the current i_{SET} is highly sensitive to the gate voltage, but also any perturbation of the SET's electrostatic environment, in particular, electrons hopping in or out of a neighbor quantum dot [[Wei1997](#), [Kiyama2018](#)].

The particular shape of the Coulomb peaks (and therefore the sensitivity of the SET, defined as $\frac{\partial i_{\text{SET}}}{\partial V_{\text{SET}}}$) has been extensively studied by the community [[Beenakker1991](#), [Averin1991](#), [Stopa1993](#), [Song2015](#)]. Depending on the temperature several regimes of evolution are observed. First, for high temperatures the SET conduction G is considered through a quasi-continuum of states and is therefore described as:

$$G/G_{\text{max}} = \cosh^{-2} \left(\frac{\alpha V_{\text{SET}}}{2.5 k_B T} \right) \quad \text{if } h\Gamma, \Delta E_{\text{orb}} \ll k_B T \ll E_C \text{ (classical regime)}, \quad (1.11)$$

where G_{max} is the maximum conductance at the degeneracy point, α the gate α -factor, T the electronic temperature, and Γ the tunnel coupling rate between the SET and the reservoirs (considered here equal for the left and right one). However, in our systems, $T \simeq 100 \text{ mK}$ is usually low compared to the energy level spacing ΔE_{orb} so that the transport through the SET is carried via a single orbital state of the SET. In this case, the conductance is defined as:

$$G/G_{\text{max}} = \cosh^{-2} \left(\frac{\alpha V_{\text{SET}}}{2 k_B T} \right) \quad \text{if } h\Gamma \ll k_B T \ll \Delta E_{\text{orb}}, E_C \text{ (sequential regime)}. \quad (1.12)$$

In [Figure 1.4\(d\)](#), we compare the evolution of the conductance G as a function of the SET gate voltage. When the electronic temperature is reduced the conductance peak becomes sharper around the degeneracy point $V_{\text{SET}} = 0$. It is therefore desirable to reduce as low as possible the temperature of the sample to have a highly sensitive electrometer. However, even for extremely low temperatures, the Coulomb peak does not become infinitely sharp. Indeed, when the reservoir-SET tunnel coupling becomes large compared to the thermal energy we enter the tunnel broadened

regime where the shape of the peak is described by the Breit-Wigner formula [Breit1936]:

$$G/G_{max} = \frac{(h\Gamma)^2}{(h\Gamma)^2 + (\alpha V_{SET})^2} \quad \text{if } k_B T \ll h\Gamma \text{ (tunnel broadened)}. \quad (1.13)$$

As we can see in Figure 1.4(d), in this case, the Coulomb peak has a Lorentzian shape and its sharpness is defined entirely by the reservoir-SET tunnel coupling. Looking at Equation 1.13, it is desirable to reduce Γ in order to increase the sensitivity of the readout. However, with reducing Γ comes the technical challenge to measure extremely low values of current which limits the measurement bandwidth. In the end, the perfect SET for remote charge sensing is operated at a low enough temperature $T \simeq 100\text{mK}$ and tunnel coupling $\Gamma \simeq 1\text{GHz}$, so that the broadening of the Coulomb peak is defined by Γ and the measurement bandwidth is not limited by the capacity to measure low values of currents.

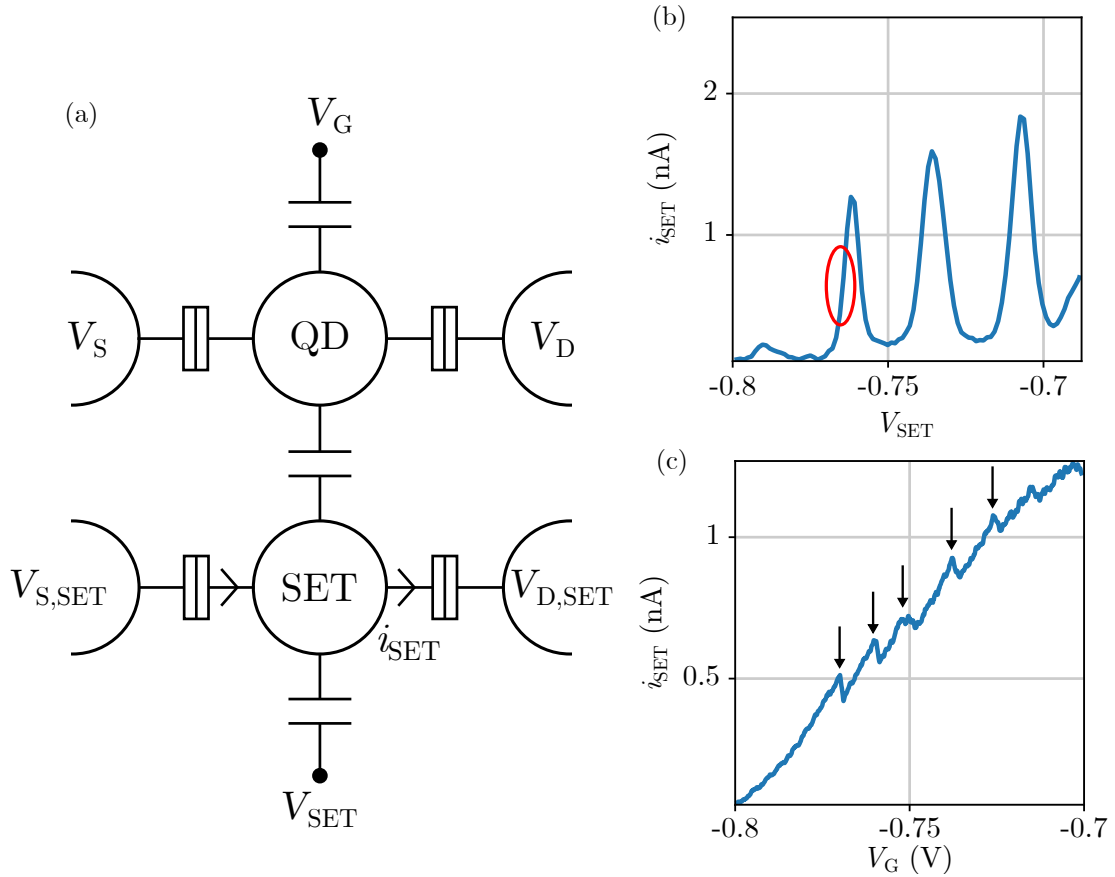


Figure 1.5: Remote charge sensing via a single electron transistor acting as an electrometer. **a**, Schematic circuit of a quantum dot sensed by a single electron transistor. The source and drain of the quantum dot are grounded and the voltage V_G controls its chemical potential. The SET is biased using its dedicated source and drain to induce a current i_{SET} across it and is capacitively coupled to the quantum dot. **b**, Coulomb peaks measured across the single electron transistor. On the side of the peaks, the current flowing across the SET is highly sensitive to its electric environment. The SET gate voltage is adjusted on the side of a Coulomb peak (see red circle). **c**, Observation of steps in the SET current corresponding to a variation of charge in the sensed quantum dot.

To detail the working principle of the remote electrometer we present the system pictured in [Figure 1.5\(a\)](#), where we consider a SET acting as a sensing dot capacitively coupled to a quantum dot being the probed dot. Both quantum dots are tunnel coupled to a source and drain, capacitively coupled to a gate, and have the same working principle introduced in the previous paragraph. In this simplified picture, we neglect the second-order cross capacitance for instance between the sensing dot gate and the sensed dot. The sensed dot is capacitively coupled to the SET so that no electrons are exchanged between the two, however, electrons can be loaded using the electron reservoirs. As shown in [Figure 1.5\(b\)](#), the sensing dot is tuned on the side of a Coulomb peak using the voltage V_{SET} in order to maximize the current i_{SET} sensitivity to the electrostatic environment. An electron entering the sensing dot electrostatic environment is viewed as a more negative V_{SET} gate voltage shifting the Coulomb peak position. To demonstrate this effect we sweep the voltage V_G to modify the electron occupation of the sensed dot while recording the sensing dot current and observe the typical trace shown in [Figure 1.5\(c\)](#). Two main effects are observed as V_G is increased, first a global increase in the SET current corresponds to the capacitive coupling between the gate G and the SET. On top of this general trend, we observe sharp jumps in i_{SET} highlighted by black arrows. Each jump corresponds to an electron tunneling from the source (or drain) to the sensed dot.

The charge occupation information of the sensed quantum dot is therefore contained in the current jumps. The size of the current variation is directly related to the sensitivity of the SET with respect to the sensed dot (typically $1 \text{ nA } e^{-1}$). The sensitivity is a function of different factors such as the distance between the SET and the quantum dot and the derivative of the SET current with respect to the SET gate voltage at the readout position ($\frac{\partial i_{\text{SET}}}{\partial V_{\text{SET}}}$). Using this variation in the sensitivity depending on the quantum dot distance it is possible to sense several quantum dots using a single SET [[Chanrion2021](#), [Philips2022](#)].

1.2 Electron spin states

In the previous sections, we discussed the electrostatic properties of electrons in a quantum dot system. The demonstrated level of control allowed recent works to use the charge degree of freedom to encode so-called charge qubits for quantum computing [[Gorman2005](#), [Peterson2010](#), [Stehlik2012](#)]. However, despite the developments made in materials and pulse shaping, the relaxation ($\sim 20 \text{ ns}$) and coherence time ($\sim 1 \text{ ns}$) of such qubits remain too low to reach high fidelity operations [[Petta2004](#), [Li2015](#)]. This is mostly due to the predominance of charge noise in semiconducting materials. To tackle this issue, we chose in this work to encode the quantum information on the spin degree of freedom of the electron. Unlike charge, the spin couples weakly to charge noise, but it is sensitive to global and local fluctuations of the magnetic field mostly induced in semiconducting platforms by the nuclear spins of the atoms compos-

ing the host material [Yoneda2018]. Hopefully, it is possible to mitigate the effect of the magnetic fluctuators on the spin qubit coherence time by either implementing dynamic decoupling techniques [Malinowski2017] or choosing a low-nuclear-spin host platform via isotope purification [Veldhorst2014, Eng2015]. In this section, we will first detail the simplest case of a single spin stored in a single quantum dot and then study the core of this work, the two-electron spin state stored in a double quantum dot.

1.2.1 Electron spin states in a single quantum dot

One electron spin state

The spin operator in quantum physics is defined as $\hat{S} = (\hat{S}_x, \hat{S}_y, \hat{S}_z)$ and is analogous to a measurement of the angular momentum of the particle. More precisely, the electron has a spin number $S = \frac{1}{2}$ which defines the two eigenstates of \hat{S}_z as :

$$\hat{S}_z \left| \pm \frac{1}{2} \right\rangle = \pm \frac{1}{2} \hbar \left| \pm \frac{1}{2} \right\rangle, \quad (1.14)$$

where $\hbar = \frac{h}{2\pi}$ is the normalized Planck constant. If we now assume that the electron is experiencing a static magnetic field along the z -axis of amplitude B_z , the Hamiltonian of the system is written as:

$$H_{spin} = \hbar \gamma_e B_z \cdot \hat{S}_z \quad (1.15)$$

with the gyromagnetic ratio $\gamma_e = \frac{g^* \mu_B}{\hbar}$ where g^* is the Landé-factor and μ_B the Bohr magneton. The eigenstates of such Hamiltonian are therefore the one of the S_z operator, and they are commonly written as $|\uparrow\rangle$ and $|\downarrow\rangle$ when the spin is aligned and opposed with the magnetic field respectively. Moreover, the applied magnetic field has for effect to lift the degeneracy between the two states by the Zeeman splitting:

$$\begin{aligned} E_{\uparrow} &= \frac{1}{2} \hbar \gamma_e B_z \\ E_{\downarrow} &= -\frac{1}{2} \hbar \gamma_e B_z. \end{aligned} \quad (1.16)$$

Since the electron g -factor is negative $g^* = -0.425$ in GaAs 2DEGs, the ground state of the system is the spin aligned with the magnetic field [Nowack2007]. The g -factor is defined by the band gap energy of the crystal, the effective mass of the electrons in the heterostructure, and the spin-orbit splitting of the valence band [Weisbuch1977].

Two electrons spin states

In the previous section, we studied the single spin system under a static magnetic field. However, in this work, all the experiments have been conducted with at least two electrons. We will therefore develop here how having two indistinguishable electrons in the same quantum dot affects the spin of the whole system.

To understand how we build the two-electron spin states, we have to take into account the Pauli exclusion principle and the fact that the electrons are fermions. Therefore, the wavefunction describing their quantum state must be antisymmetric with respect to the exchange of two particles. To meet these conditions, we will describe the possible states of the system by decomposing them into tensor products of a state describing its orbital state in the quantum dot, and a spin part describing the spin state of the electrons.

Under these conditions, we can build the spin states by considering a quantum dot with its two lowest energy orbital states $|g\rangle$ and $|e\rangle$ as represented in [Figure 1.6\(b\)](#). We first consider the case of the electron spins being antiparallel, since the electrons are indistinguishable the spin part of the wavefunction is either described by $\frac{|\uparrow\downarrow\rangle - |\downarrow\uparrow\rangle}{\sqrt{2}}$ or $\frac{|\uparrow\downarrow\rangle + |\downarrow\uparrow\rangle}{\sqrt{2}}$. In the first (second) case, the spin part of the wavefunction is antisymmetric (symmetric), the orbital part of the wavefunction must therefore be symmetric (antisymmetric) which defines the S and T_0 spin states:

$$\begin{aligned} |S\rangle &= |gg\rangle \otimes \frac{|\uparrow\downarrow\rangle - |\downarrow\uparrow\rangle}{\sqrt{2}} \\ |T_0\rangle &= \frac{|ge\rangle - |eg\rangle}{\sqrt{2}} \otimes \frac{|\uparrow\downarrow\rangle + |\downarrow\uparrow\rangle}{\sqrt{2}}. \end{aligned} \quad (1.17)$$

If we now consider the case where the electron spins are parallel, the spin part of the wavefunction is either $|\uparrow\uparrow\rangle$ or $|\downarrow\downarrow\rangle$. In this case, the spin part is symmetric, we therefore need to construct as previously an antisymmetric orbital part of the wavefunction. Doing so we define the T_+ and T_- states as:

$$\begin{aligned} |T_+\rangle &= \frac{|ge\rangle - |eg\rangle}{\sqrt{2}} \otimes |\uparrow\uparrow\rangle \\ |T_-\rangle &= \frac{|ge\rangle - |eg\rangle}{\sqrt{2}} \otimes |\downarrow\downarrow\rangle. \end{aligned} \quad (1.18)$$

Through these considerations, we have constructed the four lowest energy spin states. In the following work, the singlet spin state is often referred to as S and the three triplet states as T_0 , T_+ , and T_- . It is possible to construct similar wavefunctions involving higher excited orbital states of the quantum dot, however, most of the experiments performed in this work can be interpreted by considering the described states.

Considering the orbital part of the states, we observe that the triplet spin states involve an electron on the excited orbital of the quantum dot, while for the singlet spin state both electrons are in the ground state. At zero magnetic field $|S\rangle$ is therefore energetically separated from the $|T\rangle$ states by the exchange energy J_0 . It is interesting to notice that in general for a two-electron quantum dot $J_0 < E_{orb}$, the single electron quantum dot orbital energy defined in [Equation 1.4](#). Indeed, the antisymmetry of the orbital part of $|T_0\rangle$ and the occupation of different orbitals reduce the Coulomb energy of the triplet states with respect to the singlet one [[Tarucha2000](#), [Hanson2007](#)]. We will see in the following sections that this energy difference is at the core of the spin readout techniques. If we now consider the spin part, $|S\rangle$ and $|T\rangle$ have a total spin number of $S = 0$

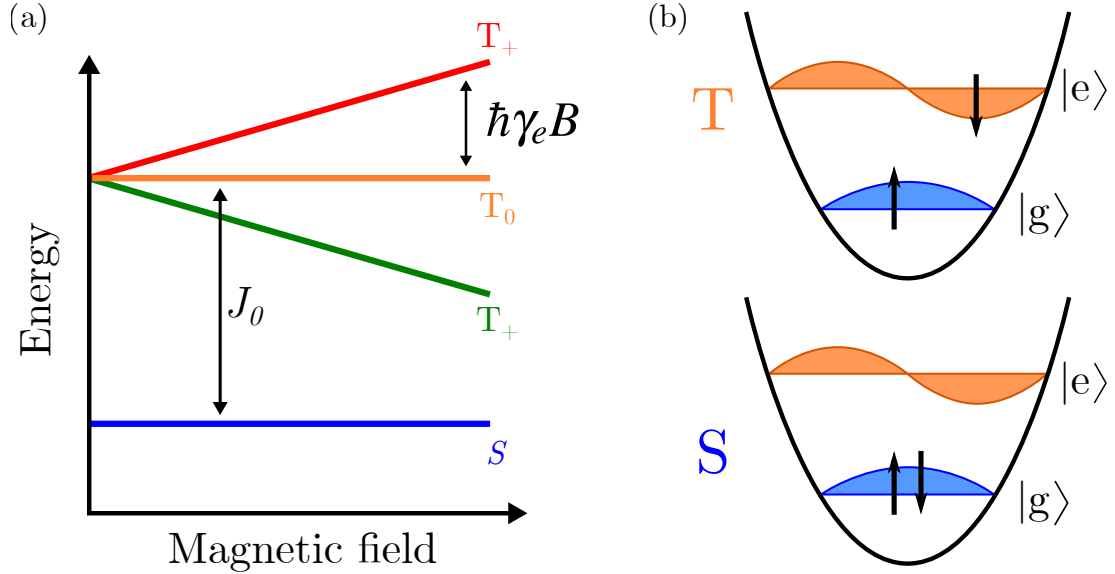


Figure 1.6: Description of the two-electron spin states in a single quantum dot. **a**, Energy diagram of the first four two-electron spin states. The S and T_0 states are separated by the exchange energy J_0 . The three triplet states degeneracy is lifted by the Zeeman splitting $E_Z = \hbar\gamma_e B$ using a magnetic field B . **b**, Schematic representation of the orbital part differentiating a singlet from a triplet spin state.

and $S = 1$ respectively. It is therefore possible to lift the three triplet spin states degeneracy by applying a magnetic field as observed in [Figure 1.6\(a\)](#). Indeed, $|T_+\rangle$ and $|T_-\rangle$ have a non-zero magnetic moment $m_s = \pm 1$ and are therefore subject to the Zeeman splitting. For high magnetic field values ($B > 4$ T), the Zeeman splitting overcomes J_0 and the ground state of the quantum dot is $|T_+\rangle$ [[Petta2005a](#)].

1.2.2 Two-electron spin states in a double quantum dot

We now consider two tunnel-coupled quantum dots containing a total of two electrons and we will study the effect of the double quantum dot parameters on the previously described spin states. The double quantum dot is described by two main values, first the tunnel coupling t_c is mostly given by the potential barrier height between the quantum dots. Secondly, the potential detuning ε is given by the energy difference between the two potential minima. As we can see in [Figure 1.7](#), in GaAs/AlGaAs quantum dots these two parameters are electrically controllable by tuning the gate voltages defining the double quantum dot.

We note the possible charge configurations as (n_L, n_R) where n_L and n_R are the number of electrons located in the left and right quantum dot respectively. When two electrons are loaded into the system three charge configurations are possible depending on the potential detuning value $(2,0)$ $(0,2)$ or $(1,1)$. The $(1,1)$ charge configuration is energetically favorable when $\varepsilon \simeq 0$, indeed the Coulomb repulsion energy is minimized by having the electrons separated. However, it is possible to overcome this repulsion and reach the $(2,0)$ and $(0,2)$ charge configurations when $\varepsilon \ll -E_C$ and $\varepsilon \gg E_C$ respectively.

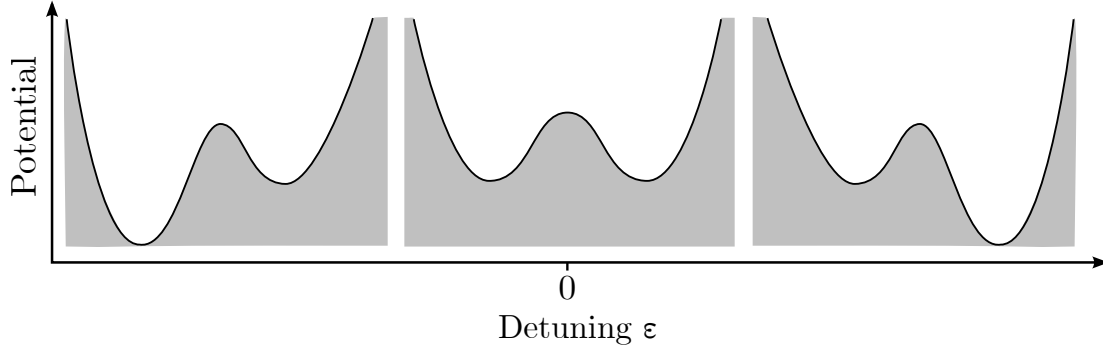


Figure 1.7: Schematic of the potential detuning control in a double quantum dot. Evolution of the potential landscape when the potential detuning of the double quantum dot is being modulated. The occupation by the two electrons of the left, right or both quantum dots can be favored using the potential detuning parameter.

To describe the system, we consider as before the two first orbitals of each quantum dot and a spin conservative tunneling process coupling the three possible charge states. The most basic model for describing this system is the Fermi-Hubbard one and assumes a constant charging energy [Burkard2021]. While other models exist such as the Hartree-Fock, Heitler-London, and Heisenberg [Hu2000, Hu2001, van der Wiel2006], the Fermi-Hubbard model with the description of the hyperfine interaction with nuclear spins gives a qualitative description of the experimental observations made in this thesis. Under these assumptions, the singlet spin state is described in the $(2,0)$, $(1,1)$, $(0,2)$ basis as:

$$H_{|S\rangle} = \begin{pmatrix} E_C + \varepsilon & t_c & 0 \\ t_c^* & 0 & t_c \\ 0 & t_c^* & E_C - \varepsilon \end{pmatrix}. \quad (1.19)$$

The same reasoning is performed for the $|T_0\rangle$ state by simply adding J_0 when the two electrons are located in the same quantum dot:

$$H_{|T_0\rangle} = \begin{pmatrix} E_C + J_0 + \varepsilon & t_c & 0 \\ t_c^* & 0 & t_c \\ 0 & t_c^* & E_C + J_0 - \varepsilon \end{pmatrix}. \quad (1.20)$$

The $|T_+\rangle$ and $|T_-\rangle$ states are described by the same Hamiltonian as $|T_0\rangle$ by taking into account

the Zeeman splitting energy when an external magnetic field B is applied:

$$H_{|T_{\pm}\rangle} = H_{|T_0\rangle} \pm \hbar\gamma_e B \begin{pmatrix} 1 & 0 & 0 \\ 0 & 1 & 0 \\ 0 & 0 & 1 \end{pmatrix}. \quad (1.21)$$

Finally, we can construct the complete Hamiltonian describing the first 16 two-electron spin states in a double quantum dot as:

$$H_{\text{DQD}} = \begin{pmatrix} H_{|S\rangle} & 0 & 0 & 0 \\ 0 & H_{|T_0\rangle} & 0 & 0 \\ 0 & 0 & H_{|T_+\rangle} & 0 \\ 0 & 0 & 0 & H_{|T_-\rangle} \end{pmatrix}. \quad (1.22)$$

To understand the particularities of this system, we start by considering the situation of an uncoupled double quantum dot $t_c = 0$ without magnetic field $B = 0$. In [Figure 1.8\(a\)](#), we represent the eigenvalues of H_{DQD} as a function of the potential detuning ε . In this case, independently of the spin state when the two electrons are in the (0,2) charge configuration ($\varepsilon > E_C$) the energy state will follow a $-\varepsilon$ dependence, here we retrieve the situation discussed in [section 1.2.1](#) where the $|S\rangle$ and $|T\rangle$ states are separated by J_0 and the three triplet spin states are degenerated. However, when considering the (1,1) charge configuration ($-E_C < \varepsilon < E_C$) the state energy is constant and equal to zero, indeed the energy given to the electron in the right quantum dot through the potential detuning is perfectly compensated by the one in the left quantum dot. In this regime of potential detuning, singlet and triplet spin states are degenerated. Indeed, the triplet spin states do not involve an electron occupying an excited orbital state of the quantum dots since the electrons are separated into two quantum dots.

We now perform the same analysis for $t_c > 0$, electron transfer from one quantum dot to another is now possible, and the energy diagram is represented in [Figure 1.8\(b\)](#). We observe in this case a hybridization of the $|S(1,1)\rangle$, $|S(0,2)\rangle$ and $|T_0(1,1)\rangle$, $|T_0(0,2)\rangle$ states near $\varepsilon = E_C$ and $\varepsilon = E_C + J_0$ respectively. It is characterized by an avoided crossing defined by the tunnel coupling amplitude. Interestingly, a non-zero tunnel coupling has for effect the bending of the energy states lowering the energy of the singlet spin state branch with respect to the triplet one. The exchange energy increases as the potential detuning and tunnel coupling grows, and will be used in this work to perform coherent oscillations between the two states. For $\varepsilon = 0$ this splitting referred to as exchange energy is defined in the Hubbard approximation as [[Reed2016](#), [Burkard2021](#)]:

$$J(\varepsilon = 0) = E_{T_0} - E_S = \frac{1}{2} \left(J_0 + \sqrt{E_C^2 + 8t_c^2} - \sqrt{(E_C + J_0)^2 + 8t_c^2} \right). \quad (1.23)$$

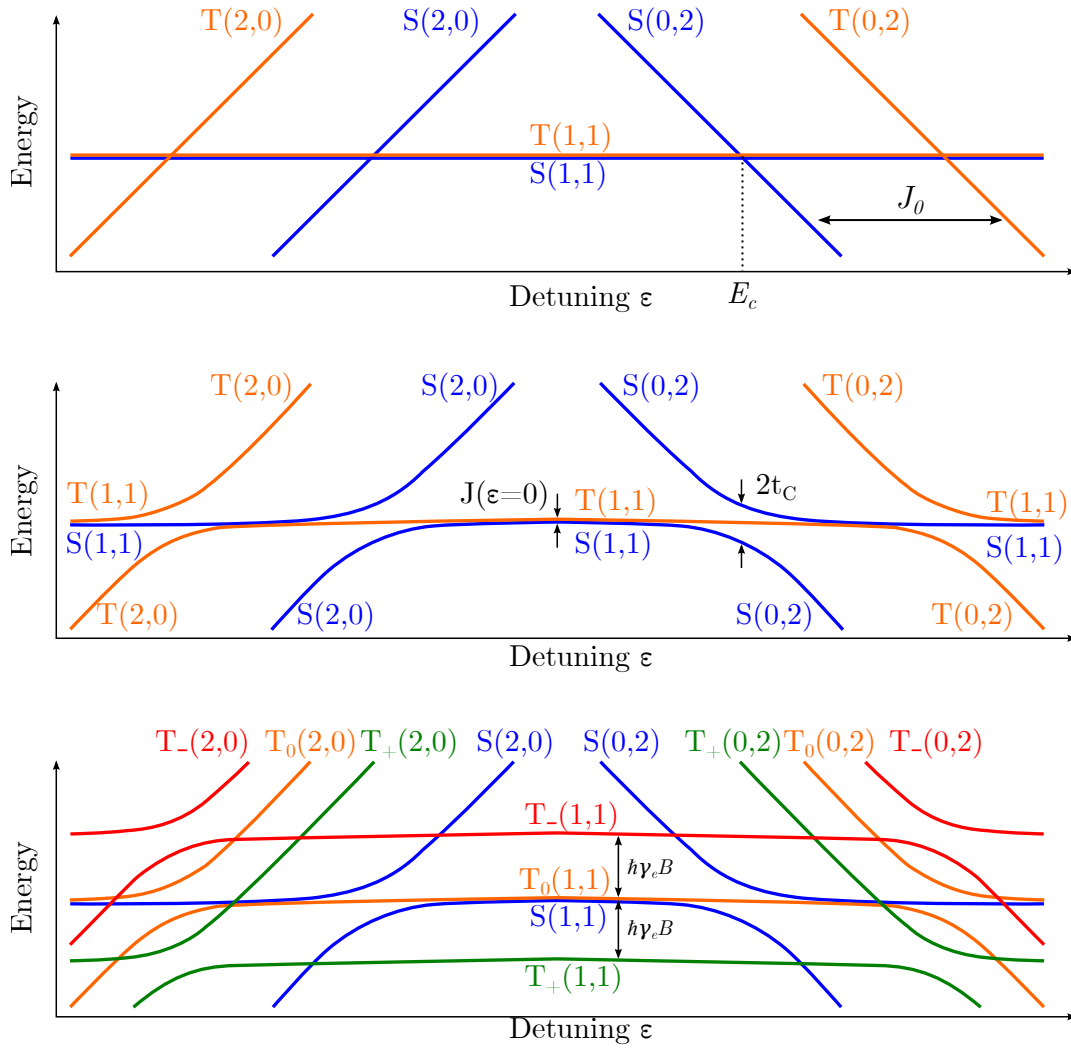


Figure 1.8: Two-electron spin states in a double quantum dot. Energy diagram of the two-electron spin states as a function of the potential detuning ε . **a**, $t_c = 0$ and $B = 0$, when the two electrons are in the (0,2) charge configuration ($\varepsilon > E_C$) the energy state will follow a $-\varepsilon$ dependence. **b**, $t_c > 0$ and $B = 0$, we observe the apparition of an avoided crossing between the states of same spin component but different charge configurations. **c**, $t_c > 0$ and $B > 0$, the degeneracy between the three triplet spin states is lifted by the Zeeman splitting.

Finally, in [Figure 1.8\(c\)](#) we consider the complete case where $t_c > 0$ and $B > 0$ and observe the Zeeman splitting lifting the degeneracy between the three triplet spin states. In practice, small avoided crossings (100 neV) appear at every S , T_+ , and S , T_- state intersections coupling the singlet spin state to T_+ and T_- , but they are not captured by the Fermi-Hubbard model. Their origin arises from the spin-orbit coupling or transverse hyperfine interaction as we will see in the following section.

1.3 Couplings to the environment

Now that we described the different two-electron spin states in a double quantum dot, we focus on the interaction between the spin states and their environment. More precisely, we will define the so-called hyperfine interaction between the nuclear spins of the host material and the two spins forming the qubit system. In this section, we will restrain the discussion to the so-called ST_0 qubit where the qubit states are defined as $|0\rangle = |S\rangle$ and $|1\rangle = |T_0\rangle$. We will see how these interactions enable complete electrical control of such qubit. Other definitions of the qubit are found in the literature such as ST_{\pm} but their actual implementation requires manipulation techniques beyond the scope of this thesis [[Petta2010](#), [Nichol2015](#), [Burkard2021](#)].

1.3.1 Bloch sphere, relaxation, and decoherence

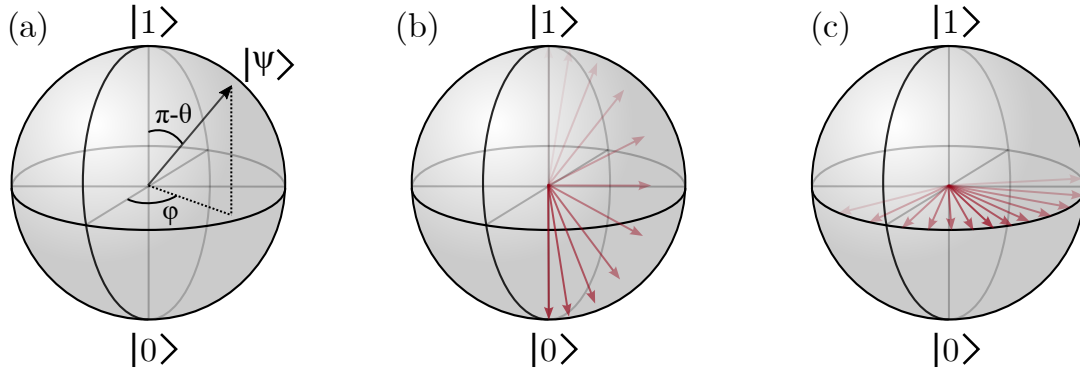


Figure 1.9: Quantum state evolution in the Bloch sphere. **a**, Representation of an arbitrary quantum state in the Bloch sphere. **b**, Illustration of the relaxation process characterized by the T_1 value. **c**, Illustration of the decoherence process resulting in a random phase and characterized by the T_2^* value.

A useful tool to introduce when discussing qubit evolution is the representation in the Bloch sphere. As mentioned in the introduction a qubit state $|\psi\rangle$ is written as:

$$|\psi\rangle = a|0\rangle + b|1\rangle, \quad (1.24)$$

where $a, b \in \mathbb{C}$ and $|a|^2 + |b|^2 = 1$. The normalization condition naturally leads to representing the

state as a point on the surface of a sphere of radius equal to 1. The qubit state is therefore rewritten as:

$$|\psi\rangle = \cos\left(\frac{\theta}{2}\right)|0\rangle + \sin\left(\frac{\theta}{2}\right)e^{i\phi}|1\rangle, \quad (1.25)$$

where the angles $\theta, \phi \in \mathbb{R}$ describe the quantum state on the Bloch's sphere as represented in [Figure 1.9\(a\)](#). In this representation, the $|0\rangle$ and $|1\rangle$ are respectively positioned at the south and north pole of the sphere.

During the operation of a qubit, it is necessary to set the values of θ and ϕ with the highest precision possible in order to perform high-fidelity operations. But the qubit being coupled to a non-controlled environment makes θ and ϕ subject to errors that we detail here.

We first discuss the relaxation process which corresponds to the qubit decaying to its ground state. Relaxation in the Bloch's sphere is represented in [Figure 1.9\(b\)](#) by an instantaneous collapse of the wavefunction to the south pole ($|0\rangle$ state). This relaxation process is characterized by the so-called T_1 time quantifying the time during which a qubit can keep its stored energy before exchanging it with the environment. In ST_0 qubits hosted in the GaAs/AlGaAs heterostructure, the relaxation is mostly induced by the coupling to the phonons of the crystalline structure and is therefore highly dependent on the energy splitting between the excited state and the ground state [[Fujisawa1998](#), [Meunier2007](#)]. In a single quantum dot, the relaxation from $|T_{\pm}\rangle$ to $|S\rangle$ is a non-monotonous function of the energy splitting between the two states and can vary from 0.1 ms to 2 ms [[Meunier2007](#)]. In the case of relaxation of $|T_0\rangle$ to $|S\rangle$ the energy splitting between the two states is fixed by the exchange energy J_0 (mostly defined by the confinement potential and Coulomb interaction), this results in a fixed relaxation rate of around 100 μ s for applied magnetic fields below 2 T [[Shen2007](#)]. In a double quantum dot, the value of relaxation of $|T_0(1,1)\rangle$ to $|S(0,2)\rangle$ has been experimentally observed to be highly dependent on the double quantum dot parameters, especially its potential detuning value (allowing to tune the energy splitting between the two states) and the magnetic field gradient between the two quantum dots [[Barthel2012](#)]. Indeed, T_1 was found to increase with increasing detuning following an ε^2 dependence.

Error along the ϕ value of the qubit, due to an uncertain and fluctuating environment, is not characterized by an exchange of energy but by a dephasing process. Indeed, as we can see in [Figure 1.9\(c\)](#) the latitude on the Bloch's sphere remains the same but the phase information is lost. This loss of information can be separated into two types called dephasing and decoherence with respective characteristic times T_2^* and T_2 . First, dephasing is observed when an operation is performed on an ensemble of qubits, or repeated on a single qubit. Each qubit or repetition of the operation experiences slightly different environmental parameters leading to uncertainty over the reached state at the end of the operation. Dephasing is therefore induced by spatial variations of the Hamiltonian parameters (in the case of an ensemble of qubits) or by slow fluctuations of the Hamiltonian parameters compared to the qubit operation time (in the case of a single qubit). Experimentally, the T_2^* value is estimated by a Ramsey experiment consisting in measuring the decay time of the free evolution of the qubit in a superposition of state $\frac{|0\rangle+|1\rangle}{\sqrt{2}}$ for instance). We will see in the following paragraph how a random hyperfine magnetic field generated by the

nuclear spins leads to low values of $T_2^* \simeq 10\text{ns}$ in the GaAs/AlGaAs platform. Interestingly, these spatial (or slow) variations of the qubit environment can be experimentally stabilized using dynamic nuclear polarization (DNP) techniques [Bluhm2010], or via rapid feedback on the qubit control [Shulman2014] to reach higher values of dephasing time $T_2^* \simeq 2\mu\text{s}$.

Second, decoherence characterizes the randomization of the phase of a single qubit due to variation of the Hamiltonian describing its evolution on fast timescales (compared to the typical operation time of the qubit). In GaAs/AlGaAs since the ST_0 qubit is a decoherence-free subsystem with respect to the magnetic field, decoherence is mostly due to GHz charge noise. In the case of dephasing, the randomly acquired phase by each member of the ensemble (or at each repetition of the operation) is constant and can therefore be reversed using dynamical decoupling techniques such as Hahn-echo [Hahn1950] or Carr-Purcell-Meiboom-Gill (CPMG) sequences [Bluhm2011]. This allows the experimenter to distinguish decoherence from dephasing. However, this is true only if it is possible to perform coherent operations on the qubit faster than the typical evolution time of the environment parameters of the ensemble of qubits. Depending on the dynamical decoupling technique used and its frequency, dephasing is, therefore, more or less suppressed leading to a variety of characteristic timescales ($T_2^{\text{Hahn}} \simeq 200\mu\text{s}$, $T_2^{\text{CPMG}} \simeq 30\mu\text{s}$) which all satisfy the following inequality:

$$T_2^* \leq T_2^{\text{CPMG}}, T_2^{\text{Hahn}} \leq 2T_1. \quad (1.26)$$

In the end, the characteristic values of relaxation decoherence and dephasing times are highly correlated to the platform used to host the qubit. For instance spin qubits using donors in nuclear-spin-free ^{28}Si exhibit coherence times exceeding seconds thanks to correct identification and suppression of the main decoherence sources [Tyryshkin2012]. In parallel to the development of materials, an ongoing effort of the community is also aiming at the development of faster manipulation and measurement techniques allowing to accelerate the feedback loop required to perform dynamical decoupling.

1.3.2 Hyperfine interaction

All the atoms composing the GaAs/AlGaAs heterostructure possess a non-zero nuclear spin value, interacting with the electron spin via hyperfine coupling. Indeed, the large size of the quantum dot compared to the heterostructure lattice unit cell has for consequence the electron spin interacting with many nuclear spins generating a random magnetic field referred to as Overhauser magnetic field (see Figure 1.10). In numerous experiments this interaction has been identified as the main source of decoherence of spin qubits in this particular platform [Johnson2005, Petta2005a, Koppens2005, Koppens2006]. It is therefore necessary to understand the interaction between the spin qubit and an ensemble of nuclei spins in order to develop techniques limiting this effect.

Single spin

We start by considering the case of a single spin coupled to a large ensemble of nuclear spins as represented in [Figure 1.10](#) and review the theory developed in [[Schulden1978](#), [Merkulov2002](#), [Khaetskii2002](#)]. This model will be used as a foundation to understand the decoherence mechanism of a ST_0 qubit operated in a double quantum dot.

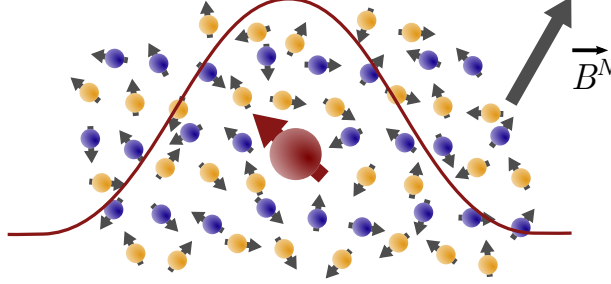


Figure 1.10: Hyperfine interaction with a single electron spin. The large ensemble of nuclear spins present in the heterostructure couples to the electron spin in the quantum dot via the hyperfine interaction. The ensemble of nuclear spins is modelled as a random effective magnetic field \vec{B}^N whose x , y , and z components follow a Gaussian distribution centered around zero.

The hyperfine contact interaction between the electron spin (denoted \hat{S}) and the lattice nuclear spins $\hat{I}_{\beta,j}$ is written as [[Paget1977](#)]:

$$H_{hf} = \hbar\gamma_e \sum_{\beta,j} b_{\beta} v_0 |\psi(\vec{r}_{j,\beta})|^2 \hat{S} \cdot \hat{I}_{\beta,j}. \quad (1.27)$$

Where $\psi(\vec{r}_{j,\beta})$ is the electron wavefunction and v_0 is the unit cell volume. The interaction is summed over all the unit cell j and the non-zero nuclear spins β . Each atom β generates its effective hyperfine field b_{β} depending on its hyperfine structure. Typically, in GaAs the isotopes are ^{75}As ($b_{75\text{As}} = -1.84\text{ T}$), ^{69}Ga ($b_{69\text{Ga}} = -1.52\text{ T}$) and ^{71}Ga ($b_{71\text{Ga}} = -1.95\text{ T}$).

It is interesting to rewrite H_{hf} by introducing a collective operator for the nuclear spins $\hat{B}^N = \sum_{\beta} b_{\beta} \sum_j v_0 |\psi(\vec{r}_{j,\beta})|^2 \hat{I}_{\beta,j}$:

$$H_{hf} = \hbar\gamma_e \hat{B}^N \cdot \hat{S} \quad (1.28)$$

The typical energy splitting between nuclear spin levels is in the order of 10 neV for an applied magnetic field of 1 T. Comparing this energy to the experimentally achievable thermal energy in dilution cryostat ($k_B T \simeq 1\ \mu\text{eV}$), we understand that it is impossible to fully polarize the ensemble of nuclear spins. In this high-temperature regime, the nuclear spin bath fluctuates and can therefore be considered as an additional random magnetic field \vec{B}^N referred to as the Overhauser magnetic field. The Overhauser field follows an isotropic 3D Gaussian distribution centered around zero and of standard deviation:

$$\sigma_{nuc} = \frac{B_{max}^N}{\sqrt{N}}, \quad (1.29)$$

where $B_{max}^N \simeq 5.3\text{ T}$ is the magnetic field generated by the nuclear spins in the low-temperature regime (all spins polarized), and N is the number of nuclear spins interacting with the single

electron spin. As seen previously the typical quantum dot size is around 100 nm and contains roughly $N \sim 10^6$ atoms yielding a standard deviation of $\sigma_{nuc} \simeq 5$ mT.

The random value of \vec{B}^N evolves with a characteristic time of 1 s along the axis parallel to the applied magnetic field [Barthel2009]. Along the two perpendicular axes, the characteristic time is shorter and around 10 μ s [Reilly2008]. If we now consider that a few tens of ns are needed to perform a typical spin qubit operation, we can consider that the nuclear spin configuration is static during a single realization of the operation. However, in between two operations, the readout often limits the repetition of the sequence to ~ 0.1 ms, we will consider its fluctuations between successive repetitions of the same operation. To understand how a random magnetic field can affect the spin state, we write the equation of motion of a spin state in a magnetic field \vec{B} . Here \vec{B} is the sum of the applied magnetic field $\vec{B}^{app} = (B_x^{app}, B_y^{app}, B_z^{app})$ and the Overhauser magnetic field \vec{B}^N [Merkulov2002]:

$$\hat{S}(t) = (\hat{S}_0 \cdot \vec{n}) \vec{n} + (\hat{S}_0 - (\hat{S}_0 \cdot \vec{n}) \vec{n}) \cos(\gamma_e t) + (\hat{S}_0 - (\hat{S}_0 \cdot \vec{n}) \vec{n}) \times \sin(\gamma_e t), \quad (1.30)$$

where \hat{S}_0 is the initial spin state and $\vec{n} = \vec{B}/|\vec{B}|$ the unit vector pointing in the direction of the total magnetic field (external and Overhauser) and $\gamma_e = \frac{g^* \mu_B}{\hbar} |\vec{B}|$. We now average the evolution of the spin state over the Gaussian distribution of \vec{B}^N and consider that $B_z^{app} \gg |\vec{B}^N|$. Under these conditions the evolution of the z-component of the spin state is not affected by the Overhauser magnetic field. However, the transverse components of the spin state $\langle \hat{S}_{trans.} \rangle$ decays as:

$$\langle \hat{S}_{trans.} \rangle(t) = \frac{\hat{S}_{trans.}}{2} \left(1 + e^{-\frac{1}{2}(\gamma_e \sigma_{nuc} t)^2} \right). \quad (1.31)$$

In the end, the randomness in the environment leads to dephasing and is characterized by [Merkulov2002, Taylor2007]:

$$T_2^* = \frac{\sqrt{2}}{\gamma_e \sigma_{nuc}}. \quad (1.32)$$

Taking into account the typical value $\sigma_{nuc} = 5$ mT, T_2^* is around 7 ns limiting drastically the coherence of the single spin system in AlGaAs heterostructures. Interestingly, it is possible to estimate the Overhauser magnetic field value faster than its fluctuation [Shulman2014]. Based on the extracted information a feedback loop can be implemented on the qubit control parameters allowing to limit the broadening in the possible Overhauser magnetic field values. Through this technique, T_2^* is increased above 2 μ s.

Two-electron spin in a double quantum dot

Now that we have developed the effect of the hyperfine interaction on a single spin, we move to the case where we consider a two-electron spin state in a double quantum dot. As represented in Figure 1.11(a), the electrons are located in two tunnel-coupled quantum dots experiencing a different effective magnetic field \vec{B}_L^N and \vec{B}_R^N for the left and right quantum dot respectively. Using

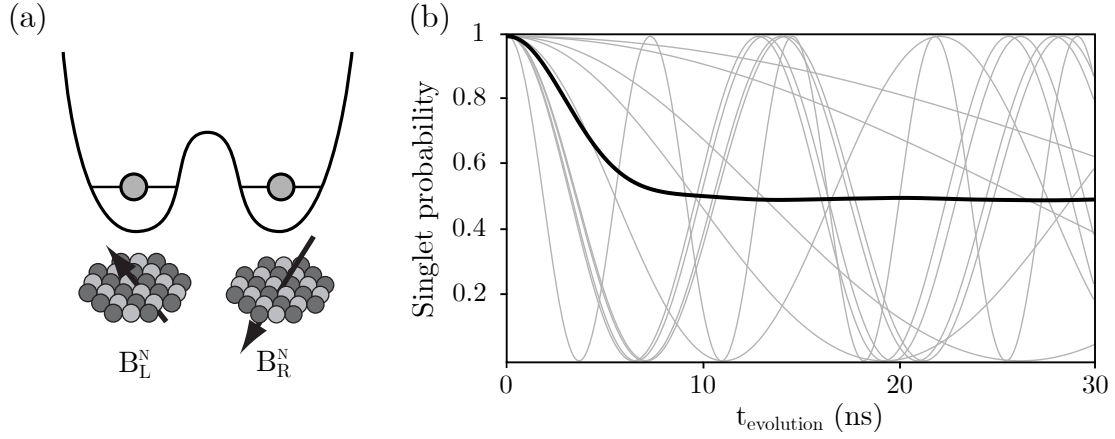


Figure 1.11: Hyperfine interaction for two electrons in a double quantum dot. **a**, In the (1,1) charge state configuration the two electrons experience a different effective magnetic field due to the randomness of the hyperfine magnetic field. Since these two effective magnetic fields are uncorrelated it results in an inhomogeneous decoherence time T_2^* and therefore state mixing. **b**, Decoherence of a singlet spin state under $H_{(1,1),m_s=0}$ (see Equation 1.35). When $J \ll \Delta B_z^N$ the oscillation frequency is mostly defined by the hyperfine magnetic field gradient which follows a Gaussian distribution of standard deviation σ_{nuc} . In gray, we plot the oscillations for specific values of ΔB_z^N and in black we averaged over 5000 realizations. The averaged trace exhibits the singlet spin state decoherence mechanism when electrons are experiencing different Larmor precession frequencies in two different quantum dots with a low J . The simulation parameters are $J = 1$ neV and $\sigma_{nuc} = 5$ mT yielding a $T_2^* = 7$ ns.

the same formalism developed in the previous section we can write the interaction between the two-electron spin state and the Overhauser field as [Hung2013]:

$$H_{hf} = \hbar\gamma_e(\vec{B}_R^N \cdot \hat{S}_R + \vec{B}_L^N \cdot \hat{S}_L), \quad (1.33)$$

where \hat{S}_L and \hat{S}_R are the spin state of the electron located in the left and right quantum dot respectively. To have a better vision of the effect of this interaction on the different possible spin states we project it onto the $\{S, T_0, T_+, T_-\}$ basis and obtain:

$$H_{hf} = \hbar\gamma_e \begin{pmatrix} 0 & \Delta B_z^N & \frac{\Delta B_x^N + i\Delta B_y^N}{\sqrt{2}} & \frac{-\Delta B_x^N + i\Delta B_y^N}{\sqrt{2}} \\ \Delta B_z^N & 0 & 0 & 0 \\ \frac{\Delta B_x^N - i\Delta B_y^N}{\sqrt{2}} & 0 & B_{z,R}^N + B_{z,L}^N & 0 \\ \frac{-\Delta B_x^N - i\Delta B_y^N}{\sqrt{2}} & 0 & 0 & -(B_{z,R}^N + B_{z,L}^N) \end{pmatrix}, \quad (1.34)$$

where $B_{z,L}^N$ and $B_{z,R}^N$ and the z -components of the Overhauser magnetic field in the left and right quantum dot respectively, and $\Delta B_i^N = B_{i,L}^N - B_{i,R}^N$ is the magnetic field difference between the two quantum dots along the i axis. Through this Hamiltonian, we observe that all the triplet spin states are coupled to the singlet spin state via either the z component of the magnetic field gradient for T_0 or the transverse one for T_+ and T_- .

In the case of the operation of a ST_0 qubit (large Zeeman splitting), the sub-system is described by the following Hamiltonian:

$$H_{(1,1),m_s=0} = \begin{pmatrix} J & \hbar\gamma_e\Delta B_z^N \\ \hbar\gamma_e\Delta B_z^N & 0 \end{pmatrix} \quad (1.35)$$

where J is the exchange coupling between the two spin states, controlled via either the interdot tunnel coupling or the potential detuning as seen in [section 1.2.1](#). Since $m_s = 0$ for both spin states, the ST_0 qubit is insensitive to global variations of the magnetic field. However, it is still subject to the magnetic field gradient present in between the two quantum dots through the term ΔB_z^N present in the Hamiltonian. As seen previously, the magnetic field gradient arises from the local Overhauser magnetic field of each quantum dot and is the main source of decoherence of single electron spins. To illustrate its impact, we simulate a T_2^* experiment by computing the time evolution of a singlet spin state when $J \ll \hbar\gamma_e\Delta B_z^N$. We consider again here that the value of ΔB_z^N remains constant during the evolution of the spin state but changes when the experiment is repeated. The singlet spin state probability is plotted in gray as a function of the evolution time in [Figure 1.11\(b\)](#) for several random values of ΔB_z^N following a Gaussian distribution centered around zero and with a standard deviation $\sigma_{nuc} = 5$ mT. We observe that the frequency of the oscillations is dictated by the energy splitting between the two states $\hbar\gamma_e\Delta B_z^N$. When averaging these oscillations over 5000 realizations of the experiment (black curve in [Figure 1.11\(b\)](#)) the oscillations are damped and leave the place to the envelope of a Gaussian distribution with characteristic time $T_2^* = 7$ ns. For long evolution times $t_{evolution} \gg T_2^*$, the singlet spin state probability decreases (loss of coherence) and tends to 50 %. In this regime, the state becomes a statistical mixture of S and T_0 spin states.

1.4 Spin readout techniques

The direct measurement of a single electron spin is a scientific challenge achieved in 2004 by D. Rugar et al. [[Rugar2004](#)]. However, its demonstration involved magnetic resonance force microscopy techniques which are impracticable in the design of a scalable quantum computing platform based on spin qubits where thousands of electron spins must be measured in a few ms. To circumvent this technical difficulty and provide efficient and scalable solutions to measure a single or two-electron spin state, the community has developed different techniques that we detail here. As we have seen in [subsection 1.1.3](#), it is experimentally achievable to measure the charge configuration of a small system of quantum dots by using a SET acting as a local electrometer. Most of the spin readout techniques are therefore relying on a spin-to-charge conversion process where the spin information is converted into charge configuration information.

1.4.1 Single spin readout

The first spin-to-charge conversion presented relies on the energy splitting between the two states we want to discriminate. As seen previously, this splitting is obtained via the use of a static magnetic field in the case of a single spin and via the naturally present exchange energy in the case of a two-electron spin state. To generalize the discussion we will therefore consider here a ground state $|G\rangle$ and an excited one $|E\rangle$. This readout has been first implemented by Elzerman et al. in 2004 [Elzerman2004] in order to read out the polarization of a single spin stored in a GaAs/AlGaAs quantum dot and is therefore usually referred to as Elzerman readout. Since then, it has also been used to perform the readout of a two-electron spin state allowing the discrimination between a singlet spin state and a triplet spin state [Meunier2006].

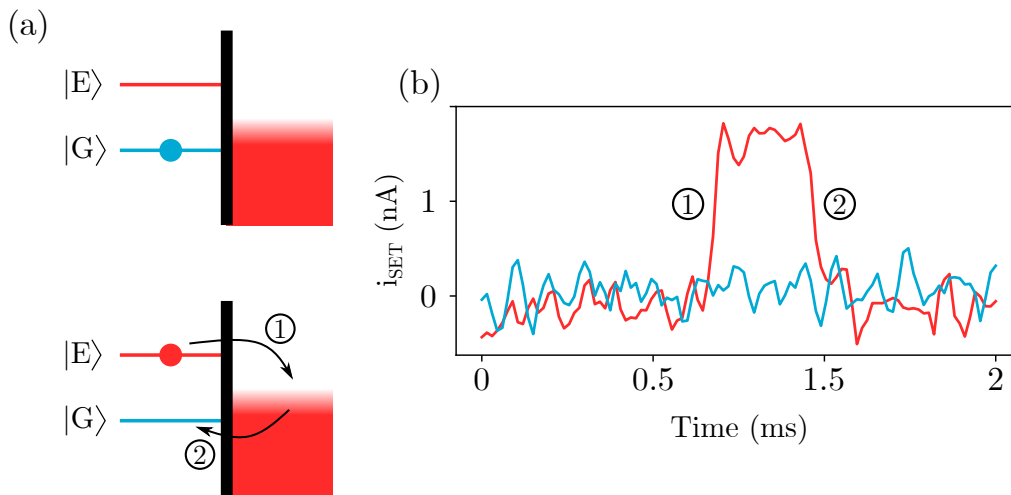


Figure 1.12: Energy selective spin readout or Elzermann readout. **a**, Energy diagram when the system is in the readout position. For the readout to be efficient the Fermi level of the reservoir must be carefully tuned in between the two probed energy levels of the quantum dot. When the system is in the ground state (top sketch) no energy states are available in the reservoir for the electron to tunnel, and we do not observe charge variation in the quantum dot. The bottom sketch corresponds to the spin state being in the excited state, in this case the electron can tunnel to the reservoir and be loaded back into the ground state. **b**, SET record during the readout. In the case of the excited state, a blip is observed in the signal corresponding to the electron tunneling to the reservoir and being reloaded in the ground state. By placing a threshold, we can therefore infer the initial spin state of the electrons.

To explain the Elzerman readout working principle we consider the system composed of a quantum dot tunnel-coupled to an electron reservoir following a Fermi distribution. The quantum dot occupation is determined via a SET acting as a local electrometer. As shown in Figure 1.12(a), for the readout to be efficient the Fermi level (E_F) of the reservoir must be placed in the middle of the energy levels of the states probed. As we have seen in subsection 1.1.2, the chemical potential of the quantum dot is easily adjusted using a gate capacitively coupled to the quantum dot. If we now consider the case where the system is in its ground state (top sketch in Figure 1.12(a)) we observe that all the states of the reservoir at this energy are occupied and the electron cannot tunnel out of the quantum dot. The current flowing through the SET remains therefore constant as

represented by the blue trace in [Figure 1.12\(b\)](#). If we now consider the situation where the system is in its excited state (bottom sketch in [Figure 1.12\(b\)](#)), we observe that states of the reservoir are indeed available at this energy. The system will therefore undergo the following dynamics, first an electron will tunnel out to the reservoir and a new one will be reloaded in the ground state of the quantum dot. In this situation, the SET signal will be sensitive to this change of occupation in the quantum dot and will display a sudden jump as seen in the red trace of [Figure 1.12\(b\)](#). If one is able to record this sudden jump single-shot readout of the spin state is possible.

The experimental implementation of such technique is limited by several drawbacks. First, it requires precise calibration of the quantum dot chemical potential for the Fermi level of the reservoir to sit in the middle of the two probed states. Then, the operating temperature of the device must be low compared to the energy splitting between the two states. In the case of single spin readout, this means that $\hbar\gamma_e B \gg k_B T$ and for the two-electron spin state readout $J_0 \gg k_B T$. While the external magnetic field is easily tuned experimentally it is harder to enhance the exchange energy since it is mostly defined by the confinement potential. Moreover, the relaxation rate of the excited spin state must be low compared to the quantum dot to reservoir tunneling rate so that the electron in the excited state has the time to tunnel to the reservoir before relaxing to the ground state. However, the tunnel rate must not be too high compared to the measurement bandwidth otherwise the SET current jump would not be recorded making the measurement impossible. In the end, the system must follow the following conditions:

$$T_1^{-1} \gg \Gamma \gg BW, \quad (1.36)$$

where BW is the measurement bandwidth and Γ the quantum dot to reservoir tunneling rate [[Keith2019](#)]. By operating with low electron temperatures and using high-bandwidth cryogenic amplifiers Mills et al. demonstrated a readout fidelity above 99 % [[Mills2022](#)]. Finally, the hardware overhead to implement such readout is heavy when considering spin-based quantum computing in two-dimensional arrays of quantum dots. Indeed, having one reservoir for each quantum dot in such dense structures would require additional technological developments [[Vinet2018](#)]. To circumvent these limitations several techniques have been developed using an analogous approach to the operation of charge-coupled device (CCD) where the electron is shuttled across the array to perform readout on its extremity [[Baart2016](#)].

1.4.2 Pauli spin blockade readout

The Elzerman readout technique relies on an electron tunneling or not to an electron reservoir depending on its spin state. The technique presented in this section referred to as Pauli spin blockade (PSB) also relies on a tunneling event but in this case not to a continuum of states but to a neighbor quantum dot. The Pauli spin blockade technique allows the discrimination between the singlet and the three triplet spin states and relies on a charge configuration difference at a specific potential detuning position. It has first been observed in vertically coupled quantum dots

[Ono2002] and then in laterally coupled quantum dots [Johnson2005] via current measurement across a double quantum dot system. We will see here how this technique allows performing high fidelity single-shot readout.

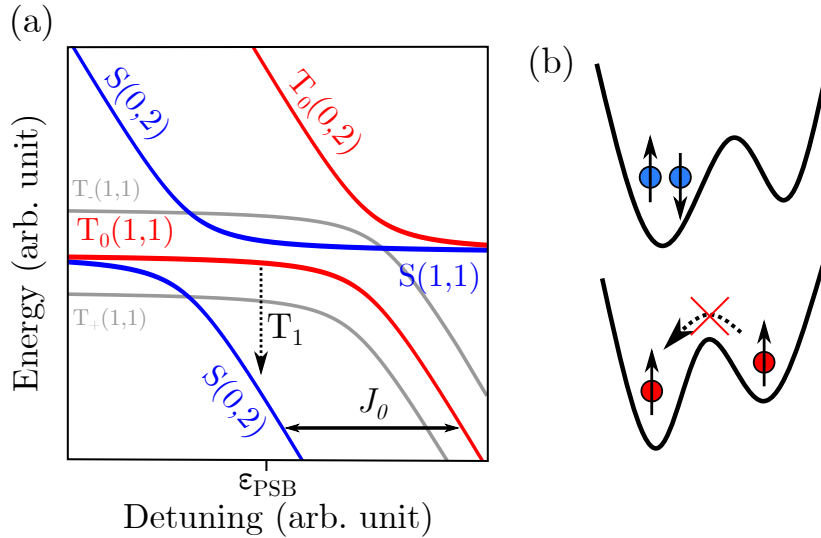


Figure 1.13: Pauli spin blockade readout. **a**, Energy diagram of the two-electron spin states close to the Pauli spin blockade region. **b**, Sketch of the spin states at the Pauli spin blockade position. For the same value of detuning the singlet spin state is preferably in the (0,2) charge configuration, while the triplet spin states are blocked in the (1,1) charge configuration.

We first consider a double quantum dot system filled with two electrons and probed by a SET. The first two-electron spin states of such a system are represented as a function of the potential detuning as depicted in Figure 1.13(a). The readout consists in pulsing the potential detuning of the double quantum dot to the Pauli spin blockade position ϵ_{PSB} indicated in Figure 1.13(a). At this position, it is energetically favorable for the singlet spin state to be in the (0,2) charge configuration while the three triplet spin states are blocked in the (1,1) one. This difference in the charge configurations arises from the exchange energy separating (in terms of potential detuning) the position of the spin states avoided crossings. The charge configuration difference is held until the $|T_0(1,1)\rangle$ state relaxes to $|S(0,2)\rangle$. This relaxation is usually few tens of microseconds long in GaAs/AlGaAs quantum dots [Barthel2012]. When the measurement bandwidth is high enough compared to T_1^{-1} , single-shot readout of the spin state is possible [Connors2020].

While being the method achieving the highest readout fidelity due to its robustness against temperature and noise some drawbacks must be addressed [Yang2020, Niegemann2022]. Indeed, the Elzerman readout requires the readout of a full electron difference in the quantum dot occupation, the Pauli spin blockade readout requires the readout between two charge configurations. This slight difference in the electron position in the system can be hard to discriminate before the relaxation of the spin state. This results in a trade-off between spending enough time averaging the signal in order to discriminate with high fidelity the charge state at the Pauli spin blockade position while being faster than the spin state relaxation. Moreover, while requiring less hardware overhead than the Elzerman type readout, Pauli spin blockade readout requires the use of two

electrons to extract in the end only one bit of information (either S or T). These two issues are at the core of [chapter 4](#), where we propose a solution to inhibit the effect of the T_1 relaxation and use this new capability to perform complete discrimination between the four two-electron spin states S , T_0 , T_+ , and T_- .

1.5 Recent advancements for Pauli spin blockade readout

We present in this section the recent advancements in the community to address the previously identified drawbacks of spin readout. With the many proposals for dense arrays of spin qubits the development of readout methods with the highest possible fidelity and lowest hardware footprint has become a necessity. We will see how different methods can release constraints on the global array architecture by first presenting a latched readout facilitating the charge readout and a cascade-based mechanism allowing to delocalize the electrometer from the location where spin-to-charge conversion is performed.

1.5.1 Latching mechanism

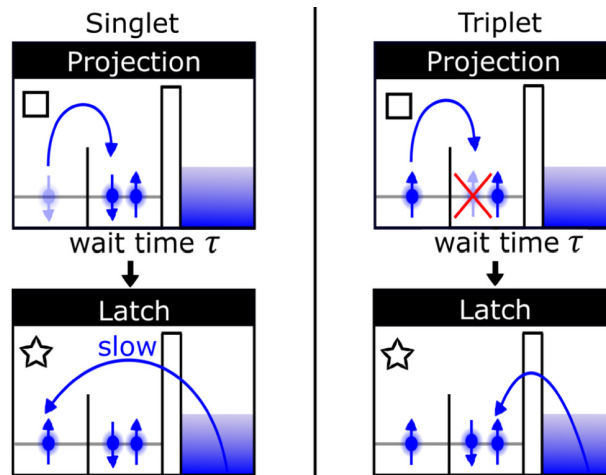


Figure 1.14: Latched Pauli spin blockade readout, reproduced from [Seedhouse2021]. Schematic of the different steps involved in a latched PSB readout. The readout relies on the tunnel rate difference between the left and right quantum dots with the reservoir. A singlet state is mapped to the (02) charge state while the triplet one is mapped to (12) .

In 2018 Harvey-Collard et al. introduced to the community an enhanced version of the PSB readout [[Harvey-Collard2018](#)] called latched-PSB. This readout aimed at solving an inherent limitation of the PSB readout by mapping singlet and triplet spin states to charge states with a full electron difference. Thus increasing the signal difference between the two states and decreasing the time required to discriminate them with high fidelity.

To explain the latched-PSB readout principle we consider the system presented in [Figure 1.14](#)

composed of a double quantum dot with an electron reservoir highly coupled to the right quantum dot and weakly coupled to the left one. We note (i, j) the charge state of the double quantum dot, where i and j are the charge occupation of the left and right quantum dots respectively. The first step consists in performing a classic PSB spin-to-charge conversion, again at the end of this step the charge state of the double quantum dot is either $(0,2)$ or $(1,1)$ if the electrons are forming a singlet or triplet spin state. From there, the system is pulsed in the $(1,2)$ charge configuration region and a charge readout is performed. In the case of the triplet spin state, the coupling between the right quantum dot and the electron reservoir is in the GHz regime allowing fast loading of the third electron in the system. In the case of a singlet spin state, the loading of the third electron is slow due to the weak coupling between the left quantum dot and the reservoir. Therefore, before charge tunneling happens from the reservoir to the left quantum dot we can observe either a $(0,2)$ or $(1,2)$ charge state depending on the initial spin state. It is interesting to note that in this type of readout the mechanism limiting the signal lifetime is not the relaxation of the triplet spin state to the singlet one but rather the charge state relaxation from $(0,2)$ to $(1,2)$ which is typically one order of magnitude higher than the typical value of T_1 in GaAs/AlGaAs.

In the end, this technique allows for releasing constraints on the charge readout design by providing a bigger signal difference to be measured and a longer lifetime of the said signal. This technique is today widely used in a variety of platforms to reach high fidelity readout for instance 99.86 % in a silicon donor-quantum dot system [Harvey-Collard2018], > 99 % in CMOS double quantum dot device [Urdampilleta2019], and 99.3 % in Si-Mos devices [Zhao2019]. However, the integration of such readout in a dense quantum dot array still needs to be demonstrated due to its rather large hardware footprint. Indeed, the necessity to have an electron reservoir and an electrometer close to the double quantum dot where the measurement is performed could require again additional technological developments.

1.5.2 Cascade mechanism

The PSB readout has demonstrated the highest readout fidelities in semiconductor quantum dots for ST qubits, but the charge information that must be read at the end of the projection is very local. In dense quantum dot array structures, the presence of an electrometer close to the projection position is not guaranteed. To overcome this issue several proposals for spin-based quantum computing are suggesting the use of gate-based reflectometry readout, which removes the need for an electrometer and a reservoir in order to read out the charge state of the array. However, the achieved readout fidelities are not yet reaching the threshold level for fault-tolerant quantum computation [Urdampilleta2019, Zheng2019, Pakkiam2018, West2019]. Another solution could be to shuttle the qubit on the side of the array close to an electrometer in order to perform the readout [Baart2016, Mortemousque2021a]. Again this technique has some severe limitations such as the necessity to provide a clear path in the array for the qubit to be shuttled. An interesting path to circumvent these limitations has been proposed by Van Diepen et al. 2021 [van Diepen2021]. This technique is inspired by the cascade mechanism used in avalanche photodiodes for instance.

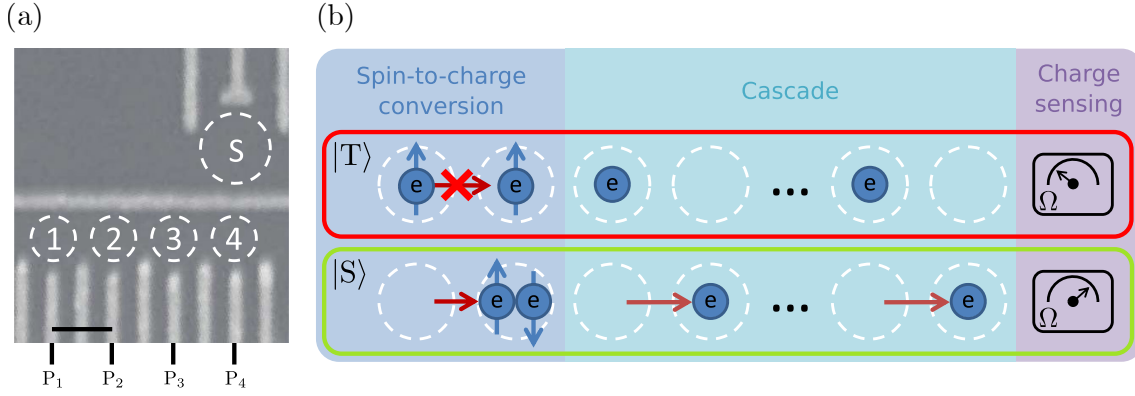


Figure 1.15: Electron cascade for distant spin readout, reproduced from [van Diepen2021]. **a**, Quadruple linear quantum dot array used to demonstrate the cascade readout mechanism. The expected position of the quantum dots is indicated by the white dashed circles and the position of the SET is indicated by S. **b**, Cascade mechanism principle. In the triplet spin state configuration, the system is blockaded and remains in the (1101) charge state configuration. On the contrary, the singlet spin state allows tunneling of the leftmost electron to the right neighbor quantum dot, triggering the cascade mechanism ejecting an electron in the right reservoir to reach the (0200) charge state.

Here the tunneling or not of a spin state at the PSB position will trigger the displacement of a charge located in a neighbor quantum dot towards the detector due to Coulomb repulsion.

The demonstration of this novel type of readout called cascade-PSB, has been conducted in a quadruple quantum dot linear array based on the GaAs/AlGaAs platform and shown in Figure 1.15(a). In this sample, mimicking a dense structure, the sensor is placed at the extremity of the array where design constraints are supposedly less intense than in the middle of the structure. We note the charge distribution in the quantum dot array ($ijkl$) where i, j, k , and l is the occupation of quantum dot 1, 2, 3, and 4 respectively. The cascade-PSB measurement scheme is illustrated in Figure 1.15(b) and consists in first initializing the array in the (1101) charge configuration with the electrons in quantum dot 1 and 2 forming a random spin state (S or T). Moreover, the system is tuned so that $\mu(0201) > E_F > \mu(1101)$ where $\mu(0201)$, $\mu(1101)$ is the chemical potential of the (0201) and (1101) charge state occupation and E_F the Fermi level of the right reservoir. In this situation, if two electrons are present in quantum dot 2 the rightmost electron will preferentially tunnel to the right reservoir due to Coulomb repulsion. From there, a PSB spin-to-charge conversion is performed by forcing the electron in quantum dot 1 into quantum dot 2. In the case of a triplet spin state, tunneling is blocked and the system remains in the (1101) charge state. In the case of a singlet spin state, the system reaches the (0201) charge state and the presence of an extra electron in quantum dot 2 triggers the cascade mechanism which consists here in an electron tunneling to the right reservoir, in this situation the system reaches the (0200) charge state.

The use of the cascade-PSB readout showed an increase of factor 3.5 in the signal-to-noise ratio (SNR) differentiating the two spin states compared to a PSB readout performed in the same configuration. This enhancement in the readout signal comes from two contributions. The first one is inherent to the cascade mechanism which induces electron displacement in a quantum dot

closer to the sensor compared to the PSB readout. The sensor sensitivity decreasing with the distance it induces a bigger signal for the same amount of noise hence the increased SNR. Second, the cascade-PSB maps a singlet and triplet spin state to charge states containing a total of two and three electrons respectively and therefore with a full electron difference. Whereas, the PSB readout relies only on a change in the charge configuration of the array. Combining these two effects in the cascade-based readout it reaches fidelity of $> 99.9\%$ where the PSB is limited to 85.6% .

To conclude, the hardware overhead needed to implement cascade-based or latched-based readout remains fairly large with the need of extra quantum dots or electron reservoirs dedicated to the readout process. Moreover, T_1 relaxation at the readout position of the triplet to singlet spin state can still trigger an unwanted cascade lowering the readout fidelity.

1.6 Conclusion

In this chapter, we presented the concepts and techniques required to isolate and readout electron spins. We saw that it was possible to isolate electrons in quantum dots by depleting a 2DEG provided by a GaAs/AlGaAs heterostructure using metallic nanostructures. We then developed the remote charge sensing technique allowing us to identify in a non-invasive manner the charge occupation of a quantum dot. Single and two-electron spin states have been introduced as well as their interaction with the nuclear spin bath produced by the host material. From this study, the electron spin degree of freedom has been identified as a potential candidate to realize quantum computing. We then studied the readout spin qubits through spin-to-charge conversion mechanisms and their performances in the context of quantum computing using spin qubits in large and dense quantum dot arrays.

2

Experimental setup and RF-reflectometry

Contents

2.1	Introduction	37
2.2	Device presentation	37
2.3	Sample fabrication	38
2.3.1	Process flow in the clean room	38
2.3.2	Electrostatic potential simulations	41
2.4	Cryogenics	42
2.5	Electronics	44
2.5.1	DC/AC signal generation and signal acquisition	44
2.5.2	Printed circuit board design	45
2.6	Software environment	46
2.6.1	Measurement software	46
2.6.2	Raw data analysis	49
2.7	High fidelity RF-SET based charge readout	50
2.7.1	Introduction	50
2.7.2	RF-SET working principle and theoretical design	51
2.7.3	Device and resonant circuit elements	53
2.7.4	Reflectometry setup	56
2.7.5	Single-shot readout and fidelity benchmark	59
2.7.6	Conclusion	62

2.1 Introduction

The aim of this Ph.D. is to demonstrate an enhancement of the quantum dot array tunability and the PSB readout efficiency via a high level of control on the interdot potential barriers. For this purpose, we fabricated a triple quantum dot linear array with a neighbor SET acting as a charge sensor based on the GaAs/AlGaAs heterostructure platform. In this chapter, we start by detailing the protocol used in the clean room facility to fabricate the GaAs/AlGaAs samples and the simulation tools used to estimate the suitable gate voltages to define the triple quantum dot. Then, we focus on the machinery used to reach cryogenic temperatures needed to operate quantum dots. We also extensively describe the measurement apparatus by listing the different instruments and the electronic circuits used to control the quantum devices. Finally, the software environment used to control the different instruments and treat the raw data is presented. In the last section, we detail the concept and techniques involved in the realization of RF-reflectometry based charge sensing. We demonstrate a rapid and high fidelity charge readout using an on-chip matching circuit.

2.2 Device presentation

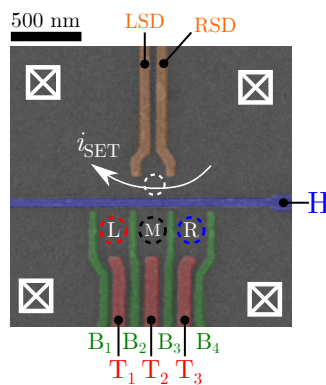


Figure 2.1: Typical linear quantum dot array measured. The sample is composed of a linear triple quantum dot array where each dot is labelled L, M, and R for the left, middle, and right quantum dot respectively and a SET acting as a local electrometer.

The sample fine structure is presented in [Figure 2.1](#), with the associated gate names and expected quantum dot positions. The sample is composed of a linear triple quantum dot array where each dot is labelled L, M, and R for the left, middle, and right quantum dot respectively and a SET acting as a local electrometer. On each side of the array are present grounded ohmic contacts acting as electron reservoirs and will be used to load electrons into the structure. The quantum dots of the array are defined by three types of gates colorized differently in the SEM image presented in [Figure 2.1](#). First the barrier gates (green) are mostly designed to confine the quantum dots along the x -axis of the sample and tune the reservoir-quantum dot tunnel coupling for B_1 and B_4 , while

gates B_2 and B_3 are designed to tune the interdot tunnel coupling. The plunger gates (red) were designed to confine the electrons along the vertical axis while providing a knob to tune the chemical potential of each quantum dot independently. Finally, the horizontal gate (blue) completes the confinement of the quantum dot along the y -axis and separates the array from the SET.

2.3 Sample fabrication

The fabrication of all the nanostructures presented in this work requires advanced nano-fabrication techniques performed in a clean room environment, which have been developed by the research group throughout the different projects. Especially, the manufacturing of nanometric gates disposed in complex and dense layouts has been at the core of the work done in the clean room facility and we benefit here from this legacy [Chanrion2021, Jadot2021, Mortemousque2021a]. In this section, we develop the process used to fabricate the samples measured in this thesis.

2.3.1 Process flow in the clean room

The two different samples measured in this thesis were fabricated using the GaAs/AlGaAs platform. These heterostructures are fabricated by the group of Andreas Wieck at the Ruhr University in Germany. The heterostructure used in this work was grown by molecular beam epitaxy and provides at cryogenic temperatures a 2DEG located 110 nm below the surface of the crystal which has a carrier mobility of $9 \times 10^5 \text{ cm}^2 \text{ V}^{-1} \text{ s}^{-1}$ and an electron density of $2.79 \times 10^{11} \text{ cm}^{-2}$. We present briefly here the step to fabricate the devices measured in this thesis using the heterostructure before going into details about each step :

1. 2DEG patterning via etching of the crystal using a piranha solution
2. Creation of ohmic contacts to the 2DEG and bonding pads
3. Patterning of alignment marks for laser and electron beam lithography
4. Patterning of the nanometric gates on top of the crystal in the center using electron beam lithography
5. Patterning of electric contacts between the bonding pads and the fine structure using laser lithography

The first step of the device fabrication, presented in [Figure 2.2\(a\)](#), consists in shaping the 2DEG into a central square part called mesa where the actual gates of the device (fine structure) will be located and 4 paths at each corner of the square for electrical contact of the 2DEG later on. Since 24 devices are fabricated at the same time on the wafer, this patterning is necessary to isolate them electrically. The desired pattern is insolated on a 400 nm thick layer of photosensitive resist

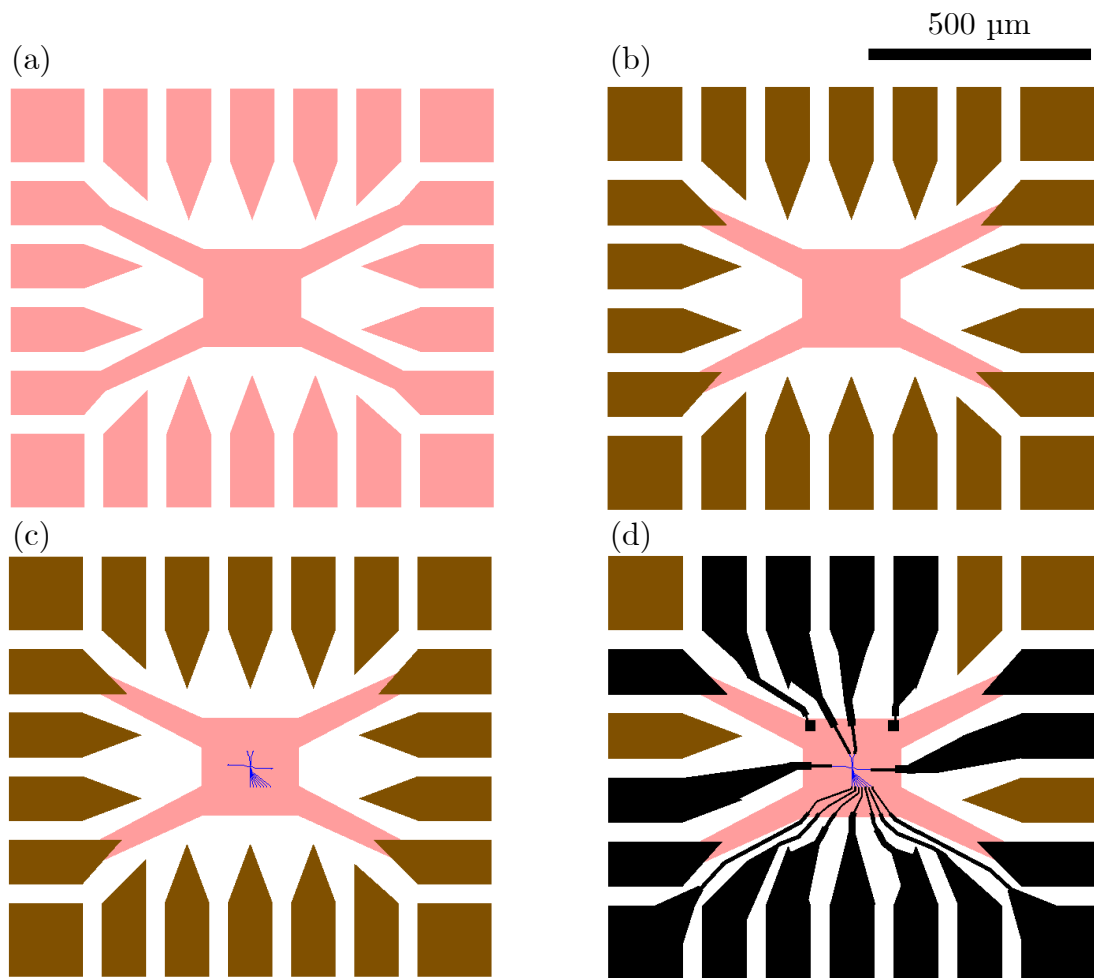


Figure 2.2: Process flow used to fabricate the samples measured. **a**, Mesa etching with a central square for the fine structure and four lines for later ohmic contacts. **b**, Ohmic contact deposition to electrically contact the bonding pads to the previously etched 2DEG. **c**, Electron beam lithography defining the nanometric gates of the sample (fine structure). **d**, Laser lithography defining the electric traces between the bonding pads and the fine structure.

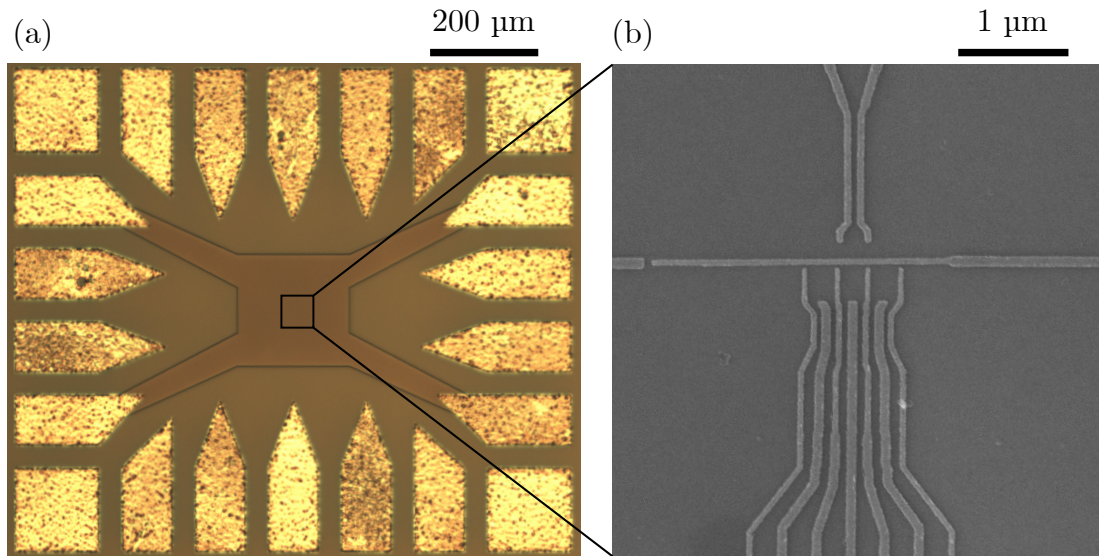


Figure 2.3: Optical microscope and SEM image of the sample during fabrication. **a**, Optical microscope image of the sample after the mesa etching and the deposition of ohmic contacts and bonding pads have been performed. **b**, SEM image of the fine structure after deposition and lift-off of a sample similar to the one measured in this thesis.

(S1805) using laser lithography. The etching of 150 nm of the surface crystal is then performed using a piranha solution composed of $\text{H}_2\text{O}_2/\text{H}_3\text{PO}_4$ whose etching rate was calibrated on a dummy sample. The remaining resist is finally removed using two different baths of acetone and IPA.

Now that the mesa shape is defined, we need to create 4 ohmic contacts at each end of the mesa lines. The electrical contacts to the 2DEG should be of low resistance compared to the typical one of a sensing dot $\sim 12 \text{ k}\Omega$ so that the current is limited by the quantum transport in the fine structure. To do so, the sample is again covered with a 400 nm thick layer of photosensitive resist and the desired pattern is shaped using laser lithography as shown in [Figure 2.2\(b\)](#). Then we deposit successive layers of metal composed of Ni(5 nm)/Ge(60 nm)/Au(120 nm)/Ni(10 nm)/Au(100 nm). The deposition is performed in an electron beam evaporator in two steps for each metal layer of the ohmic contact. First, the crucible containing the desired metal is selected and a high-power electron beam evaporates the metallic bid. Then, the created gas rises into the high vacuum chamber and solidifies when it contacts the sample, the operation is repeated for each layer of metal. Once the deposition is finished, the resist mask and excess metal are removed via lift-off technique in an acetone bath. The sample is finally annealed during 1 min at 450°C so that the metal alloy created diffuses from the surface of the crystal to the 2DEG location 110 nm below. This annealing step is critical to ensure a low resistance ($5 \text{ k}\Omega$ at room temperature and 250Ω at cryogenic temperatures) between the bonding pads and the 2DEG. An optical microscope image of the sample at this stage of the process is shown in [Figure 2.3\(a\)](#).

[Figure 2.2\(c\)](#) shows the next step of the fabrication which consists in defining the fine structure. To do so the sample is coated with 70 nm of poly(methyl methacrylate) (PMMA) and the resist is insolated with the correct pattern using electron beam (e-beam) lithography. The insolated resist is developed in a bath of methyl-isobutyl-ketone (MIBK) and the sample is placed back into the

electron beam evaporator. A metallic layer composed of Ti(3 nm)/Au(12 nm) is deposited on the sample. The metal is then removed from the non-insolated locations via a lift-off in a bath of acetone. The fine structure integrity of the different samples fabricated is then observed via SEM imaging as shown in Figure 2.3(b). We check that the expected gate geometry has been developed and that no gates are shorted together or broken which would be detrimental to the sample.

Finally, to contact the fine structure to the bonding pads the sample is again coated with PMMA and laser lithography is performed, as shown in Figure 2.2(d). The resist is developed in MIBK and a metallic layer composed of Ti(20 nm)/Au(100 nm) is deposited. A final lift-off is performed to define electric contact between the different gates of the fine structure and their corresponding bonding pads.

The sample is then taken out of the clean room in an anti-static box to the wire bonding machine. This machine allows us to contact the bonding pads of the sample to the measurement PCB presented in Figure 2.6 using gold wire bonding. During this whole operation, the device and PCB remain grounded to prevent any electrical static discharge in the fine structure.

2.3.2 Electrostatic potential simulations

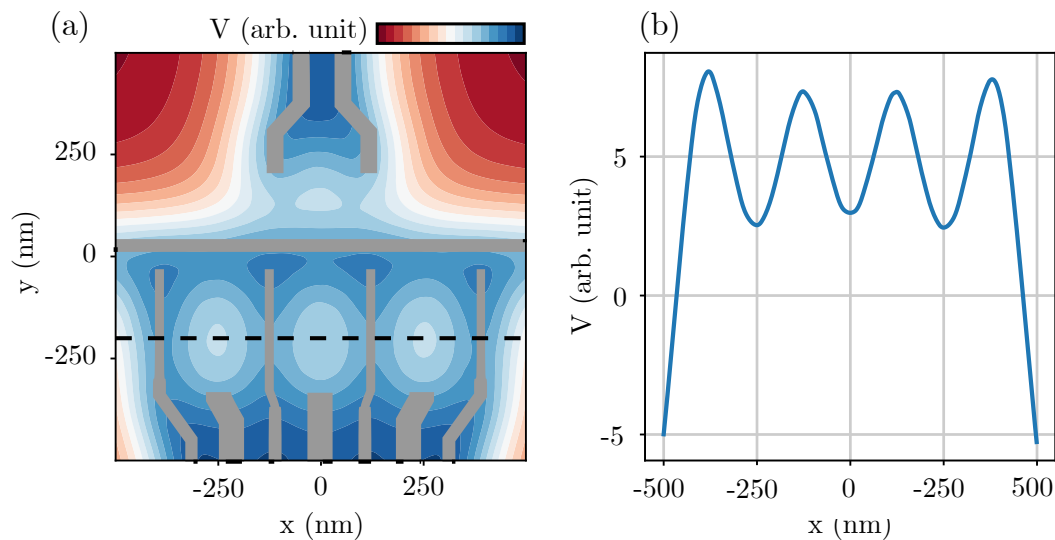


Figure 2.4: Electrostatic potential landscape simulation. **a**, Simulation of the electrostatic potential landscape generated 110 nm below the crystal surface by the voltage applied on the gates. **b**, Horizontal cut of the electrostatic potential landscape along the dashed line in **a**. According to the simulation, it is possible to form three potential wells in the array.

In order to assist the design and the tuning of the sample fabricated, we developed a numerical simulation based on the Comsol™ workspace. This simulation is based on a Poisson solver and takes into account the geometry, position and voltage applied to the different gates to compute the expected electrostatic potential landscape induced at the depth of the 2DEG. The result of the simulation is plotted in Figure 2.4(a), the voltages used as input for the different gates are -1 V for the barrier gates, -0.4 V for the plunger gates, -1 V for the horizontal gate and -0.6 V for the sensing dot gates. We observed three electrostatic potential wells where the three quantum dots of

the structure are supposed to be located. We also verify the ability to, at least on the simulation, adjust all quantum dots to similar chemical potentials. Performing such simulation gives a starting point and a rough idea of the voltage to apply to gates when the sample is cooled down for the first time. However, to be predictive and more efficient some key ingredients are missing such as the random Si dopants positions, the number of electrons occupying each quantum dot, and the overall disorder in the heterostructure [Bednarek2008].

2.4 Cryogenics

To reach the required cryogenic temperatures, we used two He3/He4 dilution refrigerators. For the RF-SET experimentation presented at the end of this chapter, a home-built wet cryostat of base temperature 20 mK was used. The charge control and spin measurements presented in [chapter 3](#) and [chapter 4](#) were performed in a commercial CryoConcept™ dry dilution cryostat of base temperature 10 mK. Both cryostats share a common working principle below the initial cooling down to 4.2 K, reached via either a liquid helium bath (wet) or a high-pressure pulse tube (dry).

A dilution refrigerator is based on an idea developed by H. London in 1951 and was first realized experimentally in 1965 by P. Das [Das1965]. The cooling power of the refrigerator below the temperature of liquid He arises from the peculiar nature of the isotope mixture of ^3He and ^4He . When this mixture is cooled down below 870 mK at equilibrium it separates into two phases. The first one, referred to as pure, is almost 100 % composed of ^3He and the second one, referred as dilute, is composed of 6.4 % of ^4He and 93.6 % of ^3He at equilibrium. In this regime, the dilution process of ^3He from the pure phase to the dilute one is an endothermic process providing cooling power at the interface between the two phases. The refrigeration is therefore obtained by forcing a continuous flow of a pre-cooled ^3He into a phase of ^4He , thus the cooling power obtained at the dilution interface will depend on the ^3He flow imposed. In practice, the important stages of the dilution unit are shown in [Figure 2.5\(a\)](#), and we describe briefly the different stages the ^3He flow undergoes in a dry dilution cryostat:

- The ^3He inlet is cooled down to 4.2 K via either a high-pressure pulse tube or a liquid helium bath.
- It is then cooled down to ~ 1 K via expansion using a Joule-Thomson valve (not represented in the scheme).
- Then, it is further cooled down to a few tens of mK via heat exchangers with the dilute phase.
- In the mixing chamber the ^3He atoms are diluted in the ^4He phase.

- Finally, the diluted ^3He atoms are evaporated from the dilute phase using a turbomolecular pump connected via a low-impedance tube to the still. The low pressure provided by the pump combined with the large surface area of the still maximizes the flow of ^3He in the dilution circuit and therefore the cooling power.

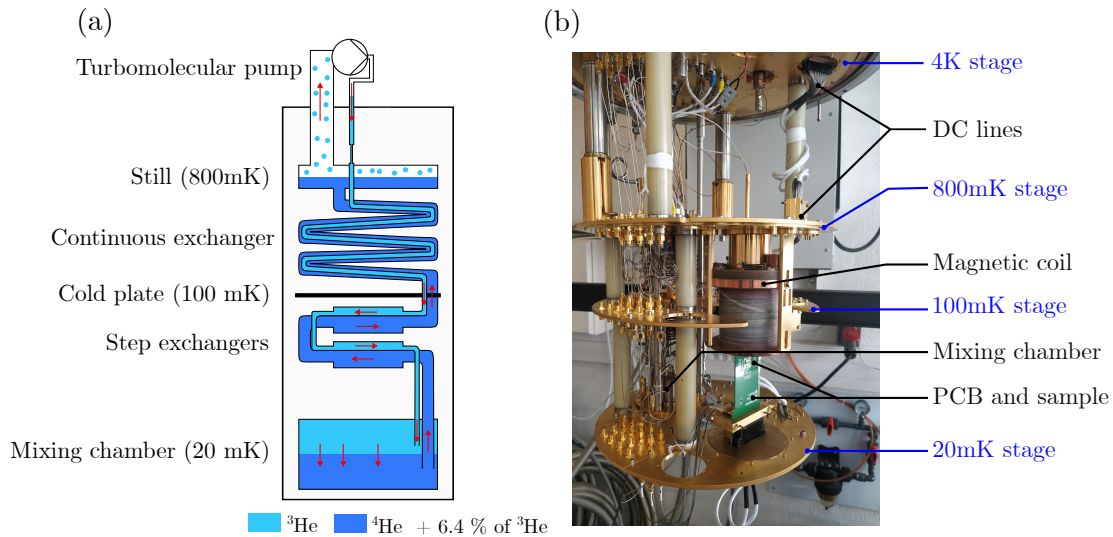


Figure 2.5: Dry dilution cryostat used to perform the experiments presented in [chapter 3](#) and [chapter 4](#). **a**, Schematic of the working principle of a dilution cryostat. **b**, Photography of the dry dilution cryostat.

The low cooling power obtained via the dilution requires us to reduce at a maximum the different sources of heat reaching the mixing chamber. To do so, the whole dilution unit is placed under vacuum (10^{-6} mbar) to suppress heat exchange with the exterior, moreover thermal shields are thermally anchored to the different stages of the cryostat to block black body radiation emitted from the vacuum chamber. We will see in the next section that the quantum device needs to be connected to room-temperature electronics while bringing a minimum heat load to the sample. As shown in [Figure 2.5\(b\)](#), the DC and RF control lines of the device are thermally anchored to the different stages of the cryostat and thorough filtering and attenuation are discussed in [subsection 2.5.1](#). Moreover, attention is pointed to insulating thermally the different stages of the cryostat, via the use of superconducting wires to power the magnetic coil for instance.

Thanks to the attention given to heat exchanges in the system, the mixing chamber provides a cooling power of $100\ \mu\text{W}$ at 20 mK which increases by one order of magnitude at each stage of the cryostat. In the end, the quantum device is anchored to the mixing chamber to ensure the lowest thermal noise possible. The superconducting coil used to apply a static magnetic field to the sample is anchored to the 800 mK stage providing a low enough temperature for the coil to remain superconducting while having enough cooling power to cool down rapidly the large amount of metal. The rest of the cryogenic electronics such as the cryogenic amplifier used in the reflectometry setup requires $\sim 27\ \text{mW}$ dissipation to reach its maximum amplification, it is therefore placed at the 4 K stage of the cryostat.

2.5 Electronics

2.5.1 DC/AC signal generation and signal acquisition

The typical sample measured in this thesis is composed of 12 gates and 4 ohmic contacts that need to be polarized and manipulated over a range of a few volts. In order to control the sample, two voltage sources were used in this work. The first one is a low noise ($25 \text{ nV}/\sqrt{\text{Hz}}$ at 10 kHz) homemade digital-to-analog converter (DAC) with a range of $[-5 \text{ V}, 5 \text{ V}]$. This DAC is controlled via a field-programmable gate array (FPGA) board and the output signal is updated every $6 \mu\text{s}$. The DAC outputs are connected to the sample inside the cryostat via a commercial custom designed Axon™ wire harness. The DC cables of the harness are made of a stainless steel shell and a NiCu core providing 100 DC lines with a cut-off frequency of 10 MHz. This allows to dissipate as heat the high frequency noise into the stages of the cryostat where it is thermally anchored (see [Figure 2.5\(b\)](#)). In our experiments, the DAC voltage source is used to typically perform μs manipulation of the sample such as stability diagrams or electron loading in the structure.

In quantum computing, the manipulation must be performed faster than the retention time of the quantum state. This time is quantified by $T_2^* \simeq 10 \text{ ns}$ in the GaAs/AlGaAs platform [[Laird2006](#)]. It is therefore desirable to operate certain gate voltages at the nanosecond timescale. To generate these high frequency pulses, we used an arbitrary waveform generator (AWG) Tektronix™ 5014C. This AWG provides 4 programmable outputs with a sampling frequency of 1.2 GHz and an amplitude of $\pm 5 \text{ V}$ with a rise time of approximately 950 ps. The AWG is connected to the sample via 4 individual RF lines present in the cryostat with a bandwidth of 850 MHz. All lines are gradually attenuated according to the cooling power of the cryostat at each stage, to first reduce the heat load on the mixing chamber of the cryostat and second minimize the transmitted electrical noise to the sample which is detrimental in the operation of spin qubits [[Kriner2019](#)]. The total value of attenuation is necessarily a compromise between limiting the transmitted noise and having a sufficient pulse amplitude to manipulate the sample. As seen in [chapter 1](#), the typical charging energy (energy needed to add an electron to a quantum dot) in the GaAs/AlGaAs platform is around a few meV. Considering a typical gate lever-arm of $1/20$ [[Kouwenhoven2001](#)], the pulse amplitude that should be applied to the sample gates is around 20 mV. In this work we chose a total attenuation of -17 dB , giving a maximum pulse amplitude of $\pm 700 \text{ mV}$, enough to transfer several electrons from one quantum dot to another.

Finally, to record the signal coming out of the sample we use analog-to-digital converters (ADC). In this thesis, two types of measurement were used to read out the charge configuration of the quantum dot array. First using a radio-frequency setup for impedance measurements where the signal was acquired using a commercial National Instruments BNC-2110 with a maximum sampling frequency of 1.25 MHz and a resolution of $153 \mu\text{V}$. And second a trans-impedance amplifier (TIA) for DC current measurements where we used an ADC directly embedded in the FPGA providing a sampling frequency of 200 kHz.

2.5.2 Printed circuit board design

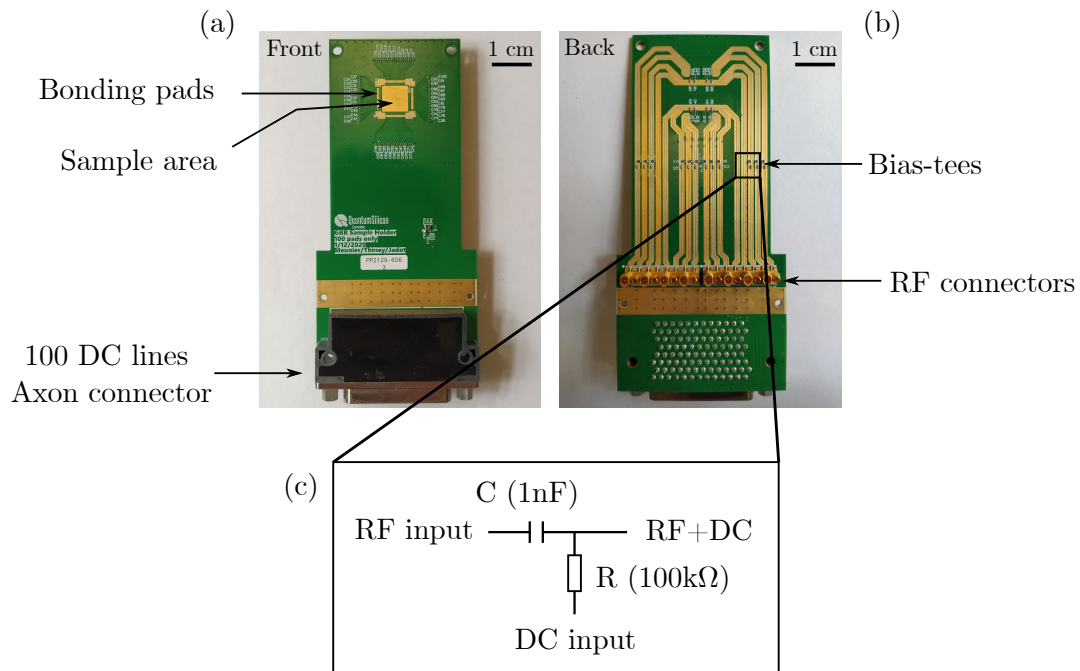


Figure 2.6: PCB photography and bias-tee characteristics. **a, b**, Front and back photography of the PCB used to connect the sample to the electronic setup. **c**, Lump element circuit of the bias-tees used to add the DC signal from the DAC and the RF one from the AWG. The RC circuit forms a high/low pass filter with a cut-off frequency of 1.6 kHz depending on the input port. This particular PCB has only been used in the experiments presented in [chapter 3](#) and [chapter 4](#). The rest of the experiments have been performed on an older version of it.

To connect the sample to the refrigerator lines and the DC and AC voltage sources, we glued the sample on a homemade printed circuit board (PCB) shown in [Figure 2.6](#). On top of the PCB an area dedicated to the sample is surrounded by electric pads for wire bonding. These electric pads are connected to the cryostat DC lines via a personalized Axon™ connector located on the front side of the PCB. On the back side of the PCB, 16 SMP connectors are dedicated to the RF lines. As mentioned in the previous paragraph, the sample voltage gates need to be DC biased and manipulated at the nanosecond timescale via RF lines. To achieve this signal addition SMD capacitances of 1 nF are soldered in line and the RF is connected via a SMD resistance of 100 kΩ to one of the DC lines. The equivalent electric circuit is detailed in [Figure 2.6\(c\)](#) and is composed of a DC and RF input port. Depending on the input port, the RC circuit acts either as a low or high pass filter with a cut-off frequency of $f_c = 1/(2\pi RC) = 1.6\text{kHz}$. We opted for this value of cut-off frequency by considering that the DC part of the signal should only provides a constant offset while the AWG performs all the ns and μs manipulations. This includes rapid coherent spin manipulation and longer manipulations such as charge loading and quantum dot array control where the system needs to be held in a certain configuration during a few μs . In practice, the charge loading and general quantum dot array control were still performed using the DC controls due to the memory of the AWG limiting the number of playable waveforms in a single experiment.

2.6 Software environment

2.6.1 Measurement software

In the experiments presented in [chapter 3](#) and [chapter 4](#), we will see that the different instruments controlling the device or collecting data from it need to be orchestrated at the μs timescale above typical operating software speed and thus require the use of reprogrammable control boards. We decided to develop a measurement apparatus centered around the FPGA acting as a master instrument to control the DAC, ADC, and the AWG.

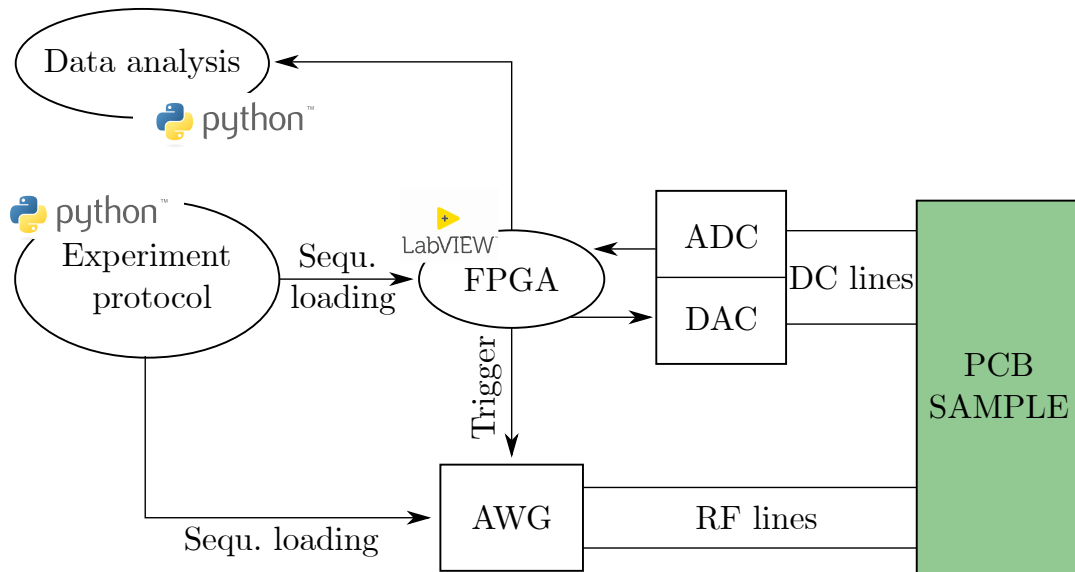


Figure 2.7: Software and hardware architecture used to conduct experiments.

To control all the instruments introduced in [subsection 2.5.1](#) we developed a software architecture presented in [Figure 2.7](#). A typical experiment follows this procedure:

1. Loading of the AWG memory with the desired waveforms using a Python driver (see example in [Listing 2.2](#)).
2. Loading of the FPGA memory via a user-friendly Python script (see example in [Listing 2.1](#)).
3. Beginning of the FPGA fast sequence triggering DACs updates, pre-loaded AWG waveforms and ADC acquisition.
4. Raw ADC data points are stored in .h5 file which is finally treated via various Python scripts depending on the experiment performed

Using preloaded pulse sequences in the FPGA and AWG is mandatory to accelerate the repetition rate of the experiments and to not be limited by the network communication bandwidth ($\sim 1\text{ kHz}$). The FPGA contains a list of possible operations such as:

- Updating DAC output in $6\ \mu\text{s}$

- Wait a defined time comprise between 100 ns and several minutes
- Send trigger to activate slave instruments such as the AWG, RF switches, VNA, ...
- Start data acquisition from the ADC

```

1 #####
2 ###  FPGA FAST SEQUENCE
3 #####
4 seq.append({"Trigger out", "1110"})
5
6 seq.append({"B1", -0.65})
7 seq.append({"B2", -0.84}) # LOAD 1e
8 seq.append({"Timing", 1000})
9
10 seq.append({"B1", -0.93}) # ELECTRON ISOLATION
11 seq.append({"B2", -0.5})
12 seq.append({"B1", -1.1})
13 seq.append({"Timing", 1000})
14 seq.append({"B2", -0.78})
15 seq.append({"B3", -1.0}) # DC POSITION
16 seq.append({"Timing", 1000})
17
18 seq.append({"Trigger out", "1101"}) # TRIGGER AWG
19 seq.append({"Timing", 30}) # WAIT FOR AWG
20 seq.append({"Trigger out", "1111"}) # RESET TRIGGER
21
22 seq.append({"Trigger out", "0011"}) # START ACQUISITION
23 seq.append({"Timing", 5000}) # WAIT FOR ACQU.
24 seq.append({"Trigger out", "1111"}) # RESET TRIGGER
25
26 seq.append({"End"}) # STOP
27
28 Map.sequence = seq
29 #####
30 ###  MAP 5ms ADC acqu., 81*81, 200 AVERAGE
31 #####
32 Map.sweep_dim = [5, 81, 81, 200]

```

Listing 2.1: Typical script used to load the DAC/ADC and trigger sequence into FPGA memory. Associated with the AWG script in [Listing 2.2](#) it produces the sequence needed to perform the freeze map protocol presented in [Figure 3.7](#)

A typical FPGA sequence script written in Python language is presented in [Listing 2.1](#) and makes use of all the operations presented above. An initial pulse sequence is performed by sequentially updating DAC values and waiting 1 ms for the raising time induced by the bias-tees. This DC manipulation is dedicated to slow manipulations allowing us to load electrons in the quantum dot array and isolate them from the reservoirs. Once the desired DC position is reached

the FPGA triggers the AWG which performs its preprogrammed pulse sequence manipulating the voltage gates at the nanosecond timescale. The typical duration of such a pulse sequence is around a few μs , therefore the FPGA is ordered to wait during $30\ \mu\text{s}$. Once the AWG manipulation is finished, we reach the final part of the script where the ADC acquisition is triggered by the FPGA for a duration of 5 ms.

```

1 #EXPERIMENT DIMENSIONS
2 Map = AWG_map(sweep_dim=[81, 81], waveform_duration=1100)
3
4 #[V_B3,V_B2, Time spend at position, Ramp time to reach next coordinate]
5 path = [[0., 2., 100, 0],\
6         [-0.484, 2., 100, 0],\
7         [-0.36, 0., 100, 0]]
8
9 V_B3 = [pt[0] for pt in path]
10 V_B2 = [pt[1] for pt in path]
11 T = [pt[2] for pt in path]
12 Tramp = [pt[3] for pt in path]
13
14 #CREATE PULSE SEQUENCE FOR B3 CHANNEL
15 Path_B3 = WE.Path(name = 'Path_B3',\
16                  channel = 'awg_B3',\
17                  V_A=V_B3[0],V_B=V_B3[1],V_C=V_B3[2],V_D=V_B3[3],\
18                  T_A=T[0],T_B=T[1],T_C=T[2],T_D=T[3],\
19                  T_AB=Tramp[0],T_BC=Tramp[1],T_CD=Tramp[2],\
20                  unit = 'ns',\
21                  Delay = 500,\
22                  )
23
24 Path_B3.ramp_parameter('V_{B,B3}', -0.6, -1.8, 1)
25 Path_B3.ramp_parameter('V_{C,B3}', -0.6, -1.8, 1)
26 Map.add_object(Path_B3)
27
28 #CREATE PULSE SEQUENCE FOR B2 CHANNEL
29 Path_B2 = WE.Path(name = 'Path_B2',\
30                  channel = 'awg_B2',\
31                  V_A=V_B2[0],V_B=V_B2[1],V_C=V_B2[2],V_D=V_B2[3],\
32                  T_A=T[0],T_B=T[1],T_C=T[2],T_D=T[3],\
33                  T_AB=Tramp[0],T_BC=Tramp[1],T_CD=Tramp[2],\
34                  unit = 'ns',\
35                  Delay = 500,\
36                  )
37
38 Path_B2.ramp_parameter('V_{A,B2}', 0, 2., 2)
39 Path_B2.ramp_parameter('V_{B,B2}', 0., 2., 2)
40 Map.add_object(Path_B2)
41
42 #LOAD AWG MEMORY

```

```
43 AWG_fast_send(Map.waveforms,Map.channel_names)
```

Listing 2.2: Typical script used to load the desired sequence for a freeze map in the AWG memory.

As mentioned in the previous paragraph, the AWG memory is loaded ahead of the experiment with the different waveforms needed to perform the desired manipulation. In Listing 2.2, we present a typical Python script used to load the memory and it consists in three main parts that we detail here. First, an empty array of the correct dimension is created according to the experiment needs. In this case, two parameters are varied we therefore create a 2D array of 81×81 waveforms of 1100 ns. Then, the empty array is filled for each channel of the AWG with objects corresponding to diverse pulse shapes whose characteristics are given by the attributes of the said object. Here we use arbitrary path objects, corresponding to a list of coordinates in the (V_{B2}, V_{B3}) parameter space with associated timestamps. Moreover, here we vary two coordinates at each realization of the experiment. During this thesis, a variety of such objects have been developed from simple square pulses to more complex patterns useful for spin state manipulations. Finally, the waveform array constructed is loaded in the AWG memory, waiting for the FPGA trigger to begin.

2.6.2 Raw data analysis

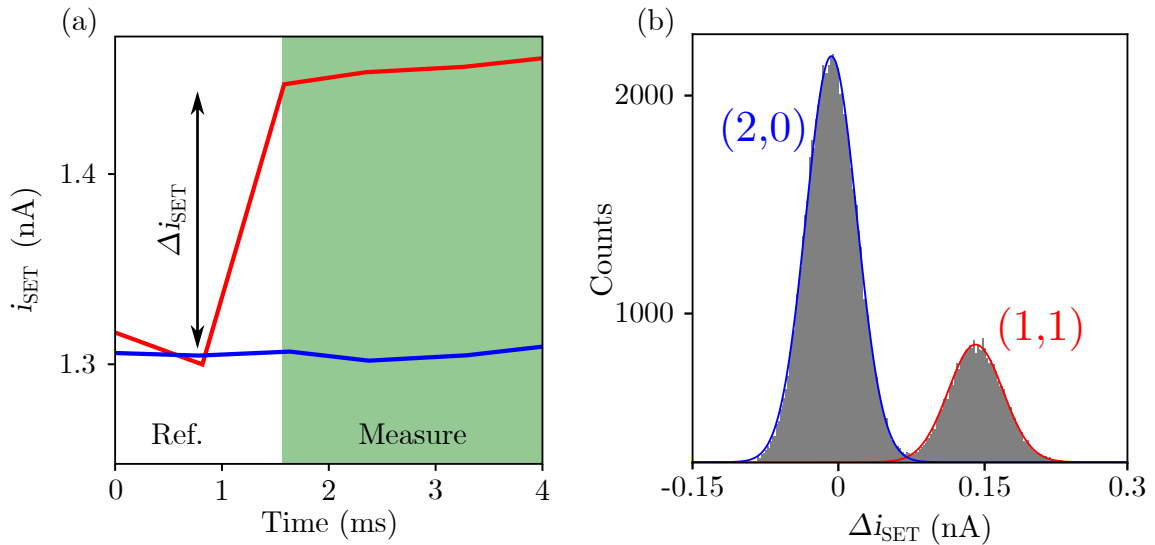


Figure 2.8: Raw data treatment performed during a charge readout procedure. **a**, Typical ADC trace obtained at the end of a charge readout procedure shot. The signal is segmented, averaged and compared to the reference to construct the histogram in **b**. **b**, Histogram constructed from the treated trace. The histogram is fitted to a sum of two Gaussian distributions to infer the charge occupation of the quantum dot array and extract the relevant parameters of the readout.

As we can see in Figure 2.7, once the signal has been digitalized by the ADC, the FPGA sends it to the experiment computer for it to be treated by a Python script. The main interest of this method is to be able to monitor treated data that is easily interpreted by the experimentalist, while the experiment is still ongoing. The usual experiment duration is a few minutes and the data shown to the experimentalist is updated every 10 ms. A complete library of data analysis scripts has been

developed during this thesis from simple signal treatment such as averaging or segmentation, to more complex one used to display readout fidelities for instance. The experimentalist is exposed to highly treated data, that allows him/her to interpret the experiment during its execution. For instance, an abnormally low readout fidelity could be the sign of a detuned SET or an incorrect readout position that we can correct before the end of the experiment, and therefore gain time and efficiency in the data acquisition process.

As an example, we detail the data treatment developed for a charge configuration readout in a double quantum dot of the sample presented in [Figure 2.1](#). The different steps of the raw data treatment are presented in [Figure 2.8](#) and start with the segmentation of the ADC trace into one reference and one actual measurement ([Figure 2.8\(a\)](#)). The measurement segment is averaged and the obtained value is compared to the reference to obtain Δi_{SET} in order to suppress low frequency modulations of the signal. The readout is repeated for various parameters we want to study, and the obtained values of Δi_{SET} are used to construct the histogram in [Figure 2.8\(b\)](#). The next step consists in fitting the histogram to two Gaussian curves in order to set a threshold maximizing the readout fidelity between the two possible charge states (2,0) and (1,1). To do so, we use peak recognition allowing us to coarsely know the position and amplitude of the two Gaussian curves. These parameters are then fed as starting points to the curve fitting program which finally outputs the optimum threshold and the subsequent readout fidelity following the equations presented in [subsection 2.7.5](#).

In the end, this development in the data treatment procedure has been one of the main reasons for the sped-up in the data acquisition, and it will be pushed one step further in the future by including automated feedback on the experiment parameters.

2.7 High fidelity RF-SET based charge readout

2.7.1 Introduction

As mentioned in [section 1.4](#), the spin information must be converted in charge configuration information in order to be read out. It is therefore necessary to develop fast, high fidelity, and scalable charge readout procedures to determine in the most efficient way the electron disposition in an array of quantum dots. In this section, we develop the work done to implement radiofrequency-SET (RF-SET) measurements in GaAs/AlGaAs gate-defined quantum dots. We will see the experimental difficulties inherent to this measurement technique and the use of tunable electric elements as an efficient way to optimize the matching between the quantum device and the RF circuitry [[Ares2016](#), [Apostolidis2020](#), [Connors2020](#)].

2.7.2 RF-SET working principle and theoretical design

Using SETs as highly sensitive local electrometers to determine the charge configuration of neighbor quantum dots is an efficient way to implement high fidelity readout. However, as seen in [subsection 1.1.3](#) the operation of such an electrometer requires measuring the conductance of the SET tuned on the side of a Coulomb peak. In the paradigm of a DC readout via room-temperature current-to-voltage converters, the bandwidth of the measurement is limited to a few kHz. To overcome this issue, Schoelkopf proposed in 1998 to perform a RF-reflectometry measurement of the SET conductance [[Schoelkopf1998](#)]. Indeed, working in the RF domain provides:

- High bandwidth measurements ($\simeq 8$ MHz) thanks to the low parasitic capacitance of the high frequency RF lines [[Reilly2007](#)].
- Low frequency $1/f$ noise suppression by demultiplexing the signal at a few hundred of MHz.
- The possibility to probe several SETs conductance with one RF circuit using frequency multiplexing [[Hornibrook2014](#)].

To experimentally implement such readout strategy, one needs to take into account the fact that most of the available RF circuitry is $Z_0 = 50\Omega$ matched. Since the typical SET resistance is in the order of $\frac{h}{2e^2} = 12.5\text{k}\Omega \gg Z_0$, directly measuring the SET conductance would result in a mismatch and the SET would reflect most of the incoming RF signal. To reduce the impedance of the SET close to Z_0 it is embedded in a LC resonant circuit as shown in [Figure 2.9\(a\)](#).

The total complex impedance of the circuit is defined as [[Vigneau2022](#)]:

$$\begin{aligned} Z &= j\omega L + \frac{G}{1 + jC\omega} \\ &= \frac{G}{G^2 + (C\omega)^2} + j\omega \left(L - \frac{C}{G^2 + (C\omega)^2} \right), \end{aligned} \quad (2.1)$$

where G is the varying conductance of the SET, C is the capacitance and L is the inductance all three forming a so-called tank circuit. The circuit is connected to a 50Ω transmission line, we will develop here the matching conditions of the tank circuit with respect to the transmission line. First, we determine the circuit resonance frequency when $Im(Z) = 0$:

$$\omega_0 = 2\pi f_0 = \frac{1}{\sqrt{LC}} \text{ assuming, } \frac{LG^2}{C} \ll 1. \quad (2.2)$$

Finally, injecting [Equation 2.2](#) in [Equation 2.1](#) the impedance of the circuit excited close to the resonance frequency simplifies as:

$$Z(\omega_0) = \frac{LG}{C}. \quad (2.3)$$

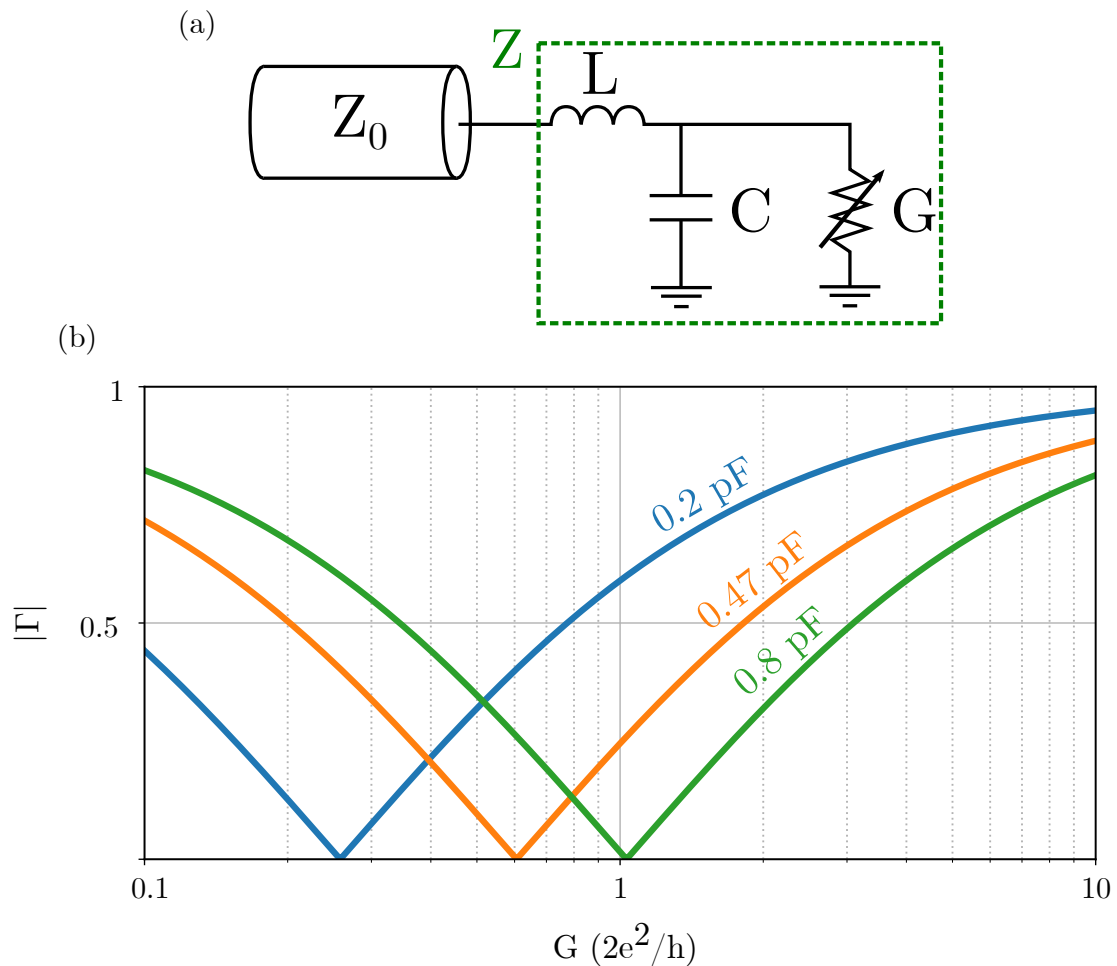


Figure 2.9: RF-SET working principle **a**, Lumped element model of the tank circuit used to $50\ \Omega$ match the SET to the rest of the RF-circuitry. It is composed of the SET modelled as a variable conductance and a LC resonator. **b**, Reflection coefficient of the tank circuit as a function of the SET conductance for three values of C assuming $L = 500\ \text{nH}$. Matching is observed when $|\Gamma(Z)| = 0$, around this position the reflection coefficient is highly sensitive to any conductance variation of the SET.

In a RF-SET measurement, one of the experimental parameter accessible is the reflection coefficient of the tank circuit at the resonance frequency, defined as $\Gamma = (Z - Z_0)/(Z + Z_0)$. In [Figure 2.9](#), we plotted the simulated reflection coefficient as a function of the conductance value for three different values of capacitances, assuming $L = 500$ nH. We observe for each simulated result a point where $|\Gamma(Z)| = 0$ called the matching point. Around this position $\Gamma(Z)$ is highly sensitive to any variation of the conductance. To access the variation of conductance of the SET via the measurement of the reflected signal, it is therefore necessary to operate the tank circuit close to the matching point. However, as seen in [subsection 1.1.3](#) the SET acts as a local electrometer only when it is tuned on the side of a Coulomb peak where its conductance is close to $0.5 \frac{2e^2}{h}$. The condition to design a tank circuit sensitive to the SET conductance variations which is also sensitive to its electric environment can therefore be summarized as:

$$G_{match} = \frac{CZ_0}{L} \simeq \frac{e^2}{h}. \quad (2.4)$$

This condition is met in this theoretical circuit for $C = 0.47$ pF and $f_0 = 328$ MHz. It is worth noting that the conductance value at which the tank circuit is matched to the RF circuitry and the resonance frequency is tunable via the capacitance of the circuit. In the following we will implement such an RF circuitry to perform RF-SET based charge measurements. We will see the experimental difficulties to satisfy [Equation 2.4](#) at cryogenic temperatures and the solutions implemented to circumvent them.

2.7.3 Device and resonant circuit elements

To implement the measurement, we designed the sample presented in [Figure 2.10\(a,b\)](#) based on the GaAs/AlGaAs platform. The sample is fabricated in the clean room following the protocol presented in [section 2.3](#). The device is composed of two rows of quantum dots facing each other. The sample is tuned in the correct regime by applying voltages to all non-grayed gates, the resulting potential landscape forms two face-to-face quantum dots (green and red circle). In this design, the green quantum dot is used as a SET to determine the charge configuration of the red quantum dot. The chemical potential and therefore the conductance of the SET is mostly controlled by the voltage applied on the top left gate V_{SET} . The two quantum dots being capacitively coupled, any change in the red quantum dot charge configuration will result in a shift of the SET chemical potential that is recorded via a change in the SET conductance. To record the conductance changes of the SET, we form a resonant LC circuit composed of the SET itself, the parasitic capacitance C_p of the sample, and the PCB and an on-chip superconducting inductance L . As seen in [subsection 2.7.2](#) the requirement to implement an RF-SET readout is to have a 50Ω matched resonant circuit for a SET conductance close to $0.5 \frac{2e^2}{h}$. Satisfying [Equation 2.4](#) is experimentally challenging. Indeed, classically C_p is fixed by the RF lines, PCB, bonding wires, and the sample geometry, all contributing more or less in a hard-to-predict way. However, from previous realizations, we know that $C_p \simeq 0.5$ pF, mostly defined by the PCB and sample geometry. In this paradigm, the

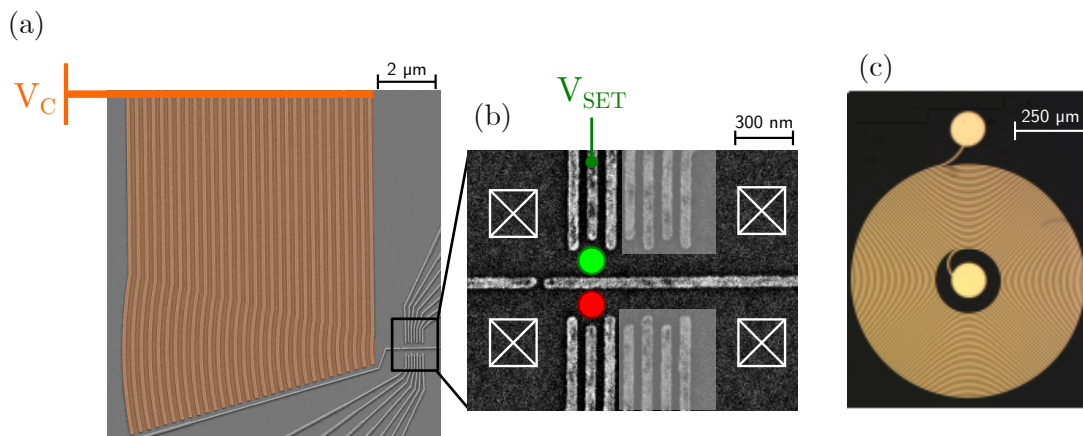


Figure 2.10: Sample measured, on-chip varactor and superconducting on-chip inductance. **a**, Colorized SEM image of the sample fabricated on the GaAs/AlGaAs platform and measured via the RF reflectometry setup. A resonant RLC circuit is formed using the inductance in **c**, the parasitic capacitance of the PCB, bonding wires and sample gates and the conductance of the green quantum dot shown in **b**. In this sample a non-negligible portion of the parasitic capacitance is formed between the orange gate and the 2DEG below. Applying a negative voltage V_C to the gate depletes the 2DEG which reduces the parasitic capacitance of the gate. The orange gate is used as an on-chip varactor and is characterized in [Figure 2.12](#). **b**, Zoom on the fine structure of the sample composed of 3 face to face linear quantum dots. In this experiment the grayed gates are not polarized and grounded. The rest of the gates form two quantum dots capacitively coupled, the red quantum dot occupancy is measured using the green quantum dot as a SET. The conductance of the SET is tuned using the voltage V_{SET} applied on the plunger gate of the green quantum dot and therefore change the conductive element of the tank circuit. **c**, 500 nH homemade on-chip superconducting inductance. The inductance is one spiral of 60 nm thick Nb deposited on intrinsic Si. Two bonding pads are present to electrically connect the inductance to the PCB and to one of the ohmic contacts of the SET.

only experimental knob remaining to tune the impedance matching of the tank circuit is the inductance value. The free choice of inductance is not enough to guarantee good impedance matching, especially at low temperatures where the values of all the elements composing the tank circuit are subject to slight deviations.

To overcome this issue, we implemented in this sample an on-chip varactor to have in situ tuning of the circuit capacitance giving an extra experimental knob to satisfy [Equation 2.4](#). The varactor is presented in [Figure 2.10\(a\)](#) and is a metallic gate located between the ohmic contact of the 2DEG and the SET. This $480 \mu\text{m}^2$ orange gate forms a capacitance with the 2DEG located 110 nm below. The stripe-like patterning of the gate limits electron back-scattering during the electron beam lithography, protecting the fine structure of the sample from strong proximity effects. Considering the small spacing between the stripes (200 nm), the gate effectively acts as a plain metal sheet when it is fully polarized. Considering the dielectric stack of GaAs and AlGaAs between the 2DEG and the gate shape we estimate the capacitance to be around 570 fF. The tunability of this capacitance arises from the ability to control the density of electrons below the gate by applying a negative voltage to the gate. Moreover, for highly negative voltages (< -1 V), we expect to be able to totally deplete the electrons below the metallic gate and therefore suppress almost completely the capacitance it forms with the 2DEG. In the end, we expect to be able to add to the already present ~ 400 fF a tunable value of capacitance from 0 to 570 fF.

We designed the inductance of the circuit using the following criteria:

- Allow impedance matching for $G = e^2/h$ with respect to [Equation 2.4](#) to have a maximum sensitivity of the RF-SET to its electric environment.
- Resonance value of the tank circuit should be around a few hundred MHz with respect to [Equation 2.2](#) to be in the operating range of the RF circuitry elements.
- A predictable value at cryogenic temperatures.
- Robust for applied magnetic fields between ± 500 mT, this magnetic field separates energetically the three triplet spin states which is mandatory for operations of ST_0 qubits.

The group has historically used SMD inductances mounted on the PCB, but those elements have demonstrated poor reliability with hard-to-predict values for the inductances at cryogenic temperatures. In this work, we chose to use homemade superconducting inductances providing a precise value of inductance while having low input resistance and parasitic capacitance. These inductances were made by D. J. Niegemann in the Nanofab clean room by depositing a 60 nm thick wire of Nb on top of intrinsic silicon. The thin film of Nb forming the inductance has a superconducting transition temperature of around 7 K [[Gubin2005](#)] and a critical field of 1.5 T at 4 K [[Zaytseva2020](#)]. An optical microscope photograph of a similar inductance used in this work is presented in [Figure 2.10\(c\)](#). The inductance value is mostly defined by the size and the number of wire loops, and we chose for this work a value of 500 nH by expecting a residual parasitic capacitance of $\simeq 0.4$ pF. Theoretically, this selection of components for the resonant

circuit should result in a $50\ \Omega$ matching for a SET conductance from e^2/h to $2e^2/h$ depending on the polarization of the varactor. The change in total capacitance will also affect the resonance frequency of the tank circuit, and we expect to be able to tune its value from around 270 MHz to 380 MHz.

2.7.4 Reflectometry setup

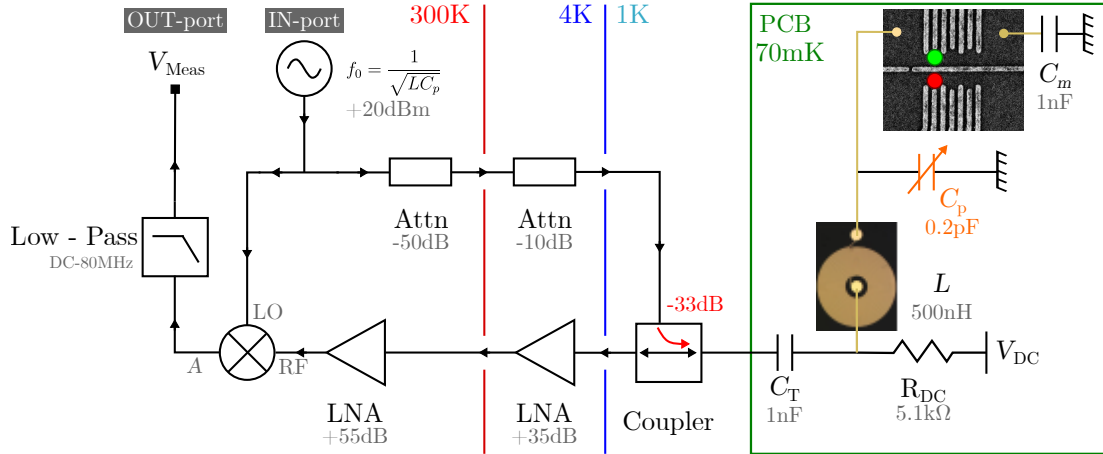


Figure 2.11: Reflectometry setup used to perform RF-SET charge sensing. Diagram of the reflectometry setup used to probe the resonator formed by the parasitic capacitance C_p , the inductance L and the green quantum dot conductance. The parasitic capacitance arises from the PCB, the inductance, the wire bonds and the GaAs sample itself. In the IN-port of the setup, a RF tone at the resonant frequency of the circuit is generated at room temperature and is separated power wise by a splitter. Half of the input power is directed to the resonator via a first -50 dB attenuator at 300 K and a second one of -10 dB clamped on the 4 K stage of the cryostat. Then the signal passes through a directional coupler which provides a -33 dB attenuation before reaching the PCB. The resonator reflects a variable portion of the signal depending on its complex impedance. The reflected signal is directed to the amplification line via the directional coupler. The amplification line is composed of two stages to reach a total value of 90 dB, the first part is done at the 4 K stage of the cryostat via a CITLF4 low noise amplifier (LNA) from Cosmic Microwave Technology, Inc. The second part is done at room temperature via a homemade amplifier of 55 dB. After amplification the signal is demodulated by comparison with the signal generated at the IN-port. The demodulator outputs the amplitude difference between the two signals, this output is low pass filtered via a homemade 80 MHz filter before being acquired by the ADC.

To probe the tank circuit fabricated with the elements in [subsection 2.7.3](#), we designed and implemented the RF circuit presented in [Figure 2.11](#). It is composed of three main elements that we will detail here: an attenuation line for the input signal in the cryostat, an amplification line for the reflected signal and the tank circuit embedding the sample. A RF source Windfreak™ SynthHD generates a 20 dBm signal at the resonant frequency of the tank circuit $f_0 = 1/\sqrt{LC_p}$ injected at the IN-port of the RF circuit. The signal power is then split in two by a homemade splitter, the first half of the signal is directed to the local oscillator port of the mixer and the second part to the cryostat. Before entering the cryostat RF lines the signal is first attenuated by a -50 dB attenuator at room temperature. The signal enters the cryostat and is again attenuated at the 4 K

stage by -10 dB. It is then directed to the PCB by a directional coupler with an input attenuation of -33 dB thermally anchored to the 1 K stage of the cryostat. In this setup, the RF signal reaches the ohmic contact of the sample with a power of -76 dBm corresponding to a peak-to-peak voltage of $50 \mu\text{V}$ which is low enough to prevent any damage on the sample. On the PCB itself, two elements are present: the tank circuit and a bias-tee. The bias-tee is formed using SMD elements soldered onto the PCB and referred to, in [Figure 2.11](#), as C_T and R_{DC} . It is used to apply a DC bias to the ohmic contact of the SET and perform DC current measurements of the quantum dots. The tank circuit is composed of the inductance L , the total capacitance C_p and the SET presented in [Figure 2.10](#).

As mentioned in [subsection 2.7.2](#), to have access to the variation of SET conductance and therefore the red quantum dot charge configuration it is necessary to record the reflected signal amplitude. Due to the low power of the input signal necessary to avoid heating, the reflected signal has an amplitude too small to be directly measured and needs to be amplified. To do so the signal from the tank circuit is directed to the amplification line by the directional coupler. The signal is first amplified at the 4 K stage by a 35 dB CITLF4 low noise amplifier (LNA) and again by 55 dB at room temperature by a LNA. Finally, demodulation by the input signal is performed using a passive MiniCircuits™ mixer. The output signal is low pass filtered by a homemade RC circuit with a characteristic cut-off frequency of 80 MHz to remove any residual RF component before being acquired by an ADC with a maximum sampling rate of 1.25 MHz.

Before characterizing the tank circuit RF response, we perform a calibration of the SET conductance G as a function of V_{SET} using the following protocol. First, all the gates defining the SET are connected to the ground, and we record the current flowing from the top left reservoir to the top right as a function of the bias. We observe a linear behavior of the current as a function of the bias with a slope equal to $R_{\text{open}} = 510 \Omega$. The residual resistance R_{open} extracted from this calibration is attributed to the one of the cryostat cables $\simeq 200 \Omega$ and the ohmic-2DEG contact resistance. Then, the bias is fixed to $V_{\text{bias}} = 100 \mu\text{V}$ (close to the RMS value of the RF signal) and the gates are polarized in order to form a SET. We record the current flowing through the SET (I_{SET}) as a function of the voltage applied to the plunger gate V_{SET} controlling mostly the chemical potential of the SET. Finally, the conductance of the SET as a function of the plunger gate voltage is computed as:

$$G(V_{\text{SET}})^{-1} = \frac{V_{\text{bias}}}{I_{\text{SET}}(V_{\text{SET}})} - R_{\text{open}}. \quad (2.5)$$

Thanks to this calibration we know the conductance of the SET and we have an experimental knob to control it.

To fully characterize the tank circuit in this RF circuit, we show in [Figure 2.12\(a\)](#) the frequency response of the circuit before demodulation. We observe a clear resonance in the amplitude response signal located at 501 MHz with a quality factor of around $Q \simeq 15$. As expected, the resonance amplitude shows a clear dependence with the SET conductance detailed in [Figure 2.12\(b\)](#). To perform this characterization of the tank circuit, the SET conductance is varied and calibrated by using the voltage applied on the gate controlling the SET chemical potential V_{SET} . The varac-

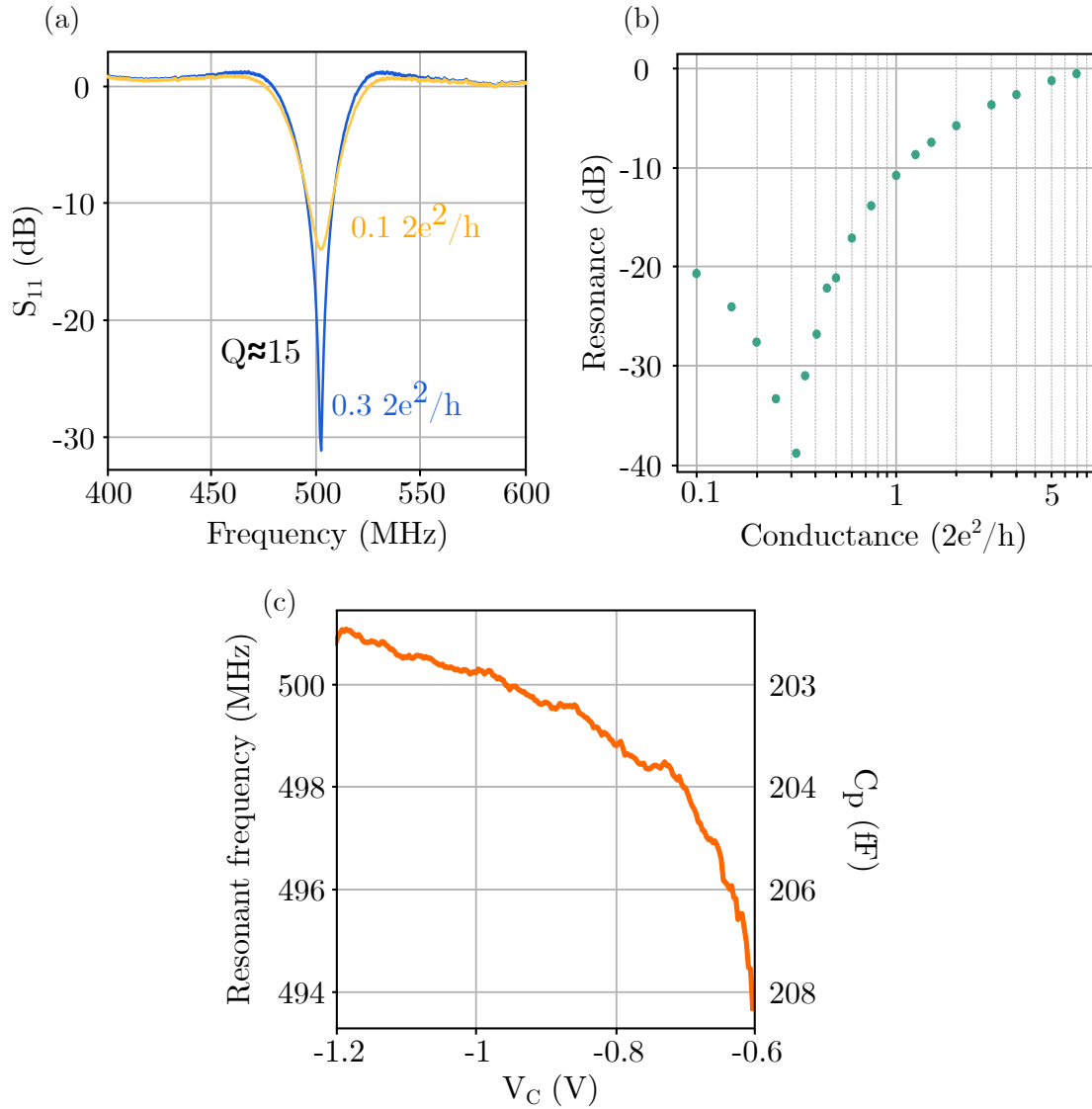


Figure 2.12: RLC circuit characteristics, matching parameters and on-chip varactor characterization. **a**, VNA response of the RLC circuit for two values of the green dot conductance. The resonance is located between 494 MHz and 501 MHz depending on the varactor capacitance. **b**, Resonance amplitude as a function of the sensing dot conductance. Matching of the tank circuit is observed for conductance of $0.3 \frac{2e^2}{h}$. Around this position, the resonance amplitude is highly sensitive to the SET conductance. **c**, Characterization of the varactor effect on the tank circuit resonant frequency. The resonance frequency $f_{res} = \frac{1}{2\pi\sqrt{LC_p}}$ is tunable over 7 MHz by adjusting the voltage applied to the orange gate (V_C) in Figure 2.10. The varactor introduces an extra knob to tune the matching conductance of the tank circuit.

tor is set to its minimal value of capacitance, and we record the amplitude of the resonance as a function of the conductance G of the SET. We observe a clear dip in the resonance value around $0.3 \times 2e^2/h$, at this conductance the tank circuit is matched to the RF circuit and the tank circuit absorbs -40 dB of the incoming signal. To ensure the best sensitivity of the RF-SET any variation of the SET conductance should result in a maximized variation of the resonance amplitude. Looking at [Figure 2.12\(b\)](#), this requirement is fulfilled close to the matching point, we will therefore need to operate the SET at a conductance close to $0.3 \times 2e^2/h$.

We finally characterize the varactor introduced in [subsection 2.7.3](#). To do so we measure the resonance frequency of the tank circuit as a function of the voltage applied to the varactor V_C . It is defined as $f_0 = \frac{1}{2\pi\sqrt{LC_p}}$ knowing that $L = 500$ nH we can extract the capacitance of the circuit. In [Figure 2.12\(c\)](#), we show the f_0 and the resulting capacitance as a function of the voltage applied to the varactor. We observe a variation of f_0 over 7 MHz inducing a change of the capacitance from 203 fF to 208 fF. As expected, the capacitance increases with the voltage applied to the gate V_C , indeed for high voltages ($V_C \simeq -0.6$ V) the 2DEG is not fully depleted below the grid and results in significant additional capacitance. For even higher voltages, the capacitance formed by the varactor is so high that the impedance of the resonant circuit is far from 50Ω which results in the complete vanishing of the resonance. It is therefore impossible to track the evolution of the resonance frequency for high values of V_C . On the other hand, when a more negative voltage is applied, the electrons of the 2DEG are being repelled far away from the metallic gate diminishing the extra capacitance. For even lower voltage applied the capacitance seems to saturate indicating that all the electrons below the gate have been repelled. However, the range on which the varactor can be tuned (a few fF) is far from the expected one in the theoretical calculations. We interpret this difference as a signature of our incapacity to measure higher values of capacitance due to the too strong mismatch between the RF circuitry and the tank circuit. Moreover, at these values of V_C (< -1 V) the 2DEG below the gate is supposedly depleted, the small change in capacitance observed is therefore attributed to the capacitance formed between the edge of the gate and the 2DEG surrounding the gate. In the end, the varactor was polarized at -1.2 V to completely deplete the electrons below the gate and achieve a matching for the desired value of SET conductance.

2.7.5 Single-shot readout and fidelity benchmark

Now that we developed the methodology used to measure the SET conductance variations, we will perform single-shot charge detection.

As mentioned previously, RF-SET measurements rely on a SET tuned on the side of a Coulomb peak, where the conductance of the SET is highly sensitive to its electric environment. Therefore, any change in the charge configuration of a neighbor quantum dot will result in a change of the SET conductance that we are able to record using the RF circuit described in [subsection 2.7.4](#). The experimental implementation of this readout starts therefore by calibrating the SET on a Coulomb peak side. This is performed in [Figure 2.13\(a\)](#) where we record the filtered output of the RF circuit V_{meas} as a function of the gate voltage V_{SET} . For $V_{\text{SET}} < -0.35$ V no variation is observed,

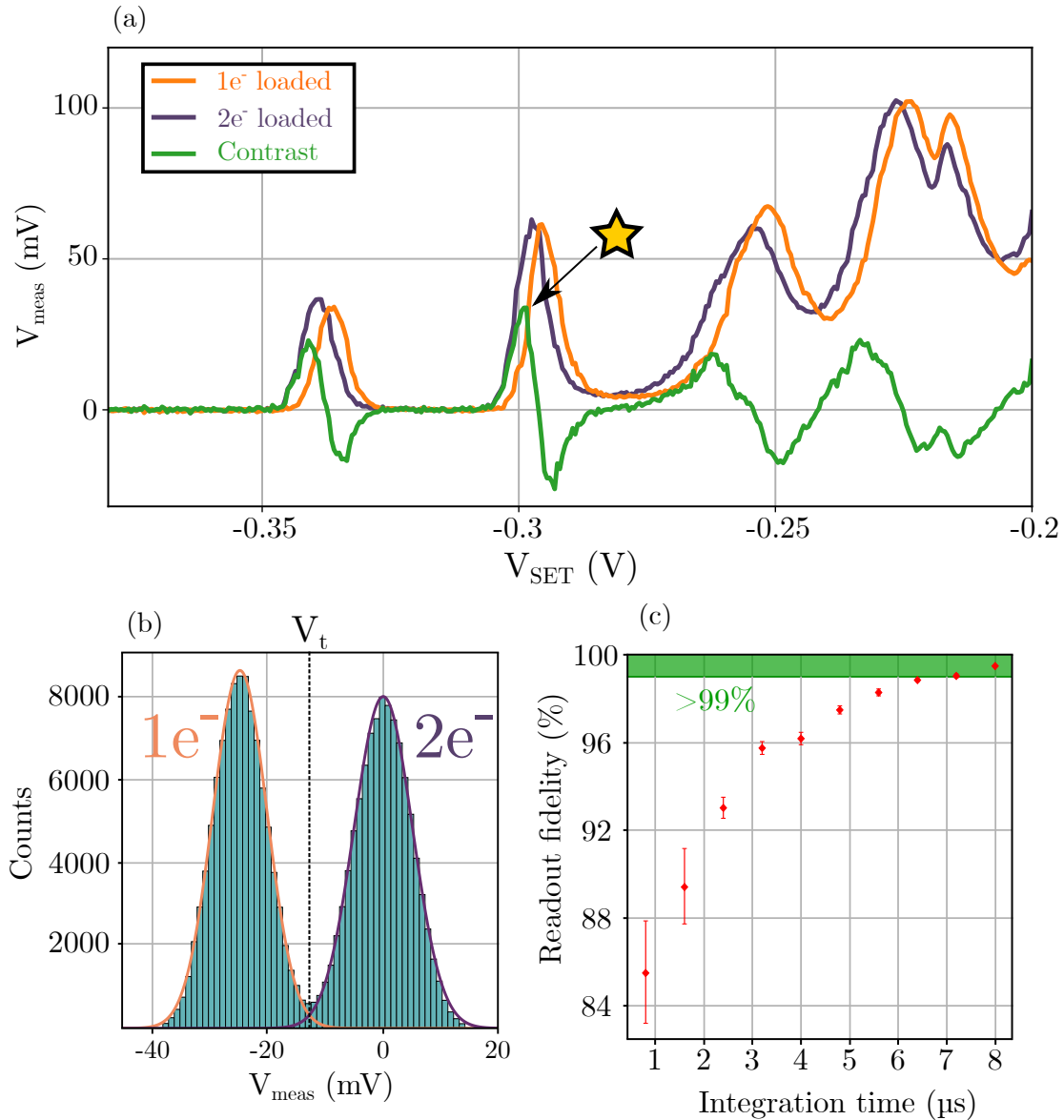


Figure 2.13: Remote charge sensing via RF-SET measurements and fidelity benchmark. **a**, SET Coulomb peaks observed by varying the chemical potential of the quantum dot using the voltage applied on the gate V_{SET} for different charge occupations of the red quantum dot. As expected contrast between the two initializations is observed only on the side of Coulomb peaks where the quantum dot conductance is highly sensitive to the electric environment. The readout is performed by acquiring V_{meas} at the position indicated by the yellow star where the contrast for the two initializations reaches a maximum. **b**, Histogram of V_{meas} averaged during 8 μs for one and two electrons loaded in the red quantum dot. The sum of two Gaussian distributions is fitted to the histogram, the left one corresponds mostly to the shots where one electron is present in the dot and the right one to two electrons loaded. By placing a threshold between the two distributions each shot can be labelled, and single-shot readout is performed. **c**, Readout fidelity as a function of the time spent averaging the signal V_{meas} . The fidelity is computed by extracting the overlap between the two fitted Gaussian distributions in c. The readout fidelity reaches a maximum of 99.5 % for an integration time as low as 8 μs .

in this regime $\mu(0) \gg \mu_S, \mu_D$ and the conductance is completely suppressed. Increasing V_{SET} , we observe a succession of Coulomb peaks.

To determine the optimized readout position we sequentially load either one or two electrons in the sensed dot (red dot in [Figure 2.10](#)) using the loading map protocol described in [subsection 3.2.2](#) and sweep gate voltage. We observe a clear shift of the SET conductance between the two initializations due to the modification in the local electric field induced by the extra charge present in the sensed quantum dot. We plot in green the difference between the two curves and chose the readout position where it is maximized (yellow star on the figure).

Using this calibrated readout position, we perform single-shot charge readout by acquiring the signal V_{meas} during $T_{\text{int}} = 8\mu\text{s}$ for one and two electrons loaded in the sensed quantum dot. We repeat the operation 200000 times and plot the histogram of the averaged single-shot traces in [Figure 2.13\(b\)](#). The histogram shows two well-separated distributions corresponding to the two charge configuration initialization. We fit the histogram of the data to the function :

$$G(V_{\text{meas}}) = g_1(V_{\text{meas}}) + g_2(V_{\text{meas}}) \quad (2.6)$$

where,

$$g_i(V_{\text{meas}}) = \frac{A_i}{\sqrt{2\pi\sigma_i^2}} e^{-\frac{(V_{\text{meas}} - \mu_i)^2}{2\sigma_i^2}} \quad (2.7)$$

is a Gaussian distribution of amplitude A_i , a standard deviation σ_i , and a mean μ_i corresponding to the initialization with one electron for $i = 1$ and two electrons for $i = 2$. To perform single-shot readout and label correctly the single-shot outcomes we need to define a threshold voltage V_t , any measurement outcome below the threshold will be associated to one electron loaded in the red quantum dot while a measurement above the threshold is associated to a charge configuration of 2 electrons. The threshold is defined to maximize the readout fidelity defined as [\[Connors2020\]](#) :

$$F = \frac{1}{2}(f_1 + f_2) \quad (2.8)$$

where f_i is the fidelity associated to an occupation i of the quantum dot :

$$f_1 = \frac{\int_{-\infty}^{V_t} g_1(V_{\text{meas}}) dV_{\text{meas}}}{\int_{-\infty}^{+\infty} g_1(V_{\text{meas}}) dV_{\text{meas}}} \quad \text{and} \quad f_2 = \frac{\int_{V_t}^{+\infty} g_2(V_{\text{meas}}) dV_{\text{meas}}}{\int_{-\infty}^{+\infty} g_2(V_{\text{meas}}) dV_{\text{meas}}} \quad (2.9)$$

In [Figure 2.13](#) we study the figure of merit of single-shot readout which consists in observing the dependence of the fidelity as a function of the time spent acquiring the signal. We observe a clear dependence of the readout fidelity increasing as expected for longer integration times when most of the measurement noise is being averaged out. We achieve a readout fidelity of $99.0 \pm 1.8\%$ for an integration time of $7.2\mu\text{s}$, the fidelity is increased to $99.51 \pm 0.09\%$ for an even longer integration time of $8\mu\text{s}$.

To optimize furthermore the readout fidelity it would be necessary to conduct additional measurements. First, a correct extraction of the noise temperature at the end of the amplification chain

would be necessary to make sure that the measurement is limited by the 4 K amplifier. Second, in this section we only consider the amplitude of the measured signal, but it is possible to perform similar measurements of the signal phase. A complete measurement in the I-Q plane would be a good way to make sure that the measurement is optimized.

2.7.6 Conclusion

In the end, we demonstrated a rapid and high fidelity charge readout using a SET embedded in a resonant circuit. This resonant circuit has been optimized in terms of matching conditions using homemade on-chip components allowing the operation of the SET at its most sensitive functioning point. We fully characterized the RF circuit via classic RF measurements determining the resonant frequency, capacitance and matching point of the tank circuit. Finally, we performed single-shot readout of the charge configuration in $8\ \mu\text{s}$ of a neighbor quantum dot with a fidelity close to the state of the art [[Connors2020](#)]. Unfortunately, these developments in rapid charge readout were performed in a setup different from the one used for the experiments presented in [chapter 3](#) and [chapter 4](#). The difference of quantum device, PCB, and cryostat resulted in different matching conditions that we did not have time to optimize. Therefore, the rest of the measurements performed in this thesis have been conducted using simpler room temperature DC measurements.

3

Charge control in an isolated quantum dot array and on-demand segmentation

Contents

3.1	Introduction	65
3.1.1	Device presentation	65
3.1.2	Charge readout via DC current measurements	67
3.2	Operation of a QD array in the isolated regime	67
3.2.1	Stability diagrams in the open regime	67
3.2.2	Electron loading procedure	69
3.2.3	Probing the isolated regime boundaries	72
3.2.4	Detuning control of a double quantum dot in the isolated regime	73
3.3	Controlled quantum dot array segmentation via a highly tunable interdot tunnel coupling	74
3.3.1	Introduction	74
3.3.2	Metastable charge state lifetime	76
3.3.3	Demonstration of on-demand array segmentation	77
3.4	Conclusion	83

3.1 Introduction

As seen in [chapter 1](#), arrays of quantum dots (QDs) are identified as one possible road for scaling up electron spin-based quantum processors [[Vandersypen2017](#), [Veldhorst2017](#), [Vinet2018](#), [Li2018](#)]. In this context, the ability to displace controllably individual electrons plays an important role for realizing elementary operations within the array. Displacement at the QD scale induces coherent manipulation and interaction [[Petta2005b](#), [Brunner2011](#), [Watson2018](#), [Yoneda2018](#)]. While shuttling of the electrons at multi-dot scale enables array filling [[Volk2019](#), [Mortemousque2021a](#)], and functionalities for long distance quantum interconnection [[Mills2019b](#), [Jadot2021](#)]. These capabilities come with potential sources of errors such as incorrect positioning of the electrons in the array. It is therefore desirable to find protocols to minimize their impact on the rest of the qubits, especially when the charging energy is insufficient to allow protection against the electron displacement. Recent demonstrations of highly tunable interdot tunnel coupling [[Bertrand2015b](#), [Eenink2019](#), [Mortemousque2021a](#)] could offer strategies to protect the electron spin information while enabling quantum manipulation capabilities.

In this chapter, we will study in particular a triple linear array of QDs in a regime where the QDs are decoupled from electron reservoirs. The ability to decouple QD arrays from electron reservoirs is now commonly used in semiconductor devices and is usually referred to as the isolated regime [[Bertrand2015b](#), [Bayer2017](#), [Philips2022](#)]. The main advantages are the reduction of the system complexity via a reduction of the available charge states and an increased tunability of the system parameters (potential detuning and interdot tunnel coupling) [[Mortemousque2021a](#), [Chanrion2021](#), [Jadot2021](#)]. Building on these previous realizations, we will demonstrate a highly tunable interdot tunnel barrier and a protocol allowing to characterize the relaxation of metastable charge states of the quantum dot array. From there, we perform an on-demand segmentation of the array by isolating a single electron in a quantum dot and performing electron displacement in the rest of the array.

3.1.1 Device presentation

The sample measured in the rest of the thesis is also based on the GaAs/AlGaAs platform and is presented in [Figure 3.1\(a\)](#). The fabrication process has been developed in [section 2.3](#). The sample is composed of a linear triple QD array where each dot is labelled L, M and R for the left, middle and right QD respectively and a SET acting as a local electrometer. On each side of the array are present grounded ohmic contacts acting as electron reservoirs and will be used to load electrons into the structure. The QDs of the array are defined by three types of gates colorized differently in the SEM image presented in [Figure 3.1\(a\)](#). First, the barrier gates (green) are mostly designed to confine the QDs along the x -axis of the sample and tune the reservoir-QD tunnel coupling for B_1 and B_4 , while the gates B_2 and B_3 are designed to tune the interdot tunnel coupling. The plunger gates (red) were designed to confine the electrons along the vertical axis, while providing a knob to tune the chemical potential of each QD independently. Finally, the horizontal gate (blue)

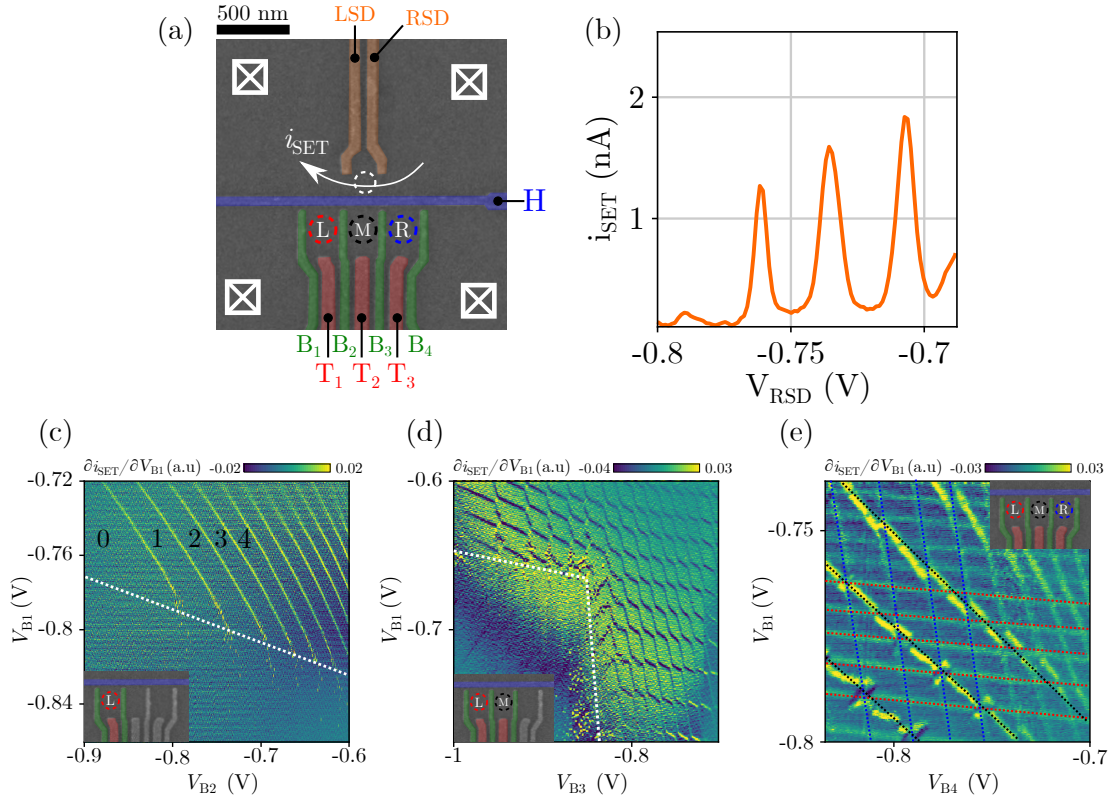


Figure 3.1: Measured device, stability diagrams of a single, double and triple quantum dots in the open regime. **a**, False color SEM image of a device similar to the one measured in this work. The approximate location of the QDs defined by the metallic gates are indicated by the dashed circles and the ohmic contacts are pictured as the white crossed squares. The charge configuration of the array is probed via a SET working as a local electrometer which is defined by the orange gates. **b**, Characterization of the SET. A $100 \mu\text{V}$ bias is set to the ohmic contacts of the SET and the voltage applied to gate RSD is swept which displays clear Coulomb peaks. The SET is tuned on the side of one of the Coulomb peaks to act as a highly sensitive electrometer. **c**, **d**, **e**, Stability diagrams for single, double and triple QD configuration of the array. Below the white dashed line in **b**, the charge degeneracy lines disappear indicating that the QD-reservoir tunnel rate is lower than the sweep rate of the experiment (250 mV s^{-1}). In this region the electron tunneling from or to the reservoir is impossible in the duration of the experiment, we identify this regime as the isolated regime. In **e**, the colored dotted lines correspond to charge transitions of the QD with the same color.

completes the confinement of the QD along the y -axis and separates the array from the SET. All the gates of the sample are polarized via the homemade DAC presented in [subsection 2.5.1](#) which allows changes of the applied voltage at the $10\ \mu\text{s}$ timescale. As we will see here and in [chapter 4](#), the experiment requires manipulating the interdot tunnel coupling and the chemical potential of the QDs at the nanosecond timescale. To do so the gates B_2 , B_3 and T_2 are connected to an AWG via bias-tees with a cut-off frequency of $1.6\ \text{kHz}$ as shown in [subsection 2.5.2](#).

3.1.2 Charge readout via DC current measurements

The SET is formed by the orange gates RSD and LSD and is biased with $100\ \mu\text{V}$ via the ohmic contact located at the top right of the sample. An I-V converter with a bandwidth of approximately $1\ \text{kHz}$ is connected to the top left ohmic contact and allows us to record the current flowing through the SET i_{SET} . To characterize the SET, we monitor i_{SET} and vary the voltage applied to gate RSD, the result is shown in [Figure 3.1\(b\)](#). We observe clear oscillations of the current corresponding to Coulomb peaks. When the SET is tuned on the side of one of these peaks, i_{SET} becomes highly sensitive to the local electric environment. Any charge variation in the array would therefore result in a jump of the SET current.

3.2 Operation of a QD array in the isolated regime

We will develop here the different techniques engineered to perform the loading of the electrons in the isolated regime and the distribution of electrons via interdot shuttling.

3.2.1 Stability diagrams in the open regime

To ensure the possibility to form QDs in the array and understand the effect of each gate on the potential landscape, we start by performing stability diagrams. Stability diagrams experiments are widely used in the community to determine the charge configuration, the interdot tunnel coupling and the gates lever-arm [[Volk2019](#), [Lawrie2020](#), [Mortemousque2021b](#)]. It consists in sweeping a given set of gates of the sample to change its charge configuration while recording the current i_{SET} . The SET acting as a local electrometer, we should observe jumps in the current when the charge configuration of the array is modified.

To perform the first stability diagram, we polarize the gates B_1 , T_1 , and B_2 in order to form a single dot at position L in the sample. The rest of the array is polarized to negative enough values preventing the electrons to tunnel from or to the right reservoir. We sweep the voltages applied to B_1 and B_2 while recording the SET current and plot the resulting stability diagram in [Figure 3.1\(c\)](#). Globally two effects on the SET current are observed, the first one is the global variation across the gate voltage space which corresponds to the capacitive coupling between

the gates defining the quantum dot array and the SET. Indeed, when the gates are swept during the stability diagram it slightly detunes the SET from the side of the Coulomb peak resulting in this overall change of the SET current derivative. To mitigate this effect we compensate for the capacitive coupling of the array gates by sweeping the gates RSD and LSD during the experiment in order to maintain the functioning point on the side of a Coulomb peak. The second effect appears as lines and is associated with integer charge variations in the QD. These lines separate stable charge occupation regions and are referred to as charge degeneracy lines. For $V_{B1} > -0.8$ V navigating along the x -axis of the diagram allows us to change the charge occupation of the QD, this indicates the ability of the voltage applied to B_2 (V_{B2}) to change the chemical potential of the QD L. In this configuration, it is even possible to determine the absolute number of charges. Indeed, for the most negative values of V_{B2} we do not observe any more charge degeneracy lines while our detector remains sensitive, indicating that the QD is empty of electrons. Setting the system to higher values of V_{B2} , we add one electron in the QD each time a line is crossed. We can identify and label on top of the stability diagram up to 10 electrons present in the QD. Now, if we navigate along the y -axis in the diagram we observe that the charge degeneracy lines are sharp and well-defined for $V_{B1} > -0.8$ V. In this region, the reservoir-QD tunnel coupling is in the GHz regime and electron exchange between the QD and the reservoir is possible. However, when the voltage applied to gate B_1 is lowered below -0.8 V, the charge degeneracy lines first become stochastic and individual charge jumps are observed before completely disappearing. In this region, the electron exchange through the reservoir is no longer possible and the QD-reservoir tunnel coupling rate is small compared to the measurement sweep rate, here 250 mV s^{-1} . This region is referred to as the isolated regime and is delimited by the white dashed line on the stability diagram. In the following sections, we will operate the array exclusively in this regime to fix the number of electrons present in the array during the experiment. In the end, we learn through this diagram that gate B_2 is efficient to change the chemical potential of QD L, and gate B_1 controls mostly the QD-reservoir tunnel coupling.

We now polarize the array in order to form a DQD at positions L and M and perform the stability diagram shown in [Figure 3.1\(d\)](#) using the methodology described before, here B_2 is polarized at -0.6 V. For $V_{B1} > -0.65$ V and $V_{B3} > -0.8$ V, the stability diagram displays a classic honeycomb pattern proving the ability to form a DQD [[van der Wiel2002](#)]. In this honeycomb pattern, the horizontal charge degeneracy lines are associated to charge variations in L and the vertical ones to M. Indeed, due to the geometry of the sample we expect the gates B_1 and B_3 to affect mostly the chemical potential of QD L and M respectively. In the configuration of a DQD, we again observe a disappearance of the charge degeneracy lines for $V_{B1} < -0.65$ V and $V_{B3} < -0.8$ V. The same interpretation can be conducted, and we attribute this disappearance to a low reservoir-QD tunnel coupling. In this configuration, gates B_1 and B_3 can finally be used for different purposes, first we have seen that we were able to tune the chemical potential of the QDs and second to tune the reservoir-QD tunnel coupling.

We finally polarize the whole array in order to form a triple QD and perform again a sta-

bility diagram using the gates B_1 and B_4 as shown in [Figure 3.1\(e\)](#), here B_2 and B_3 gates are polarized at -0.65 V. We observe in this case a more complex honeycomb pattern composed of three types of charge degeneracy lines that we categorized by their slopes in the voltage gate space [[Schröer2007](#)]. Using the previous observations made on gate B_1 we expect it to affect principally the chemical potential of QD L, we can therefore highlight the horizontal charge transitions and associate them to QD L. Using a symmetry argument the gate B_4 should also mostly affect the chemical potential of QD R, we can again associate the vertical charge transitions to QD R. Finally the last type of charge degeneracy lines which are diagonal are associated to M, indeed the QD being located in the middle of both gate we expect a similar effect of each gate on the chemical potential of QD M.

In the end, performing these stability diagrams helped us to understand the effect of each gate on the array parameters. Indeed, we have seen that the barrier gates B_1 and B_4 located on each side of the array were able to efficiently tune the QD-reservoir tunnel coupling while being able to tune the chemical potential of L and R. For the barrier gates B_2 and B_3 located within the array, we have demonstrated their ability to tune simultaneously the chemical potential of the QDs located to the left and the right of the barrier. In addition, these gates control the interdot tunnel couplings, as we will see in [section 3.3](#). We also see the difficulty to determine the absolute number of charges present in a system composed of more than one QD due to the high number of charge degeneracy lines when electron exchange is possible with the reservoirs as well as between the quantum dots. Indeed, using the same methodology (counting the number of degeneracy lines from 0) would result in a wrong identification of the array charge state if only one charge degeneracy line is missed, which can easily happen if the electrometer is detuned for instance. Operating with a fixed number of electrons greatly simplifies the picture by suppressing the electron exchange of the quantum dot with the reservoir and limiting the number of charge transitions. In the following section, we first load a predetermined number of electrons in the single-dot regime, before closing the coupling with the reservoir and allowing access to the other quantum dots.

3.2.2 Electron loading procedure

We start by implementing a protocol called loading map allowing us to initialize a known number of charges in QD L and isolate them from the reservoirs. This technique is commonly used now in semiconductor devices to simplify the tuning process of the sample via a reduction of the available charge states and to enhance the array parameters operation range [[Bertrand2015b](#), [Jadot2021](#), [Mortemousse2021a](#), [Chanrion2021](#)].

To do so, the array is tuned in a particular configuration to use QD L to load electrons in the system via the left reservoir. This regime is achieved by tuning the M and R QD chemical potentials high compared to the right reservoir Fermi energy and the L QD chemical potential while setting a low tunnel coupling between QD R and the right reservoir. In the end, it is impossible for electrons to enter the array via the right reservoir or access QD M and R. In the stability diagram [Figure 3.2\(a\)](#), we have seen that it was possible to tune the reservoir-QD tunnel rate via

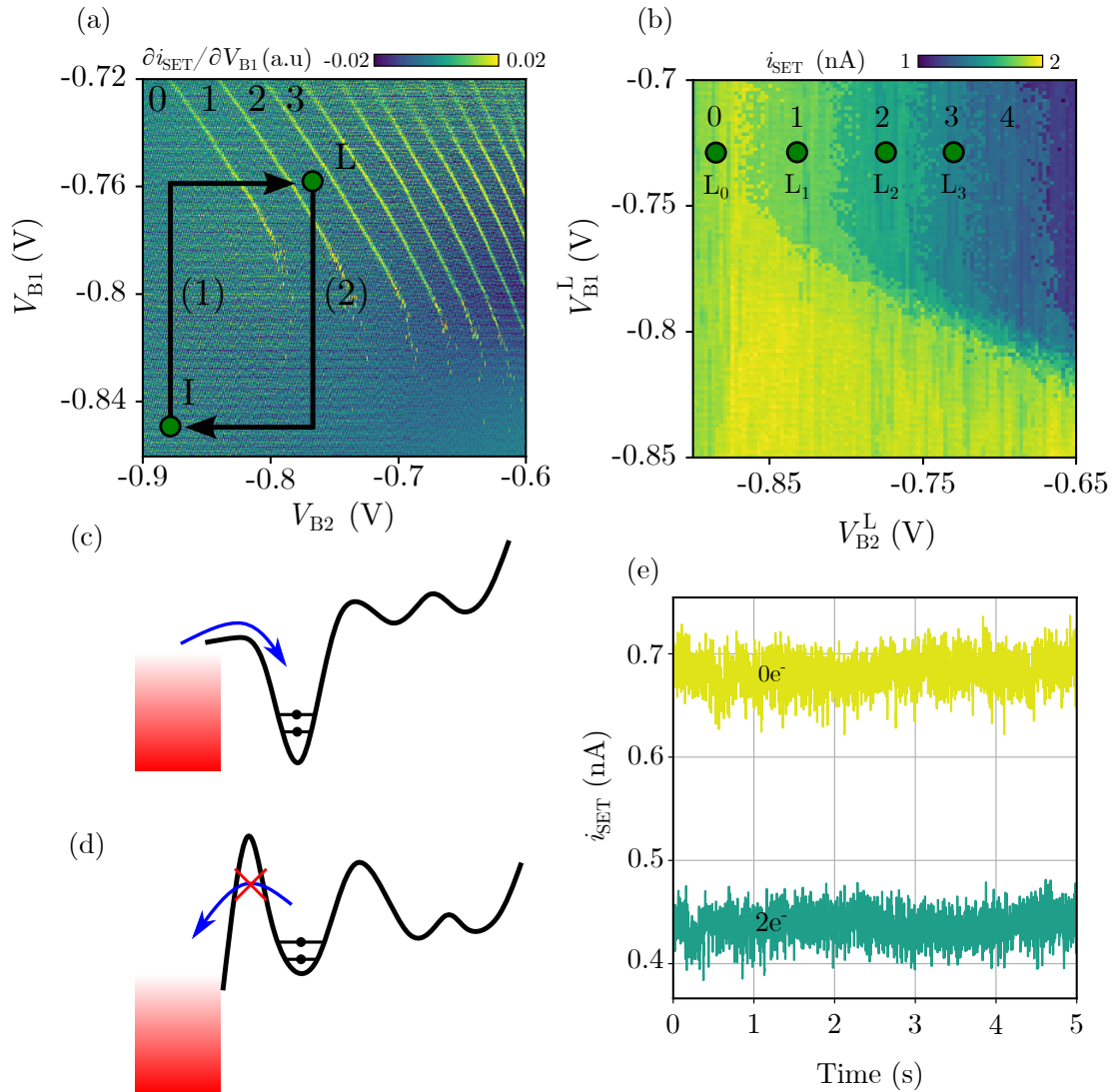


Figure 3.2: Loading map protocol and procedure to isolate the array from the reservoirs. **a**, Stability diagram of the leftmost QD of the array. The derivative of the current measured across the SET is plotted as a function of the voltage applied on B_1 and B_2 gates controlling respectively the reservoir-QD tunnel barrier height and the chemical potential of the QD. The electron occupation number is indicated for the first four charge regions of the stability diagram. **b**, Loading map protocol result. The measurement is performed by initializing the QD empty of any electrons at position I and applying the pulse sequence sketched on top of **a**. At the end of the pulse sequence i_{SET} is integrated during 5 ms and the averaged value is plotted as a function of the coordinates of point L. Each pixel of the figure corresponds to one realization of the pulse sequence and electrometer measurement. This procedure is used to identify the regions where it is possible to load an arbitrary number of electrons in the isolated regime. The position used to load i electrons in the QD is identified by L_i . **c**, Sketch of the potential landscape when the system is pulsed at position L_2 . **d**, Sketch of the potential landscape when the system is brought back to position I. The electrons are kept in the QD for any chemical potential of the QD due to the low QD-reservoir tunnel coupling. **e**, QD charge occupation at position I after initially loading zero or two electrons. No tunneling in or out events is recorded during 1000 5 s repetitions.

the voltage applied on gate B_1 . We use this feature to implement a protocol allowing us to load up to 5 electrons in QD L and isolate them from the reservoirs by applying the pulse sequence sketched on top of the stability diagram. The array is first initialized empty of any electrons at the position I in the isolated regime, then the reservoir-QD tunnel coupling and the chemical potential of the QD are sequentially pulsed to reach position L. The L position is held during 1 ms before bringing the system back into the isolated regime at the position I via a negative pulse applied again sequentially on B_1 and B_2 . Once the pulse sequence is over the SET current is acquired and averaged during 5 ms. In [Figure 3.2\(b\)](#), we plotted the averaged current as a function of the coordinates of point L ($V_{B_2}^L, V_{B_1}^L$). In this plot each pixel represents one realization of the pulse sequence described above. It is interesting to note here that the readout is always performed at the same position in the voltage gate space, this allows us to tune the electrometer at this particular position. By doing so, we have an optimized response without worrying about the capacitive coupling between the gates and the SET reducing the sensitivity like in the stability diagrams presented in [Figure 3.1](#). Indeed, in the loading map we observe 5 different levels of i_{SET} corresponding to different charge configurations of the QD. For $V_{B_2}^L < -0.8$ V, we observe a large region of the same current level corresponding to zero electrons in QD L. In this regime, the QD-reservoir tunnel coupling is too low to permit electron loading during the time spent at position L. On the contrary for $V_{B_2}^L > -0.8$ V, the diagram shows areas whose boundaries correspond to the one of the stability diagram. For this probed position the QD-reservoir tunnel rate is high compared to the probe time at position L and the QD reaches the equilibrium with the reservoir. When the system is pulsed back to position I, the electrons are isolated from the reservoir due to the low reservoir-QD tunnel coupling. The high chemical potential of the left QD guarantees that all the loaded electrons should eventually tunnel back to the reservoir leaving the QD empty. However, due to the low tunnel coupling to the reservoirs it is possible to hold this metastable configuration longer than the measurement time (here 5 ms). In the end, we define three positions L_1 , L_2 , and L_3 that will be used to load up to three electrons in the isolated regime.

Through the loading map, we observe the inability to isolate more than 5 electrons in a single QD. This limitation is attributed to a lack of tunability over the coupling rate between the electrons sitting on highly excited orbitals of the QD and the reservoir. Indeed, these excited orbital states have associated wavefunctions with a bigger spatial expansion and therefore a bigger overlap with the reservoir. For the same potential barrier height, an electron located on an excited orbital will therefore preferentially tunnel to the reservoir compared to one located in lower orbital states. One way to circumvent this issue and to be able to trap a high number of electrons is to perform repeated sequences of loading and shuttling of a smaller number of charges [[Mortemousque2021a](#)].

To estimate how long the electron is held isolated from the reservoirs we either load zero or two electrons using the positions L_0 and L_2 previously identified. Then, the SET current i_{SET} at position I is monitored during 5 s, the measured signal is plotted in [Figure 3.2\(e\)](#). A variation of the charge occupation of the QD would result in a jump of the SET current and as expected we observe no such events during the whole acquisition. To ensure this observation we repeat

the experiment 1000 times and never observed a charge variation in the array. The probability to have no relaxation events in 1000 experiments of 5 s is defined as $e^{-5000/\tau}$ where τ is the isolation characteristic time. We can therefore ensure with a 99 % fidelity that $\tau > 4.9 \times 10^5$ s. It is therefore possible to load and isolate the electrons from the reservoirs for a longer time than the typical experiment $\simeq 1$ s [Philips2022].

3.2.3 Probing the isolated regime boundaries

Now that we identified the electron loading positions, we focus on the limits of the isolated regime in the voltage gate space through the experiment presented in Figure 3.3(a) called a losing map.

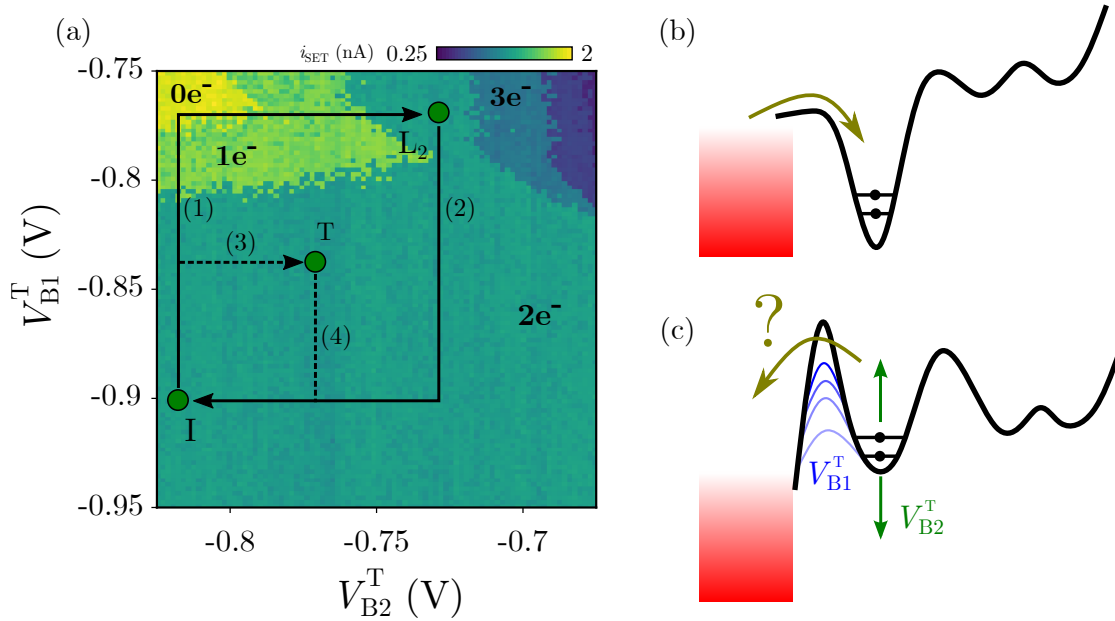


Figure 3.3: Losing map protocol and isolated regime limits in the voltage gate space. **a**, Losing map of L identifying the limits of the isolated regime. Each pixel corresponds to a single shot experiment where two electrons are loaded in L and isolated from the reservoirs using pulses (1) and (2). The system is then pulsed to the varied position T during 1 ms using pulse (3) and brought back to I using pulse (4). Finally, the current i_{SET} is averaged during 5 ms. **b**, Sketch of the potential landscape at position L. **c**, Sketch of the potential landscape at position T, probing different positions in the B_1 and B_2 voltage gate space to draw the limits of the isolated regime.

The system is initialized empty of electrons in the isolated regime at position I, then it is pulsed to position L_2 to load two electrons in the QD. At this position, the potential landscape is sketched as in Figure 3.3(b). The QD is pulsed back to position I to reach a metastable state in the isolated regime as discussed previously. The goal now is to probe the system at a varied position T in the V_{B_1} and V_{B_2} voltage gate space and check the number of electrons in the QD at the end of the probe pulse. By doing so, the voltages applied to B_1 and B_2 are sequentially pulsed during 1 ms at coordinates $T(V_{B_2}^T, V_{B_1}^T)$. Then, the system is pulsed back to position I in order to perform a charge state readout by acquiring the SET current during 5 ms. In Figure 3.3(a), we plotted the averaged current as a function of the coordinates of point T. Here again, we can clearly distinguish different levels of current corresponding to different electron occupations of the QD that we can identify

and label. We observe for $V_{B1}^T < -0.85$ V a large region of homogenous i_{SET} values, the electrons loaded into the structure are kept in the structure for all the probed values of the voltage applied on gate B_2 . In this regime of low QD-reservoir tunnel rate, electron exchange is prevented during the probe pulse at position T regardless the QD chemical potential. For $V_{B1} > -0.85$ V, the tunneling through the reservoir is possible again and the number of electrons can be controlled using the voltage applied on B_2 . Now that we have identified the isolated regime region in the voltage gate space, we can operate the array in this regime by being careful to never go out of the bounds found by this experiment.

3.2.4 Detuning control of a double quantum dot in the isolated regime

We have previously demonstrated the ability to initialize a fixed number of electrons and their isolation from the reservoirs via the control of the QD-reservoir tunnel coupling. In this section, we demonstrate the operation of DQD with a fixed number of charges in the isolated regime and especially the ability to reach all the possible charge states in a DQD loaded with an arbitrary number of electrons.

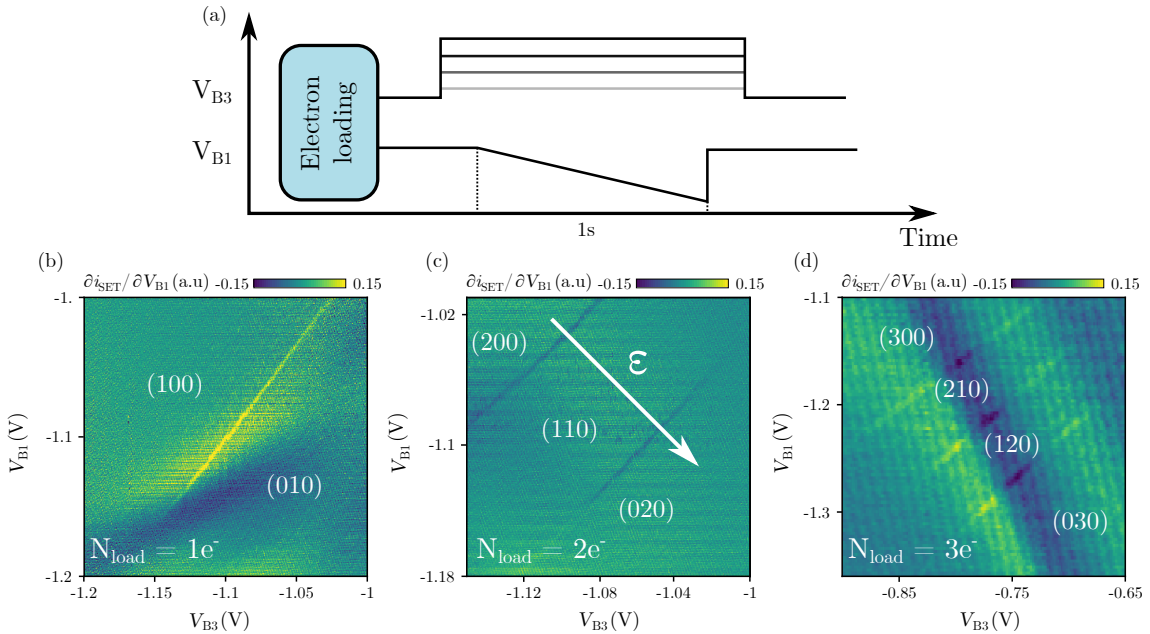


Figure 3.4: Detuning control of a double quantum dot in the isolated regime. **a**, Schematic representation of the voltage applied to gate B_1 and B_3 in order to perform one trace of the stability diagram presented in (b, c, d). **b, c, d**, Stability diagram of the L-M DQD in the isolated regime when 1, 2 or 3 electrons are loaded in the array via the loading map procedure. We observe diagonal charge degeneracy lines indicating the similar effect of gates B_1 and B_3 for tuning the chemical potential of L and M respectively. The different occupation in each region is labelled on top of the diagram, and we define the detuning axis perpendicular to the charge degeneracy lines.

The experimental demonstration of interdot shuttling is presented in Figure 3.4(a) and consists in loading up to three electrons using the loading map protocol described previously. While keeping the charges in the isolated regime, we sweep the voltage applied on gate B_1 to progressively transfer charges from QD L to M while recording the SET current. At the end of the sweep, the

array is emptied and reloaded and the B_1 sweep is repeated for another voltage applied to B_3 .

In Figure 3.4(b,c,d), we show the stability diagrams resulting from this procedure. We observe diagonal charge degeneracy lines corresponding to charge transitions of the L-M DQD. As expected the efficiency of gates B_1 and B_3 to transfer charges in the DQD is equivalent due to the symmetry of the system. To label the charge configuration regions, we make the assumption that the voltage applied to B_1 and B_3 mostly affects the chemical potential of L and M respectively, and that the R dot is inaccessible for the electrons. We can therefore associate the region of the top left of all the diagrams to the configuration where all the electrons are present in QD L. From there, we navigate to the bottom right of the diagram and add one electron to the QD M each time a line is crossed, we note the charge configuration of the array (l, m, r) with l , m and r the charge occupation of QD L, M and R respectively. For a system of n dots containing k electrons we expect $\binom{n+k-1}{k}$ charge states, in our system it is verified in the configuration of a DQD with up to three electrons loaded in the structure. In the end, we are able to operate a DQD in the isolated regime and access all the charge states available by varying only the voltage applied to B_1 and/or B_3 .

3.3 Controlled quantum dot array segmentation via a highly tunable interdot tunnel coupling

3.3.1 Introduction

We previously demonstrated the ability to load a fixed number of electrons in a DQD and isolate them from the reservoirs to operate in the so-called isolated regime. Operating in such a regime greatly simplified the stability diagram of the DQD system, and helped us to identify the different charge states available. In this section, the isolation process is pushed one step further by demonstrating QD-QD decoupling. Finally, we develop a methodology to segment a linear QD array and discuss the novel features enabled by a highly tunable interdot tunnel coupling.

We start by characterizing the inter-dot tunnel rate from the sub-Hz to GHz regime via the study of metastable charge states and achieve complete isolation both from the reservoirs and the neighbor QD of up to three electrons. We will refer this regime as the fully isolated regime. Then, we implement two functionalities demonstrating the potential of the array partitioning process. First, an enhancement of metastable charge state lifetime and their readout at a fixed and optimized position in the voltage gate space, and then charge displacement and readout in the partitioned array.

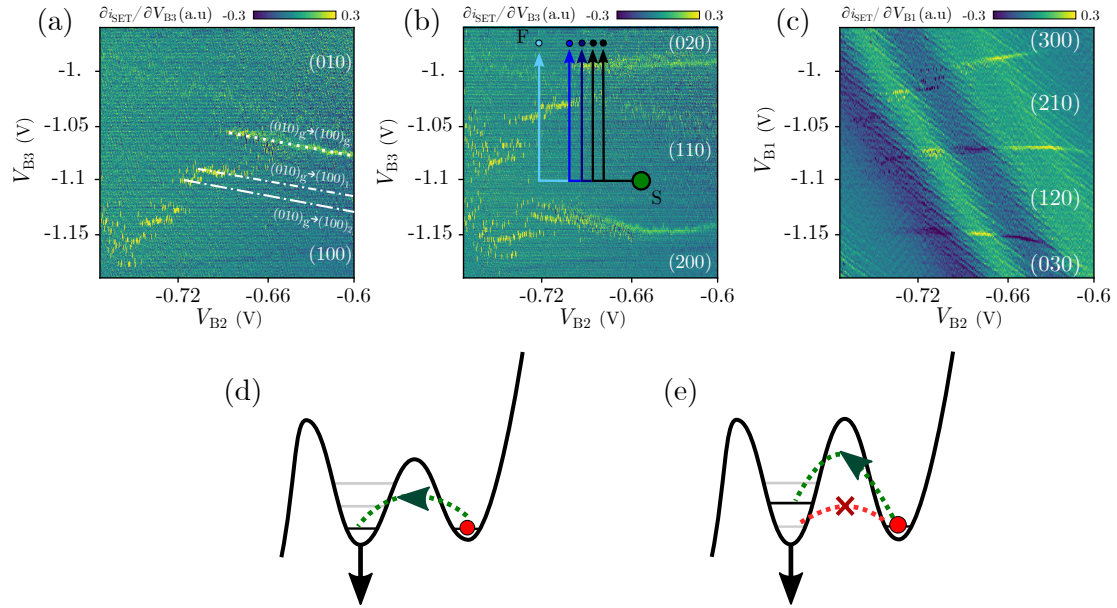


Figure 3.5: 1, 2 and 3 electrons stability diagram of a DQD in the fully isolated regime. **a**, **b**, **c**, Stability diagram of the L-M DQD performed with a fixed number of charges respectively 1,2 and 3 in the fully isolated regime. The detuning and the tunnel coupling of the L-M DQD are swept using relevant gates B_3 and B_2 . It is possible to obtain all charge states of the DQD by sweeping B_3 gate voltage over around 200 mV. For a negative enough voltage applied on B_2 the stability diagram exhibits excited charge states of the DQD that are only observable in the low tunnel coupling regime. Charge configurations of the array are indicated in white. Point S and F are used to perform the experiment presented in [Figure 3.6](#) and are described in the main text. **d**, Sketch of the electric potential across the DQD when the tunnel coupling is high enough to allow charge transfer during the sweep of B_3 . **e**, Similar to **d** but for an interdot tunnel coupling to low to ensure charge transfer to the ground state of QD L. Charge transfer is therefore obtained via excited charge states of QD L whose wavefunctions have a larger spatial expansion.

3.3.2 Metastable charge state lifetime

Stability diagrams

To implement the fully isolated regime where the QDs of the array are decoupled from the reservoirs and from their neighbor QD, we start by characterizing the L-M DQD in terms of tunnel coupling. To do so, we performed the isolated stability presented in Figure 3.5 using a similar protocol to the experiment presented in Figure 3.4, the only difference being that the swept gates are now B_3 and B_2 or B_1 and B_2 . We first focus on the stability diagram in Figure 3.5(a) where only one electron is loaded initially in the structure but the same analysis can be conducted for two and three electrons loaded. For $V_{B_2} > -0.66$ V, a well-defined charge degeneracy line separates the two charge states and varying the voltage applied on gate B_3 allows us to transfer charges from L to M like in Figure 3.4(a). In this region of the stability diagram, the interdot tunnel rate is high enough to allow an adiabatic charge transfer between the two QDs during the sweep of V_{B_3} . When the voltage applied to B_2 is reduced below -0.66 V, we observe the apparition of stochastic events before seeing the charge degeneracy line completely disappearing and reappearing for lower values of V_{B_3} . Analogous to the QD-reservoir decoupling, this phenomenon is attributed to the L-M interdot tunnel rate becoming comparable first and then smaller with respect to the measurement sweep rate, here 250 mV s^{-1} . However, in this case the charge degeneracy line does not disappear completely but is rather shifted to higher values of potential detuning of the DQD. To explain this behavior we need to take into account the excited orbital states of the quantum dots. Indeed, in the regime where the interdot tunnel rate is high compared to the sweep rate of the detuning, the charge transfer during the sweep is ensured via tunneling to the ground orbital state as depicted in Figure 3.5(d). When the interdot tunnel coupling is drastically reduced the charge transfer through this state is unlikely to happen in the duration of the sweep. The shift of the degeneracy line towards larger values of detuning is therefore the signature of tunneling between the orbital ground state $(010)_g$ and the first excited orbital states of QD L noted $(100)_1$ and $(100)_2$. In this low interdot tunnel coupling regime the excited orbital wavefunctions of QD L are expected to have a larger overlap with the ground state of QD M resulting in preferential tunneling. These tunneling events are therefore happening when the $(010)_g$ becomes resonant with the excited orbitals of QD L providing *in-situ* spectroscopy of the QD.

In the end, using these stability diagrams we are able to access all the charge states available using the voltage applied on B_3/B_1 . We are also able to tune the interdot tunnel coupling via the voltage on B_2 gate. This new tuning knob provided us with a way to observe the signature of excited orbital states of QD L. Moreover, we will use this tuning capability to decouple QDs and reach the fully isolated regime.

Characterization of the metastable charge state lifetime

To reach the fully isolated regime we need to precisely characterize the dependence of the interdot tunnel rate with respect to the voltage applied to gate B_2 . To do so, we study in this section the

lifetime of metastable charge states as a function of the interdot tunnel coupling. This study will confirm our capability to prevent charge displacement in the array via a high level of control in the low interdot tunnel coupling regime.

In order to quantify the interdot tunnel rate dependence with the voltage applied on gate B_2 , we designed the pulse sequence sketched on top of the stability diagram in Figure 3.5(b). First, two electrons are loaded and the system is brought in the (110) charge configuration at position S. From this point, the tunnel coupling is lowered to the desired value $V_{B_2}^F$ using a voltage pulse on gate B_2 . After 100 ns the detuning is set to reach the (020) charge state region via a voltage pulse on B_3 . At this position, the (110) charge state becomes a metastable charge state with a limited lifetime. To track the evolution of the charge state, we record the current i_{SET} during up to 1 s. The measurement is then repeated 1000 times for $V_{B_2}^F$ values between -0.72 V and -0.68 V. As an example, we show in Figure 3.6(b) selected records of the SET current for $V_{B_2}^F = -0.69$ V where we observe sharp single jumps of i_{SET} from 0.55 nA to 0.75 nA. These events are associated with a charge variation in the L-M DQD, precisely in this case the relaxation of the (110) charge state to (020). To extract the lifetime of the (110) charge state, we compute the probability $P_{(110)}$ to observe the (110) charge state as a function of the waiting time at position F. To do so we define a threshold halfway between the two current levels represented by the black dashed line in Figure 3.6(b). For the 1000 traces, a current above or below the threshold is associated to respectively (110) or (020) charge state. The binarized traces are averaged for each $V_{B_2}^F$ value tested to compute $P_{(110)}$ as shown in Figure 3.6(c). The probability traces are fitted to an exponential decay function to extract the characteristic lifetime of the (110) charge state. Finally, the extracted lifetime is plotted in Figure 3.6(d) as a function of $V_{B_2}^F$ and we observe that it can be tuned over 4 orders of magnitude in a few tens of mV. This indicates again the efficiency of the gate B_2 to tune the potential barrier height in between the L-M DQD in the low inter-dot tunneling regime. In particular for $V_{B_2}^F \leq -0.72$ V, no relaxation events are visible in a thousand 1 s-long time traces. Since the probability to see no relaxation events in 1000 experiments of 1 s is defined as $e^{-1000\Gamma}$, we can therefore ensure with a fidelity of 99 % that the relaxation rate $\Gamma < 10^{-2}$ Hz.

In the end, we demonstrate the ability to reduce the inter-dot tunnel rate well below the Hz regime to reach the fully isolated regime of the QD array. In the following, we will explore the possibilities offered by this new characteristic, especially for the initialization and readout of charge configurations in the array.

3.3.3 Demonstration of on-demand array segmentation

The capability to operate over such a wide range of interdot tunnel coupling enables functionalities for future prospects in spin qubit technology [Li2018]. Indeed, freezing on a fast timescale, the electron dynamics results in a well separated and metastable charge configuration that can be efficiently probed. Proof of principle experiment is performed in a tunnel coupled double quantum dot (DQD) with up to three electrons. The protocol consists of loading a specific charge configuration in the double dot, decreasing on a fast timescale the interdot tunnel barrier, and then tuning the

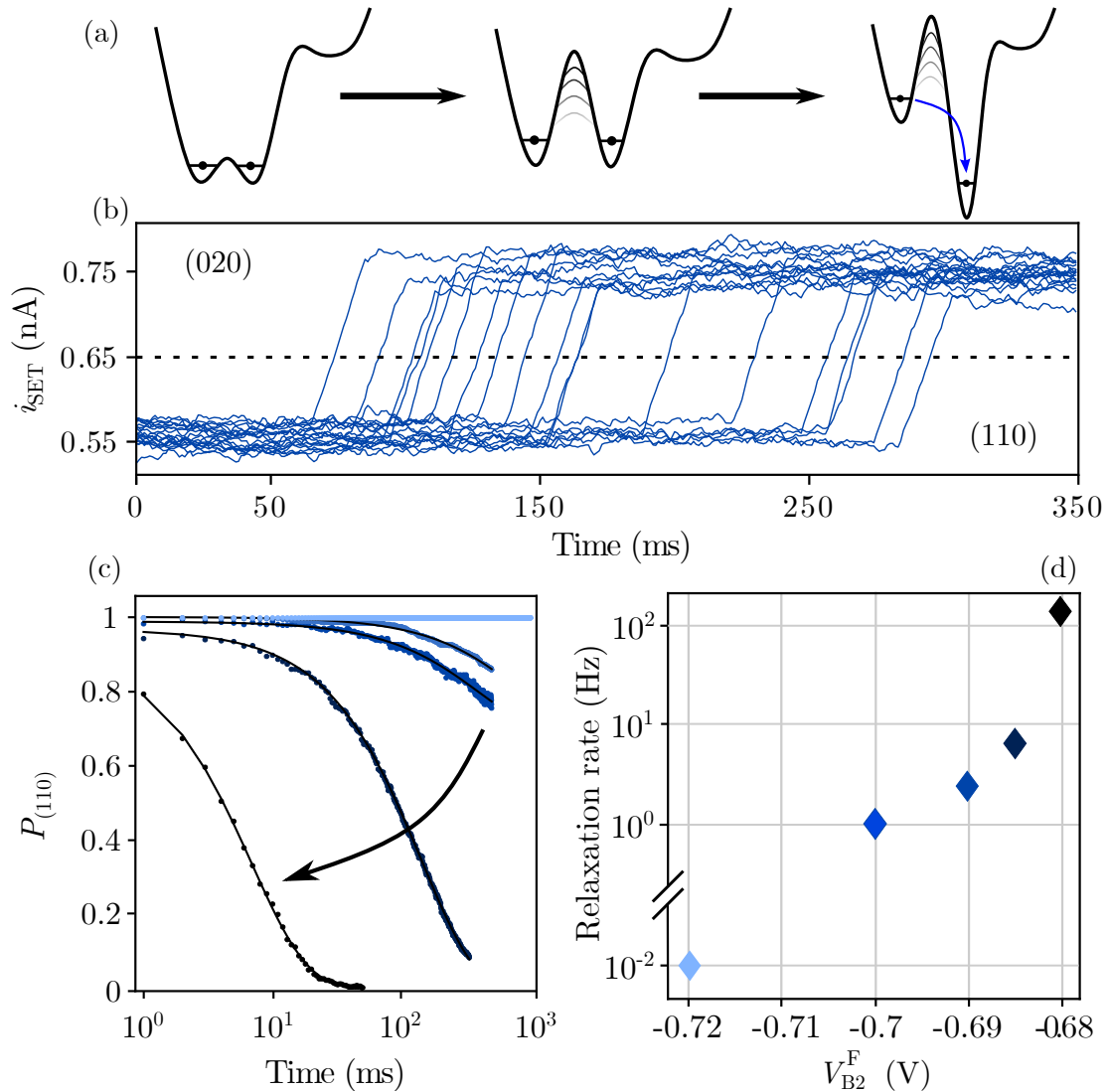


Figure 3.6: Probing relaxation process of a metastable charge state in DQD. **a**, Schematic of the potential landscape during the relaxation procedure. The system is initialized to point P in the (110) charge configuration. The tunnel barrier height between the dots is set by applying a pulse of varying amplitude V_{B2}^F . The system is then brought back in the region where the equilibrium charge state of the array is (020). **b**, Selected single-shot measurements of (110) to (020) relaxation for $V_{B2}^F = -0.69$ V. The current i_{SET} displays single event relaxation. A moving average filter is applied to the traces for clarity. **c**, Relaxation of the (110) to (020) charge state observed for different tunnel barrier height. A threshold is defined halfway between the two current levels represented by a dashed line in **a**. For the 1000 traces, a current above or below this threshold is associated to respectively (110) or (020) charge state. The binarized traces are averaged for each V_{B2}^F value tested to compute the (110) population. Experimental data are represented as solid points and the solid black line is an exponential decay fit. For $V_{B2}^F = -0.72$ V we do not observe any relaxation event in 1000 shots of 1 s. **d**, Relaxation rate of the (110) to the (020) charge state as a function of the freeze point (F) coordinate.

system to a working point at which the charge detection has been optimized while preserving the charge configuration. Moreover, it permits arbitrary partitioning of the QD array in sub-systems allowing for easier tuning and manipulation via a reduction of the available charge states by the system.

Initialization and readout of metastable charge states

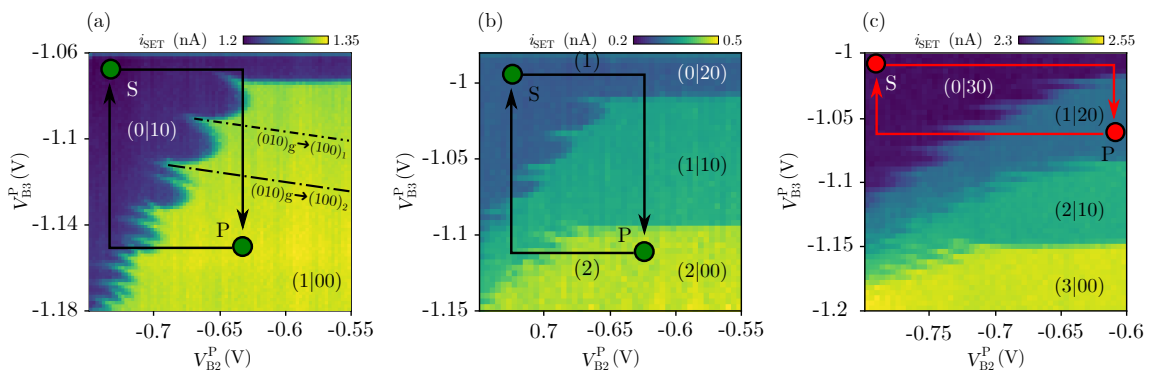


Figure 3.7: 1, 2 and 3 electrons freeze map in a DQD. **a,b,c**, 1,2 and 3 electrons freeze map of the L-M DQD. The measurements are obtained by performing the pulse sequence sketched on top of the three figures. The system is initialized for all the figures at position S, with all the electrons loaded in QD L and in the sub-Hz interdot tunneling rate regime. From there, the measurement sequence can be decomposed in three parts. The first one is here to probe the DQD at a certain position in the voltage gate space point P. The second part brings back the system at point S by first reducing the tunnel coupling of the DQD in the sub-Hz and therefore freeze the charge configuration obtained at point P. Finally, the current i_{SET} is averaged during 5 ms and plotted as a function of the point P coordinates $P(V_{B2}^P, V_{B3}^P)$. Each pixel is the average of 50 realizations of the protocol. Different levels of current are identified and labeled as different charge configuration of the DQD.

We demonstrate here the initialization, manipulation and readout of metastable charge states of up to three electrons in a DQD using a freeze map protocol. It consists of setting the system at a given detuning and tunnel coupling value before pulsing the inter-dot tunnel rate to the sub-Hz regime at the ns timescale to freeze the obtained charge configuration. Followed by a charge readout, this protocol allows us to identify the detuning and tunnel coupling regions where a charge transfer is possible and perform charge readout of metastable charge states at a fixed and optimized position in the voltage gate space. We detail the freeze map protocol in the following paragraph and in addition to the already described notation for the charge states labelling, we introduce a vertical bar | indicating a sub-Hz tunnel coupling rate in between the QDs. For instance (1|10) means that L and M contain one electron each, R is empty and that the charge tunneling between L and M is prevented for the whole experiment duration.

We detail here the case where only one electron is loaded in the system, corresponding to [Figure 3.7\(a\)](#), but a similar analysis can be conducted for two ([Figure 3.7\(b\)](#)) and three ([Figure 3.7\(c\)](#)) electrons loaded in the system. The trajectory applied to perform the freeze map protocol is sketched in [Figure 3.7\(a\)](#), and starts in the (0|10) charge state at point S. Two 100 ns pulses

are applied sequentially via the AWG to the gates B_2 and B_3 to set the system to point P. Then, the interdot tunnel rate is lowered to the sub-Hz regime and the detuning is set back to position S. Finally, the current i_{SET} is averaged during 5 ms and plotted as a function of the point P coordinates $P(V_{B_2}^P, V_{B_3}^P)$. Each pixel of this plot is the average of 50 realizations of this protocol.

Depending on the coordinates of point P ($V_{B_2}^P, V_{B_3}^P$), we obtain two possible values of i_{SET} corresponding to either the $(0|10)$ or $(1|00)$ charge state. Compared with the isolated stability diagram in Figure 3.5(a), we observe the same charge transitions at $V_{B_3} = -1.06$ V and $V_{B_2} = -0.65$ V. However, the freeze map gives a more detailed picture of the first excited charge states of QD M, appearing as lobes on the leftmost part of the diagram. Indeed, as the tunnel coupling decreases, the charge tunneling involves states of increasing energy. These freeze maps thus provide an additional spectroscopy of the excited charge states of QD M. This agreement between the stability diagram and the freeze map is also observed for 2 and 3 electrons loaded in the array as shown in Figure 3.7(b,c) considering that B_1 and B_3 have an opposite but similar effect on the potential detuning of the L-M DQD.

To conclude, we demonstrated the capability to initialize metastable charge configurations for a duration long enough to permit their readout at an optimized position in the voltage gate space. This study is a first demonstration of the novel initialization and readout protocols induced by the high level of control over the inter-dot tunnel coupling.

Isolating subparts of the array

In addition to an improvement of the initialization and readout of the charge states of a DQD, the fully isolated regime also grants us the possibility to isolate subparts of the QD array to simplify its tuning and manipulation. In this section, we demonstrate the control of the rest of the array while keeping an electron fully isolated in a QD. To do so we will initialize a metastable charge state of the L-M DQD in order to isolate a single electron in L. Then, we will progressively transfer the charges remaining in M to R to control the number of charges present in the M-R subsystem.

The first step of the experimental procedure consists in loading 3 electrons in the isolated regime and reach the (030) charge state. From there, a $(1|20)$ metastable charge configuration is initialized by pulsing the voltages applied on gate B_2 and B_3 , the sequence performed in order to do so is sketched on top of the freeze map in Figure 3.7(c). The next step consists in opening the tunneling between M and R by applying -0.65 V on gate B_3 , and lowering the chemical potential of QD R by increasing the voltage applied on B_4 to -1.15 V. In this voltage configuration the L-M interdot tunnel coupling is pulsed during 1 ms using a voltage pulse of amplitude $V_{B_2}^T$. Following the pulse, the detuning of L-R is ramped using the voltage applied on gate B_4 while the SET current is recorded. To summarize the pulse sequence, we present in Figure 3.8(b) a chronograph of the voltages applied to produce the protocol described above. The derivative $\partial i_{\text{SET}} / \partial V_{B_4}^R$ is plotted as a function of $V_{B_4}^R$ and $V_{B_2}^T$ in Figure 3.8(c).

In this stability diagram we observe two regimes of the system. The first one for $V_{B_2}^T < -0.75$ V where are present two degeneracy lines indicating that the sub-array composed of QD M and R

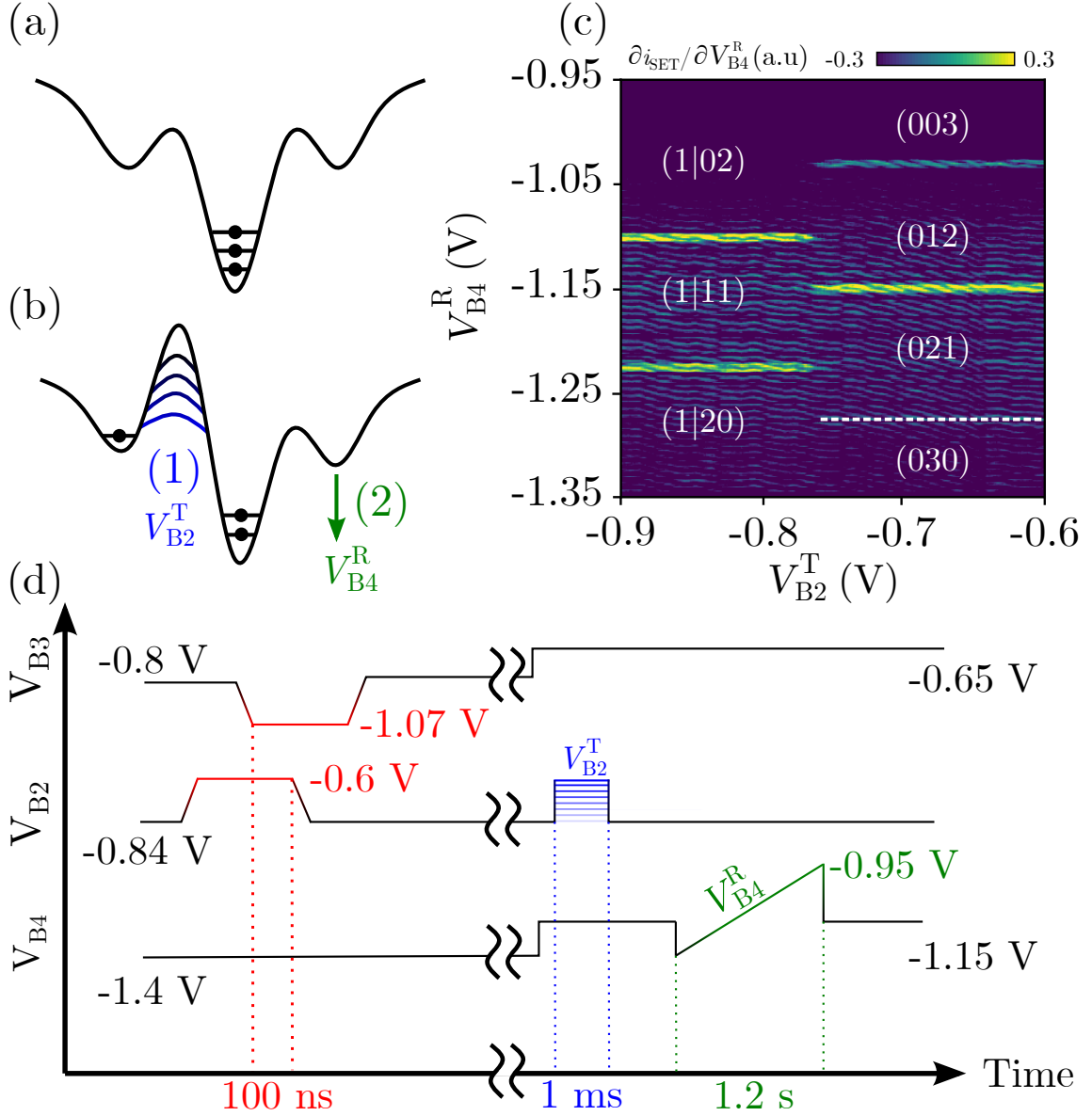


Figure 3.8: Isolating sub-parts of the linear QD array. **a**, Schematic of the potential landscape at the initialization point. The array is initialized in the (0|30) charge configuration. Using the calibration made by the freeze map in Figure 3.7(c) the system is brought to the metastable (1|20) charge configuration. **b**, Schematic of the potential landscape at the beginning of the stability diagram of **c**. For different values of the tunnel coupling between the L and M dot the chemical potential of the R dot is slowly lowered allowing the electrons to tunnel from M to R. **c**, Stability diagram performed while a sub-part of the array is fully isolated. For $V_{B2}^T < -0.75$ V the electron in the L QD is unable to tunnel back to the M QD and the only charge state seen on the stability diagram are (1|20), (1|11) and (1|02). For higher values of V_{B2}^T the electron in L tunnels back to M and all charge states of 3 electrons in a DQD are observed. **d**, Chronograph of the voltages applied on gate B2, B3 and B4. The pre-sequence is dedicated to create a metastable charge state (1|20) using the pulse sequence described in Figure 3.7(c). Then the voltage applied on B2 gate is pulsed during 1 ms to V_{B2}^T and finally the chemical potential of the R QD is ramped while the current i_{SET} is recorded.

contains only two electrons while the third one is isolated in L. Indeed, due to the low L-M interdot tunnel coupling, the electron in L cannot tunnel back to QD M, in this configuration the only charge states available by the array are $(1|02)$, $(1|11)$ and $(1|20)$. They are identified and labelled on top of the stability diagram. On the other hand for a pulse amplitude $V_{B2}^T > -0.75$ V, we observe a third line, indicating that the M-R sub-array now contains three electrons. In this regime, the electron stored initially in L had the ability to tunnel back during the V_{B2}^T pulse. Indeed, this configuration allows the relaxation of the (120) to the (030) charge state and the resulting stability diagram corresponds to a classical one for three electrons in a DQD. To conclude, we are able to fully isolate electrons in a sub-part of the QD array while being able to access all the other charge states in the rest of the structure. This study demonstrates the ability of the fully isolated regime to lower the complexity of the stability diagrams by reducing the number of charge states available by the electrons but also to access metastable charge states of the system (for instance $(1|20)$ instead of (030)) in [Figure 3.8](#))

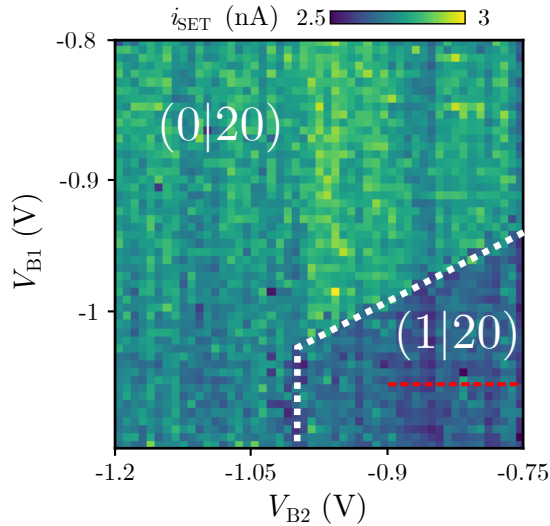


Figure 3.9: Verification of the charge occupation of the array during the partial freeze experiment. Charge detection in L after a partial freeze of the array in the $(1|11)$ charge configuration. The system is pulsed in the $(1|11)$ region in [Figure 3.8](#) during 1 ms before coming back in the $(1|20)$ region. At this position, we pulse the voltage applied on gate B_1 and B_2 during 1 ms and we record the electrometer signal. Two regions of different signal level are observed discriminating two charge configuration of the array. For high values of voltage applied on B_1 the tunneling to the left reservoir becomes possible and the system is no more in the isolated regime. We therefore label this region as $(0|20)$ and the second one to $(1|20)$. A dashed red line is here to represent the axis on which the array segmentation experiment is performed. The ability to observe an electron exiting the system from L at the end of the partial freeze experiment demonstrates the presence of all the electrons during the whole experiment.

The observations made in [Figure 3.8](#) are interpreted as the ability to set the array in a configuration where one electron is present in each QD while the left electron is no more coupled to the rest of the array $(1|11)$. However, it is also possible to explain this data by assuming that the left electron has been lost to the left reservoir during the manipulation of the tunnel barrier. In [Figure 3.9](#), we ensure that the array still contains three electrons at the end of the experiment

by emptying L in to reach the $(0|20)$ configuration. To do so we perform the same manipulation presented in Fig. 5 to initialize the array in the $(1|11)$ configuration, this position is held during 1 ms before coming back to $(1|20)$. We then verify the presence of an electron in L by pulsing the voltage on B_1 and B_2 during 1 ms on a large range before performing a charge readout. We plot in [Figure 3.9](#) the output of the electrometer as a function of the voltage pulse amplitude, and we observe two regions delimited by the white dashed line. This variation of the charge configuration is associated with the electron in L exiting the array to the left reservoir. We can therefore label the two regions as $(0|20)$ for the one at high chemical potential and high QD-reservoir coupling and $(1|20)$ for the other one. We finally ensure that the experiment presented in Fig. 5 is performed in the $(1|20)$ region proving that no electrons are lost during the manipulation. Of course, as for reservoir-QD tunneling, the ability to freeze the electron transfer is limited to a specific voltage range. Nevertheless, this range is often enough to benefit QD array tuning.

3.4 Conclusion

The control of the tunnel couplings and the chemical potential of each QD on fast timescales allowed us to initialize an arbitrary metastable charge state of up to three electrons in a DQD. The freeze map protocol developed in this section allowed us to enhance the lifetime of metastable charge states and perform readout of these particular states at a fixed and optimized position in the voltage gate space. This demonstration is of particular interest for Pauli spin blockade spin-to-charge conversion whose fidelity is limited by the lifetime of such metastable charge states as we will see in [chapter 4](#) [[Barthel2009](#)]. We finally performed a segmentation of the array by decoupling a QD filled with one electron in a metastable configuration while performing charge displacement and readout in the rest of the structure. By doing so we observed a reduction of the number of charge states available for the system and therefore a reduction of the complexity while tuning the QD array. The partitioning protocol opens the door to more complex applications such as the operation of larger 1D or 2D arrays of QDs while keeping the low dimensionality of simple and independent sub-systems [[Mills2019a](#)].

4

Complete two-electron spin state readout in a double quantum dot

Contents

4.1	Introduction	86
4.2	Pauli spin blockade in the fully isolated regime	86
4.2.1	Frozen Pauli spin blockade readout protocol	87
4.2.2	Spin initialization	92
4.2.3	Readout fidelity benchmark	96
4.2.4	Application: Exchange interaction characterization	99
4.2.5	Application: Exchange oscillations	101
4.3	Tools for complete spin state readout	106
4.3.1	S-T+ adiabatic transformation	106
4.3.2	Parity readout	109
4.4	Complete two-electron spin state readout protocol	113
4.4.1	Presentation of the protocol	113
4.4.2	Characterization on various initial spin states	115
4.4.3	Complete readout procedure for two-electron spin manipulations	117
4.5	Conclusion	119

4.1 Introduction

Pauli principle plays a central role in the functioning of individual electron spin qubits in semiconductor quantum dot arrays [Boter2021, Philips2022]. For rapid and high-fidelity spin readout, it is required to convert the spin information into distinct charge configurations. To implement it, the basic building block is a tunnel coupled double quantum dot system filled with an electron acting as a qubit and one as an ancilla and probed via a close-by electrometer or RF-gate reflectometry [Urdampilleta2019, Betz2015]. Obtaining the full spin information of the two-electron system in this simple unit cell requires nevertheless extra hardware such as QDs or electron reservoirs, which represents an important overhead for future scaling of the platform [Nowack2011]. In this chapter, we propose and demonstrate a strategy to perform a complete spin state readout of a two-electron system with a minimal footprint. It is based on the repetition of three single shot measurements using Pauli spin blockade and the development in the control of the potential detuning (ϵ) at the ns timescale and of the tunnel coupling (t_c) between the GHz and the sub-Hz regime developed in the previous chapter. It allows us to completely separate in the ϵ, t_c parameter space the two important processes of the readout: fast spin to charge conversion and the charge configuration readout in the sub-Hz interdot tunnel coupling regime where the system is unaffected by charge state relaxation. Doing so, the three basic measurement procedures and their repeatability are investigated: a high fidelity S - T readout ($F_{\text{PSB}} = 98.43\%$) preserving the initial spin state is demonstrated. Second, via precise navigation in the ϵ, t_c parameter space, we engineered and characterized an on-demand parity readout procedure relying on a selective relaxation hotspot of T_0 to S and reached a fidelity of $F_{\text{parity}} = 93.3\%$. We then study the selective transformation of T_+ to S via an adiabatic passage through the avoided crossing and demonstrate a transformation fidelity of 79.9%. Finally, we characterize the complete readout procedure allowing to discriminate a S, T_0, T_+ and T_- spin state by interleaving spin readout and manipulations on the two same electrons. This complete readout procedure is implemented for three different initializations and in more complex spin manipulation sequences such as exchange controlled oscillations to test its validity.

4.2 Pauli spin blockade in the fully isolated regime

In the previous chapter, we demonstrated the capability to isolate electrons in a linear quantum dot array both from the reservoirs and their neighbor QDs. More precisely we managed to extend the lifetime of a metastable (1,1) charge state by reducing the interdot tunnel coupling rate below the Hz regime. This key feature will be used here to develop a high fidelity spin readout based on the PSB measurement procedure.

4.2.1 Frozen Pauli spin blockade readout protocol

Pauli spin blockade readout relies on the charge state difference of the three triplet spin states (T) compared to the singlet one (S) at the PSB position in the energy diagram. At this position, the T spin states are blocked in the (1,1) charge state due to the Pauli exclusion principle, while the S spin state allows a charge transfer and is mapped to (0,2). After the spin-to-charge conversion process, the readout relies on an essential second step consisting of the fast charge state discrimination of a ground (0,2) charge state and a metastable (1,1) one. In gate-defined GaAs/AlGaAs, the community has reported a lifetime of $|T_0(1,1)\rangle$ close to $T_1 \simeq 10\mu\text{s}$ (see [Figure 4.1\(a\)](#)) at the PSB position, limiting highly the fidelity of the readout procedure [[Barthel2012](#)]. Indeed, we can see in [Figure 4.1\(b\)](#) the classic figure of merit for such readouts where the readout error is plotted as a function of the electrometer signal integration time. For $T_{int} \ll T_1$, the error decreases with the time spent averaging the signal. In this regime, the readout error is limited by the charge readout SNR. By spending more time averaging, noise is reduced and the charge readout becomes more precise. In ideal conditions, the error should tend to zero for an infinitely long integration time. However, after a few μs it starts increasing again. In this regime the $|T_0(1,1)\rangle$ relaxation to $|S(0,2)\rangle$ becomes non-negligible ($T_{int} \simeq T_1$) and the probability for a T_0 state to be mislabelled as S increases reducing the overall fidelity of the readout procedure.

To overcome the issue of comparable T_1 and charge signal integration time, several methods have been developed to reduce the time needed to discriminate with high fidelity the two charge configurations mapping the S and T states, via either decreasing the noise in the measurement apparatus or increasing the signal differentiating the two spin states. As demonstrated in [section 2.7](#), the use of RF-reflectometry apparatus allows faster measurements of charge states in QDs by getting rid of $1/f$ noise in the MHz regime. To reduce even more the noise, an ongoing effort is aiming at limiting noise amplification of such circuits via the use of a traveling wave parametric amplifier (TWPA) almost reaching the quantum noise floor [[Schaal2020](#)]. In both cases, it comes with the cost of more complex measurement apparatus. On the other hand, latching- and cascade-based mechanisms recently allowed an enhancement of the output signal of the spin-to-charge conversion mechanisms, improving the spin readout efficiency for an identical noise and integration time [[Nakajima2017](#), [Harvey-Collard2018](#), [van Diepen2021](#)]. However, at the end of the readout procedure, the initial spin state is destroyed due to the presence of an extra electron or its fast displacement in the array, meaning that the readout is not repeatable. Moreover, the implementation of such readouts requires more quantum hardware such as quantum dots and electron reservoirs limiting the scalability of the structure.

Measurement principle

In this work, we chose a method that consists in increasing the lifetime of the metastable $|T_0(1,1)\rangle$ spin state and performing the charge readout at a fixed and optimized position in the voltage gate space as envisioned by [[Li2018](#)]. In the following we name this readout frozen Pauli spin blockade (FPSB). The FPSB measurement procedure that we will demonstrate in this section is presented

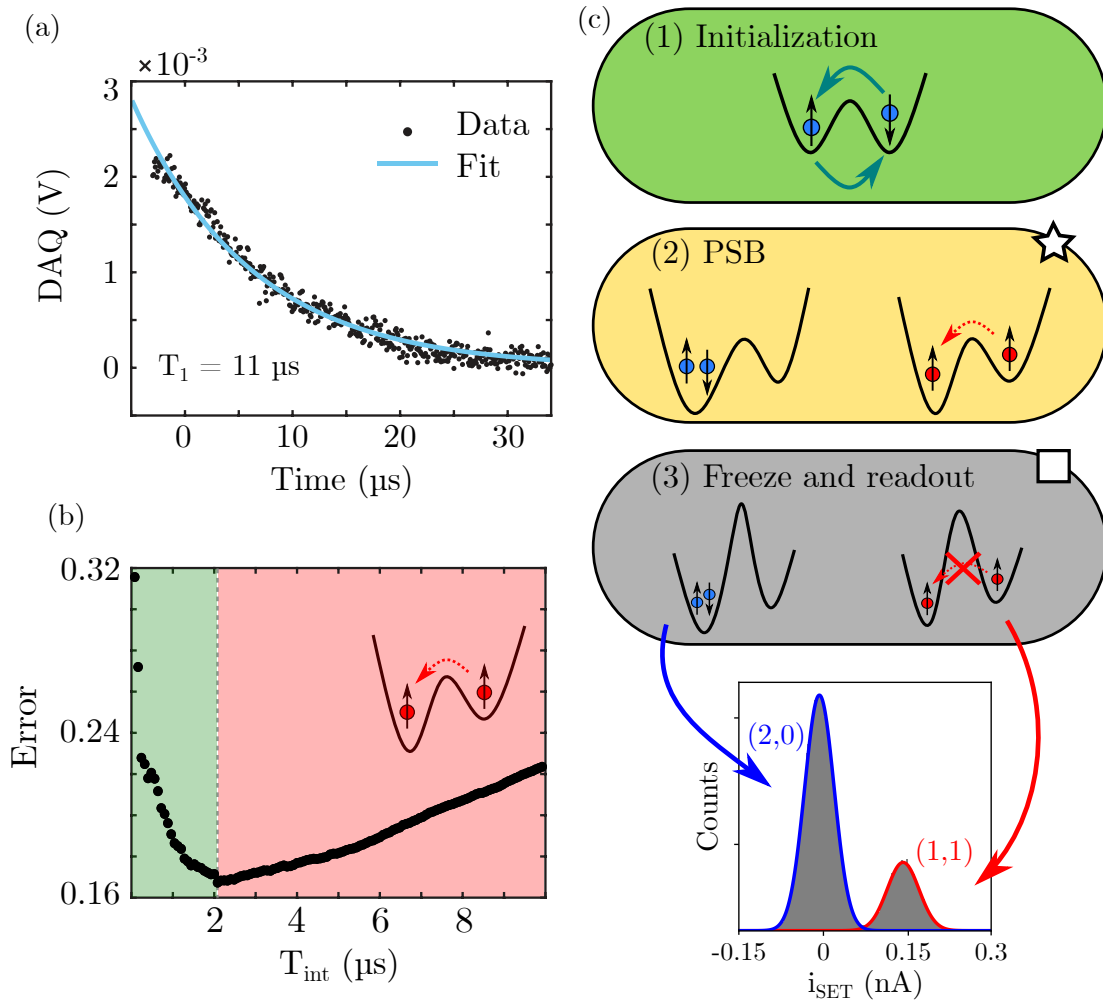


Figure 4.1: Frozen Pauli spin blockade measurement principle and advantages. **a**, T_1 relaxation of the T_0 state to the S one. In GaAs/AlGaAs devices the T_1 relaxation is usually in the order of a few tens of μs . Adapted from [Connors2020]. **b**, S - T readout fidelity as a function of the integration time for a classic PSB measurement. The two regimes are identified first, the charge readout limited one in green and the T_1 limited in red. Adapted from [Connors2020]. **c**, Frozen PSB three-step procedure. The system is initialized in an unknown two-electron spin state which we want to determine. The DQD is pulsed during a few ns only ($T_{\text{pulse}} \ll T_1$) to the PSB position in order to perform a spin-to-charge conversion process. From there the interdot tunnel barrier is closed via again a ns pulse to freeze the charge configuration obtained during the conversion process. Finally, a charge readout is performed to determine the charge configuration of the electrons in the DQD.

schematically in [Figure 4.1\(c\)](#). The two electrons will be first initialized in a random spin state that we want to identify. From there the system is pulsed on a nanosecond timescale to the PSB position in order to perform the spin-to-charge conversion process. By spending a time short compared to T_1 at the PSB position a relaxation of the $|T_0(1, 1)\rangle$ state to $|S(0, 2)\rangle$ is unlikely to happen. Indeed, considering $T_1 = 10\mu\text{s}$ in our platform if we are able to spend less than 10 ns at the PSB position we can in theory preserve the triplet state with a 99.9 % probability. The obtained charge configuration is finally frozen by pulsing the interdot tunnel coupling in the sub-Hz regime. At this position, the charge transfer is suppressed during the whole readout step duration and the $|T_0(1, 1)\rangle$ metastable state cannot change its charge configuration. The electrometer signal is finally averaged during the time necessary to obtain a high fidelity charge state discrimination.

In the end, this novel readout procedure allows us to spend the desired amount of time at the charge readout position without worrying about spin state relaxation reducing the overall readout fidelity. After demonstrating experimentally this readout procedure, we will see how this new key feature of the readout allows us to perform a complete two-electron spin state readouts by discriminating S , T_0 , T_+ , and T_- in a succession of three FPSB performed on the same electrons.

Measurement protocol and calibration

To implement the FPSB readout we use the same sample previously described in [subsection 3.1.1](#) in the DQD configuration. In this chapter a fixed magnetic field of 150 mT is applied parallel to the sample in order to separate in energy the three triplet spin states. The DQD is loaded with two electrons in the isolated regime via the loading map procedure, operating the DQD in this regime allows us to control the interdot tunnel coupling over several orders of magnitude, especially in the sub-Hz which is required to implement the FPSB readout (see [chapter 3](#)). The DQD operating positions are calibrated by performing a stability diagram using the gate voltages B_2 and B_3 controlling the potential detuning ε and the interdot tunnel coupling t_c respectively. The result is plotted in [Figure 4.2\(a\)](#) and as described in the previous chapter, we observe two discontinuous charge degeneracy lines separating the three possible charge states of two electrons in a DQD. Following one of the charge degeneracy lines, we identify two possible regimes of the inter-dot tunnel coupling. The first one is the high tunnel coupling regime ($t_c \simeq \text{GHz}$) obtained for $V_{B_2} > -0.68 \text{ V}$. In this regime, electrons are transferred from one dot to the other by varying V_{B_3} . For $V_{B_2} < -0.68 \text{ V}$, the charge degeneracy line is shifted to lower values of V_{B_3} indicating that the inter-dot tunnel rate is lower than the measurement sweep rate, in this case 250 mV s^{-1} [[Bertrand2015b](#), [Eenink2019](#)].

Using the tuning capabilities to set the DQD in an arbitrary charge configuration and change the interdot tunnel coupling we will now implement the FPSB protocol. It relies on two operating positions indicated on top of the stability diagram which need to be carefully calibrated in order to achieve a high fidelity spin state readout. The first one is the PSB position at the white star in [Figure 4.2\(a\)](#) close to the (1,1) and (0,2) charge state transition where the spin-to-charge conversion process is performed, we will see here how to calibrate this position. The second one is the charge

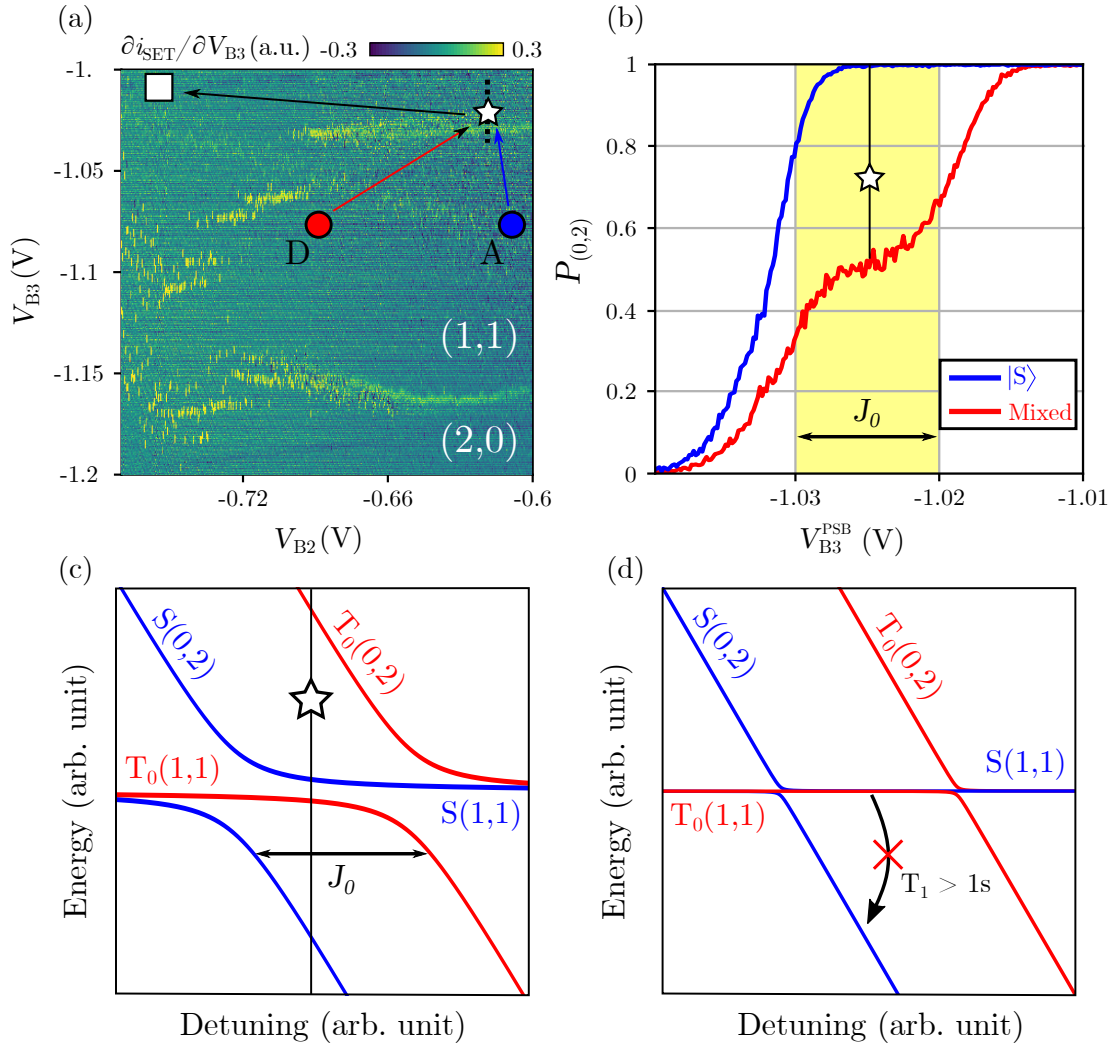


Figure 4.2: Calibration of the frozen PSB measurement. **a**, Pulse sequence performed to calibrate the PSB position. The system is initialized in a S or mixed S - T_0 state via a 500 ns voltage pulse at position **A** or **D** respectively. It is then pulsed to the PSB position (white star) during 20 ns to perform a spin-to-charge conversion and the configuration of the DQD is read at the white square position during 5 ms. **b**, PSB calibration experiment. The pulse sequence described in (a) is performed for a varied position of the PSB along the detuning axis. We plot the $(0,2)$ charge state probability as a function of the PSB position along the dotted line V_{B3}^{PSB} for the two possible initializations. The readout position is chosen at the white star position where the mixed state probability reaches 50%. **c**, Energy diagram at the PSB position as a function of the detuning of the DQD in the GHz regime of the interdot tunnel rate. The region in detuning where PSB is feasible is defined where the ground S state is in the $(0,2)$ charge state while the triplet one is in the $(1,1)$ charge state. T_+ and T_- state have been removed for clarity. **d**, Energy diagram at the frozen position (white square). In this regime, the $T_0(1,1)$ spin state cannot relax to $S(0,2)$ due to the sub-Hz interdot tunnel rate. T_+ and T_- states have been removed for clarity.

readout position (indicated by the white square) located in the sub-Hz interdot tunnel coupling regime where the signal of the local electrometer is acquired.

For the demonstration and calibration of the readout two different initialization of S and T states are necessary, the initializations are discussed in [subsection 4.2.2](#). Both are based on the high level of control over the interdot tunnel coupling and allow us to initialize either a S state or a so-called S - T_0 mixed state composed of a statistical mixture of 50 % S and 50 % T_0 . Experimentally, we engineered and implemented the pulse sequence sketched on top of the stability diagram in [Figure 4.2\(a\)](#). The spins are initialized in a S state at position **A** and in a S - T_0 mixed state at position **D**, from there the system is pulsed at the PSB position indicated by the white star during 20 ns to perform the spin-to-charge conversion. The pulsing time to the PSB position has been selected to be short compared to the T_1 relaxation time at the PSB position but long compared to $(ht_c)^{-1}$ so that the $|S(1,1)\rangle$ state can tunnel to $|S(0,2)\rangle$ but $|T_0(1,1)\rangle$ cannot relax to $|S(0,2)\rangle$. The pulse length was limited by the AWG rise time (~ 1 ns) and the RF cable bandwidth. At this position, a S spin state is mapped to (0,2) and T_0 , T_+ , and T_- spin states are mapped to (1,1) as shown by the energy diagram in [Figure 4.2\(c\)](#). In order to perform the charge configuration readout, the system is pulsed to the sub-Hz interdot tunnel coupling region where charge tunneling is no longer possible at the timescale of the experiment. At this position the signal of the electrometer is acquired during $T_{\text{int}} = 5$ ms to discriminate with high fidelity ($>99\%$) the charge state of the DQD. Doing so allows us to conserve the charge state obtained at the spin-to-charge conversion position during the whole duration of the readout.

To calibrate the readout in the voltage gate space, we applied the pulse sequence presented in [Figure 4.2\(a\)](#) where we performed a FPSB procedure while varying the detuning of the PSB position along the black dashed line. For each position, the pulse sequence is repeated 10000 times. We represent in [Figure 4.2\(b\)](#) the probability to measure a (0,2) charge state $P_{(0,2)}$ as a function of the PSB position $V_{B_3}^{\text{PSB}}$ for the S and S - T_0 mixed spin state initialization. For $V_{B_3}^{\text{PSB}} > -1.02$ V, we observe a regime with a high probability of (0,2) charge state for both initializations. Here, the potential detuning overcomes the single dot exchange energy J_0 and singlet and triplet spin states have their ground state in the (0,2) charge configuration making it impossible to discriminate. Similarly, for $V_{B_3}^{\text{PSB}} < -1.03$ V the two states are in the (1,1) charge configuration yielding low values of $P_{(0,2)}$ for both initializations. In these two regimes, the FPSB readout is not possible since S and T spin states are in the same charge configuration. But we observe a region in between where $P_{(0,2)}$ is dependent on the initialization position. The readout position is selected at the white star, where the $P_{(0,2)} = 0.5$ for the S - T_0 mixed state initialization which is the theoretically expected result.

From this calibration, it is possible to estimate the exchange energy of the right quantum dot by measuring the voltage range where spin readout is possible in [Figure 4.2](#). We start by determining the α -factor of gate B_3 on the potential detuning by assuming that the charging energy is $E_C = 1.5$ meV. From the stability diagram in [Figure 4.2](#), we see that the voltage span in V_{B_3} of the (1,1) charge region is $\Delta V_{B_3} \simeq 125$ mV. The α -factor for gate B_3 is therefore given by

$\alpha = \frac{2E_C}{\Delta V_{B3}} \simeq 0.03 \text{ eV V}^{-1}$ close to previously obtained values [Kouwenhoven2001]. The span of the readout region is 10 mV as shown by the yellow region in Figure 4.2(b), and yields an exchange energy of $J_0 \simeq 300 \mu\text{eV}$.

To conclude, we demonstrated a ST readout based on the PSB readout called FPSB, the developments over the control interdot tunnel coupling allowed us to add an extra step in the PSB classic procedure consisting in performing the charge readout in the sub-Hz regime. Doing so, we limit the main source of error of the classic PSB being the $|T_0(1,1)\rangle$ relaxation to $|S(0,2)\rangle$. Moreover, when the charge dynamics are blocked the spin state of the system is conserved thanks to the low single spin relaxation rate in GaAs/AlGaAs (10^{-2} Hz at 500 mT) [Camenzind2018]. The measurement procedure becomes therefore repeatable, this key functionality will be used to enhance the quantity of information extracted from the system and is presented in section 4.4.

4.2.2 Spin initialization

The calibration of the previously presented FPSB protocol relies on efficient initialization of S and T_0 spin states. In this section, we detail the two methods used to rapidly initialize a singlet state and a statistical mixture of S and T_0 states referred to as S - T_0 mixed state in this thesis.

Singlet initialization

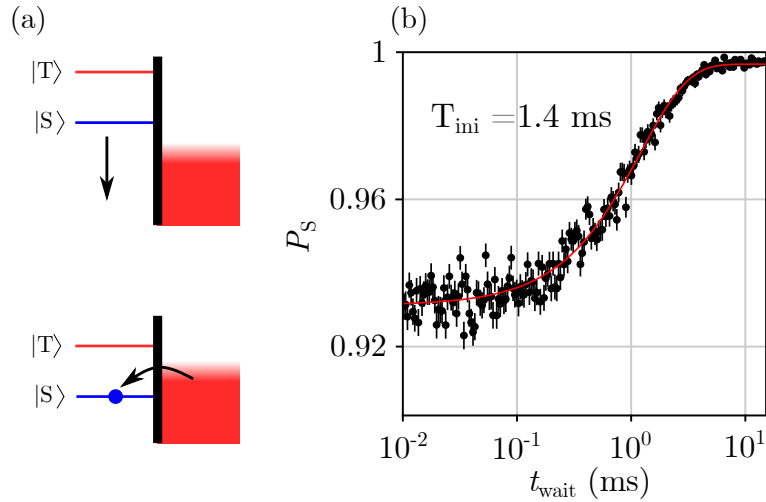


Figure 4.3: High fidelity singlet initialization via adiabatic loading and relaxation. **a**, Singlet adiabatic loading procedure. The system is initialized with all the two-electron states above the Fermi sea of the reservoir. The chemical potential is then lowered slowly compared to the quantum dot-reservoir tunnel rate ensuring that there is a sufficiently long time where the only accessible state is the singlet one. When the triplet states become finally energetically accessible the DQD is already filled with two electrons in the singlet state. This method provides a high fidelity singlet loading procedure $F_{adiabatic} \simeq 93\%$. A waiting step of 5 ms is added at the end of the adiabatic loading procedure to allow wrongly loaded triplet spin states to relax to the singlet one. **b**, Relaxation to the singlet in the $(0,2)$ charge configuration. Combining the two techniques, we reach an initialization fidelity of $99.57 \pm 0.05\%$.

High initialization fidelity of the singlet spin state can be obtained via the loading of a ran-

dom spin state and waiting during a few tens of milliseconds for the relaxation deep in the (0,2) charge state to the singlet. However, the community has developed various techniques to speed up this process down to a few microseconds via relaxation hotspots or readout feedback [Yang2013, Spence2022, Philips2022]. While being rapid these methods are either not available in the GaAs platform or require additional hardware to be implemented. In this work, we chose the combination of adiabatic loading and relaxation which allowed us to load a singlet state with high fidelity in a few milliseconds.

Usually, when two electrons are loaded in a quantum dot the probability to load a singlet state is defined as :

$$P_S = \frac{\Gamma_S}{\Gamma_S + 3\Gamma_T}, \quad (4.1)$$

where Γ_S and Γ_T are respectively the singlet and triplet tunnel coupling to the reservoir. At the loading position, the electrons in a singlet state occupy the ground orbital of the dot whereas a triplet one involves having an electron on an excited orbital. Since the excited orbitals have a larger spatial extension than the ground one, the coupling of the triplet to the reservoir is generally stronger than the singlet one $\Gamma_T \gg \Gamma_S$ [Hanson2005]. If no precautions are taken when the two electrons are loaded then the singlet initialization fidelity is usually pretty low.

To overcome this issue, we implemented an adiabatic loading of the singlet state which relies on the difference between the chemical potential sweeping rate and Γ_S . The procedure sketched in Figure 4.3(a) starts with an empty quantum dot with both singlet and triplet levels above the Fermi level of the reservoir. From there, the chemical potential of the loading dot is lowered slowly compared to Γ_S , and at some point during the lowering the only available spin state is the singlet one. Thanks to the low sweeping rate of the chemical potential compared to Γ_S this situation is held during enough time for the two electrons to be loaded in the singlet state. By the time the triplet state becomes also energetically available, the quantum dot is already loaded with two electrons. This method only allows us to initialize a singlet with a fidelity of around 93 % in a few hundred microseconds. The initialization fidelity obtained via this method is limited by the difference in tunnel rate mostly defined by the shape of the quantum dot and experimentally difficult to tune.

To reach an even higher fidelity, we combine this method with a relaxation in the (0,2) charge state region characterized in Figure 4.3(b). The electrons are initialized via the adiabatic loading procedure and set to wait in the (0,2) region during a variable time t_{wait} before performing a spin readout. We observe an exponential increase in the singlet population as a function of the relaxation time with a characteristic time of $T_{\text{ini}} = 1.4$ ms. In the end, performing an adiabatic loading followed by a relaxation of $\simeq 5T_{\text{ini}}$ allowed us to reach a measured singlet state population of 99.57 ± 0.05 %.

The remaining error in the loading procedure is attributed to the triplet state being thermally populated at the loading position. We can consider that the singlet population $P_{S,\text{max}}$ for $t_{\text{wait}} =$

10ms follows a Fermi-Dirac distribution:

$$P_{S,\max} = \frac{1}{1 + e^{-J_0/(k_B T_{el})}}, \quad (4.2)$$

where $J_0 = 300\mu\text{eV}$ is the energy splitting between the S and T states at the initialization position and T_{el} is the electronic temperature. Considering the obtained S population it yields an electronic temperature of $T_{el} \simeq 640\text{mK}$ close to previously measured values in similar systems [Bertrand2015a].

In this whole chapter whenever a singlet state is initialized we consider that the described procedure (adiabatic loading and relaxation) has been performed.

Mixing process

Now that we have seen how to initialize a singlet state, we will perform a spin manipulation allowing us to prepare a so-called S - T_0 mixed state composed of a statistical mixture of S and T_0 states. The initialization relies on the decoherence of the singlet spin state when the two electrons are separated into two distinguishable particles. This separation will be controlled via the interdot tunnel coupling as depicted in Figure 4.4(b).

To induce decoherence of the singlet spin state we will manipulate the tunnel coupling t_c at a fixed value of detuning $\varepsilon = 0$, we represent in Figure 4.4(a) the energy diagram in this configuration. For large tunnel coupling values, the DQD behaves as one large quantum dot, in this situation the singlet state is still the ground state of the system and no evolution of the spin state is expected. As explained previously, this regime indicated by point A in the energy diagram is used to initialize the system in the singlet state. When the tunnel coupling is reduced to lower values the splitting in energy J between S and T_0 state is also reduced and we reach the mixing region. In this regime the splitting between the two states is defined by the local transverse magnetic field gradient $J = g\mu_B\Delta B_z$ and the S and T_0 states are transformed into $|\uparrow\downarrow\rangle$ and $|\downarrow\uparrow\rangle$ (depending on the sign of the magnetic field gradient at the moment of the experiment). Therefore, performing a non-adiabatic transformation from an initialized singlet to the mixing region should result in coherent oscillations between the $|\uparrow\downarrow\rangle$ and $|\downarrow\uparrow\rangle$ states at frequency J .

To probe the spin evolution in this regime, we performed the experiment presented in Figure 4.4(c), where the system is initialized in the S state at a large value of interdot tunnel coupling (point A) in the (1,1) charge configuration. From there, the tunnel coupling is pulsed during a variable time τ_{mix} in the mixing region (point D) and finally pulsed back to perform a FPSB readout. We observe a rapid loss of the singlet population up to a completely random output between singlet and triplet, we fitted a Gaussian decay to the data and obtained a characteristic time of $T_2^* = 8.1\text{ ns}$.

As explained in subsection 1.3.2, ΔB_z in the AlGaAs/GaAs heterostructure is imposed by the nuclear spins of the atoms composing the crystal lattice. The distribution of the possible values of ΔB_z follows a Gaussian law of standard deviation σ_{nuc} with a characteristic changing time

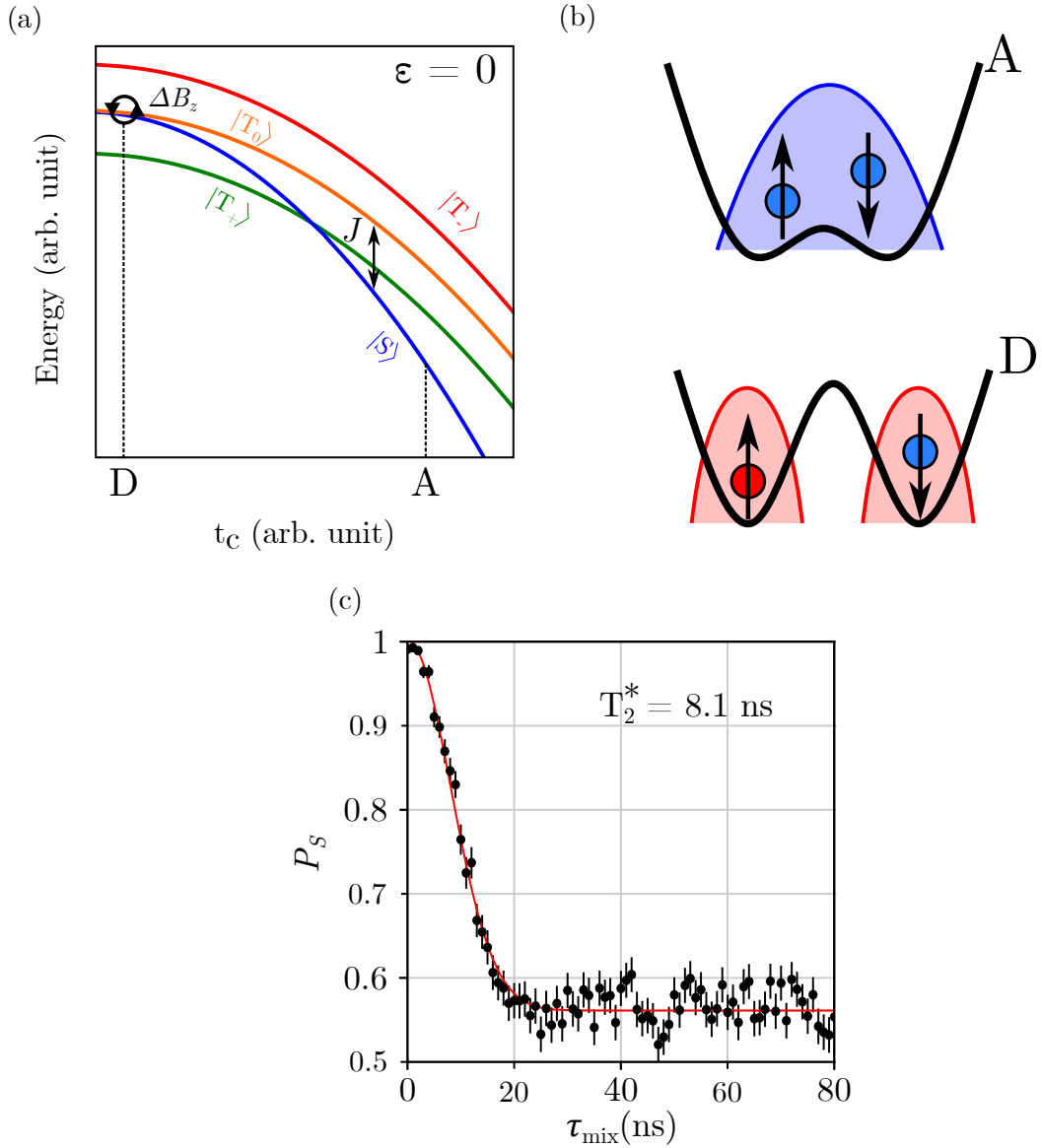


Figure 4.4: S and T_0 mixed state initialization via decoherence mechanism in the (1,1) charge configuration. **a**, Energy diagram for $\varepsilon = 0$ as a function of the interdot tunnel coupling. For high enough values of t_c the singlet state remains the ground state of the system and this position is used to initialize a singlet state. For low values of t_c appears a regime where the exchange coupling is limited by the Overhauser magnetic field $J = E_{T_0} - E_S = g\mu_B\Delta B_z$, and mixing of the two spin states occurs. **b**, Sketch of the wavefunction at the two initialization positions. In the high t_c regime the state is delocalized over the two QDs and forms a singlet state. For low t_c values, the two spins experiment different values of B_z induced by the hyperfine interaction resulting in a mixed state 50–50% S - T_0 . **c**, Spin mixing experiment. The two electrons are initialized in a singlet state in the high t_c regime (point A) then the system is pulsed during τ_{mix} in the low t_c region (point D). Finally, spin readout is performed via the FSPB procedure and we observe the loss of the initial singlet state for long separation times. A Gaussian decay is fitted, yielding a $T_2^* = 8.1$ ns.

of a few seconds. When pulsed to the mixing region the singlet spin state evolves at a random frequency taken from a Gaussian distribution of standard deviation $\gamma_e \sigma_{nuc}$. If we now average the singlet probability over many possible values of ΔB_z we obtain in black the rapid Gaussian decay observed in the experiment whose characteristic time is defined as:

$$T_2^* = \frac{\sqrt{2}}{\gamma_e \sigma_{nuc}}. \quad (4.3)$$

The fitting yields a dephasing time of $T_2^* = 8.1$ ns and we can extract the standard deviation of the Overhauser magnetic field $\sigma_{nuc} = 4.6$ mT which is in agreement with previously obtained values [Petta2005b].

In the end, we use this characteristic of the system to initialize a known population of 50 % of the T_0 spin state by pulsing the interdot tunnel coupling in the mixing region during a time $\tau_{mix} \gg T_2^*$. This ensures a complete loss of the singlet state phase and a correct initialization of the system at the condition that the experiment has lasted enough compared to the characteristic evolution time of the hyperfine magnetic field. Indeed, for the statistical mixture to approach 50 %-50 % of S and T_0 the system needs to undergo a representative sampling of the possible values of ΔB_z . All the experiments where the initialization is sensitive are therefore at least 10 min long to meet this condition [Reilly2008]. Moreover, the mixing position has been chosen in the sub-Hz regime of interdot tunnel coupling (point D in Figure 4.2(a)) to reduce as much as possible the exchange energy J as defined by Equation 1.23. This ensures that the energy splitting between the S and T_0 state is effectively defined by the Overhauser magnetic field gradient. This condition is primordial to ensure a random output for $\tau_{mix} \gg T_2^*$, as we will see in subsection 4.2.4 a residual exchange coupling due to high interdot tunnel coupling leads to a higher proportion of S state.

4.2.3 Readout fidelity benchmark

We have seen how we were able to manipulate the spin states to obtain either a pure S state via adiabatic loading and relaxation and how to initialize a known population of T_0 via the mixing process. We will now use these two initialization procedures to perform a benchmark of the readout fidelity of the FPSB method presented in subsection 4.2.1.

As explained previously the spin readout procedure is based on a spin-to-charge conversion followed by a charge readout. It is therefore necessary to assess the errors arising from the two steps of the measurement. To do so we define the two possible types of errors during a FPSB readout as sketched in Figure 4.5(a), T_{error} is the probability to measure a (0,2) charge state when the spins were actually in T state and S_{error} the opposite. It is interesting to note here that both errors S_{error} and T_{error} are actually the combination of the spin-to-charge conversion error and the charge readout error that we define as C_{error} . To assess these three parameters we initialize the system either in the S or S - T_0 mixed state using the two protocols presented previously and perform a FPSB readout. The SET current is then acquired and compared to a reference measurement performed in the (0,2) charge state to obtain Δi_{SET} . The obtained signal is averaged during a

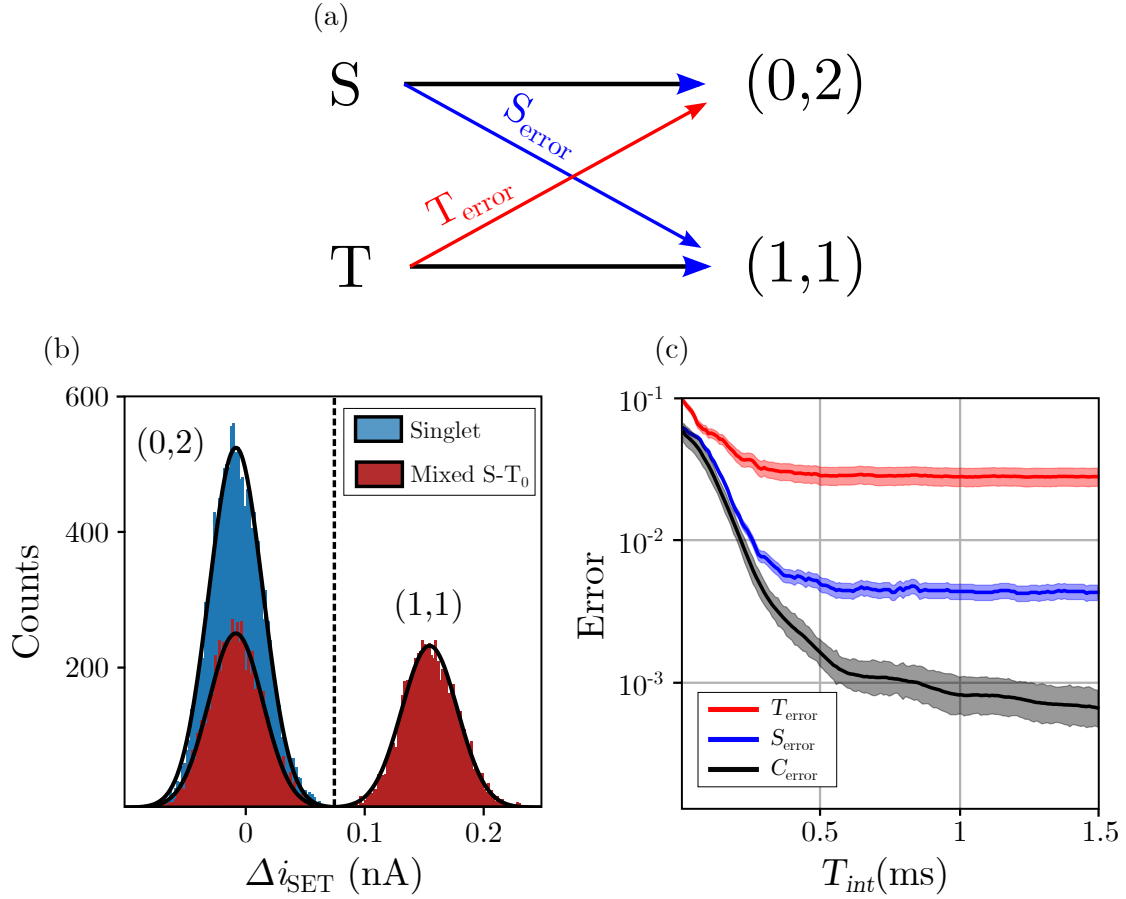


Figure 4.5: Fidelity benchmark of the frozen PSB measurement protocol. **a**, The two possible types of error during a PSB measurement. A singlet mislabelled as a triplet (S_{error}) and a triplet mislabelled as a singlet (T_{error}). The overall readout fidelity is defined as $F = 1 - (S_{\text{error}} + T_{\text{error}})/2$. **b**, Histogram of 50000 FPSB measurements for singlet and mixed $S-T_0$ initializations at an integration time of $T_{\text{int}} = 1.5$ ms. The histogram envelopes are fitted to a sum of Gaussian distributions, following the method developed in [subsection 2.7.5](#). We define a threshold (dashed line) to discriminate (1,1) and (0,2) charge states maximizing the readout fidelity. The S initialization shots are almost all located in the (0,2) configuration while equipartition is observed for the mixed $S-T_0$ one. **c**, Readout errors as a function of the signal integration time. For low integration times, the spin readout error is limited by the charge readout error. For longer integration times the spin readout error saturates where it reaches $S_{\text{error}} = 0.43 \pm 0.05\%$ and $T_{\text{error}} = 2.7 \pm 0.4\%$. In this regime the spin readout is no more limited by the ability to discriminate between the two charge states (0,2) and (1,1). Thanks to the charge freezing mechanism no effect of the T_1 relaxation is observed in the fidelity benchmark.

variable time T_{int} . The sequence is finally repeated 50000 times to construct a histogram of the acquired signal. As shown in [Figure 4.5\(b\)](#), we observe two Gaussian shapes attributed to the two possible charge configurations (0,2) and (1,1). By performing a similar treatment of the data as presented in [subsection 2.7.5](#), we are able to assess the error of the charge readout by computing the overlap between the two Gaussian curves. In [Figure 4.5\(b\)](#), we plotted C_{error} as a function of the integration time of the signal and observe a steady decrease in the error rate corresponding to the noise in the signal being averaged out.

To assess the S_{error} and T_{error} we use the following equations :

$$\begin{aligned} P_{(0,2)}^S &= 1 - S_{\text{error}} \\ P_{(0,2)}^{\text{mix}} &= \frac{1 - S_{\text{error}} + T_{\text{error}}}{2}, \end{aligned} \quad (4.4)$$

where $P_{(0,2)}^S$ and $P_{(0,2)}^{\text{mix}}$ is the probability to observe a (0,2) charge state when the system is initialized in the S state and in the S - T_0 mixed state respectively. For $T_{\text{int}} < 0.5$ ms, we observe a steady decrease of the spin readout error. In this regime the spin readout error is limited by the ability to discriminate a (2,0) charge state from a (1,1). For longer integration times the S_{error} and T_{error} saturate at 0.43 ± 0.05 % and 2.7 ± 0.4 % respectively.

Comparing our figure of merit with the one of a classic PSB measurement as in [Figure 4.1\(a\)](#), we observe the same behavior for short integration times. However, in the case of a classic measurement the readout error steadily increases for longer integration times due to the T_1 relaxation of $|T_0(1,1)\rangle$ to $|S(0,2)\rangle$. In this work, we were able to suppress this phenomenon by separating the spin-to-charge conversion and the readout position in the voltage gate space. Indeed, by spending only 20 ns at the PSB position relaxation is unlikely to happen considering a T_1 value of around 10 μ s. The charge readout is performed during an arbitrarily long time at the frozen charge position where relaxation is definitely suppressed due to a very low tunnel interdot tunnel coupling preventing the charge transfer from happening during the relaxation process.

It is worth noting that this method to assess the fidelity gives us an upper bound of the readout errors since the initialization errors cannot be properly distinguished from them. We explain the S_{error} value by considering the thermal population of the triplet state at the initialization position as seen in [subsection 4.2.2](#). Similarly, the residual error for the triplet state is attributed to calibration errors in the PSB position. Indeed, as we can see in [Figure 4.2\(b\)](#) the measured triplet probability (and therefore the T_{error} value) is highly dependent on the PSB position which can slightly shift at the timescale of the experiment. One way to overcome this limitation would be to implement a feedback loop to periodically recalibrate the PSB position.

Finally, we demonstrated the ability to perform a high fidelity spin readout by limiting the usual T_1 relaxation source of error. Moreover, at the end of a measurement cycle, no electrons are added or removed from the DQD making the measurement repeatable. This new characteristic of the measurement will allow us to perform multiple measurements in between a set of spin manipulation on the two same electrons to extract more information about the spin state.

4.2.4 Application: Exchange interaction characterization

The ability to perform a high fidelity readout of the spin state allows us to focus on the singlet evolution according to the two relevant parameters of the system, the potential detuning and the interdot tunnel coupling. This study will help us identify the different regimes possible for the spin state evolution and the position in the voltage gate space of the different spin states avoided crossings. The resulting calibration of the system is a necessary step to implement more complex spin operations such as exchange oscillations, S - T_+ adiabatic transformation, or the complete readout procedure.

The characterization starts by performing a so-called spin map which consists in probing the evolution of a S state in the V_{B2} and V_{B3} voltage gate space. The system is initialized in the S state using the protocol presented in [subsection 4.2.2](#). From there the pulse sequence drawn on top of the stability diagram in [Figure 4.6\(a\)](#) is performed. First, the system is brought at the charge freezing position in the (0,2) charge region (white square) by being careful not to step in the (1,1) charge region to prevent ending up in a S - T_0 mixed state. Then the voltages applied on gates B_2 and B_3 are pulsed simultaneously to reach position $P(V_{B2}^P, V_{B3}^P)$. At this position, the S state evolves freely during 500 ns before being pulsed sequentially at the PSB and freeze position in order to perform a FPSB readout. This sequence is repeated 500 times for each probed position P .

We plot in [Figure 4.6\(c\)](#) the averaged outcome of the FPSB measurement as a function of the point P coordinates. We first focus on the y -axis of the plot corresponding to a variation of the detuning in the DQD. As expected the S state is conserved during the 500 ns probing pulse if the point P is located in the (0,2) or (2,0) charge region. Indeed, in these configurations the two electrons are kept in the same quantum dot during the whole operation where the S state is an eigenstate of the system and no evolution is observed. However, if we now fix the detuning in the middle of the (1,1) charge region and move along the x -axis we observe different behaviors in the singlet probability P_S depending on the interdot tunnel coupling value.

For large values of tunnel coupling ($V_{B2} > -0.61$ V), we observe perfect conservation of the singlet state. In this regime, the interdot tunnel coupling is so high that the DQD behaves like a single quantum dot where the S state is again an eigenstate of the system. For intermediate values of tunnel coupling ($V_{B2} \simeq -0.7$ V), we observe a large area where $P_S = 0.5$. This region corresponds to the spin mixing, as explained in [section 4.2.2](#) here $J \ll g\mu_B\Delta B_z$ and the evolution of the singlet state is dictated by the random Overhauser magnetic field. Since $t_{pulse} \gg T_2^*$, it results in a random output between S and T_0 state. This region is used in this work to initialize a known population of T_0 .

For even lower values of tunnel coupling ($V_{B2} < -0.75$ V) we observe again a high S state probability. In this regime, the interdot tunnel coupling is so low compared to the pulse duration (500 ns) that the electrons do not have the time to tunnel from the (0,2) to the (1,1) charge state. The electrons are therefore staying in the same quantum dot during the entire procedure and the S state is conserved. However, as we have seen previously in [section 3.3.3](#), it is still possible for the electron to tunnel to the (1,1) charge state via the excited orbital states of quantum dot M . In

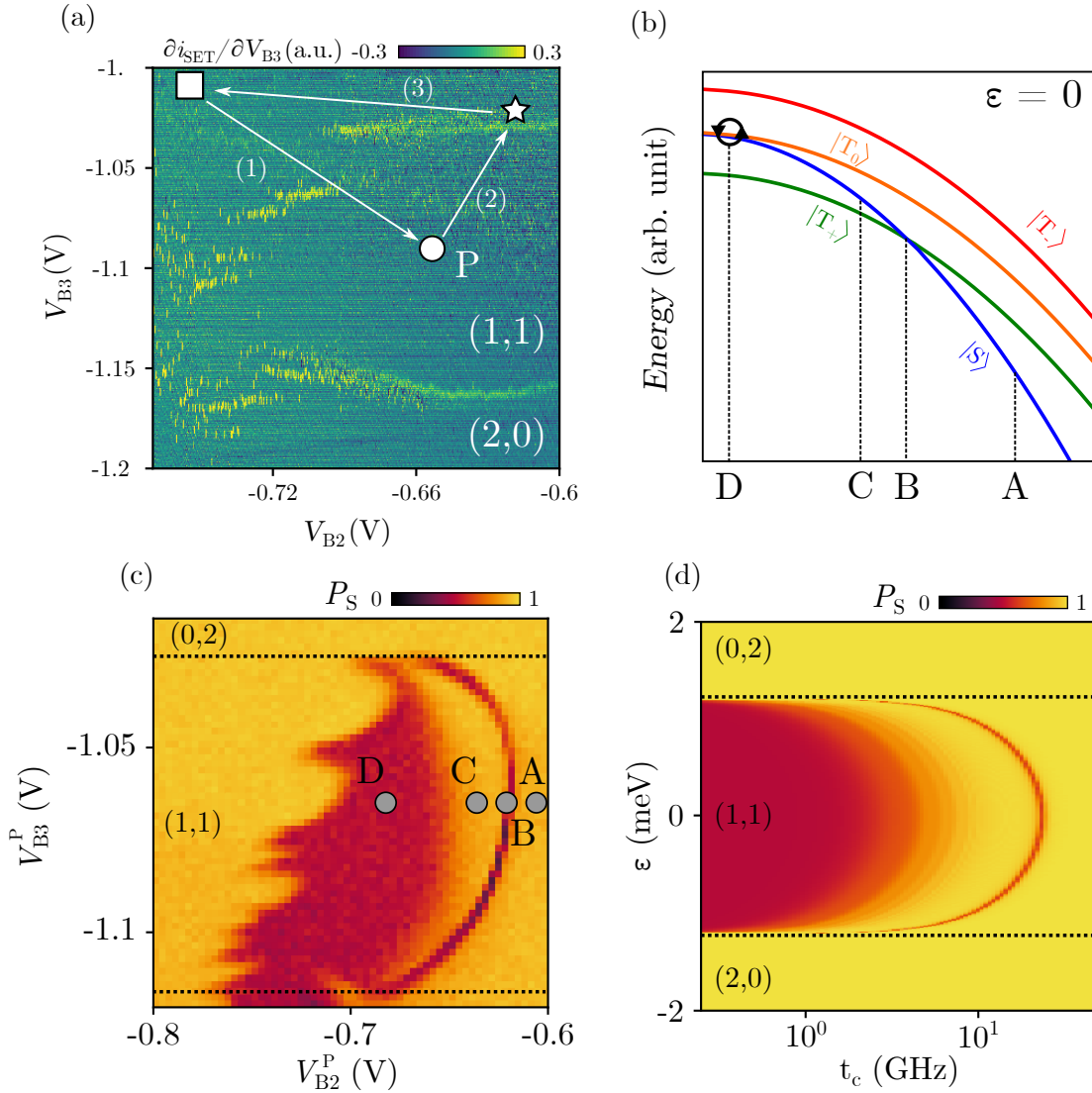


Figure 4.6: Spin map protocol and characterization. **a**, Pulse sequence applied to obtain the figure in **b**. A singlet is initialized at the square position and the system is pulsed to point P during 500 ns, from there a spin readout is performed via the FPSB protocol. **b**, Energy diagram computed for $\epsilon = 0$. The high and intermediate tunnel coupling regimes are indicated by point **D** and **A** respectively while point **B** indicates the S - T_+ avoided crossing. **c**, Singlet probability as a function of the coordinate of point P ($V_{\text{B2}}^{\text{P}}, V_{\text{B3}}^{\text{P}}$). Each pixel is the average of 500 realizations of the pulse sequence presented in **a**. The spin mixing region is identified in the middle of the figure in the area where $P_S = 0.5$, in this region $J \ll g\mu_B\Delta B_z$. We can also identify the position of the S - T_+ anticrossing (thin curved line) in the voltage gate space. For low values of V_{B2} the singlet state is preserved due to the low interdot tunnel coupling preventing the separation of the charges and therefore mixing of the spin state. We again observe the characteristic lobes of the excited orbital states allowing charge transfer in the low tunneling regime. Two horizontal black dotted lines are indicating the three charge state regions. **d**, Simulated singlet probability computed as the evolution of the singlet eigenstate during 500 ns under the Hamiltonian H_{DQD} . The main characteristics of the spin map such as the spin mixing region and the S - T_+ anticrossing branch are reproduced. Two horizontal black dotted lines are indicating the three charge state regions.

this case, we retrieve the behavior observed in the mixing region at intermediate tunnel coupling values where the singlet probability reaches 0.5. We observe similar lobes to [Figure 3.7](#), the singlet preservation being linked to charge separation [[Mortemousque2021a](#)].

In between the intermediate and high tunnel coupling regime (position B for instance), we observe a thin curved line where a non-negligible part of the initial singlet population is lost. This feature of the spin map is associated with the S - T_+ avoided crossing. Indeed, while the coupling between these two states only occurs via either the x and y components of the Overhauser magnetic field or the spin-orbit coupling it is sufficient to create a small avoided crossing allowing mixing between the two states. This crossing is extensively studied in [subsection 4.3.1](#) and will be used to initialize the spin state in the T_+ state via an adiabatic transformation of the S state.

A simple model based on the two-electron spin states and the three possible charge states of the system allows us to confirm the previously discussed features of the spin map. The model is based on a two-step procedure consisting of first computing the ground singlet eigenstate $|\Psi_S(\varepsilon, t_c)\rangle$ of the DQD Hamiltonian without hyperfine interaction H_{DQD} (defined in [section 1.2.1](#)) for the different values of ε and t_c . Once the corresponding $|\Psi_S(\varepsilon, t_c)\rangle$ is computed, it evolves during $t = 500$ ns under the spin DQD Hamiltonian with hyperfine interaction $H_{\text{DQD,hf}}$ (defined in [section 1.2.1](#)). This change in the Hamiltonian mimics the non-adiabatic pulse performed in the spin map experiment previously described and makes the simulation time effective since only one Hamiltonian needs to be diagonalized for each ε and t_c position tested. In the end, the singlet probability is computed as:

$$P_S(\varepsilon, t_c) = |\langle \Psi_S(\varepsilon, t_c) | e^{-jtH_{\text{DQD,hf}}/\hbar} | \Psi_S(\varepsilon, t_c) \rangle|^2. \quad (4.5)$$

The computation is repeated and averaged 1000 times with random values of ΔB_x , ΔB_y and ΔB_z taken from a Gaussian distribution and the resulting singlet probability is plotted as a function of the detuning and tunnel coupling in [Figure 4.6\(d\)](#). The simulation reproduces the main features of the experimental spin map and confirms the interpretation made earlier in this section. Indeed, we observe the perfect conservation of the S population for $\varepsilon > E_C$ and $\varepsilon < -E_C$ corresponding to the case where the electrons are remaining in the same quantum dot. The simulation reproduces also the conservation of S for high values of t_c where $J(\varepsilon, t_c) \ll g\mu_B\Delta B_z$ as well as the S - T_+ branch and the S - T_0 mixing region. However, we did not implement in this model the presence of the excited orbital states hence the absence of the experimentally observed lobes in the simulation at low interdot tunnel coupling.

In the end, the spin map allowed us to identify the different regimes of the DQD both in terms of detuning and tunnel coupling via the evolution of the S state. Moreover, we were able to identify in the voltage gate space the position of the S - T_0 and S - T_+ mixing regions which is necessary in order to perform more complex spin operations such as exchange oscillations for instance.

4.2.5 Application: Exchange oscillations

Since the beginning of the chapter, we have presented the control over the interdot tunnel coupling t_c as an important asset for spin manipulation and readout. Added to the more conventional

detuning control, the whole (ε, t_c) 2D space is exploited to enhance initialization, readout, and control fidelity. In particular, exchange oscillations are driven by opening the exchange interaction J with a ε or a t_c pulse. This two-qubit operation has been first implemented for spin qubits in gate-defined quantum dots by J. Petta in 2005 [Petta2005a]. In this pioneering experiment the exchange between the two spins is only controlled by the potential detuning in between the two QDs. However, since then it has been demonstrated in various works that it is possible to use a combination of detuning and interdot tunnel coupling to achieve high fidelity exchange operations [Bertrand2015b, Martins2016, Reed2016] as intended in the early proposal for spin-based quantum computing by D. Loss and D. Di Vincenzo [Loss1998].

Protocol

The experimental realization of such exchange oscillations is based on two main steps. First the initialization of an $|\uparrow\downarrow\rangle$ (or $|\downarrow\uparrow\rangle$ depending on the sign of ΔB_z) spin state at low interdot tunnel coupling values where $J \ll g\mu_B\Delta B_z$. In this region, the relevant energy scale is the Overhauser magnetic field gradient generated by the nuclear spins of the heterostructure. As a consequence, the eigenstates of the system are no longer $|S\rangle$, $|T_0\rangle$, $|T_+\rangle$, and $|T_-\rangle$ but $|\uparrow\downarrow\rangle$, $|\downarrow\uparrow\rangle$, $|\uparrow\uparrow\rangle$, and $|\downarrow\downarrow\rangle$. We detail here the procedure to perform this initialization by following the state trajectory on the Bloch sphere in Figure 4.7(a) and the pulse sequence in Figure 4.7(b):

- The system is first initialized in a S state at a large value of tunnel coupling where it is an eigenstate of the system (point A in Figure 4.6(c)).
- Then, it is pulsed at the ns timescale across the previously identified S - T_+ avoided crossing in order to conserve the initially loaded S state (point C in Figure 4.6(c)).
- From there V_{B2} is slowly ramped (500 ns) to decrease J and reach point D where $J \ll g\mu_B\Delta B_z$. The system will therefore adiabatically remain in the ground state and initializes as $|\uparrow\downarrow\rangle$ or $|\downarrow\uparrow\rangle$ depending on the sign of ΔB_z for this experimental shot.

Now, to induce rotation in the xy plane of the Bloch sphere and therefore oscillate between $|\uparrow\downarrow\rangle$ and $|\downarrow\uparrow\rangle$ spin states, it is necessary to increase in a non-adiabatic fashion the exchange coupling between the two spins. This is done using two possible manners, either via increasing the potential detuning or via increasing the interdot tunnel coupling, see Figure 4.7(c). From point D, the system is therefore pulsed to position $(V_{B2}^{\text{exch}}, V_{B3}^{\text{exch}})$ in the voltage gate space during a time $\tau_{\text{exch}} = 5$ ns. At this position the spin state oscillates in the xy plane of the Bloch sphere at a frequency $J(V_{B2}^{\text{exch}}, V_{B3}^{\text{exch}})/\hbar$. To stop the oscillations the system is pulsed back to point D. Finally, the mirror sequence of the initialization is applied to map the $|\uparrow\downarrow\rangle$ state to S and $|\downarrow\uparrow\rangle$ to T_0 .

At the end of the complete sequence, the spin state is readout via a FPSB procedure and the singlet spin state probability is given by:

$$P_S = \frac{1 + \cos\left(\frac{J(V_{B2}^{\text{exch}}, V_{B3}^{\text{exch}})\tau_{\text{exch}}}{\hbar}\right)}{2}. \quad (4.6)$$

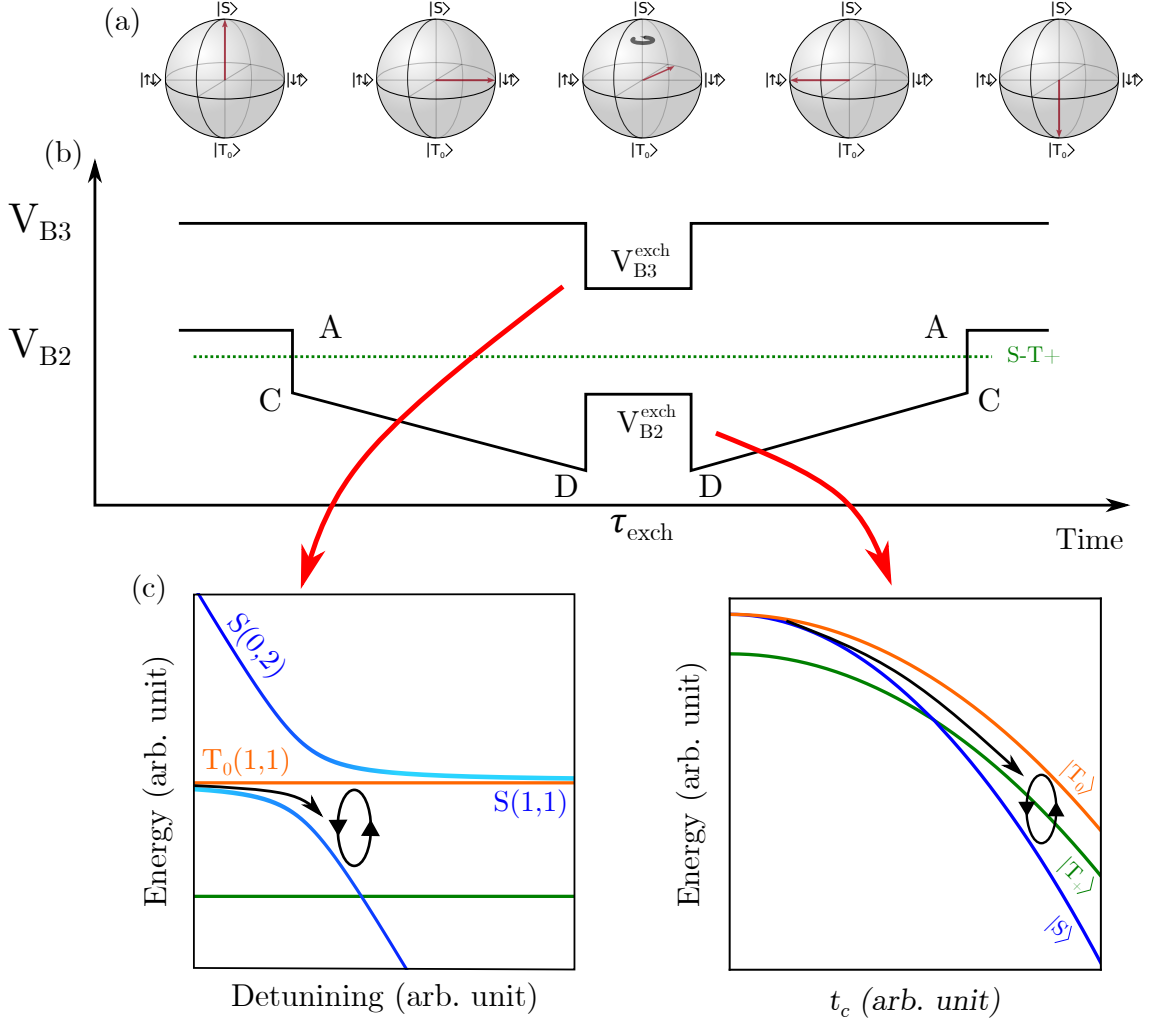


Figure 4.7: Exchange oscillations via detuning and tunnel coupling control. **a**, The evolution of the ST_0 qubit during the pulse sequence is depicted in the Bloch sphere. **b**, Pulse sequence applied to gates B_2 and B_3 in order to perform ST_0 exchange oscillations. A, C and D positions are indicated on the spin map in Figure 4.6(c). The system is initialized in a singlet state at position A and is conserved at position B via a non-adiabatic pulse across the S - T_+ crossing. Then J is adiabatically reduced using a ramp from C to D to transform the singlet state into $|\uparrow\downarrow\rangle$ or $|\downarrow\uparrow\rangle$ depending on the value of ΔB_z . From there J is increased via a simultaneous voltage pulse applied to gates B_2 and B_3 , this results in oscillations between $|\uparrow\downarrow\rangle$ and $|\downarrow\uparrow\rangle$ at a frequency J . Finally, the mirror sequence is applied to map the $|\uparrow\downarrow\rangle$ and $|\downarrow\uparrow\rangle$ states to S and T_0 and perform a FPSB spin readout. **c**, Energy diagrams depicting the two ways of controlling J via either a detuning or tunnel coupling pulse.

Through this equation we can directly see how performing such oscillations is an indirect measurement of the exchange coupling at the probed position in the voltage gate space.

Experiment

In [Figure 4.8\(a\)](#) we have experimentally implemented the protocol described in the previous section and we plot the singlet spin state probability as a function of the exchange pulse position in the voltage gate space ($V_{B2}^{\text{exch}}, V_{B3}^{\text{exch}}$). As expected by [Equation 4.6](#), we observe a so-called chevron pattern where the evolution of the singlet spin state probability is governed by [Equation 4.6](#). However, the oscillations of P_S is not observed in all the regions of the voltage gate space, especially in large values of potential detuning regions. Indeed, as explained in [chapter 1](#) the main source of decoherence in gate-defined spin qubits is the charge noise that modulates the double quantum dot parameters ε , t_c and therefore the exchange interaction. This phenomenon induces decoherence in the system with a characteristic time T_2^* . From previous works we know that J has an exponential dependence with respect to ε , we therefore expect the detuning noise sensitivity $\frac{\partial J}{\partial \varepsilon}$ to vary exponentially [[Petta2005a](#), [Bertrand2015b](#), [Thalineau2014](#)]. The regions where no oscillations are observed are interpreted as regions of the voltage gate space where $|\varepsilon|$ is high and where the system is more sensitive to charge noise and $T_2^{\text{Rabi}} \ll \tau_{\text{exch}}$ [[Dial2013](#)].

One way to increase the coherence time is to operate the system at $\varepsilon \simeq 0$ where it becomes insensitive to potential detuning noise (so-called sweet spot) and control the exchange pulse via the interdot tunnel coupling. At this sweet spot, the noise sensitivity $\frac{\partial J}{\partial \varepsilon}$ with respect to the detuning is suppressed and the qubit is only sensitive to the noise in interdot tunnel coupling $\frac{\partial J}{\partial t_c}$ [[Bertrand2015b](#)]. Experimentally this is observed along the white dotted line in [Figure 4.8\(a\)](#), where we follow the maximum contrast between the oscillations in the chevron pattern. A line cut along this axis is plotted in [Figure 4.8\(b\)](#) and we observe up to 11 oscillations in 5 ns for the highest value of V_{B2}^{exch} probed. From the oscillation frequency, we can directly infer a function of the exchange coupling along the sweet spot axis $J(V_{\varepsilon=0})$ where $V_{\varepsilon=0}$ is the zero detuning axis defined in [Figure 4.8\(a\)](#). We plot $J(V_{\varepsilon=0})$ in blue in [Figure 4.8\(c\)](#), for simplicity in the graph reading $V_{\varepsilon=0}$ is projected on the associated voltage of V_{B2}^{exch} . Using [Equation 1.23](#), we can determine through this measurement the dependence of the interdot tunnel coupling along the $\varepsilon = 0$ axis of the system that we plot in orange in [Figure 4.8\(c\)](#). We observe the ability to tune t_c from 10 GHz to 50 GHz in a few tens of mV of variation of V_{B2} demonstrating again the high level of control obtained in this sample over this crucial parameter. Here again, we have to rely on an estimation of the charging energy E_C and the exchange energy in a single dot J_0 to obtain the numerical value of the interdot tunnel coupling. Finally, it is worth noting that similarly to the detuning evolution, J is correctly described by an exponential increase $J(V_{\varepsilon=0}) = J_{\text{min}} + e^{(V_{\varepsilon=0}-V_0)/v}$.

To understand the reduction shape of the oscillation amplitude we follow [[Dial2013](#)] and define the oscillations quality factor $Q = JT_2^*/2\pi h$. The quality factor defines approximately the number of visible rotations around the Bloch sphere equator before decoherence makes the signal disappear. By assuming a quasistatic noise (ie. low frequency noise compared to T_2^*) we expect

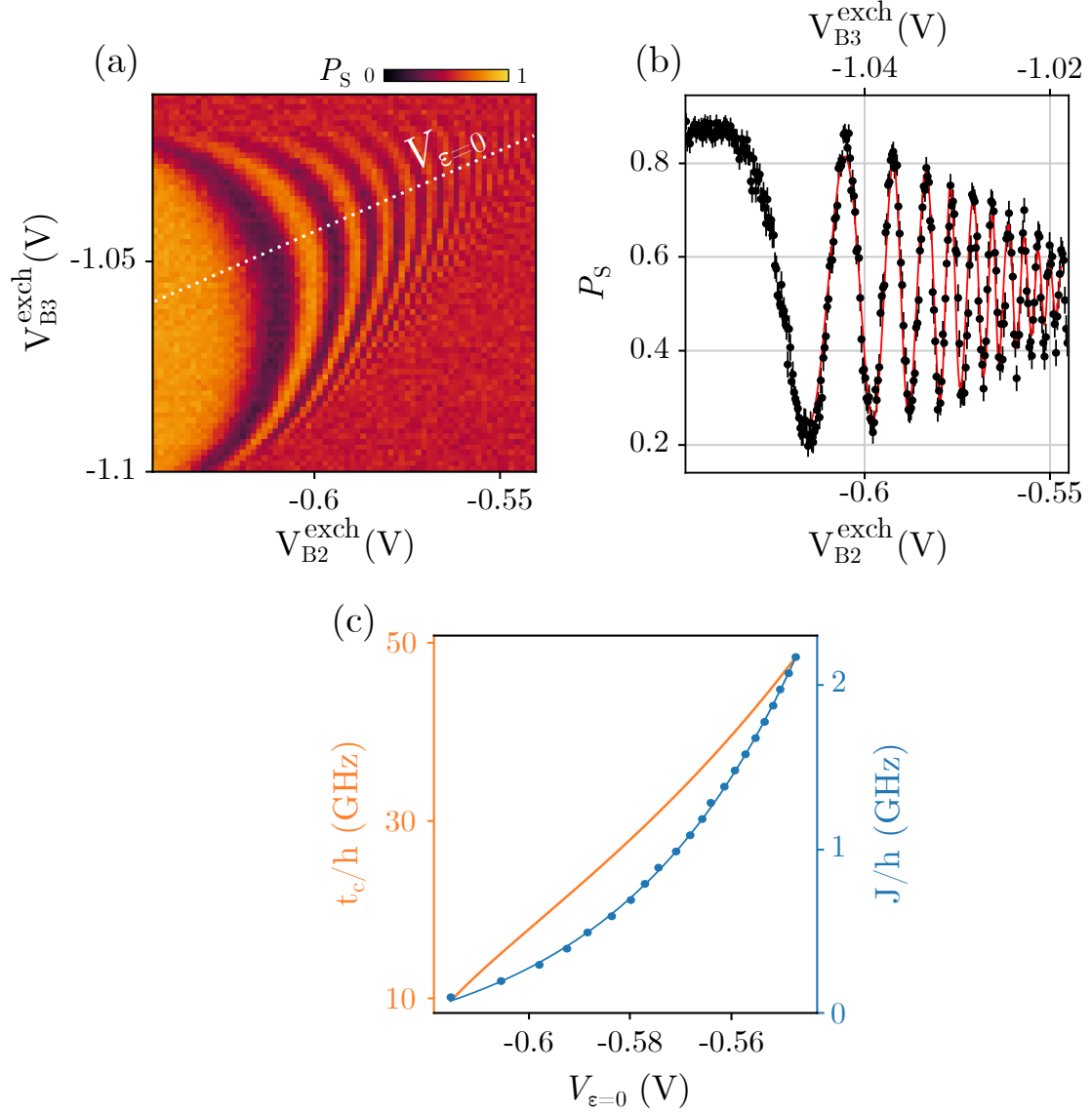


Figure 4.8: Exchange oscillations and parameter extraction. **a**, Chevron pattern induced by exchange oscillations. The pulse sequence presented in Figure 4.7 is performed and we plot the singlet probability as a function of the exchange pulse coordinates ($V_{B2}^{\text{exch}}, V_{B3}^{\text{exch}}$) for $\tau_{\text{exch}} = 5$ ns. We observe clear Rabi oscillations of the singlet population proving the validity of the pulse sequence performed. **b**, Exchange oscillations performed along the sweet spot ($\epsilon = 0$). Following the maximum visibility of the oscillations, we can determine the sweet spot axis $V_{\epsilon=0}$ in the voltage gate space. **c**, Exchange coupling and tunnel coupling extracted along the sweet spot axis in **b**. For each maximum and minimums, we can define $J = m/(2\tau_{\text{exch}})$ where $m = 0, 1, 2, \dots$. The data points are fitted to an exponential increase. t_c is computed using Equation 1.23.

in time, a Gaussian decay of the signal $e^{-(\tau_{\text{exch}}/T_2^*)^2}$ with $T_2^* \propto \left(\frac{\partial J}{\partial V_{\varepsilon=0}}\right)^{-1}$. From the previous paragraph we know that J follows an exponential dependence with respect to $V_{\varepsilon=0}$, therefore we expect $Q \propto J \left(\frac{\partial J}{\partial V_{\varepsilon=0}}\right)^{-1}$ to be more or less constant with respect to the exchange pulse amplitude. In the end, the oscillations in [Figure 4.8\(b\)](#) are fitted to:

$$P_S(V_{\varepsilon=0}) = A + B \cos\left(\frac{J(V_{\varepsilon=0})\tau_{\text{exch}}}{\hbar}\right) \times \exp\left(-\left(\frac{J(V_{\varepsilon=0})\tau_{\text{exch}}}{\hbar Q}\right)^2\right), \quad (4.7)$$

where $Q = 8.2$ is the oscillations quality factor, $A = 0.29$ and $B = 0.54$ are fitting parameters. The obtained value for Q are higher than the one obtained for SWAP operation performed using the detuning parameter ($Q \sim 2$) demonstrating the superiority of symmetric operations in terms of coherence [[Dial2013](#), [Bertrand2015a](#), [Martins2016](#)]. In this experiment, we are probing high values of exchange coupling compared to the literature where the study is often limited to $J/h \sim 200$ MHz. This results in exchange oscillations quality factor that is only limited by the electric noise whereas other works can be limited by the random Overhauser magnetic field gradient tilting the rotation axis in the Bloch sphere [[Martins2016](#)].

In the end, the chevron pattern performed allows us to identify important operating regions of the DQD system such as the symmetric operation line ($\varepsilon = 0$) in the voltage gate space. Moreover, we confirmed through this experiment our ability to control the interdot tunnel coupling at the ns timescale in the GHz regime completing the previously obtained result in [chapter 3](#) where we demonstrate the same result in the sub-Hz regime.

4.3 Tools for complete spin state readout

We have seen previously that the FPSB protocol allowed us to enhance the readout fidelity while conserving the electrons in the system at the end of the measurement. This feature of the measurement protocol allows us to perform repeated measurements of the electrons to enhance the quantity of information extracted from the system. Combining spin manipulations and repeated FPSB readouts plays a central role in the complete readout procedure giving the capability to discriminate the four possible spin states (S , T_0 , T_+ , and T_-). These particular spin manipulations are detailed in this section and consist in first a selective transformation of a T_+ spin state into S via an adiabatic ramp. Then we will demonstrate an on-demand parity readout protocol based on the fast and selective relaxation of the T_0 state to S .

4.3.1 S-T+ adiabatic transformation

In [subsection 4.2.4](#), we have localized in the voltage gate space the position of the S - T_+ avoided crossing by the observation of the S state evolution. We experimentally observed that when the

system was pulsed in a non-adiabatic manner exactly on the avoided crossing it was possible to form a statistical mixture of S - T_+ states. However, to implement the complete readout it is necessary to engineer a procedure allowing us to transform rapidly with the highest possible fidelity a S into a T_+ state and vice versa. While being rapid the S - T_+ mixture does not fulfill the requirements of reversibility and fidelity. We develop here a different method relying on the adiabatic transformation of the spin states via a ramp performed across the avoided crossing [Fogarty2018, Petta2010, Stehlik2012].

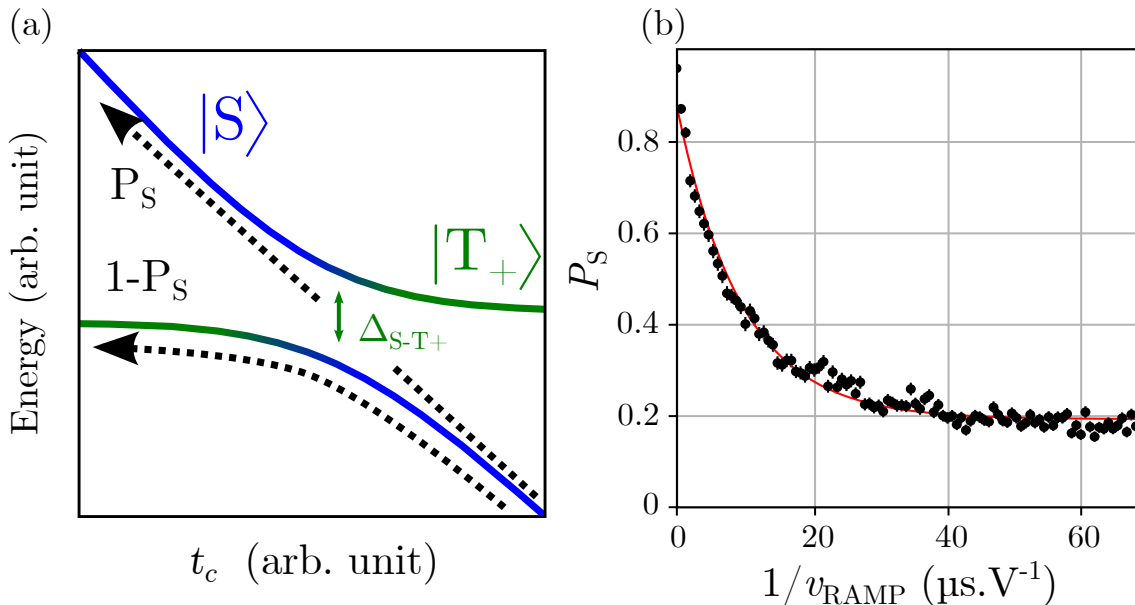


Figure 4.9: Landau-Zener S - T_+ transformation. **a**, Illustration of the energy diagram around the S - T_+ avoided crossing. The coupling between the two states via the transverse hyperfine magnetic field gives rise to an energy splitting $\Delta_S - T_+$. Using this anti-crossing it is possible to convert a fraction of an initial state into the other one via an adiabatic ramp performed across the splitting. **b**, Singlet return probability after a ramp across the S - T_+ anti-crossing. The electrons are initialized as a singlet state at point A on the spin map in Figure 4.6(c). Then the system is ramped at different speeds V to position C by varying the voltage applied on gate B_2 . We observe the ability to transform up to 80 % of the initial singlet population into T_+ via a slow ramp through the avoided crossing. The data are fitted to an exponential decay as expected by the Landau-Zener formula, yielding the best fit for $\Delta_{S-T_+} = 300$ neV.

In Figure 4.9(a), we consider the crossing between the S and T_+ states coupled by Δ_{S-T_+} . The origin of the coupling between the two states arises from two sources in the GaAs/AlGaAs spin qubit platform. First, the hyperfine magnetic field gradient whose effect is extensively discussed in section 1.3.2. Second, the total spin of the two electron spin system can be influenced by its orbital motion due to the spin-orbit interaction [Stepanenko2012]. The spin-orbit interaction can be described as an external magnetic field perpendicular to the electron motion in the double quantum dot and only experienced when electrons are displaced in the system [Nichol2015].

We show in Figure 4.9(a) the experimental procedure to follow in order to perform a hyperfine driven transformation of S to T_+ . The two electrons are initialized in the S spin state at large value of tunnel coupling in the (1,1) charge configuration. It is then ramped to lower values at a given

rate to cross the S - T_+ avoided crossing. If the tunnel coupling is rapidly swept compared to Δ_{S-T_+} , the transformation is non-adiabatic and the spin state remains the state here a S . On the other hand, if the sweep rate is low the state will remain in the ground state during the whole process and the initial S state will be transformed into T_+ . In the end, the probability to remain in a S state at the end of the sweep P_S is calculated using the Landau-Zener criteria [Landau1965,Zener1932] :

$$P_S = \exp\left(\frac{-2\pi\Delta_{S-T_+}^2}{\hbar\Gamma}\right) \text{ where } \Gamma = \frac{dE}{dt}. \quad (4.8)$$

In order to estimate our ability to perform on-demand adiabatic or non-adiabatic S - T_+ state transformation, we initialize the system in the S state at position A in Figure 4.6(c). The voltage applied to gate B₂ is then ramped at a speed v_{RAMP} to reach position C, during this ramp the system passes the previously identified S - T_+ crossing. Finally, a FPSB is performed and the outcome singlet probability P_S is plotted as a function of the inverse of the sweep speed. As expected, we observe for high speeds conservation of the initial S state in this regime the state transfer is completely non-adiabatic in regard to the S - T_+ transition. However, when the sweeping speed is decreased the state transfer is adiabatic and up to 80 % of the initial singlet population is transferred to the T_+ state. We fitted an exponential decay to the experimental data and extracted a typical rate of $v_{\text{RAMP}} = 0.1 \text{ V } \mu\text{s}^{-1}$. Using the dependence of the exchange energy J as a function of the voltage gate V_{B2} obtained in Figure 4.8(c) ($\sim 10^{-3} \text{ eV V}^{-1}$), we convert the voltage rate to an energy rate and obtain $v_{\text{RAMP}} = 10^{-4} \text{ eV } \mu\text{s}^{-1}$. Now using Equation 4.8, we can extract the coupling between the S and T_+ spin states and obtain $\Delta_{S-T_+} \simeq 100 \text{ neV}$. As seen in section 1.3.2, the coupling between S and T_+ is given in the (1,1) charge configuration by $\Delta_{S-T_+} = \hbar\gamma_e \frac{\sqrt{(\Delta B_x^N)^2 + (\Delta B_y^N)^2}}{\sqrt{2}}$. In section 4.2.2, we extracted the standard deviation of ΔB_z^N and obtained 4.6 mT, by assuming that the Overhauser magnetic field along the x and y axis follows similar dynamics we can expect the coupling to be around $\Delta_{S-T_+} = 100 \text{ neV}$, in agreement with the experimentally obtained value.

According to the Landau-Zener formula Equation 4.8, for infinitely slow ramping speeds the population transfer from S to T_+ should be perfect. However, we observe experimentally a saturation of the transfer probability at around 80 %. This saturation can be explained by a residual sweeping speed defined as $\Gamma_{\text{res}} = \frac{-2\pi\Delta_{S-T_+}^2}{\hbar \ln(1-0.8)} \simeq 0.5 \mu\text{eV ns}^{-1}$. Thus, we estimate the equivalent residual sweeping voltage speed to be $500 \mu\text{V ns}^{-1}$. One non-negligible part of this residual speed is explained by the limited digitalization of the AWG used to perform the voltage ramp across the avoided crossing. Indeed, the AWG has an output resolution of $600 \mu\text{V}$ which corresponds on the sample, taking into account the RF line attenuation, to a digitalization of around $60 \mu\text{V}$. The typical bandwidth of the AWG is 1 GHz the minimal sweeping rate of the gate voltage is therefore $60 \mu\text{V ns}^{-1}$ close to the residual value obtained experimentally. In the future to have a better transformation fidelity, it will be therefore desirable to use electronics with higher digitalization or perform dynamic filtering when a ramp is performed. The rest of the transformation infidelity could be explained by magnetic and charge noise also limiting the adiabaticity of the pulse [Qi2017,Nichol2015].

To conclude we have implemented a few μs long pulse sequence composed of a ramp allowing us to transform up to 80 % of S into T_+ . It is worth noting that this procedure is completely reversible meaning that we expect the same transformation rate of a pure T_+ state into S . This is going to be verified by the complete readout procedure in [section 4.4](#).

4.3.2 Parity readout

Classically, a PSB measurement allows to discriminate the S state from T_0 , T_+ , and T_- . However, it has been demonstrated that the relaxation of the T_0 state to S is strongly enhanced by spin-orbit coupling or spin state mixing by setting the system at a particular position in the parameter space close to the PSB [[Barthel2012](#),[Seedhouse2021](#),[Yang2020](#),[Niegemann2022](#)]. A spin readout performed in such conditions will give the same signal for a S and T_0 and is referred to as a parity readout. This type of readout is a requirement needed to perform the complete readout procedure, and we will demonstrate here how we were able to implement it in an isolated DQD.

The lift of T_0 blockade on a timescale shorter than the one usually observed at the PSB position relies on spin state mixing induced by either spin-orbit coupling or hyperfine magnetic field depending on the spin qubit platform used. We describe here the precise process happening for the GaAs/AlGaAs one. The PSB position is usually located near the (1,1)/(0,2) charge transition, as we can see in the energy diagram in [Figure 4.11\(c\)](#). In this region the $|T_0(1,1)\rangle$ spin state is isolated from the other states energy-wise. As said earlier, the characteristic relaxation time of a such state in these conditions is around $10\ \mu\text{s}$ [[Barthel2012](#),[Barthel2009](#)]. However, this relaxation process is strongly enhanced by slightly increasing the potential detuning to reach position R_1 where the $|T_0(1,1)\rangle$ and $|S(1,1)\rangle$ states are nearly degenerated. At this position, indicated by the circular arrows in [Figure 4.10\(c\)](#), spin mixing between the two states occurs in a few ns via the z component of the Overhauser magnetic field gradient (see [section 4.2.2](#)). The initial T_0 state is therefore transformed in $|S(1,1)\rangle$ which rapidly relaxes to $|S(0,2)\rangle$ via phonon emission at a rate Γ_S [[Barthel2012](#),[Meunier2007](#),[Fujisawa1998](#)].

The calibration of such a hotspot in the voltage gate space is a necessary step to implement the parity readout. To do so, we performed the procedure described in [Figure 4.10\(a\)](#), where we fully characterized in the ε and t_c parameter space the relaxation of the S and T_0 state.

The procedure starts by initializing the spin state in the $|S(1,1)\rangle$ state at a large value of t_c . From there the interdot tunnel coupling is pulsed during 500 ns at position D in [Figure 4.10\(a\)](#) to initialize a $|S(1,1)\rangle$ - $|T_0(1,1)\rangle$ mixed state. The system is then pulsed to the coordinates $(V_{B2}^{\text{PR}}, V_{B3}^{\text{PR}})$ during $5\ \mu\text{s}$. Finally, a FPSB procedure is performed as described in [section 4.2](#), and we plot the S state probability P_S in [Figure 4.10\(b\)](#) as a function of the pulse coordinates. We observe lobes of high and low values of P_S alternating as the potential detuning of the DQD increases.

To explain this behavior, we plot in [Figure 4.10\(c\)](#) the energy diagram of the relevant states as a function of ε . As mentioned earlier, the system is initialized at the position D in the energy diagram (S - T_0 mixed state), from there it is set at a certain value of detuning at the ns timescale. At this value of t_c , we expect the pulse to be non-adiabatic regarding the (1,1)/(0,2) charge transition,

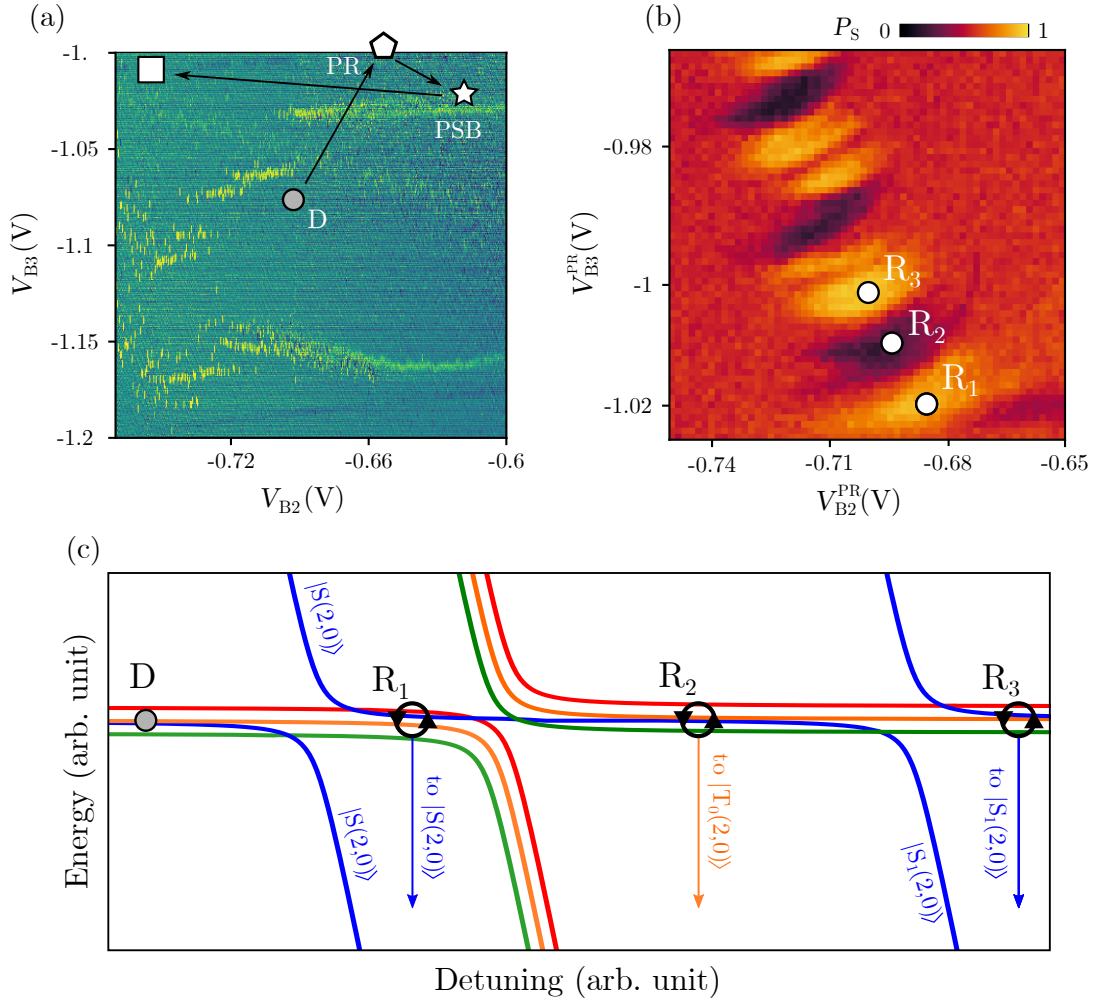


Figure 4.10: Calibration of the relaxation hotspot in the voltage gate space. **a**, Pulse sequence used to calibrate the parity readout position. The system is initialized in a singlet state and pulsed in the (1,1) charge region at position D in order to prepare an equipartition of S and T_0 population. The system is then pulsed to the pentagon during $5\ \mu\text{s}$ at coordinates $(V_{B2}^{PR}, V_{B3}^{PR})$, finally a FPSB procedure is applied to determine the proportion of S at the end of the relaxation pulse. **b**, Singlet probability at the end of the pulse sequence presented in (a) as a function of the pulse coordinates $(V_{B2}^{PR}, V_{B3}^{PR})$. We observe lobes of high singlet probability indicating that the initialized T_0 state has relaxed to the S state during the $5\ \mu\text{s}$ pulse. The position R_3 where the highest singlet probability is recorded, is selected as the parity readout position. **c**, Energy diagram of the relevant spin states and identification of the region where $|T_0(1,1)\rangle$ and $|S(1,1)\rangle$ mixing can occur.

therefore the $|S(1,1)\rangle$ and $|T_0(1,1)\rangle$ states are conserved. From there, different outcomes are possible depending on the detuning amplitude of the pulse, close to position R_1 the spin states are nearly degenerated and mixing occurs. As soon as the $|T_0(1,1)\rangle$ state is transformed into $|S(1,1)\rangle$ it relaxes to the ground state $|S(0,2)\rangle$ via phonon emission, this behavior corresponds to the bottom lobe of high P_S in [Figure 4.10\(b\)](#).

Between positions R_1 and R_2 , the $|S(1,1)\rangle$ and $|T_0(1,1)\rangle$ split in energy due to the charge state avoided crossing of the T_0 state and the initial mixed state is conserved. When the system is brought close to position R_2 mixing between the state is again possible. However, at this position, relaxation is possible to the two states $|S(0,2)\rangle$ and $|T_0(0,2)\rangle$ (relaxation to T_+ and T_- states is disregarded due to the spin-flip process, typically \simeq ms [[Shen2007](#)]). Nevertheless, in previous experiments the singlet relaxation rate $|S(1,1)\rangle$ to $|S(0,2)\rangle$ was found to follow an ε^{-2} dependence [[Barthel2012](#), [Fujisawa1998](#)] and should therefore be negligible compared to the $|T_0(1,1)\rangle$ to $|T_0(0,2)\rangle$ relaxation at this position. The low P_S lobe around position R_2 arises from the following dynamic: the $|S(1,1)\rangle$ state is transformed into $|T_0(1,1)\rangle$ via spin mixing which preferentially relaxes to $|T_0(0,2)\rangle$.

The succession of high and low probability lobes is finally repeated for higher detuning involving higher excited charge states of the DQD system. For instance, at position R_3 , mixing between $|S(1,1)\rangle$ and $|T_0(1,1)\rangle$ is again possible and relaxation to $|S_1(0,2)\rangle$ state (S state involving an electron on the first excited level of the quantum dot) is the dominant one yielding at the end of the procedure a high P_S value. The position retained at the end of the calibration is the one yielding the highest singlet return probability in a $5\ \mu\text{s}$ pulse, here point R_3 in [Figure 4.10\(b\)](#).

The experiment presented in [Figure 4.10](#) does not certify that the relaxation hotspot is T_0 state selective. We ensure it by performing the pulse sequence sketched on top of the stability diagram in [Figure 4.11\(a\)](#). The electrons are initialized in either a S - T_0 or S - T_+ mixed state via a $500\ \text{ns}$ pulse at position D or B respectively. The system is then pulsed during a variable time T_{PR} at the parity readout position indicated by the white pentagon. Finally, a FPSB procedure is applied to the system. In [Figure 4.11\(b\)](#), we plotted the S probability as a function of the time spent at the parity readout position for the S - T_0 and S - T_+ mixed state initializations. In the case of the spin states with $m_s = 0$, we observe a rapid relaxation of the T portion of the signal to S state with a characteristic time of $1/\Gamma_S = 300\ \text{ns}$. This fast relaxation is the signature of the T_0 relaxation hotspot that can be used to perform a parity readout measurement scheme. In the case of the S - T_+ state, we observe the conservation of the T proportion of the signal during the whole duration spent at the parity readout position. As expected the T_+ relaxation is not enhanced at this position and no relaxation is observed demonstrating the selectivity of the relaxation hotspot.

Now that we have characterized the T_0 relaxation hotspot we integrate it in a more complex pulse sequence in order to perform a parity readout. The electrons are initialized in a S state at a large value of interdot tunnel coupling, from there the system is pulsed along the red dashed line in [Figure 4.11\(a\)](#) during $500\ \text{ns}$. At the end of the spin state evolution, the system is pulsed to the parity readout position for $5\ \mu\text{s}$ and finally, a FPSB readout is performed. In [Figure 4.11\(c\)](#), we plot

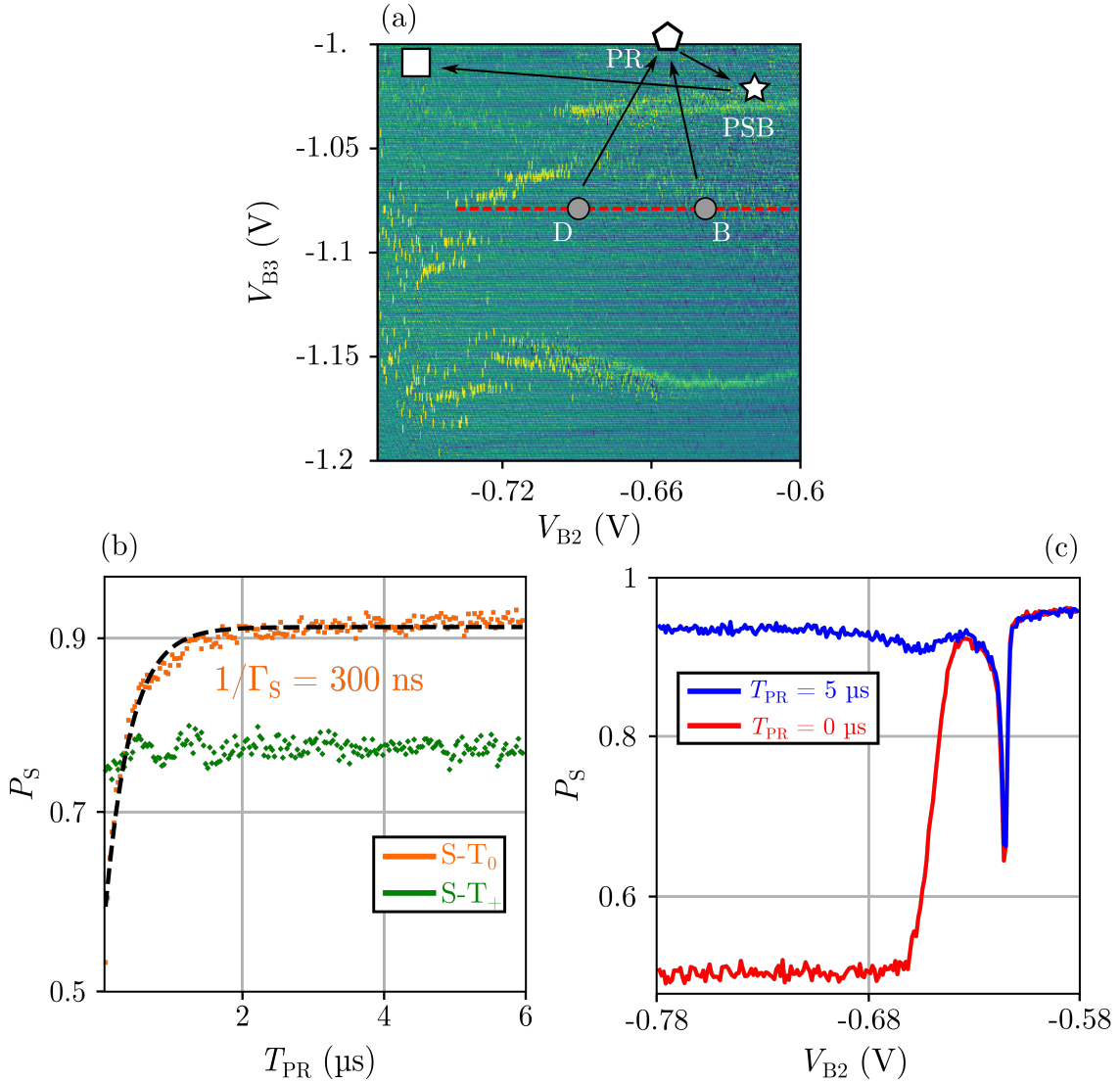


Figure 4.11: Parity readout via a selective relaxation hotspot of T_0 . **a**, Pulse sequence performed to ensure selectivity of the T_0 relaxation hotspot. The electrons are initialized either in a mixed state of $S-T_0$ at position D or a mixture of $S-T_+$ at position B. The system is then pulsed to the relaxation hotspot (white pentagon) during $5 \mu\text{s}$ to perform a rapid T_0 relaxation to the S state. **b**, Selective relaxation and the parity readout hotspot. We perform the pulse sequence described in **a** for the two possible initializations and vary the time T_{PR} spent at the hotspot position (white pentagon). **c**, Application of the parity readout in a spin map experiment. We vary the initialization position along the red dotted line in **b** and activate or not the parity readout by pulsing or not to the hotspot position.

the S probability as a function of the pulse position along the dashed line (V_{B2}). When the system is not pulsed to the parity readout position ($T_{PR} = 0\mu\text{s}$), we retrieve the behavior observed in the spin map experiment presented in [Figure 4.6](#). Indeed, in this case we are performing a classic FPSB measurement giving us the proportion of S at the end of the 500 ns evolution. However, when the system is pulsed to the parity readout position during a time long enough to allow T_0 relaxation to S , we observe a single drop in P_S corresponding to the previously identified S - T_+ avoided crossing. In this readout configuration, the S - T_0 mixing region observed for low values of interdot tunnel coupling is no longer present.

In the end, we engineered and implemented a pulse sequence allowing us to perform an on-demand parity readout in a few μs only. Since this novel readout is based on the previously developed FPSB, it inherits most of its key features such as the repeatability and the possibility to implement it easily in more complex pulse sequences. These two conditions are mandatory to implement it in the complete readout procedure that we will present in [section 4.4](#).

4.4 Complete two-electron spin state readout protocol

In addition to a higher readout fidelity, the ability to preserve the initial spin state at the measurement position allowed us to engineer a readout protocol maximizing the quantity of information extracted from the system. Indeed, a parity or PSB measurement yields only one bit of information despite having a system containing two. In this section, we develop a protocol entitled complete readout which allows us to discriminate between the four spin states S , T_0 , T_+ , and T_- . The measurement is based on the repeatability of the FPSB allowing us to perform a sequence of three distinct manipulations and measurements to determine the two-electron spin state.

4.4.1 Presentation of the protocol

In [Figure 4.12](#) we explain the complete readout procedure by detailing each step performed in between the FPSB measurements. The first step of the complete readout consists of a simple FPSB measurement performed as described in [section 4.2](#). If the output is (0,2) the shot is attributed to a S state no matter what the output of the following measurements are, if the output is (1,1) the state is one of the three triplet states and we have to consider the two following measurements. In the second step, we perform a parity readout to discriminate T_0 from T_+ and T_- . Again the charge configuration is read and a (0,2) is associated to T_0 while (1,1) is either a T_+ or a T_- state and the last measurement needs to be taken into account. To discriminate the last two spin states an adiabatic passage is performed through the S - T_+ avoided crossing. After this passage, the spin state is read using a frozen PSB measurement and a (0,2) output is attributed to T_+ since the transformation is selective. Finally, the (1,1) output is attributed to T_- . In the following section, we will use this set of rules to classify the 8 possible outcomes of the complete readout procedure.

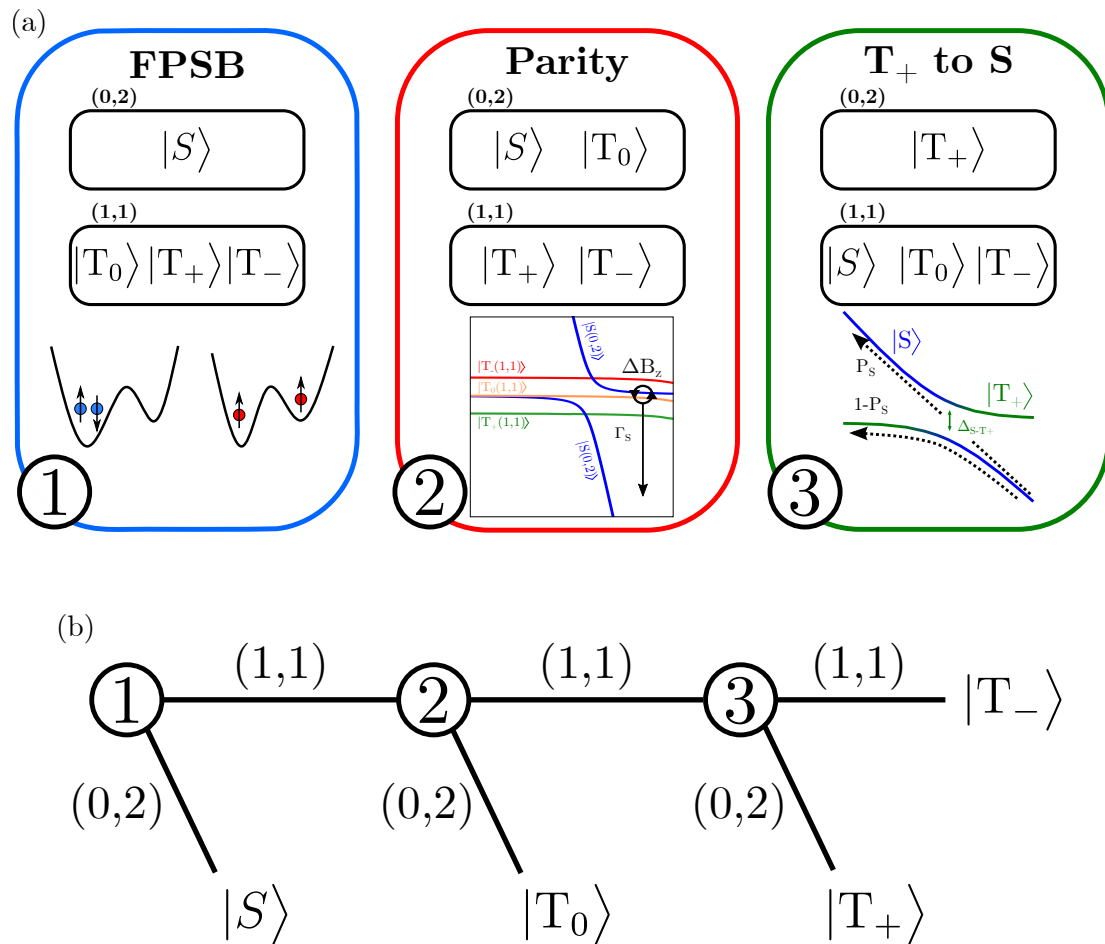


Figure 4.12: Complete readout and description of the three-step procedure. **a**, Role of the three steps in the complete readout. The procedure relies on three FPSB measurements interleaved with specific spin manipulation in order to discriminate the four spin states S , T_0 , T_+ , and T_- . The first step consists in performing a FPSB measurement to discriminate a S state from the three T states. Then a parity readout is performed using the T_0 hotspot allowing us to discriminate the T_0 state from T_+ and T_- . Finally, a selective transformation of T_+ into S followed by a FPSB measurement separates the T_+ and T_- populations. **b**, State attribution depending on the measurement outcome at the end of each step of the complete readout procedure.

4.4.2 Characterization on various initial spin states

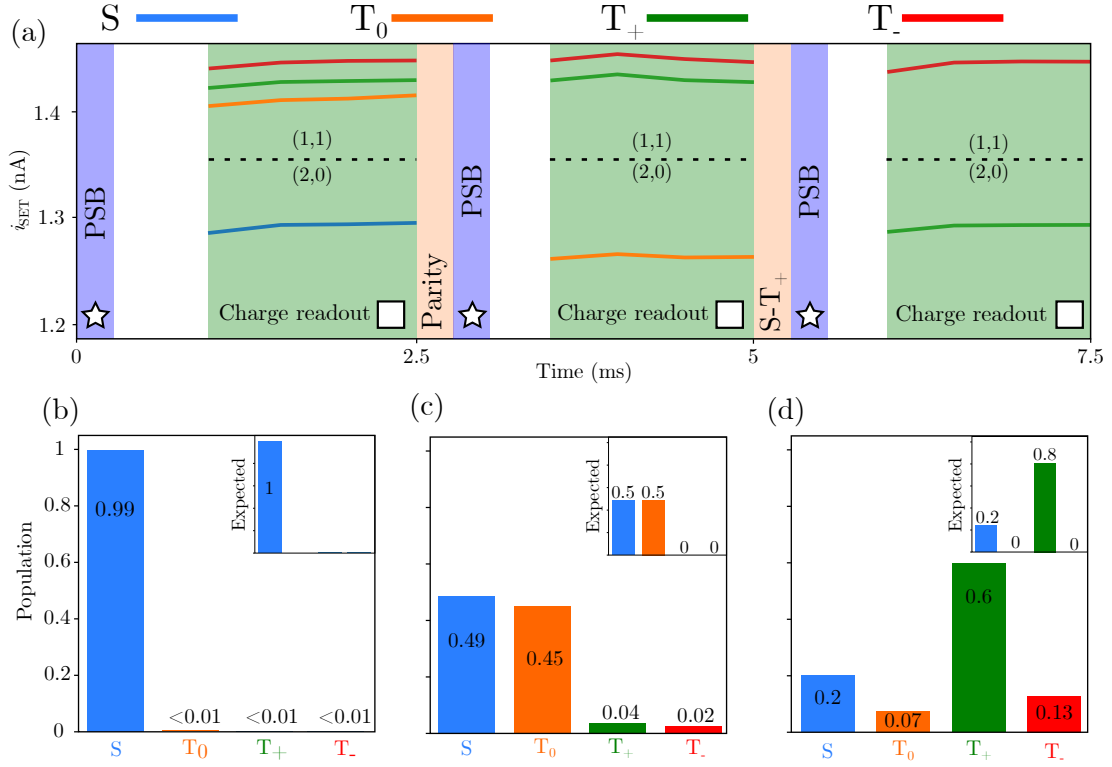


Figure 4.13: Experimental realization of the complete readout protocol. **a**, Typical measured current across the SET during the three different steps of the readout for the four possible spin states. Blue shaded areas corresponds to a pulse to the PSB position, the green shaded one is when the system is at charge readout position. The PSB, parity and $S-T_+$ shaded area are artificially extended in the chronogram and the SET traces are slightly offset for clarity. The white area corresponds to the time needed for the system to stabilize for readout after a manipulation. **b**, **c**, **d**, Output of the complete readout procedure for singlet state, $S-T_0$ mixed state and T_+ initialization. The inset corresponds to the expected result for an errorless complete readout procedure.

In Figure 4.13(b),(c),(d), the complete readout procedure is implemented for three different initializations to test its validity. The first one consists in waiting for the relaxation to the S ground state during 5 ms in the (0,2) charge region. We obtain $99.7 \pm 0.1\%$ of S state population in agreement with the PSB readout fidelity obtained previously. To test the ability of the complete readout to discriminate the T_0 state efficiently, we initialize a $S-T_0$ mixed state and again apply the readout procedure to it. The result is shown in Figure 4.13(b), we observed an excess of S and T_0 close to the expected values. For T_0 , we obtained 45 % probability instead of 50 % this discrepancy is attributed to the limited fidelity of the parity readout (see the following paragraph). Finally, we initialized a $79.9 \pm 0.4\%$ population of T_+ via an adiabatic ramp through the anticrossing as presented in the previous section. The result of the readout procedure is plotted in Figure 4.13(c) and we indeed observed an excess of T_+ state indicating again the validity of the readout for this state. In this situation, the readout is mainly limited by the transformation rate of a S into a T_+ and vice versa. Due to this limited transformation rate, 19 % of the T_+ population is mislabelled as T_- resulting in 0.13 probability to observe this state.

	Readout output	Initialization		
		S	Mixed S - T_0	Ramp S - T_+
S	(2,0)/(2,0)/(2,0)	0.24	0.09	0.03
	(2,0)/(2,0)/(1,1)	0.76	0.4	0.14
	(2,0)/(1,1)/(2,0)	< 0.01	< 0.01	0.02
	(2,0)/(1,1)/(1,1)	< 0.01	< 0.01	< 0.01
T_0	(1,1)/(2,0)/(2,0)	< 0.01	0.08	0.02
	(1,1)/(2,0)/(1,1)	< 0.01	0.37	0.05
T_+	(1,1)/(1,1)/(2,0)	< 0.01	0.04	0.6
T_-	(1,1)/(1,1)/(1,1)	< 0.01	0.027	0.13

Table 4.1: Outcome probability of all the measurements possible for the three initializations tested. For each initialization, the measurement procedure is repeated 10000 times. All the charge readout outputs are associated with one of the four spin states. The highlighted outputs are the ones to be maximized if the complete readout procedure was errorless.

The repetitive measurements performed on the three different initialized populations allow us to evaluate the fidelity of each stage of the complete readout procedure. Indeed, by taking into account only the first charge measurement in Table 4.1 for the S and mixed S - T_0 initializations, we can conduct the same calculations to obtain the S - T discrimination fidelity in the complete readout procedure $F_{\text{PSB}}^{\text{comp}} = 98.7 \pm 1.1\%$.

To assess the fidelity of the parity readout, we define the errors $S_{\text{error}}^{\text{p}}$, $T_{0,\text{error}}^{\text{p}}$ the probability to measure an even state when the system is initialized in S and T_0 respectively. Similarly, $T_{+,\text{error}}^{\text{p}}$ and $T_{-,\text{error}}^{\text{p}}$ are the probabilities to measure an odd state when the system is in the T_+ and T_- states. To compute each contribution in the infidelity of the parity readout we have the ability to initialize a S state, a mixed S - T_0 state and a statistical mixture composed of r of T_+ and $1 - r$ of S where r is the transformation rate of the adiabatic ramp presented in the main text. We finally relate the measurement errors to the outcome through the following equations:

$$P_{\text{odd}}^S = 1 - S_{\text{error}}^{\text{p}}, \quad (4.9)$$

$$P_{\text{odd}}^{\text{mixed}} = 1 - \frac{S_{\text{error}}^{\text{p}} + T_{0,\text{error}}^{\text{p}}}{2}, \quad (4.10)$$

$$P_{\text{odd}}^{\text{ramp}} = (1 - r)(1 - S_{\text{error}}^{\text{p}}) + rT_{+,\text{error}}^{\text{p}} \quad (4.11)$$

where P_{odd}^S , $P_{\text{odd}}^{\text{mixed}}$ and $P_{\text{odd}}^{\text{ramp}}$ is the odd spin state probability when the system is initialized in respectively S , S - T_0 and S - T_+ . We define $S_{\text{error}}^{\text{p}}$, $T_{0,\text{error}}^{\text{p}}$, $T_{+,\text{error}}^{\text{p}}$ and $T_{-,\text{error}}^{\text{p}}$ as the readout infidelity for a S , T_0 , T_+ , and T_- state. The three populations of odd states are obtained by summing the probabilities to obtain a (0,2) charge state measurement during the parity stage in the complete readout protocol. This procedure allows us to evaluate the fidelity of the parity readout embedded in the complete procedure. The S - T_+ transformation rate $r = 79.9 \pm 0.4\%$ is obtained by summing

the probability to obtain a (1,1) readout at the first measurement in the complete readout procedure when the system is initialized via the adiabatic ramp. In this case, we are assuming that the adiabatic ramp does not create any spin state different from S and T_+ and therefore any (1,1) measurement at the S - T readout stage is necessarily a T_+ .

Solving the system of equations by using the data presented in [Table 4.1](#) we obtain $S_{\text{error}}^{\text{P}} = 0.4 \pm 0.1 \%$, $T_{0,\text{error}}^{\text{P}} = 13.2 \pm 1.9 \%$ and $T_{+,\text{error}}^{\text{P}} = 6.5 \pm 0.6 \%$. Unfortunately, here we have no way to evaluate $T_{-,\text{error}}^{\text{P}}$ since we cannot initialize it. We define the overall parity readout fidelity embedded in the complete readout as $F_{\text{parity}}^{\text{comp}} = 1 - (S_{\text{error}}^{\text{P}} + T_{0,\text{error}}^{\text{P}} + T_{+,\text{error}}^{\text{P}} + T_{-,\text{error}}^{\text{P}})/4 = 93.3 \pm 1.1 \%$. The infidelity difference between the S and T_0 state is attributed to an uncontrolled relaxation of the $|T_0(1,1)\rangle$ state to $|T_0(0,2)\rangle$ before the mixing process transforms it to $|S(1,1)\rangle$ at the parity readout position (see [Figure 4.10](#)). For $T_{+,\text{error}}^{\text{P}}$, such a high value could be explained by initialization errors that we cannot distinguish from the measurement ones in our experiment. Indeed, an undesired creation of T_0 state during the initialization of S - T_+ via the adiabatic ramp would reduce the overall fidelity of the T_+ state during the parity readout since it cannot be distinguished from a T_0 during the first stage of the complete readout procedure.

Similarly, we compute the T_+ readout fidelity using the following equations:

$$P_{T_+}^{\text{S}} = S_{\text{error}}^{\text{T}}, \quad (4.12)$$

$$P_{T_+}^{\text{ramp}} = r(1 - T_{+,\text{error}}^{\text{T}}) + (1 - r)S_{\text{error}}^{\text{T}} \quad (4.13)$$

where $P_{T_+}^{\text{S}}$ and $P_{T_+}^{\text{ramp}}$ are the probabilities to measure a T_+ state in the complete readout procedure when the system is initialized in a S and S - T_+ respectively. We define $S_{\text{error}}^{\text{T}}$, $T_{+,\text{error}}^{\text{T}}$ the T_+ readout infidelity when the system is initialized in a S and T_+ state respectively. Solving the system we obtain $S_{\text{error}}^{\text{T}} = 1 \pm 1 \times 10^{-3} \%$ and $T_{+,\text{error}}^{\text{T}} = 25 \pm 1 \%$ mainly limited by the transformation rate of the S to the T_+ state. In this set of experiments, we do not have access to the infidelity when the system is initialized in the T_0 and T_- state. We finally define the fidelity of the T_+ measurement as $F_{\text{T}}^{\text{comp}} = 1 - (S_{\text{error}}^{\text{T}} + T_{+,\text{error}}^{\text{T}})/2 = 87 \pm 1 \%$.

4.4.3 Complete readout procedure for two-electron spin manipulations

We finally performed two-electron spin manipulations to ensure the possibility of the complete readout procedure to be inserted in more complex pulse sequences. In [Figure 4.14\(a\)](#), we performed a simple pulse on the inter-dot tunnel coupling and observed through the scope of the complete readout procedure the evolution of a S state. For $V_{\text{B}2} > -0.61 \text{ V}$, t_c is large enough for the S to remain the ground state, it is therefore conserved during the pulse duration and we observe a high probability of S . Lowering slightly more the tunnel coupling we observe a sharp drop in the S probability associated to an increase in the T_+ one, as explained previously at this position the two spin states are degenerated and mixing occurs. For even lower values of t_c , the S and T_0 probabilities both reach 50%, this ensures the observation made at the beginning of the section about the S - T_0 mixing region. In this regime we observe an excess of the T_+ population ($2.8 \pm 0.6 \%$)

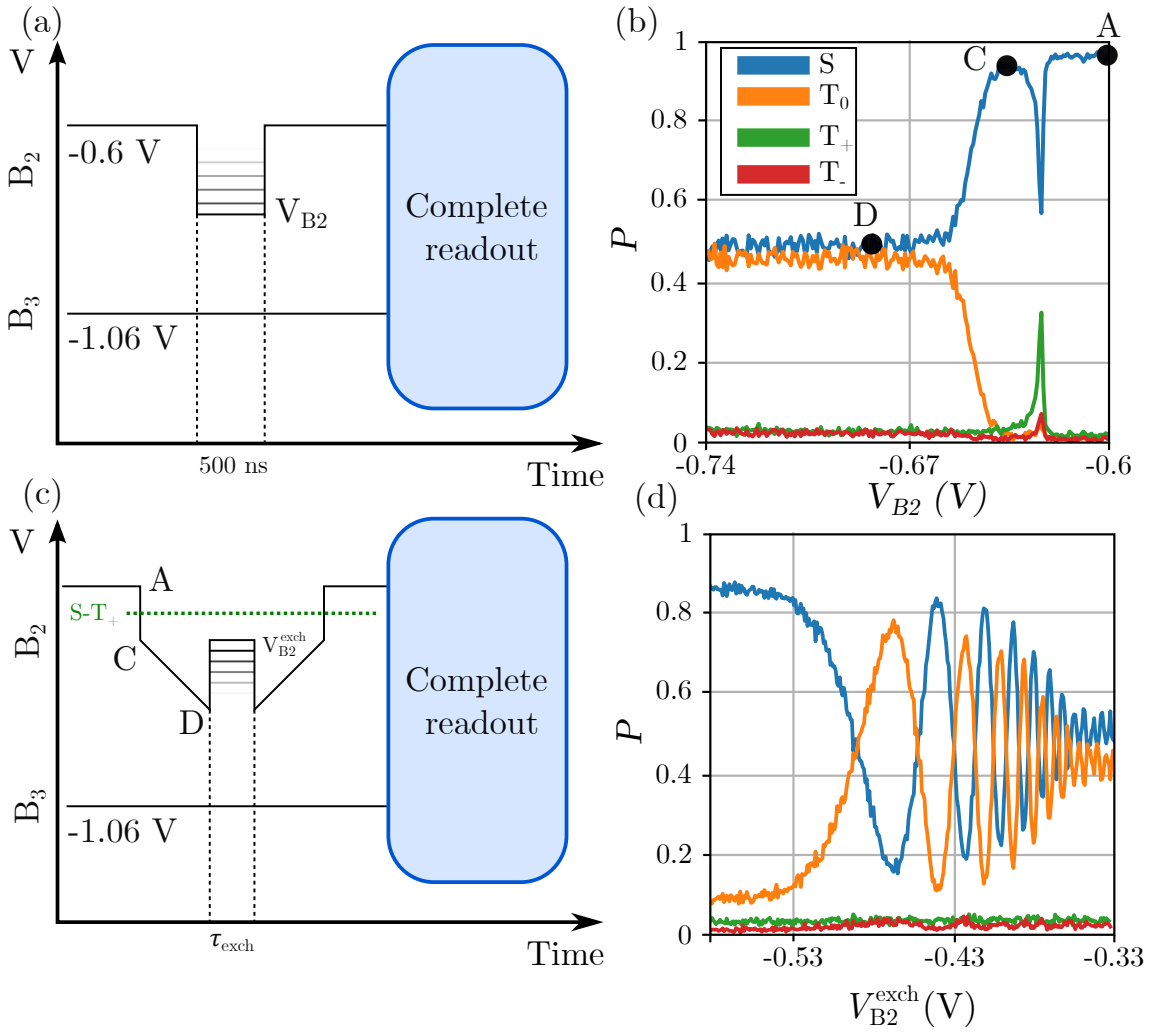


Figure 4.14: Spin state operations observed via the complete readout procedure. **a**, Pulse sequence performed to obtain **(b)**. The system is initialized in a singlet state at a large value of t_c ($V_{B_2} = -0.6$ V) in the (1,1) charge state region ($V_{B_3} = -1.06$ V), the inter-dot gate B_2 is pulsed during 500 ns at a variable amplitude V_{B_2} . A complete readout procedure is then performed, the output is classified using the methodology described in Figure 4.12. **b**, Singlet transformation with respect to the inter-dot tunnel coupling. **c**, Pulse sequence used to perform $S-T_0$ exchange oscillations. The initial S state is conserved from point A to C via a non-adiabatic pulse across the $S-T_+$ avoided crossing. It is then transformed adiabatically to $|\uparrow\downarrow\rangle$ or $|\downarrow\uparrow\rangle$ (depending on the sign of ΔB_z) via a ramp from C to D. From there, the exchange coupling J is increased via an inter-dot tunnel coupling pulse $V_{B_2}^{\text{exch}}$ during a fixed time $\tau_{\text{exch}} = 1.6$ ns. During this time the system evolves at a frequency J between $|\uparrow\downarrow\rangle$ and $|\downarrow\uparrow\rangle$, and finally the mirrored sequence is applied to stop the oscillations and map the two states to S and T_0 . **d**, Spin state probability at the end of the exchange pulse sequence. As expected the S and T_0 probabilities are oscillating out of phase. We observe a negligible leakage to the T_+ and T_- states proving the efficiency of the procedure to perform a SWAP operation.

associated to the passage through the S - T_+ avoided crossing being slightly adiabatic.

In [Figure 4.14\(d\)](#), we performed exchange controlled SWAP gate at the symmetric operation point to have a strong enhancement of the coherence time [[Bertrand2015b](#), [Martins2016](#), [Reed2016](#)]. Observing such operation through the scope of the complete readout procedure is of major interest to study state leakage. Indeed, this whole procedure is error-prone due to the high level of control needed over the shape of the pulses. As we can see in [Figure 4.14\(c\)](#), the S - T_+ crossing and the exchange pulse needs to be performed non-adiabatically while the basis transformation from S - T_0 to $|\uparrow\downarrow\rangle$ and $|\downarrow\uparrow\rangle$ must be adiabatic which is experimentally challenging. As expected the S and T_0 probabilities are oscillating out of phase while the T_+ and T_- ones are remaining low thanks to an efficient non-adiabatic pulse. The T_0 probability oscillations are centered around 45 % while the S is centered around 50 %. This offset is due to the limited parity readout fidelity and has already been observed in the mixing experiment in [Figure 4.13\(c\)](#). However, the oscillation amplitude, even for low exchange coupling, does not exceed 60 %, the complete readout procedure indicates us that the main limitation comes from the adiabatic transformation performed from the S/T_0 basis to $|\uparrow\downarrow\rangle/|\downarrow\uparrow\rangle$ and vice versa. A non-adiabatic pulse of the initial S state in the low tunnel coupling regime would result in state mixing process as described in the beginning of this work, which reduces the overall amplitude of the oscillation amplitude. This level of understanding of the error source is unlocked by the capability to discern the four spin states. Indeed, in the same situation a simple PSB readout would have been insufficient to distinguish an unwanted mixing of the S state from an unwanted transformation of S to T_+ when the avoided crossing is past during the initialization.

4.5 Conclusion

In this section, we demonstrated a high fidelity spin readout procedure based on PSB by separating in the voltage gate space the spin-to-charge conversion position from the charge readout. To do so, we performed the charge conversion via nanosecond AWG pulses orders of magnitude faster than the typical relaxation time observed in the GaAs/AlGaAs qubit platform. The resulting charge configuration was readout at a fixed and optimized position where the tunnel coupling was sub-Hz to prevent any charge variation of the DQD during the electrometer signal acquisition and therefore errors during the readout due to triplet state relaxation. This novel readout protocol allowed a clear improvement of the readout fidelity and opened the door to more complex readout procedures thanks to its repeatability. Indeed, we were able to interleave a parity readout based on a selective relaxation hotspot of T_0 to S and an adiabatic transformation of T_+ to S in between three sequential FPSB readouts to perform complete state discrimination of the two-electron spin states (S , T_0 , T_+ , and T_-). We confronted the complete readout procedure to various spin initializations to assess its validity and finally implemented it after inducing spin dynamics thanks to the

exchange energy control via the interdot tunnel coupling.

In this version of the readout protocol, the measurement speed is highly limited by the charge readout step performed using DC measurements of the SET current. All the spin manipulations presented including the relaxation process requires at maximum a pulse length of 5 μs . This limitation could be easily lifted by implementing an RF-SET type of readout allowing to discriminate charge states of a DQD in a few hundred of ns [Connors2020]. Moreover, to improve the overall fidelity of the complete readout each individual spin manipulation needs to be carefully calibrated and optimized. Following this, the limited S - T_+ transformation rate is also one of the biggest sources of errors in the readout procedure. However, the engineering of large and controlled spin-orbit interaction via electric or magnetic control has been demonstrated in various spin qubit platforms and could be a solution to increase the transformation rate fidelity [Nichol2015].

Conclusions and perspectives

The goal of this thesis was to develop a series of protocols on charge control and spin state readout allowing for fast and efficient readout of spin qubits while limiting the hardware overhead. Towards this objective, we first focused on the charge readout of the array by implementing experimentally an RF-SET based readout in the GaAs/AlGaAs platform. We tried to tackle through this device the experimental difficulties to obtain experimentally a $50\ \Omega$ -matching condition between the RF-circuitry and the electrometer. The particularity of this work was the use of homemade on-chip elements to build the resonant circuit. These developments allowed us to reduce the uncertainty about the actual values of the inductance and capacitance composing the tank circuit at cryogenic temperatures. We used a superconducting inductance made of niobium and a varactor directly embedded in the quantum device allowing for in-situ tuning of the resonant frequency and matching conditions. The resonant circuit was fully characterized using classical RF measurements determining the resonant frequency, capacitance, and matching conditions. We determined through these measurements that using the varactor it was possible to tune the resonant frequency and the capacitance of the tank circuit over 7 MHz and 5 fF respectively. Through this approach, we managed to optimize the matching conditions while operating the SET in its most sensitive configuration and achieved a single-shot charge readout fidelity of $99.51 \pm 0.09\%$ in only 8 μs . In the near future, the goal is to simplify the use of such readout techniques by performing numerical generation and demodulation of the RF signal by a single instrument.

Then, we moved to the actual operation of a linear triple quantum dot array where we focused on initialization and readout of metastable charge states. By operating the quantum dot array isolated from the electron reservoirs, we increased the tunability of its parameters and achieved a sub-Hz to GHz control over the interdot tunnel rate. This high level of control over the tunnel coupling and the chemical potential of each quantum dot of the array allowed us to initialize arbitrary metastable charge states of up to three electrons in a double quantum dot. The freeze map protocol developed allowed us to enhance the lifetime of metastable charge states and perform readout at a fixed and optimized position in the voltage gate space. Finally, we engineered and experimentally implemented an array segmentation protocol by decoupling a quantum dot filled with one electron while performing charge displacement and readout in the rest of the array. This protocol aimed at the reduction of the system complexity by reducing the number of charge states available for the system.

More than that, this protocol is the first step in the demonstration of possible large scale readout in 2D quantum dot arrays. As seen through this thesis, the presence of electron reservoir or SETs

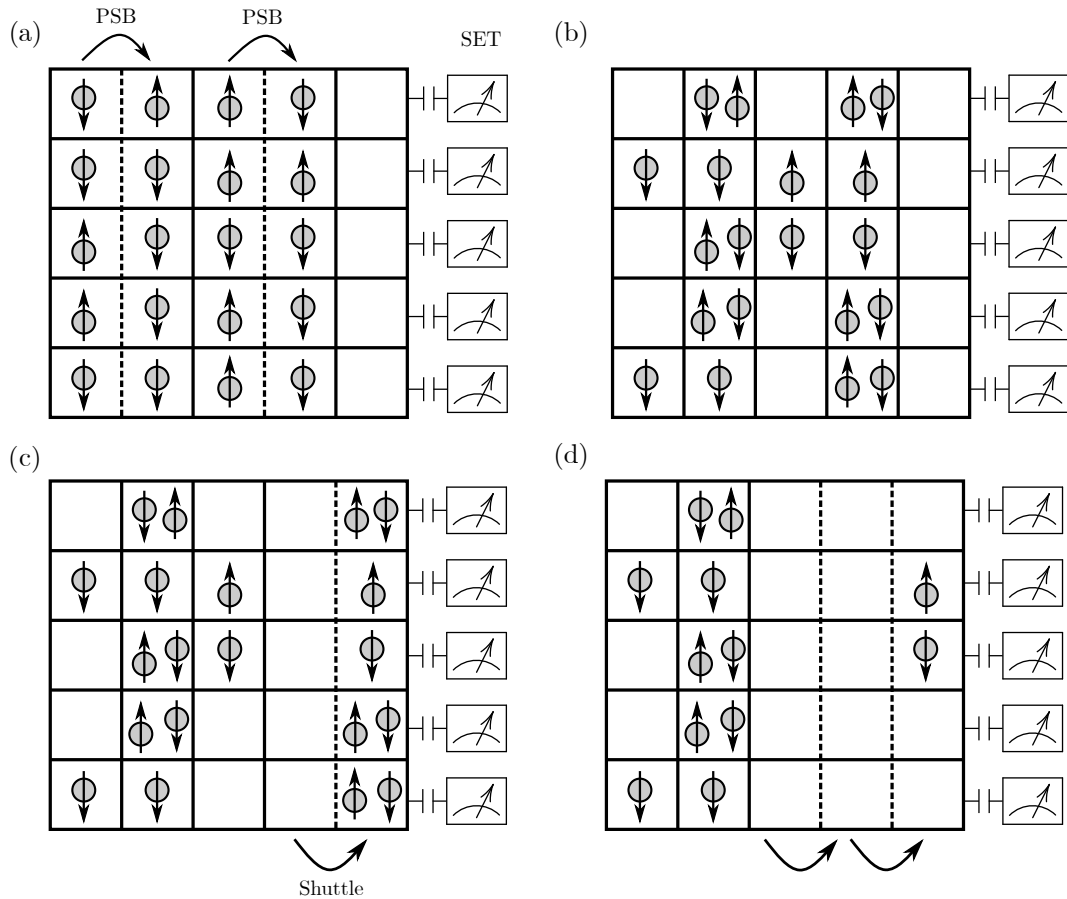


Figure 4.15: Segmentation and shuttling protocol for spin readout in dense spin qubit array structures. The schematic represent a scalable 5×5 QD array with rows and column addressing of the interdot tunnel couplings. The quantum dot column located on the right-hand side of the array is composed of loading/readout quantum dots. They are therefore connected to electron reservoirs to allow array filling and they are capacitively coupled to SETs to allow remote charge sensing. In this schematic a dotted and solid line indicate an interdot tunnel coupling in the GHz and sub-Hz regime respectively. We assume that the array has been previously loaded with one electron in each dot and that readout must be performed on the array. **a**, Spin to charge conversion using Pauli spin blockade projection on the right neighbor electron. **b**, Array segmentation step. All the interdot tunnel barriers of the system are set in the sub-Hz regime to prevent any electron displacement due to relaxation for instance. **c**, Sequential opening of the array columns to allow electron shuttling towards the right side of the array where the SETs are located. Once the electrons have reached the extremity of the array charge readout is performed and the dots are emptied. **d**, Readout sequence of the second column.

coupled to each quantum dot and the individual addressing of the quantum dot parameters such as the tunnel coupling with its four next neighbors or its chemical potential is not guaranteed in large scale structures allowing spin based quantum computing. It is therefore necessary to find protocols allowing to perform high fidelity initializations, manipulations and readout with limited control over the array. Here we will try to show how our segmentation protocol could be helpful to perform high fidelity spin readout in a $N \times N$ quantum dot array. As hardware limitations, we impose the position of the SETs and the reservoirs to be located only on the right-hand side of the array. We justify this choice by assuming that in such a structure the layout constraints will be less extreme on the side of the array allowing to implement the actual charge readout. In terms of quantum dot control, we assume a line and column addressing of the interdot tunnel barriers and of the chemical potential [Li2018], this gate layout has been experimentally tested with minor variations and seems to be promising [Chanrion2021, Borsoi2022]. We schematically represented such a structure in Figure 4.15 and detail the readout procedure:

- The array has been initialized with one electron in each quantum dot, an operation has been realized and now readout must be performed.
- The horizontal interdot tunnel barriers are set in the sub-Hz regime to prevent any charge displacement along the y -axis of the array as well as every two vertical barriers. The other vertical barriers are set in the GHz regime and the electrons are pushed to their neighbor quantum dot in order to perform a PSB projection (see Figure 4.15(a)).
- Once the projection is done (in a few nanoseconds), the charge configuration of the array is frozen by setting all the interdot tunnel barriers in the sub-Hz regime at the nanosecond timescale, see Figure 4.15(b). Doing so, all the charge dynamics due to relaxation for instance are blocked and the charge readout can be delayed from the spin to charge conversion.
- The next step consists in shuttling whole columns of charges towards the right-hand side where the readout quantum dots are located. To do so we sequentially open the interdot tunnel barrier and transfer the charges to the right column as shown in Figure 4.15(c). Once the electrons located in the readout quantum dots, the signal of the SET is acquired during enough time to allow high fidelity charge discrimination and finally the quantum dots are emptied to leave place to the next column of electrons.
- As shown in Figure 4.15(d) the shuttling sequence is repeated until the whole array has been emptied.

In the end, this protocol would allow high fidelity spin readout in a dense structure with limited hardware.

We focused in the last part of this thesis on the spin state readout of the electrons stored in the array by developing a technique based on a Pauli spin blockade readout called frozen Pauli spin blockade. In this particular experiment, we benefited from the control over the detuning and interdot tunnel coupling to separate in the voltage gate space the spin-to-charge conversion

($t_c/h \sim \text{GHz}$) from the charge readout position ($t_c/h \sim \text{Hz}$). Doing so, it allowed us to spend the desired amount of time at the charge readout position to achieve high fidelity discrimination between the charge states without worrying about spin state relaxation altering the overall spin state readout fidelity. We achieved through this original readout protocol, a singlet and triplet spin state readout fidelity of 98.43 % limited only by the calibration of the PSB position. More than achieving a high fidelity readout, this new protocol allowed us to perform repeated measurements and manipulation on the two same electrons. Building on this new capability, we wanted to show how to maximize the number of spins read in one measurement shot while limiting the quantum hardware overhead by demonstrating a complete two-electron spin state readout allowing to discriminate the four two-electron spin states S , T_0 , T_+ , and T_- . We achieved this result by interleaving a parity readout based on a relaxation hotspot of T_0 to S spin state and an adiabatic transformation of T_+ to S spin state. We confronted the complete readout procedure to various initializations to assess its validity and extracted a parity readout fidelity of 93.3 % and a ST_+ transformation rate of 79 % and finally identified the DC charge readout and the ST_+ adiabatic transformation as the limiting operation for the duration and fidelity respectively. Thus, we are now looking forward to implementing RF-based readout in the sample using the techniques developed in [chapter 2](#). On top of that, we are considering experimental solutions to initialize a known population of T_- spin state in order to confirm the complete readout procedure. One way to go would be to add a micromagnet providing a magnetic field gradient, displacing an electron in the gradient produces a synthetic oscillating magnetic field perpendicular to the static applied one. This technique referred to as electric dipole spin resonance (EDSR) is today widely used to perform efficient single spin rotations [[Yoneda2018](#)] and could be used in our case to initialize a T_- state.

The poor coherence times achieved in the GaAs/AlGaAs ($T_2^* \sim 10\text{ns}$) platform due to hyperfine interaction is pushing the spin qubit community towards host materials that can be purified from nuclear spins such as Si or Ge. What we want to emphasize through the many protocols developed in this work besides the obvious complexity reduction obtained in the readout procedure, is its versatility and its ability to be implemented in various spin qubit platforms with little adjustments. Indeed, high controllability over the interdot tunnel barrier has been recently achieved in Si-MOS devices [[Eenink2019](#)] and should in theory allow the implementation of the freeze map and frozen PSB protocols. Moreover, several works have reported the possibility to perform parity readout in Si-MOS [[Seedhouse2021](#), [Niegemann2022](#)] and Si/Ge devices [[Philips2022](#)] based on similar relaxation hotspots of T_0 to S . Adding to that the possibility to perform adiabatic transfers of S to T_+ [[Fogarty2018](#)], we can conclude that most of the techniques and knowledge developed in this thesis to perform a complete readout protocol should be easily transferable to most of the platforms. However, we expect the operation time to transform the triplet spin states to the singlet one via relaxation hotspot and adiabatic transfers to be slower in silicon devices than in the GaAs/AlGaAs platform.

Bibliography

- [Apostolidis2020] P. Apostolidis, B. J. Villis, J. F. Chittock-Wood, A. Baumgartner, V. Vestertinen, S. Simbierowicz, J. Hassel et M. R. Buitelaar. *Quantum Paraelectric Varactors for Radio-Frequency Measurements at mK Temperatures*, July 2020.
- [Ares2016] N. Ares, F. J. Schupp, A. Mavalankar, G. Rogers, J. Griffiths, G. A. C. Jones, I. Farrer, D. A. Ritchie, C. G. Smith, A. Cottet, G. A. D. Briggs et E. A. Laird. *Sensitive Radio-Frequency Measurements of a Quantum Dot by Tuning to Perfect Impedance Matching*. *Physical Review Applied*, vol. 5, no. 3, page 034011, March 2016.
- [Arute2019] Frank Arute, Kunal Arya, Ryan Babbush, Dave Bacon, Joseph C. Bardin, Rami Barends, Rupak Biswas, Sergio Boixo, Fernando G. S. L. Brandao, David A. Buell, Brian Burkett, Yu Chen, Zijun Chen, Ben Chiaro, Roberto Collins, William Courtney, Andrew Dunsworth, Edward Farhi, Brooks Foxen, Austin Fowler, Craig Gidney, Marissa Giustina, Rob Graff, Keith Guerin, Steve Habegger, Matthew P. Harrigan, Michael J. Hartmann, Alan Ho, Markus Hoffmann, Trent Huang, Travis S. Humble, Sergei V. Isakov, Evan Jeffrey, Zhang Jiang, Dvir Kafri, Kostyantyn Kechedzhi, Julian Kelly, Paul V. Klimov, Sergey Knysh, Alexander Korotkov, Fedor Kostritsa, David Landhuis, Mike Lindmark, Erik Lucero, Dmitry Lyakh, Salvatore Mandrà, Jarrod R. McClean, Matthew McEwen, Anthony Megrant, Xiao Mi, Kristel Michielsen, Masoud Mohseni, Josh Mutus, Ofer Naaman, Matthew Neeley, Charles Neill, Murphy Yuezhen Niu, Eric Ostby, Andre Petukhov, John C. Platt, Chris Quintana, Eleanor G. Rieffel, Pedram Roushan, Nicholas C. Rubin, Daniel Sank, Kevin J. Satzinger, Vadim Smelyanskiy, Kevin J. Sung, Matthew D. Trevithick, Amit Vainsencher, Benjamin Villalonga, Theodore White, Z. Jamie Yao, Ping Yeh, Adam Zalcman, Hartmut Neven et John M. Martinis. *Quantum Supremacy Using a Programmable Superconducting Processor*. *Nature*, vol. 574, no. 7779, pages 505–510, October 2019.

- [Aspect1982] Alain Aspect, Jean Dalibard et Gérard Roger. *Experimental Test of Bell's Inequalities Using Time-Varying Analyzers*. Physical Review Letters, vol. 49, no. 25, pages 1804–1807, December 1982.
- [Averin1986] D. V. Averin et K. K. Likharev. *Coulomb Blockade of Single-Electron Tunneling, and Coherent Oscillations in Small Tunnel Junctions*. Journal of Low Temperature Physics, vol. 62, no. 3, pages 345–373, February 1986.
- [Averin1991] D. V. Averin, A. N. Korotkov et K. K. Likharev. *Theory of Single-Electron Charging of Quantum Wells and Dots*. Physical Review B, vol. 44, no. 12, pages 6199–6211, September 1991.
- [Baart2016] Timothy Alexander Baart, Mohammad Shafiei, Takafumi Fujita, Christian Reichl, Werner Wegscheider et Lieven Mark Koenraad Vandersypen. *Single-Spin CCD*. Nature Nanotechnology, vol. 11, no. 4, pages 330–334, April 2016.
- [Barends2014] R. Barends, J. Kelly, A. Megrant, A. Veitia, D. Sank, E. Jeffrey, T. C. White, J. Mutus, A. G. Fowler, B. Campbell, Y. Chen, Z. Chen, B. Chiaro, A. Dunsworth, C. Neill, P. O'Malley, P. Roushan, A. Vainsencher, J. Wenner, A. N. Korotkov, A. N. Cleland et John M. Martinis. *Superconducting Quantum Circuits at the Surface Code Threshold for Fault Tolerance*. Nature, vol. 508, no. 7497, pages 500–503, April 2014.
- [Barthel2009] C. Barthel, D. J. Reilly, C. M. Marcus, M. P. Hanson et A. C. Gossard. *Rapid Single-Shot Measurement of a Singlet-Triplet Qubit*. Physical Review Letters, vol. 103, no. 16, page 160503, October 2009.
- [Barthel2012] C. Barthel, J. Medford, H. Bluhm, A. Yacoby, C. M. Marcus, M. P. Hanson et A. C. Gossard. *Relaxation and Readout Visibility of a Singlet-Triplet Qubit in an Overhauser Field Gradient*. Physical Review B, vol. 85, no. 3, page 035306, January 2012.
- [Baumgartner1997] P. Baumgartner, W. Wegscheider, M. Bichler, G. Schedelbeck, R. Neumann et G. Abstreiter. *Single-Electron Transistor Fabricated by Focused Laser Beam-Induced Doping of a GaAs/AlGaAs Heterostructure*. Applied Physics Letters, vol. 70, no. 16, pages 2135–2137, April 1997.
- [Bayer2017] Johannes C. Bayer, Timo Wagner, Eddy P. Rugeramigabo et Rolf J. Haug. *Charge Reconfiguration in Arrays of Quantum Dots*. Physical Review B, vol. 96, no. 23, page 235305, December 2017.
- [Bednarek2008] S. Bednarek, K. Lis et B. Szafran. *Quantum Dot Defined in a Two-Dimensional Electron Gas at a n-AlGaAs/GaAs Heterojunction: Simula-*

-
- tion of Electrostatic Potential and Charging Properties*. Physical Review B, vol. 77, no. 11, page 115320, March 2008.
- [Beenakker1991] C. W. J. Beenakker. *Theory of Coulomb-blockade Oscillations in the Conductance of a Quantum Dot*. Physical Review B, vol. 44, no. 4, pages 1646–1656, July 1991.
- [Bertrand2015a] Benoit Bertrand. *Long-Range Transfer of Spin Information Using Individual Electrons*. These de doctorat, Université Grenoble Alpes (ComUE), March 2015.
- [Bertrand2015b] Benoit Bertrand, Hanno Flentje, Shintaro Takada, Michihisa Yamamoto, Seigo Tarucha, Arne Ludwig, Andreas D. Wieck, Christopher Bäuerle et Tristan Meunier. *Quantum Manipulation of Two-Electron Spin States in Isolated Double Quantum Dots*. Physical Review Letters, vol. 115, no. 9, page 096801, August 2015.
- [Betz2015] A. C. Betz, R. Wacquez, M. Vinet, X. Jehl, A. L. Saraiva, M. Sanquer, A. J. Ferguson et M. F. Gonzalez-Zalba. *Dispersively Detected Pauli Spin-Blockade in a Silicon Nanowire Field-Effect Transistor*. Nano Letters, vol. 15, no. 7, pages 4622–4627, July 2015.
- [Bluhm2010] Hendrik Bluhm, Sandra Foletti, Diana Mahalu, Vladimir Umansky et Amir Yacoby. *Enhancing the Coherence of a Spin Qubit by Operating It as a Feedback Loop That Controls Its Nuclear Spin Bath*. Physical Review Letters, vol. 105, no. 21, page 216803, November 2010.
- [Bluhm2011] Hendrik Bluhm, Sandra Foletti, Izhar Neder, Mark Rudner, Diana Mahalu, Vladimir Umansky et Amir Yacoby. *Dephasing Time of GaAs Electron-Spin Qubits Coupled to a Nuclear Bath Exceeding 200 Ms*. Nature Physics, vol. 7, no. 2, pages 109–113, February 2011.
- [Borsoi2022] Francesco Borsoi, Nico W. Hendrickx, Valentin John, Sayr Motz, Floor van Riggelen, Amir Sammak, Sander L. de Snoo, Giordano Scappucci et Menno Veldhorst. *Shared Control of a 16 Semiconductor Quantum Dot Crossbar Array*, September 2022.
- [Boter2021] Jelmer M. Boter, Juan P. Dehollain, Jeroen P. G. van Dijk, Yuanxing Xu, Toivo Hensgens, Richard Versluis, Henricus W. L. Naus, James S. Clarke, Menno Veldhorst, Fabio Sebastiano et Lieven M. K. Vandersypen. *The Spider-Web Array—a Sparse Spin Qubit Array*. arXiv:2110.00189 [cond-mat, physics:quant-ph], September 2021.
- [Bravyi1998] S. B. Bravyi et A. Yu Kitaev. *Quantum Codes on a Lattice with Boundary*, November 1998.
-

Bibliography

- [Breit1936] G. Breit et E. Wigner. *Capture of Slow Neutrons*. Physical Review, vol. 49, no. 7, pages 519–531, April 1936.
- [Brunner2011] R. Brunner, Y.-S. Shin, T. Obata, M. Pioro-Ladrière, T. Kubo, K. Yoshida, T. Taniyama, Y. Tokura et S. Tarucha. *Two-Qubit Gate of Combined Single-Spin Rotation and Interdot Spin Exchange in a Double Quantum Dot*. Physical Review Letters, vol. 107, no. 14, page 146801, September 2011.
- [Burkard2021] Guido Burkard, Thaddeus D. Ladd, John M. Nichol, Andrew Pan et Jason R. Petta. *Semiconductor Spin Qubits*, December 2021.
- [Camenzind2018] Leon C. Camenzind, Liuqi Yu, Peter Stano, Jeramy D. Zimmerman, Arthur C. Gossard, Daniel Loss et Dominik M. Zumbühl. *Hyperfine-Phonon Spin Relaxation in a Single-Electron GaAs Quantum Dot*. Nature Communications, vol. 9, no. 1, page 3454, December 2018.
- [Chanrion2021] Emmanuel Chanrion. *Charge Control in Semiconductor Quantum-Dot Arrays and Prospects for Large-Scale Integration*. These de doctorat, Université Grenoble Alpes, February 2021.
- [Cirac1995] J. I. Cirac et P. Zoller. *Quantum Computations with Cold Trapped Ions*. Physical Review Letters, vol. 74, no. 20, pages 4091–4094, May 1995.
- [Connors2020] Elliot J. Connors, Jj Nelson et John M. Nichol. *Rapid High-Fidelity Spin-State Readout in Si / Si - Ge Quantum Dots via Rf Reflectometry*. Physical Review Applied, vol. 13, no. 2, page 024019, February 2020.
- [Crespi2011] Andrea Crespi, Roberta Ramponi, Roberto Osellame, Linda Sansoni, Irene Bongioanni, Fabio Sciarrino, Giuseppe Vallone et Paolo Mataloni. *Integrated Photonic Quantum Gates for Polarization Qubits*. Nature Communications, vol. 2, no. 1, page 566, November 2011.
- [Crook2003] Rolf Crook, Abi C Graham, Charles G Smith, Ian Farrer, Harvey E Beere et David A Ritchie. *Erasable Electrostatic Lithography for Quantum Components*. vol. 424, page 4, 2003.
- [Das1965] P. Das, R. Bruyn de Ouboter et K. W. Taconis. *A Realization of a London-Clarke-Mendoza Type Refrigerator*. In J. G. Daunt, D. O. Edwards, F. J. Milford et M. Yaqub, editeurs, Low Temperature Physics LT9, pages 1253–1255, Boston, MA, 1965. Springer US.
- [Dekker1999] Cees Dekker. *Carbon Nanotubes as Molecular Quantum Wires*. Physics Today, vol. 52, no. 5, pages 22–28, May 1999.

-
- [Deutsch1985] David Deutsch et Roger Penrose. *Quantum Theory, the Church–Turing Principle and the Universal Quantum Computer*. Proceedings of the Royal Society of London. A. Mathematical and Physical Sciences, vol. 400, no. 1818, pages 97–117, July 1985.
- [Dial2013] O. E. Dial, M. D. Shulman, S. P. Harvey, H. Bluhm, V. Umansky et A. Yacoby. *Charge Noise Spectroscopy Using Coherent Exchange Oscillations in a Singlet-Triplet Qubit*. Physical Review Letters, vol. 110, no. 14, page 146804, April 2013.
- [DiVincenzo2000] David P. DiVincenzo. *The Physical Implementation of Quantum Computation*. Fortschritte der Physik, vol. 48, no. 9-11, pages 771–783, 2000.
- [Eenink2019] H. G. J. Eenink, L. Petit, W. I. L. Lawrie, J. S. Clarke, L. M. K. Vandersypen et M. Veldhorst. *Tunable Coupling and Isolation of Single Electrons in Silicon Metal-Oxide-Semiconductor Quantum Dots*. Nano Letters, vol. 19, no. 12, pages 8653–8657, December 2019.
- [Elzerman2004] J. M. Elzerman, R. Hanson, L. H. Willems van Beveren, B. Witkamp, L. M. K. Vandersypen et L. P. Kouwenhoven. *Single-Shot Read-out of an Individual Electron Spin in a Quantum Dot*. Nature, vol. 430, no. 6998, pages 431–435, July 2004.
- [Eng2015] Kevin Eng, Thaddeus D. Ladd, Aaron Smith, Matthew G. Borselli, Andrey A. Kiselev, Bryan H. Fong, Kevin S. Holabird, Thomas M. Hazard, Biqin Huang, Peter W. Deelman, Ivan Milosavljevic, Adele E. Schmitz, Richard S. Ross, Mark F. Gyure et Andrew T. Hunter. *Isotopically Enhanced Triple-Quantum-Dot Qubit*. Science Advances, vol. 1, no. 4, page e1500214, May 2015.
- [Feynman1982] Richard P. Feynman. *Simulating Physics with Computers*. International Journal of Theoretical Physics, vol. 21, no. 6, pages 467–488, June 1982.
- [Fogarty2018] M. A. Fogarty, K. W. Chan, B. Hensen, W. Huang, T. Tanttu, C. H. Yang, A. Laucht, M. Veldhorst, F. E. Hudson, K. M. Itoh, D. Culcer, T. D. Ladd, A. Morello et A. S. Dzurak. *Integrated Silicon Qubit Platform with Single-Spin Addressability, Exchange Control and Single-Shot Singlet-Triplet Readout*. Nature Communications, vol. 9, no. 1, page 4370, December 2018.
- [Fowler2012] Austin G. Fowler, Matteo Mariantoni, John M. Martinis et Andrew N. Cleland. *Surface Codes: Towards Practical Large-Scale Quantum Computation*. Physical Review A, vol. 86, no. 3, page 032324, September 2012.
-

Bibliography

- [Fuhrer2001] A Fuhrer, W Wegscheider et M Bichler. *Energy Spectra of Quantum Rings*. vol. 413, page 4, 2001.
- [Fujisawa1998] Toshimasa Fujisawa, Tjerk H. Oosterkamp, Wilfred G. van der Wiel, Benno W. Broer, Ramón Aguado, Seigo Tarucha et Leo P. Kouwenhoven. *Spontaneous Emission Spectrum in Double Quantum Dot Devices*. *Science*, vol. 282, no. 5390, pages 932–935, October 1998.
- [Georgescu2014] I. M. Georgescu, S. Ashhab et Franco Nori. *Quantum Simulation*. *Reviews of Modern Physics*, vol. 86, no. 1, pages 153–185, March 2014.
- [Gorman2005] J. Gorman, D. G. Hasko et D. A. Williams. *Charge-Qubit Operation of an Isolated Double Quantum Dot*. *Physical Review Letters*, vol. 95, no. 9, page 090502, August 2005.
- [Gubin2005] A. I. Gubin, K. S. Il'in, S. A. Vitusevich, M. Siegel et N. Klein. *Dependence of Magnetic Penetration Depth on the Thickness of Superconducting Nb Thin Films*. *Physical Review B*, vol. 72, no. 6, page 064503, August 2005.
- [Hahn1950] E. L. Hahn. *Spin Echoes*. *Physical Review*, vol. 80, no. 4, pages 580–594, November 1950.
- [Hanson2005] R. Hanson, L. H. Willems van Beveren, I. T. Vink, J. M. Elzerman, W. J. M. Naber, F. H. L. Koppens, L. P. Kouwenhoven et L. M. K. Vandersypen. *Single-Shot Readout of Electron Spin States in a Quantum Dot Using Spin-Dependent Tunnel Rates*. *Physical Review Letters*, vol. 94, no. 19, page 196802, May 2005.
- [Hanson2007] R. Hanson, L. P. Kouwenhoven, J. R. Petta, S. Tarucha et L. M. K. Vandersypen. *Spins in Few-Electron Quantum Dots*. *Reviews of Modern Physics*, vol. 79, no. 4, pages 1217–1265, October 2007.
- [Harvey-Collard2018] Patrick Harvey-Collard, Benjamin D'Anjou, Martin Rudolph, N. Tobias Jacobson, Jason Dominguez, Gregory A. Ten Eyck, Joel R. Wendt, Tammy Pluym, Michael P. Lilly, William A. Coish, Michel Pioro-Ladrière et Malcolm S. Carroll. *High-Fidelity Single-Shot Readout for a Spin Qubit via an Enhanced Latching Mechanism*. *Physical Review X*, vol. 8, no. 2, page 021046, May 2018.
- [Hornibrook2014] J. M. Hornibrook, J. I. Colless, A. C. Mahoney, X. G. Croot, S. Blanvillain, H. Lu, A. C. Gossard et D. J. Reilly. *Frequency Multiplexing for Readout of Spin Qubits*. *Applied Physics Letters*, vol. 104, no. 10, page 103108, March 2014.

- [Hu2000] Xuedong Hu et S. Das Sarma. *Hilbert-Space Structure of a Solid-State Quantum Computer: Two-electron States of a Double-Quantum-Dot Artificial Molecule*. Physical Review A, vol. 61, no. 6, page 062301, May 2000.
- [Hu2001] Xuedong Hu et S. Das Sarma. *Spin-Based Quantum Computation in Multielectron Quantum Dots*. Physical Review A, vol. 64, no. 4, page 042312, September 2001.
- [Hung2013] Jo-Tzu Hung, Łukasz Cywiński, Xuedong Hu et S. Das Sarma. *Hyperfine Interaction Induced Dephasing of Coupled Spin Qubits in Semiconductor Double Quantum Dots*. Physical Review B, vol. 88, no. 8, page 085314, August 2013.
- [Jadot2021] Baptiste Jadot, Pierre-André Mortemousque, Emmanuel Chanrion, Vivien Thiney, Arne Ludwig, Andreas D. Wieck, Matias Urdampilleta, Christopher Bäuerle et Tristan Meunier. *Distant Spin Entanglement via Fast and Coherent Electron Shuttling*. Nature Nanotechnology, vol. 16, no. 5, pages 570–575, May 2021.
- [Jelezko2004] F. Jelezko, T. Gaebel, I. Popa, M. Domhan, A. Gruber et J. Wrachtrup. *Observation of Coherent Oscillation of a Single Nuclear Spin and Realization of a Two-Qubit Conditional Quantum Gate*. Physical Review Letters, vol. 93, no. 13, page 130501, September 2004.
- [Johnson2005] A. C. Johnson, J. R. Petta, C. M. Marcus, M. P. Hanson et A. C. Gosard. *Singlet-Triplet Spin Blockade and Charge Sensing in a Few-Electron Double Quantum Dot*. Physical Review B, vol. 72, no. 16, page 165308, October 2005.
- [Jones2011] Jonathan A. Jones. *Quantum Computing with NMR*. Progress in Nuclear Magnetic Resonance Spectroscopy, vol. 59, no. 2, pages 91–120, August 2011.
- [Keith2019] D. Keith, S. K. Gorman, L. Kranz, Y. He, J. G. Keizer, M. A. Broome et M. Y. Simmons. *Benchmarking High Fidelity Single-Shot Readout of Semiconductor Qubits*. New Journal of Physics, vol. 21, no. 6, page 063011, June 2019.
- [Kennard1927] E. H. Kennard. *Zur Quantenmechanik einfacher Bewegungstypen*. Zeitschrift für Physik, vol. 44, no. 4, pages 326–352, April 1927.
- [Khaetskii2002] Alexander V. Khaetskii, Daniel Loss et Leonid Glazman. *Electron Spin Decoherence in Quantum Dots Due to Interaction with Nuclei*. Physical Review Letters, vol. 88, no. 18, page 186802, April 2002.

- [Kiyama2018] Haruki Kiyama, Alexander Korsch, Naomi Nagai, Yasushi Kanai, Kazuhiko Matsumoto, Kazuhiko Hirakawa et Akira Oiwa. *Single-Electron Charge Sensing in Self-Assembled Quantum Dots*. Scientific Reports, vol. 8, no. 1, page 13188, September 2018.
- [Klein1996] David L. Klein, Paul L. McEuen, Janet E. Bowen Katari, Richard Roth et A. Paul Alivisatos. *An Approach to Electrical Studies of Single Nanocrystals*. Applied Physics Letters, vol. 68, no. 18, pages 2574–2576, April 1996.
- [Koppens2005] F. H. L. Koppens, J. A. Folk, J. M. Elzerman, R. Hanson, L. H. Willems van Beveren, I. T. Vink, H. P. Tranitz, W. Wegscheider, L. P. Kouwenhoven et L. M. K. Vandersypen. *Control and Detection of Singlet-Triplet Mixing in a Random Nuclear Field*. Science, vol. 309, no. 5739, pages 1346–1350, August 2005.
- [Koppens2006] F. H. L. Koppens, C. Buizert, K. J. Tielrooij, I. T. Vink, K. C. Nowack, T. Meunier, L. P. Kouwenhoven et L. M. K. Vandersypen. *Driven Coherent Oscillations of a Single Electron Spin in a Quantum Dot*. Nature, vol. 442, no. 7104, pages 766–771, August 2006.
- [Kouwenhoven1997] Leo P. Kouwenhoven, Charles M. Marcus, Paul L. McEuen, Seigo Tarucha, Robert M. Westervelt et Ned S. Wingreen. *Electron Transport in Quantum Dots*. In Lydia L. Sohn, Leo P. Kouwenhoven et Gerd Schön, editeurs, Mesoscopic Electron Transport, pages 105–214. Springer Netherlands, Dordrecht, 1997.
- [Kouwenhoven2001] L. P. Kouwenhoven, D. G. Austing et S. Tarucha. *Few-Electron Quantum Dots*. Reports on Progress in Physics, vol. 64, no. 6, pages 701–736, May 2001.
- [Krunner2019] S. Krinner, S. Storz, P. Kurpiers, P. Magnard, J. Heinsoo, R. Keller, J. Lütolf, C. Eichler et A. Wallraff. *Engineering Cryogenic Setups for 100-Qubit Scale Superconducting Circuit Systems*. EPJ Quantum Technology, vol. 6, no. 1, pages 1–29, December 2019.
- [Kristensen2000] A. Kristensen, H. Bruus, A. E. Hansen, J. B. Jensen, P. E. Lindelof, C. J. Marckmann, J. Nygård, C. B. Sørensen, F. Beuscher, A. Forchel et M. Michel. *Bias and Temperature Dependence of the 0.7 Conductance Anomaly in Quantum Point Contacts*. Physical Review B, vol. 62, no. 16, pages 10950–10957, October 2000.

-
- [Ladd2010] T. D. Ladd, F. Jelezko, R. Laflamme, Y. Nakamura, C. Monroe et J. L. O'Brien. *Quantum Computers*. Nature, vol. 464, no. 7285, pages 45–53, March 2010.
- [Laird2006] E. A. Laird, J. R. Petta, A. C. Johnson, C. M. Marcus, A. Yacoby, M. P. Hanson et A. C. Gossard. *Effect of Exchange Interaction on Spin Dephasing in a Double Quantum Dot*. Physical Review Letters, vol. 97, no. 5, page 056801, July 2006.
- [Landau1965] L. D. Landau. *A THEORY OF ENERGY TRANSFER ON COLLISIONS*. In Collected Papers of L.D. Landau, pages 52–59. Elsevier, 1965.
- [Lawrie2020] W. I. L. Lawrie, N. W. Hendrickx, F. van Riggelen, M. Russ, L. Petit, A. Sammak, G. Scappucci et M. Veldhorst. *Spin Relaxation Benchmarks and Individual Qubit Addressability for Holes in Quantum Dots*. Nano Letters, vol. 20, no. 10, pages 7237–7242, October 2020.
- [Li2015] Hai-Ou Li, Gang Cao, Guo-Dong Yu, Ming Xiao, Guang-Can Guo, Hong-Wen Jiang et Guo-Ping Guo. *Conditional Rotation of Two Strongly Coupled Semiconductor Charge Qubits*. Nature Communications, vol. 6, no. 1, page 7681, July 2015.
- [Li2018] Ruoyu Li, Luca Petit, David P. Franke, Juan Pablo Dehollain, Jonas Helsen, Mark Steudtner, Nicole K. Thomas, Zachary R. Yoscovits, Kanwal J. Singh, Stephanie Wehner, Lieven M. K. Vandersypen, James S. Clarke et Menno Veldhorst. *A Crossbar Network for Silicon Quantum Dot Qubits*. Science Advances, vol. 4, no. 7, page eaar3960, July 2018.
- [Lloyd1996] Seth Lloyd. *Universal Quantum Simulators*. Science, vol. 273, no. 5278, pages 1073–1078, August 1996.
- [Loss1998] Daniel Loss et David P. DiVincenzo. *Quantum Computation with Quantum Dots*. Physical Review A, vol. 57, no. 1, pages 120–126, January 1998.
- [Mađzik2022] Mateusz T. Mađzik, Serwan Asaad, Akram Youssry, Benjamin Joecker, Kenneth M. Rudinger, Erik Nielsen, Kevin C. Young, Timothy J. Proctor, Andrew D. Baczewski, Arne Laucht, Vivien Schmitt, Fay E. Hudson, Kohei M. Itoh, Alexander M. Jakob, Brett C. Johnson, David N. Jamieson, Andrew S. Dzurak, Christopher Ferrie, Robin Blume-Kohout et Andrea Morello. *Precision Tomography of a Three-Qubit Donor Quantum Processor in Silicon*. Nature, vol. 601, no. 7893, pages 348–353, January 2022.

- [Malinowski2017] Filip K. Malinowski, Frederico Martins, Peter D. Nissen, Edwin Barnes, Łukasz Cywiński, Mark S. Rudner, Saeed Fallahi, Geoffrey C. Gardner, Michael J. Manfra, Charles M. Marcus et Ferdinand Kuemmeth. *Notch Filtering the Nuclear Environment of a Spin Qubit*. *Nature Nanotechnology*, vol. 12, no. 1, pages 16–20, January 2017.
- [Manfra2014] Michael J. Manfra. *Molecular Beam Epitaxy of Ultra-High-Quality AlGaAs/GaAs Heterostructures: Enabling Physics in Low-Dimensional Electronic Systems*. *Annual Review of Condensed Matter Physics*, vol. 5, no. 1, pages 347–373, 2014.
- [Martins2016] Frederico Martins, Filip K. Malinowski, Peter D. Nissen, Edwin Barnes, Saeed Fallahi, Geoffrey C. Gardner, Michael J. Manfra, Charles M. Marcus et Ferdinand Kuemmeth. *Noise Suppression Using Symmetric Exchange Gates in Spin Qubits*. *Physical Review Letters*, vol. 116, no. 11, page 116801, March 2016.
- [Meirav1990] U. Meirav, M. A. Kastner et S. J. Wind. *Single-Electron Charging and Periodic Conductance Resonances in GaAs Nanostructures*. *Physical Review Letters*, vol. 65, no. 6, pages 771–774, August 1990.
- [Merkulov2002] I. A. Merkulov, Al L. Efros et M. Rosen. *Electron Spin Relaxation by Nuclei in Semiconductor Quantum Dots*. *Physical Review B*, vol. 65, no. 20, page 205309, April 2002.
- [Meunier2006] T. Meunier, K.-J. Tielrooij, I. T. Vink, F. H. L. Koppens, H. P. Tranitz, W. Wegscheider, L. P. Kouwenhoven et L. M. K. Vandersypen. *High Fidelity Measurement of Singlet–Triplet State in a Quantum Dot*. *physica status solidi (b)*, vol. 243, no. 15, pages 3855–3858, 2006.
- [Meunier2007] T. Meunier, I. T. Vink, L. H. Willems van Beveren, K.-J. Tielrooij, R. Hanson, F. H. L. Koppens, H. P. Tranitz, W. Wegscheider, L. P. Kouwenhoven et L. M. K. Vandersypen. *Experimental Signature of Phonon-Mediated Spin Relaxation*. *Physical Review Letters*, vol. 98, no. 12, page 126601, March 2007.
- [Mills2019a] A. R. Mills, M. M. Feldman, C. Monical, P. J. Lewis, K. W. Larson, A. M. Mounce et J. R. Petta. *Computer-Automated Tuning Procedures for Semiconductor Quantum Dot Arrays*. *Applied Physics Letters*, vol. 115, no. 11, page 113501, September 2019.
- [Mills2019b] A. R. Mills, D. M. Zajac, M. J. Gullans, F. J. Schupp, T. M. Hazard et J. R. Petta. *Shuttling a Single Charge across a One-Dimensional Array of*

-
- Silicon Quantum Dots*. Nature Communications, vol. 10, no. 1, page 1063, December 2019.
- [Mills2022] A. R. Mills, C. R. Guinn, M. M. Feldman, A. J. Sigillito, M. J. Gullans, M. Rakher, J. Kerckhoff, C. A. C. Jackson et J. R. Petta. *High Fidelity State Preparation, Quantum Control, and Readout of an Isotopically Enriched Silicon Spin Qubit*, April 2022.
- [Mortemousque2021a] Pierre-André Mortemousque, Emmanuel Chanrion, Baptiste Jadot, Hanno Flentje, Arne Ludwig, Andreas D. Wieck, Matias Urdampilleta, Christopher Bäuerle et Tristan Meunier. *Coherent Control of Individual Electron Spins in a Two-Dimensional Quantum Dot Array*. Nature Nanotechnology, vol. 16, no. 3, pages 296–301, March 2021.
- [Mortemousque2021b] Pierre-André Mortemousque, Baptiste Jadot, Emmanuel Chanrion, Vivien Thiney, Christopher Bäuerle, Arne Ludwig, Andreas D. Wieck, Matias Urdampilleta et Tristan Meunier. *Enhanced Spin Coherence While Displacing Electron in a Two-Dimensional Array of Quantum Dots*. PRX Quantum, vol. 2, no. 3, page 030331, August 2021.
- [Nakajima2017] Takashi Nakajima, Matthieu R. Delbecq, Tomohiro Otsuka, Peter Stano, Shinichi Amaha, Jun Yoneda, Akito Noiri, Kento Kawasaki, Kenta Takeda, Giles Allison, Arne Ludwig, Andreas D. Wieck, Daniel Loss et Seigo Tarucha. *Robust Single-Shot Spin Measurement with 99.5% Fidelity in a Quantum Dot Array*. Physical Review Letters, vol. 119, no. 1, page 017701, July 2017.
- [Nakamura1999] Y. Nakamura, Yu A. Pashkin et J. S. Tsai. *Coherent Control of Macroscopic Quantum States in a Single-Cooper-pair Box*. Nature, vol. 398, no. 6730, pages 786–788, April 1999.
- [Nakata1994] S. Nakata, M. Tomizawa, M. Yamamoto, K. Ikuta et T. Mizutani. *Electrical Transport Properties and Confinement Potential Analysis of Buried AlGaAs/GaAs Quantum Wires*. Journal of Applied Physics, vol. 76, no. 4, pages 2330–2335, August 1994.
- [Nichol2015] John M. Nichol, Shannon P. Harvey, Michael D. Shulman, Arijeet Pal, Vladimir Umansky, Emmanuel I. Rashba, Bertrand I. Halperin et Amir Yacoby. *Quenching of Dynamic Nuclear Polarization by Spin–Orbit Coupling in GaAs Quantum Dots*. Nature Communications, vol. 6, no. 1, page 7682, November 2015.
- [Niegemann2022] David J. Niegemann, Victor El-Homsy, Baptiste Jadot, Martin Nurizzo, Bruna Cardoso-Paz, Emmanuel Chanrion, Matthieu Dartiailh, Bernhard
-

- Klemt, Vivien Thiney, Christopher Bäuerle, Pierre-André Mortemousque, Benoit Bertrand, Heimanu Niebojewski, Maud Vinet, Franck Balestro, Tristan Meunier et Matias Urdampilleta. *Parity and Singlet-Triplet High Fidelity Readout in a Silicon Double Quantum Dot at 0.5 K*, July 2022.
- [Noiri2022] Akito Noiri, Kenta Takeda, Takashi Nakajima, Takashi Kobayashi, Amir Sammak, Giordano Scappucci et Seigo Tarucha. *Fast Universal Quantum Gate above the Fault-Tolerance Threshold in Silicon*. *Nature*, vol. 601, no. 7893, pages 338–342, January 2022.
- [Nowack2007] K. C. Nowack, F. H. L. Koppens, Yu. V. Nazarov et L. M. K. Vandersypen. *Coherent Control of a Single Electron Spin with Electric Fields*. *Science*, vol. 318, no. 5855, pages 1430–1433, November 2007.
- [Nowack2011] K. C. Nowack, M. Shafiei, M. Laforest, G. E. D. K. Prawiroatmodjo, L. R. Schreiber, C. Reichl, W. Wegscheider et L. M. K. Vandersypen. *Single-Shot Correlations and Two-Qubit Gate of Solid-State Spins*. *Science*, vol. 333, no. 6047, pages 1269–1272, September 2011.
- [Ono2002] K. Ono. *Current Rectification by Pauli Exclusion in a Weakly Coupled Double Quantum Dot System*. *Science*, vol. 297, no. 5585, pages 1313–1317, August 2002.
- [Paget1977] D. Paget, G. Lampel, B. Sapoval et V. I. Safarov. *Low Field Electron-Nuclear Spin Coupling in Gallium Arsenide under Optical Pumping Conditions*. *Physical Review B*, vol. 15, no. 12, pages 5780–5796, June 1977.
- [Pakkiam2018] P. Pakkiam, A. V. Timofeev, M. G. House, M. R. Hogg, T. Kobayashi, M. Koch, S. Rogge et M. Y. Simmons. *Single-Shot Single-Gate Rf Spin Readout in Silicon*. *Physical Review X*, vol. 8, no. 4, page 041032, November 2018.
- [Park2002] Jiwoong Park, Abhay N. Pasupathy, Jonas I. Goldsmith, Connie Chang, Yuval Yaish, Jason R. Petta, Marie Rinkoski, James P. Sethna, Héctor D. Abruña, Paul L. McEuen et Daniel C. Ralph. *Coulomb Blockade and the Kondo Effect in Single-Atom Transistors*. *Nature*, vol. 417, no. 6890, pages 722–725, June 2002.
- [Peskin2018] Michael E. Peskin. *An Introduction To Quantum Field Theory*. CRC Press, Boca Raton, January 2018.
- [Petersson2010] K. D. Petersson, J. R. Petta, H. Lu et A. C. Gossard. *Quantum Coherence in a One-Electron Semiconductor Charge Qubit*. *Physical Review Letters*, vol. 105, no. 24, page 246804, December 2010.

-
- [Petta2004] J. R. Petta, A. C. Johnson, C. M. Marcus, M. P. Hanson et A. C. Gossard. *Manipulation of a Single Charge in a Double Quantum Dot*. Physical Review Letters, vol. 93, no. 18, page 186802, October 2004.
- [Petta2005a] J. R. Petta, A. C. Johnson, J. M. Taylor, E. A. Laird, A. Yacoby, M. D. Lukin, C. M. Marcus, M. P. Hanson et A. C. Gossard. *Coherent Manipulation of Coupled Electron Spins in Semiconductor Quantum Dots*. Science, vol. 309, no. 5744, pages 2180–2184, September 2005.
- [Petta2005b] J. R. Petta, A. C. Johnson, J. M. Taylor, E. A. Laird, A. Yacoby, M. D. Lukin, C. M. Marcus, M. P. Hanson et A. C. Gossard. *Coherent Manipulation of Coupled Electron Spins in Semiconductor Quantum Dots*. Science, vol. 309, no. 5744, pages 2180–2184, September 2005.
- [Petta2010] J. R. Petta, H. Lu et A. C. Gossard. *A Coherent Beam Splitter for Electronic Spin States*. Science, vol. 327, no. 5966, pages 669–672, February 2010.
- [Philips2022] Stephan G. J. Philips, Mateusz T. Maźzik, Sergey V. Amitonov, Sander L. de Snoo, Maximilian Russ, Nima Kalhor, Christian Volk, William I. L. Lawrie, Delphine Brousse, Larysa Tryputen, Brian Paquelet Wuetz, Amir Sammak, Menno Veldhorst, Giordano Scappucci et Lieven M. K. Vandersypen. *Universal Control of a Six-Qubit Quantum Processor in Silicon*. Nature, vol. 609, no. 7929, pages 919–924, September 2022.
- [Pla2013] Jarryd J. Pla, Kuan Y. Tan, Juan P. Dehollain, Wee H. Lim, John J. L. Morton, Floris A. Zwanenburg, David N. Jamieson, Andrew S. Dzurak et Andrea Morello. *High-Fidelity Readout and Control of a Nuclear Spin Qubit in Silicon*. Nature, vol. 496, no. 7445, pages 334–338, April 2013.
- [Preskill2021] John Preskill. *Quantum Computing 40 Years Later*, June 2021.
- [Qi2017] Zhenyi Qi, X. Wu, D. R. Ward, J. R. Prance, Dohun Kim, John King Gamble, R. T. Mohr, Zhan Shi, D. E. Savage, M. G. Lagally, M. A. Eriksson, Mark Friesen, S. N. Coppersmith et M. G. Vavilov. *Effects of Charge Noise on a Pulse-Gated Singlet-Triplet S - T - Qubit*. Physical Review B, vol. 96, no. 11, page 115305, September 2017.
- [Reed2016] M. D. Reed, B. M. Maune, R. W. Andrews, M. G. Borselli, K. Eng, M. P. Jura, A. A. Kiselev, T. D. Ladd, S. T. Merkel, I. Milosavljevic, E. J. Pritchett, M. T. Rakher, R. S. Ross, A. E. Schmitz, A. Smith, J. A. Wright, M. F. Gyure et A. T. Hunter. *Reduced Sensitivity to Charge Noise in Semiconductor Spin Qubits via Symmetric Operation*. Physical Review Letters, vol. 116, no. 11, page 110402, March 2016.

Bibliography

- [Reilly2007] D. J. Reilly, C. M. Marcus, M. P. Hanson et A. C. Gossard. *Fast Single-Charge Sensing with a Rf Quantum Point Contact*. Applied Physics Letters, vol. 91, no. 16, page 162101, October 2007.
- [Reilly2008] D. J. Reilly, J. M. Taylor, E. A. Laird, J. R. Petta, C. M. Marcus, M. P. Hanson et A. C. Gossard. *Measurement of Temporal Correlations of the Overhauser Field in a Double Quantum Dot*. Physical Review Letters, vol. 101, no. 23, page 236803, December 2008.
- [Rugar2004] D. Rugar, R. Budakian, H. J. Mamin et B. W. Chui. *Single Spin Detection by Magnetic Resonance Force Microscopy*. Nature, vol. 430, no. 6997, pages 329–332, July 2004.
- [Schaal2020] S. Schaal, I. Ahmed, J. A. Haigh, L. Hutin, B. Bertrand, S. Barraud, M. Vinet, C.-M. Lee, N. Stelmashenko, J. W. A. Robinson, J. Y. Qiu, S. Hacoen-Gourgy, I. Siddiqi, M. F. Gonzalez-Zalba et J. J. L. Morton. *Fast Gate-Based Readout of Silicon Quantum Dots Using Josephson Parametric Amplification*. Physical Review Letters, vol. 124, no. 6, page 067701, February 2020.
- [Schoelkopf1998] R. J. Schoelkopf. *The Radio-Frequency Single-Electron Transistor (RFSET): A Fast and Ultrasensitive Electrometer*. Science, vol. 280, no. 5367, pages 1238–1242, May 1998.
- [Schröer2007] D. Schröer, A. D. Greentree, L. Gaudreau, K. Eberl, L. C. L. Hollenberg, J. P. Kotthaus et S. Ludwig. *Electrostatically Defined Serial Triple Quantum Dot Charged with Few Electrons*. Physical Review B, vol. 76, no. 7, page 075306, August 2007.
- [Schulten1978] Klaus Schulten et Peter G. Wolynes. *Semiclassical Description of Electron Spin Motion in Radicals Including the Effect of Electron Hopping*. The Journal of Chemical Physics, vol. 68, no. 7, pages 3292–3297, April 1978.
- [Seedhouse2021] Amanda E. Seedhouse, Tuomo Tantt, Ross C.C. Leon, Ruichen Zhao, Kuan Yen Tan, Bas Hensen, Fay E. Hudson, Kohei M. Itoh, Jun Yoneda, Chih Hwan Yang, Andrea Morello, Arne Laucht, Susan N. Coppersmith, Andre Saraiva et Andrew S. Dzurak. *Pauli Blockade in Silicon Quantum Dots with Spin-Orbit Control*. PRX Quantum, vol. 2, no. 1, page 010303, January 2021.
- [Shen2007] K. Shen et M. W. Wu. *Triplet-Singlet Relaxation in Semiconductor Single and Double Quantum Dots*. Physical Review B, vol. 76, no. 23, page 235313, December 2007.

-
- [Shor1994] P.W. Shor. *Algorithms for Quantum Computation: Discrete Logarithms and Factoring*. In Proceedings 35th Annual Symposium on Foundations of Computer Science, pages 124–134, November 1994.
- [Shulman2014] M. D. Shulman, S. P. Harvey, J. M. Nichol, S. D. Bartlett, A. C. Doherty, V. Umansky et A. Yacoby. *Suppressing Qubit Dephasing Using Real-Time Hamiltonian Estimation*. Nature Communications, vol. 5, no. 1, page 5156, December 2014.
- [Song2015] Xiang-Xiang Song, Zhuo-Zhi Zhang, Jie You, Di Liu, Hai-Ou Li, Gang Cao, Ming Xiao et Guo-Ping Guo. *Temperature Dependence of Coulomb Oscillations in a Few-Layer Two-Dimensional WS₂ Quantum Dot*. Scientific Reports, vol. 5, no. 1, page 16113, November 2015.
- [Spence2022] Cameron Spence, Bruna Cardoso Paz, Bernhard Klemt, Emmanuel Charrion, David J. Niegemann, Baptiste Jadot, Vivien Thiney, Benoit Bertrand, Heimanu Niebojewski, Pierre-André Mortemousque, Xavier Jehl, Romain Maurand, Silvano De Franceschi, Maud Vinet, Franck Balestro, Christopher Bäuerle, Yann-Michel Niquet, Tristan Meunier et Matias Urdampilleta. *Spin-Valley Coupling Anisotropy and Noise in CMOS Quantum Dots*. Physical Review Applied, vol. 17, no. 3, page 034047, March 2022.
- [Stehlik2012] J. Stehlik, Y. Dovzhenko, J. R. Petta, J. R. Johansson, F. Nori, H. Lu et A. C. Gossard. *Landau-Zener-Stückelberg Interferometry of a Single Electron Charge Qubit*. Physical Review B, vol. 86, no. 12, page 121303, September 2012.
- [Stepanenko2012] Dimitrije Stepanenko, Mark Rudner, Bertrand I. Halperin et Daniel Loss. *Singlet-Triplet Splitting in Double Quantum Dots Due to Spin-Orbit and Hyperfine Interactions*. Physical Review B, vol. 85, no. 7, page 075416, February 2012.
- [Stopa1993] M. Stopa. *Coulomb Oscillation Amplitudes and Semiconductor Quantum-Dot Self-Consistent Level Structure*. Physical Review B, vol. 48, no. 24, pages 18340–18343, December 1993.
- [Tarucha2000] S. Tarucha, D. G. Austing, Y. Tokura, W. G. van der Wiel et L. P. Kouwenhoven. *Direct Coulomb and Exchange Interaction in Artificial Atoms*. Physical Review Letters, vol. 84, no. 11, pages 2485–2488, March 2000.
- [Taylor2007] J. M. Taylor, J. R. Petta, A. C. Johnson, A. Yacoby, C. M. Marcus et M. D. Lukin. *Relaxation, Dephasing, and Quantum Control of Electron Spins in Double Quantum Dots*. Physical Review B, vol. 76, no. 3, page 035315, July 2007.
-

- [Thalinea2014] Romain Thalinea, Sascha René Valentin, Andreas D. Wieck, Christopher Bäuerle et Tristan Meunier. *Interplay between Exchange Interaction and Magnetic Field Gradient in a Double Quantum Dot with Two Individual Electron Spin Qubits*. Physical Review B, vol. 90, no. 7, page 075436, August 2014.
- [Tyryshkin2012] Alexei M. Tyryshkin, Shinichi Tojo, John J. L. Morton, Helge Riemann, Nikolai V. Abrosimov, Peter Becker, Hans-Joachim Pohl, Thomas Schenkel, Michael L. W. Thewalt, Kohei M. Itoh et S. A. Lyon. *Electron Spin Coherence Exceeding Seconds in High-Purity Silicon*. Nature Materials, vol. 11, no. 2, pages 143–147, February 2012.
- [Urdampilleta2011] M. Urdampilleta, S. Klyatskaya, J-P. Cleuziou, M. Ruben et W. Wernsdorfer. *Supramolecular Spin Valves*. Nature Materials, vol. 10, no. 7, pages 502–506, July 2011.
- [Urdampilleta2019] Matias Urdampilleta, David J. Niegemann, Emmanuel Chanrion, Baptiste Jadot, Cameron Spence, Pierre-André Mortemousque, Christopher Bäuerle, Louis Hutin, Benoit Bertrand, Sylvain Barraud, Romain Maurand, Marc Sanquer, Xavier Jehl, Silvano De Franceschi, Maud Vinet et Tristan Meunier. *Gate-Based High Fidelity Spin Readout in a CMOS Device*. Nature Nanotechnology, vol. 14, no. 8, pages 737–741, August 2019.
- [van der Wiel2002] W. G. van der Wiel, S. De Franceschi, J. M. Elzerman, T. Fujisawa, S. Tarucha et L. P. Kouwenhoven. *Electron Transport through Double Quantum Dots*. Reviews of Modern Physics, vol. 75, no. 1, pages 1–22, December 2002.
- [van der Wiel2006] W. G. van der Wiel, M. Stopa, T. Koder, T. Hatano et S. Tarucha. *Semiconductor Quantum Dots for Electron Spin Qubits*. New Journal of Physics, vol. 8, no. 2, pages 28–28, February 2006.
- [van Diepen2021] Cornelis J. van Diepen, Tzu-Kan Hsiao, Uditendu Mukhopadhyay, Christian Reichl, Werner Wegscheider et Lieven M. K. Vandersypen. *Electron Cascade for Distant Spin Readout*. Nature Communications, vol. 12, no. 1, page 77, December 2021.
- [Vandersypen2017] L. M. K. Vandersypen, H. Bluhm, J. S. Clarke, A. S. Dzurak, R. Ishihara, A. Morello, D. J. Reilly, L. R. Schreiber et M. Veldhorst. *Interfacing Spin Qubits in Quantum Dots and Donors—Hot, Dense, and Coherent*. npj Quantum Information, vol. 3, no. 1, page 34, December 2017.
- [Veldhorst2014] M. Veldhorst, J. C. C. Hwang, C. H. Yang, A. W. Leenstra, B. de Ronde, J. P. Dehollain, J. T. Muhonen, F. E. Hudson, K. M. Itoh, A. Morello et

-
- A. S. Dzurak. *An Addressable Quantum Dot Qubit with Fault-Tolerant Control-Fidelity*. *Nature Nanotechnology*, vol. 9, no. 12, pages 981–985, December 2014.
- [Veldhorst2017] M. Veldhorst, H. G. J. Eenink, C. H. Yang et A. S. Dzurak. *Silicon CMOS Architecture for a Spin-Based Quantum Computer*. *Nature Communications*, vol. 8, no. 1, page 1766, December 2017.
- [Vigneau2022] Florian Vigneau, Federico Fedele, Anasua Chatterjee, David Reilly, Ferdinand Kuemmeth, Fernando Gonzalez-Zalba, Edward Laird et Natalia Ares. *Probing Quantum Devices with Radio-Frequency Reflectometry*. arXiv:2202.10516 [cond-mat, physics:quant-ph], February 2022.
- [Vinet2018] M. Vinet, L. Hutin, B. Bertrand, S. Barraud, J.-M. Hartmann, Y.-J. Kim, V. Mazzocchi, A. Amisse, H. Bohuslavskyi, L. Bourdet, A. Crippa, X. Jehl, R. Maurand, Y.-M. Niquet, M. Sanquer, B. Venitucci, B. Jadot, E. Chanrion, P.-A. Mortemousque, C. Spence, M. Urdampilleta, S. De Franceschi et T. Meunier. *Towards Scalable Silicon Quantum Computing*. In 2018 IEEE International Electron Devices Meeting (IEDM), pages 6.5.1–6.5.4, December 2018.
- [Volk2019] C. Volk, A. M. J. Zwerver, U. Mukhopadhyay, P. T. Eendebak, C. J. van Diepen, J. P. Dehollain, T. Hensgens, T. Fujita, C. Reichl, W. Wegscheider et L. M. K. Vandersypen. *Loading a Quantum-Dot Based “Qubyte” Register*. *npj Quantum Information*, vol. 5, no. 1, pages 1–8, April 2019.
- [Warren2022] Ada Warren et Sophia E. Economou. *Silicon Qubits Move a Step Closer to Achieving Error Correction*. *Nature*, vol. 601, no. 7893, pages 320–322, January 2022.
- [Watson2018] T. F. Watson, S. G. J. Philips, E. Kawakami, D. R. Ward, P. Scarlino, M. Veldhorst, D. E. Savage, M. G. Lagally, Mark Friesen, S. N. Copper-smith, M. A. Eriksson et L. M. K. Vandersypen. *A Programmable Two-Qubit Quantum Processor in Silicon*. *Nature*, vol. 555, no. 7698, pages 633–637, March 2018.
- [Wei1997] Y. Y. Wei, J. Weis, K. v. Klitzing et K. Eberl. *Single-Electron Transistor as an Electrometer Measuring Chemical Potential Variations*. *Applied Physics Letters*, vol. 71, no. 17, pages 2514–2516, October 1997.
- [Weinreb2007] Sander Weinreb, Joseph C. Bardin et Hamdi Mani. *Design of Cryogenic SiGe Low-Noise Amplifiers*. *IEEE Transactions on Microwave Theory and Techniques*, vol. 55, no. 11, pages 2306–2312, November 2007.
-

- [Weisbuch1977] Claude Weisbuch et Claudine Hermann. *Optical Detection of Conduction-Electron Spin Resonance in GaAs, Ga_{1-x}In_xAs, and Ga_{1-x}Al_xAs*. Physical Review B, vol. 15, no. 2, pages 816–822, January 1977.
- [West2019] Anderson West, Bas Hensen, Alexis Jouan, Tuomo Tantt, Chih-Hwan Yang, Alessandro Rossi, M. Fernando Gonzalez-Zalba, Fay Hudson, Andrea Morello, David J. Reilly et Andrew S. Dzurak. *Gate-Based Single-Shot Readout of Spins in Silicon*. Nature Nanotechnology, vol. 14, no. 5, pages 437–441, May 2019.
- [Xue2022] Xiao Xue, Maximilian Russ, Nodar Samkharadze, Brennan Undseth, Amir Sammak, Giordano Scappucci et Lieven M. K. Vandersypen. *Quantum Logic with Spin Qubits Crossing the Surface Code Threshold*. Nature, vol. 601, no. 7893, pages 343–347, January 2022.
- [Yang2013] C. H. Yang, A. Rossi, R. Ruskov, N. S. Lai, F. A. Mohiyaddin, S. Lee, C. Tahan, G. Klimeck, A. Morello et A. S. Dzurak. *Spin-Valley Lifetimes in a Silicon Quantum Dot with Tunable Valley Splitting*. Nature Communications, vol. 4, no. 1, page 2069, October 2013.
- [Yang2020] C. H. Yang, R. C. C. Leon, J. C. C. Hwang, A. Saraiva, T. Tantt, W. Huang, J. Camirand Lemyre, K. W. Chan, K. Y. Tan, F. E. Hudson, K. M. Itoh, A. Morello, M. Pioro-Ladrière, A. Laucht et A. S. Dzurak. *Operation of a Silicon Quantum Processor Unit Cell above One Kelvin*. Nature, vol. 580, no. 7803, pages 350–354, April 2020.
- [Yoneda2018] Jun Yoneda, Kenta Takeda, Tomohiro Otsuka, Takashi Nakajima, Matthieu R. Delbecq, Giles Allison, Takumu Honda, Tetsuo Kodera, Shunri Oda, Yusuke Hoshi, Noritaka Usami, Kohei M. Itoh et Seigo Tarucha. *A Quantum-Dot Spin Qubit with Coherence Limited by Charge Noise and Fidelity Higher than 99.9%*. Nature Nanotechnology, vol. 13, no. 2, pages 102–106, February 2018.
- [Zaytseva2020] Iryna Zaytseva, Aleksander Abaloszew, Bruno C. Camargo, Yevgen Syryany et Marta Z. Cieplak. *Upper Critical Field and Superconductor-Metal Transition in Ultrathin Niobium Films*. Scientific Reports, vol. 10, no. 1, page 19062, November 2020.
- [Zener1932] Clarence Zener et Ralph Howard Fowler. *Non-Adiabatic Crossing of Energy Levels*. Proceedings of the Royal Society of London. Series A, Containing Papers of a Mathematical and Physical Character, vol. 137, no. 833, pages 696–702, September 1932.

- [Zhao2019] R. Zhao, T. Tantt, K. Y. Tan, B. Hensen, K. W. Chan, J. C. C. Hwang, R. C. C. Leon, C. H. Yang, W. Gilbert, F. E. Hudson, K. M. Itoh, A. A. Kiselev, T. D. Ladd, A. Morello, A. Laucht et A. S. Dzurak. *Single-Spin Qubits in Isotopically Enriched Silicon at Low Magnetic Field*. Nature Communications, vol. 10, no. 1, page 5500, December 2019.
- [Zheng2019] Guoji Zheng, Nodar Samkharadze, Marc L. Noordam, Nima Kalhor, Delphine Brousse, Amir Sammak, Giordano Scappucci et Lieven M. K. Vandersypen. *Rapid Gate-Based Spin Read-out in Silicon Using an on-Chip Resonator*. Nature Nanotechnology, vol. 14, no. 8, pages 742–746, August 2019.

Acknowledgements

Il est jeudi soir, je suis assis au même bureau qu'il y a trois ans quand j'ai commencé ma thèse et pourtant énormément de choses ont changé. Durant ce projet de thèse j'ai eu la chance de rencontrer pas mal de personnes qui m'ont faites grandir tant scientifiquement qu'humainement et je tiens à les remercier ici.

Merci tout d'abord à toi Tristan de m'avoir confié ce projet qui a accaparé ma vie durant ces trois dernières années. Tu as su partager avec moi ta passion pour la physique des quantum dots et je me rappellerai d'un directeur de thèse impliqué et soucieux de la réussite de son étudiant.

I would like to thank Andrea Morello and Isabelle Robert to have accepted to read my thesis manuscript and I am honored by their presence in my Ph.D. defense jury. I also thank Matthieu Desjardins and David Ferrand for their participation in my Ph.D. jury.

Je tiens également à remercier mon co-encadrant de thèse Pierre-André Mortemousque, PAM, MorteMisque, PisquePoutre,... Tu as toujours été disponible pour discuter avec moi de physique des arrays et j'ai énormément appris à travers tes travaux sur le 9 dots. Tu as été pour moi un modèle en terme de rigueur scientifique à atteindre et j'espère m'en être approché durant cette thèse (peut-être par peur de tes représailles !). Je ne pense pas que j'aurais réussi cette thèse si l'équipe du Bâtiment M ne comprenait pas Baptiste aka le meilleur post-doc dont un thésard puisse rêver aka Jadiot. Tu as été un encadrant rassurant qui a toujours su trouver les bons mots pour faire ressortir le meilleur de moi-même. La découverte du varactor avec le "attends mais la fréquence elle bouge ???", ou encore l'électrocution évitée de justesse en sortie de confinement sont des souvenirs qui resteront ancrés dans ma mémoire. Merci pour ta disponibilité tard la nuit quand la Sion ne voulait pas condenser, ton attention, et ta gentillesse. Bref tu n'as aucun défaut si ce n'est peut-être ton niveau limité en ski de fond. Cette ambiance spéciale du bâtiment M ne serait rien sans son deuxième permanent Matias Urdampoupita (ça s'écrit comme ça se prononce). Merci pour tous les moments spéciaux que tu m'as accordés que ce soit une discussion de physique, un foot, un tour de vélo, un concert, une bière ou un match de rugby. Pour en finir avec les permanents et post-docs qui m'ont accompagné (porté ?) pendant cette thèse, j'invoque le dragon blanc aux yeux... euh non Chanarion aka pedagogic-man aka happiness manager aka Manu. Tu as su me faire apprécier une présentation claire et PE-DA-GO-GIQUE et me faire comprendre en quoi c'est primordial dans notre travail de tous les jours. Merci pour ta passion de la physique communicative et ta détermination à toujours aller se jeter un petit godet qu'il vente, qu'il pleuve ou qu'il neige. Promis un jour je viendrais faire un plongeon du toit de ta maison en revenant de Presles !

Pour compléter le côté Raoult du bâtiment M je voudrais faire un énorme S.O. à mon partenaire dans le crime Victor Viktorovitch ! Courage pour la fin de ta thèse et j'espère que toi aussi un jour tu auras ton propre podcast (dans l'objectif d'une kichta élastique bien tendu). Et pour finir merci à Clément mon frère jumeau de thèse qui a commencé le même jour que moi et qui fait

sa thèse dans un univers parallèle du bâtiment M. Ne lâchez rien les gars si j'ai pu le faire vous en êtes largement capable ! Je tiens aussi à remercier les autres membres du groupe: Vivien qui m'a formé de manière express à la salle blanche et qui m'a permis d'avoir un échantillon super rapidement; Matthieu D. pour les discussions sur des sujets de physique obscurs (genre la topologie et RKKouhète) et l'aide au quotidien sur git; Bruna pour les supers gâteaux et les choix de restos à Chicago; David; Bernhard et Renan. Je fais aussi un clin d'oeil aux nouveaux arrivants: Mathieu j'espère que tu pourras aller en conf à Kyoto, occupe-toi bien de Baptiste il le mérite; Oscar pour m'avoir fait découvrir les arêtes du Gerbier et la grande voie dans le 7ème degré, on y retournera pour la sortir en libre cette longueur !; Pierre.

Cette thèse n'aurait pas pu être menée à son terme sans l'implication et le haut niveau de compétence des pôles techniques de l'institut Néel. Je tiens donc tout d'abord à remercier l'ensemble du pôle Ingénierie Expérimentale et notamment Eric qui a su sauver la SionLudi de sa mort prématurée. Merci à tous le pôle NanoFab et surtout à son leader charismatique Thierry Crozes, merci pour les lithos laser entre midi et deux qui font gagner deux semaines sur le process, je ne sais pas comment on ferait sans toi ! Merci au pôle électronique pour les DACs et les convertisseurs courant-tension sans lesquelles aucune expérience ne tournerait. Merci à l'équipe administrative de QUEST et Angélique Simoes pour sa bonne humeur et son aide précieuse. Merci également à Henri pour l'aide au quotidien sur l'utilisation de tous les outils disponible au bâtiment M.

Une grosse grosse dédicace à mes meilleurs amis la cliquasse des 4M: Max mon partenaire de cordée qui a toujours su me faire oublier tous mes soucis le temps d'une grande voie ou d'une soirée, nos virées à Presles resteront toujours des moments importants pour moi même quand on a failli y passer; DL bucheron-cordiste qui aura bientôt plus de diplôme que moi si il continue comme ca, merci pour ta vision décalée du monde qui me permet de garder les pieds sur terre; Seris même si on se voit moins souvent les souvenirs refont vite surface quand on se retrouve le temps d'une teuf.

J'ai une pensée pour ma deuxième clique celle de Phelma: Sten aka acharné du boulot, on a coché de belles voies ensemble; Justine qui n'a pas voulu garder la chambre Dofus (ca dégoute); Tamara qui me rappelle toujours le sud; Félix de nous avoir permis de rentrer au Vieux Minou pour cette soirée légendaire; Martin et Suzy pour cette fabuleuse journée de pré-mariage, on a hâte du vrai cet été; Victor pour ta bonne humeur et ton oreille attentive; Clara et Adrian ça nous tarde de grimper à Cassis avec vous !

Je voudrais aussi faire un bisou à mes parents qui m'ont permis d'en arriver ici aujourd'hui sans trop d'encombre, durant l'ensemble de ma scolarité vous avez su créer un cocon dans lequel il était facile de s'épanouir. Un gros bisou à mes deux soeurs Gabriele la personne la plus courageuse que je connaisse et Jeanne la gatounette qui empêche nos parents de vieillir trop vite. Un bisou aussi pour ma troisième soeur, Fanny ma tatie de l'extrême qui a réussi à m'emmener à Cancun !!! Un grand merci au reste de ma famille notamment mes grands-parents dont je n'ai pas pu beaucoup profiter entre le COVID et la thèse j'espère que je pourrai rattraper le temps perdu. Merci également à la famille Bardet pour les beaux moments composé de naissances, ascensions

de sommets emblématiques, de leçons sur les 10⁶ variétés de bolets, de découverte de la Bretagne, de remèdes magiques pour le rhume dû à la découverte précédemment citée.

Finalement je voudrais remercier la personne la plus importante à mes yeux, celle sans qui je n'aurais pas réussi à finir d'écrire cette thèse. Dans les moments de stress tu as toujours su trouver les mots justes pour m'apaiser et c'est avec toi que j'ai partagé, je partage et espère encore partager les plus beaux moments de ma vie. Tu es depuis maintenant 7 ans ma meilleure amie, ma confidente, mon amoureuse, merci Laetitia.

